PHYSIK-DEPARTMENT

Current-Controlled Spin-Wave Interference in Magnonic Waveguides and Magnetization Dynamics in Artificial Spin Ice and Ferromagnetic Nanotubes

Dissertation
von
Florian J. Heimbach

TECHNISCHE UNIVERSITÄT
MÜNCHEN

TECHNISCHE UNIVERSITÄT MÜNCHEN
Lehrstuhl für Physik funktionaler Schichtsysteme, E10

Current-Controlled Spin-Wave Interference in Magnonic Waveguides and Magnetization Dynamics in Artificial Spin Ice and Ferromagnetic Nanotubes

Florian J. Heimbach

Vollständiger Abdruck der von der Fakultät für Physik der Technischen Universität München zur Erlangung des akademischen Grades eines

Doktors der Naturwissenschaften

genehmigten Dissertation.

Vorsitzender: Prof. Dr. Uli Gerland
Prüfer der Dissertation:
1. Prof. Dr. Dirk Grundler
2. Prof. Dr. Martin Brandt

Die Dissertation wurde am 13.05.2016 bei der Technischen Universität München eingereicht und durch die Fakultät für Physik am 24.05.2016 angenommen.

Abstract

The magnetic properties and behavior of different ferromagnetic structures have been investigated. We used micro CPWs to excite spin waves (SWs) and measure the response of the magnetization of the sample with different measurement techniques. OOMMF simulations showed an excitation of standing SWs in different parts on artificial spin ice (ASI) structures. This enabled us to probe the SW excitation in specific elements of the ASI structure and determine the switching behavior of whose magnetization. It was revealed that the magnetization configuration of adjoined elements influence the SW frequency in the excited elements. Comparison of the experimental data, with a theoretical model for switching in a perfect ASI sample revealed significant discrepancies in the behavior very likely due to surface roughness and small defects in the measured samples. Heating parts of the ASI structure via illumination with a laser enabled us to change the switching behavior in the heated regions of the structure. Utilizing a BLS setup enabled the determination of the SW intensity distribution, discovering interference effects of SWs in Y-shaped waveguides, combining two coherent SWs. With an electrical current in a conductor underneath the wave guide it was possible to change the phase difference between the SWs by about 2π and changing the resulting local intensity in this process. In a third part the EDFMR technique and transport measurement was used to investigate the magnetic reversal process as well as SW modes in ferromagnetic nanotubes. Due to the AMR effect, the transport measurements gave an insight in the magnetization behavior during the switching process of the magnetization in the tube. The evidence suggests a uniform rotation of the magnetization before the actual switching of the magnetization. By fitting of EDFMR data (spin rectification) it was possible to ascribe excited SW modes to azimuthal SWs in the tubes.

Die magnetischen Eigenschaften und das Verhalten von unterschiedlichen ferromagnetischen Strukturen wurden untersucht. Wir benutzen Mikro-CPWs um Spinwellen (SWs) anzuregen und verschiedene Messmethoden, um die Reaktion der Magnetisierung der Probe, zu erfassen. OOMMF

Simulationen zeigten die Anregung von stehenden SWs in unterschiedlichen Teilen des artificial spin ice (ASI). Dies ermöglichte uns das Sondieren der SW Anregung in bestimmten Teilen der ASI Struktur und das Erfassen des Umschaltverhaltens der Magnetisierung in diesen Elementen. Es kam auf, dass die Konfiguration der Magnetisierung von benachbarten Elementen Einfluss auf die SW Frequenz in den angeregten Elementen hat. Ein Vergleich der experimentellen Daten mit einem theoretischen Model für das Umschalten in perfekte ASI Strukturen zeigte deutliche Abweichungen im Verhalten, sehr wahrscheinlich auf Grund von Oberflächenrauheit und kleinen Defekten in den gemessenen Proben. Durch das lokale Erhitzen von Teilen der ASI Struktur mithilfe eines Lasers, war es möglich das Umschaltverhalten in den erhitzten Regionen der Struktur zu ändern. Das Verwenden eines BLS-Setups ermöglichte die Ermittlung der SW Intensitätsverteilung, was Interferenzeffekte in Y-förmigen Wellenleitern, welche zwei kohärente SWs vereinen, zeigte. Mit Hilfe von elektrischen Strom, durch einen Leiter unterhalb des Wellenleiters, war es möglich den Phasenunterschied zwischen den SWs um etwa 2π und damit die resultierende Intensität, zu ändern. Im dritten Teil wurden die EDFMR-Technik und Transportmessungen verwendet, um die Umkehrung der Magnetisierung, sowie SW-Moden in ferromagnetischen Nanoröhren zu untersuchen. Aufgrund des AMR-Effekts gab die Transportmessung Einsicht in das Verhalten der Magnetisierung während des Umschaltprozesses der Magnetisierung in den Nanoröhren. Die Ergebnisse weisen auf eine gleichförmige Rotation der Magnetisierung vor dem eigentlichem Umschalten der Magnetisierung hin. Durch anpassen von EDFMR Daten ("spin rectification"), konnten angeregte SW-Moden auf azimutale SWs zurückgeführt werden.

Contents

1. Introduction

In the last decades we experienced a significant change on our everyday live. Smartphones, tablets and microcontrollers in household aids can be found in most modern households, communicating among each other, sharing information. This was enabled by the rapid development and improvement of the miniaturization of electrical circuits and rf devices. The trend is still ongoing leading to more powerful, smaller computers and there is still room for further improvements. However, the current technique has its limits.

The diminution is limited by power density, heating the device, or the finite size of wavelengths at fixed frequencies. To overcome these obstacles, scientists are trying to find work arounds, using novel technologies and utilizing new physical effects [Itr]. A possible solution could be the coupling of electromagnetic waves to spin wave (SW). The transfer to spin waves significantly reduces the wavelength and enables an information transport with low power consumption. An important step in utilizing SWs is the development of logical gates. Several attempts have already been made mainly using interference between two electoral SW detection signals (e.g. [Kos+05] [KBW10] [Rou+15]). While this concept is working very well, it relies on a transformation of the signal back to an electrical signal. In the framework of this thesis we are trying a new approach detecting and influencing the direct interference of SWs in adjusted Y-shaped samples.

The excitation frequency of SWs depends on various parameters such as the internal field, the magnetization of the material or the different material parameter. This dependency can be used to e.g. receive information about the internal magnetic state of a sample by determining the excitation frequencies of SW modes at fix set of parameters. This and other techniques have been used in this thesis to investigate artificial spin ice (ASI) honeycomb networks. The first ASI was created by Wang et al. 2006 [Wan+06]. By arranging ferromagnetic nanoscale islands on a square lattice they generated a geometrically frustrated system. Frustration occurs in a system when competing interactions cannot be satisfied at the same time, which is leading to highly degenerated low-energy states [Far+14]. The search for

the ground state and the understanding of the behavior of frustrated systems has been a topic of interest for several decades. The insight gained in this process provided the base for theories to describe similar problems in other scientific fields e.g. the modeling of neural networks [TDC86] or protein dynamics [BW87]. With the possibility to fabricate an ASI its properties and behavior can be influenced by the material and dimensions. Also the nature of the system enables us to locally probe individual parts of the network in contrary to other frustrated systems. The ASI system utilized in the framework of this thesis is the honeycomb network. The frustration in this system was first observed by Qi et al. in 2008 [QBC08]. We were using different methods to excite and detect SWs in such networks consisting of Py or CoFeB as well as other techniques to gain further insight into their properties and behavior.

Similar methods also have been used on ferromagnetic nanotubes. In the course of the digital revolution it is also the goal to improve the techniques for the storage of information, increasing the data density and the access speed. Nowadays the most used form of data storage is the 2D magnetic hard drive. The information is stored in the magnetization of small ferromagnetic regions. However, shrinking of these areas over the last 50 years has led to a point were further reduction would require read and writing technology that is difficult or too expensive to acquire [PY15]. A new promising alternative technique for data storage is the so called race track memory [PY15]. The information gets stored by injecting domain walls (DWs) and moving them along a guiding system using an electrical current. The movement speed of the DWs back and forth is an essential parameter for the performance of the data transfer to and from the DW guide. By using a tube structure the DWs get stabilized and a higher DW traveling speed is possible [Yan+11]. Due to whose geometrical structure ferromagnetic nanotubes are also interesting for medical [Son+05] and other applications [Rüf14]. In this work we were producing ferromagnetic tubes by coating non ferromagnetic GaAs nanowires with Ni and CoFeB. Using EDFMR and transport measurements enables us to receive data from individual nanotubes despite whose small size, giving us insight in its magnetization configuration.

Overview of the thesis

The thesis is structured as follows: Chapter 2 is providing the necessary theoretical background. This is supplemented by Chap. 3 which is describing the used measurement techniques (i.e. EDFMR, AESWS or BLS) and setups. The fabrication of the samples used in this thesis can be found in Chap. 4. We are also addressing different challenges occurring during the sample preparation. The actual measurements and the interpretations can be found in Chap. 5 for artificial spin ice, Chap. 6 for Y-shaped interferometer structures and Chap. 7 for ferromagnetic nanotubes. Depending on the samples we are using different techniques to acquire the relevant data. The thesis is completed by a summary and an outlook in Chap. 8.

2. Theory

In the course of this thesis we use different methods to investigate ferromagnetic samples and their magnetic configurations. This chapter provides the theoretical background to conduct and interpret this experiments mainly following [DS09] [Blu01] [Gie05] [Hub13] [Sch13] [Neu11] [Bra14] [Bil07]. We start with the basic properties of magnetism followed by its static behavior. Thereafter we also discuss the dynamic behavior and present an analytical model for spin waves. The discussion is followed by a description of the anisotropic magnetoresistance, spin rectification and frustrated systems with a focus on artificial honeycomb spin ice structures.

2.1. Magnetism

An important material parameter is the magnetic susceptibility $\hat{\chi}$ which describes the response of the magnetization $\mathbf{M}$ in a magnetic field $\mathbf{H}$ by

$$\mathbf{M} = \hat{\chi}\mathbf{H}, \tag{2.1}$$

with $\mathbf{M}$ as microscopic magnetic moments $\mathbf{m}$ per volume [Sko08]:

$$\mathbf{M} = \frac{\mathrm{d}\mathbf{m}}{\mathrm{d}V}. \tag{2.2}$$

Because $\mathbf{M}$ and $\mathbf{H}$ don't have to be aligned to each other, $\hat{\chi}$ is a tensor. But in an isotropic material $\hat{\chi}$ becomes a scalar and we can use the value of the susceptibility to categorize materials into different groups as shown in the following categories [DS09]:

- $\chi < 0$ Diamagnetic material:
  Diamagnetic materials have only atoms or ions without a permanent magnetic moment. By applying an external magnetic field the motion of the orbital electrons is altered. This leads to a magnetic field which is, according to Lenz's law, opposing the applied field. All materials have a diamagnetic contribution. But in materials with

permanent magnetic moments, in general it is so small compared to the permanent moment, it can be neglected.

- $\chi > 0$ Paramagnetic material:
  Paramagnetic materials contain permanent magnetic moments. But in opposition to other materials there is no spontaneous long-range ordering. Without an external field the magnetic moments are randomly oriented and the net magnetization of the material is zero. By applying a field **H** the spins align parallel to **H** and therefore, the net magnetization is increased.

- $\chi >> 0$ Ferromagnet material:
  In ferromagnetic materials the permanent magnetic moments spontaneously align (below a critical temperature, the Curie temperature) even without an external field. The reason for this is the exchange interaction which is of quantum mechanical origin. However without a field **H** the magnetization of the whole sample is often not completely oriented in one direction, but is divided into different domains. The orientation inside of each domain is the same but changes from one domain to another. At $\mathbf{H} = 0$ the domains are oriented to minimize the stray field of the macroscopic sample. This leads in general to a net magnetization of zero. By applying a magnetic field the domains are oriented along the field direction. Above the Curie temperature there is no more spontaneous long range alignment and the material becomes paramagnetic.

- $\chi >> 0$ Ferrimagnet material:
  In ferrimagnetic materials magnetic moments don't only align parallel, but also antiparallel. This can be described by different sublattices with at least one having an opposed orientation. One prominent example of a ferrimagnet is YIG ($Y_3Fe_5O_{12}$). Three of the iron ions form a sublattice and the other two form an opposing sublattice resulting in a net moment of one Fe atom per molecule. In many cases ferrimagnets can be treated as ferromagnets with a net magnetization. Also similar to the ferromagnet, ferrimagnets become paramagnetic at temperatures above the Curie temperature.

- $\chi > 0$ Antiferromagnet material:
  In antiferromagnets there are also two sublattices as described in the

ferrimagnetic materials. The difference is that in antiferromagnets the opposing sublattices are of equal strength. Therefore, the magnetic moments cancel each other out leaving a net magnetization of zero. Above a critical temperature (Néel temperature) the material becomes paramagnetic.

The focus of this work is on ferromagnetic materials.
In addition to the field **H** the magnetic flux density **B** is defined as

$$\mathbf{B} = \mu_0(\mathbf{M} + \mathbf{H}) = \mu_0(\hat{\chi} + 1)\mathbf{H}. \tag{2.3}$$

With the vacuum permeability μ_0. $(\hat{\chi} + 1)$ is defined as relative permeability $\hat{\mu}_r$.

2.2. Static magnetization

To describe the magnetization dynamics in ferromagnetic materials, one important factor is the magnetic ground state. It is determined by the sum of different energy contributions which will be described in the following section. For this we are using the continuum model. There the magnetization **M** is the sum over the magnetic moments divided by the enclosed volume.

Exchange energy

In ferromagnets we can observe spontaneous magnetization at room temperature. This stands for parallelly aligned magnetic moments without an applied field. The reason for the alignment is the exchange interaction. It is the result of an energy difference between the possible states of overlapping wave functions. As a simple example we consider two electrons in neighboring atoms.

The wave function for both electrons can be spatially symmetric (Ψ_S) or antisymmetric (Ψ_A), leading to an energy E_S or E_A, respectively. However, electrons obey the Pauli exclusion principle, which states that two fermions must not be in the same state. Therefore, the complete two-particle wave function (including spin) has to be antisymmetric [DS09]. As a result one has to assign a antisymmetric spin wave function (antiparallel spins) to Ψ_S and a symmetric spin wave function (parallel spins) to Ψ_A.

In our example parallel spins (spatially antisymmetric) leads to a bigger distance and therefore, decreases the Coulomb repulsion energy [Blu01] between the electrons. On the other hand the kinetic energy of the electrons is increased [Blu01] compared to an antiparallel spin configuration. To determine which spin configuration (parallel or antiparallel) is more favorable it is common to use the Heisenberg spin Hamiltonian [Blu01][DS09]

$$\hat{\mathscr{H}} = -\sum_{i,j} J_{ij} \hat{\mathbf{S}}_i \cdot \hat{\mathbf{S}}_j, \tag{2.4}$$

where J_{ij} is the exchange integral [Blu01][DS09]

$$J_{ij} = \frac{E_\mathrm{S} - E_\mathrm{A}}{2} \tag{2.5}$$

between spin i and j. By replacing the spin operators with vectors, the exchange energy can be determined by the sum over all spin pairs,

$$\mathbf{E}_\mathrm{ex} = -\sum_{i,j} J_{ij} \mathbf{S}_i \cdot \mathbf{S}_j = -2\sum_{i<j} J_{ij} \mathbf{S}_i \cdot \mathbf{S}_j, \tag{2.6}$$

for a positive exchange integral $J > 0$ the parallel alignment of the spins is favored, leading to a ferromagnetic ordering. The strength of the exchange interaction is decreasing very rapidly with an increasing distance between two electrons. Therefore, the exchange interaction of a system can often be treated as a next neighbor problem [Kit66]. Despite the small range it is the origin of the long range ordering, due to its high strength.

In itinerant ferromagnets, which are utilized in this thesis, the exchange interaction can be described with an exchange field. It leads to a splitting between the spin-up and spin-down bands in the material [Blu01]. To determine if it is favorable to align the spins along the field and obtain a ferromagnetic state one can use the Stoner criterion [Blu01]

$$\mu_0 \mu_B^2 \lambda_\mathrm{St} D(E_F) \geq 1, \tag{2.7}$$

with the Bohr magneton $\mu_B = \frac{e\hbar}{2m_e}$, the density of states$D(E_F)$ with E_F as the Fermi energy and λ_St as an empirical parameter describing the average exchange field. If Eq. 2.7 is fulfilled, the reduction of the Coulomb energy overcompensations the increase in kinetic energy and a parallel align-

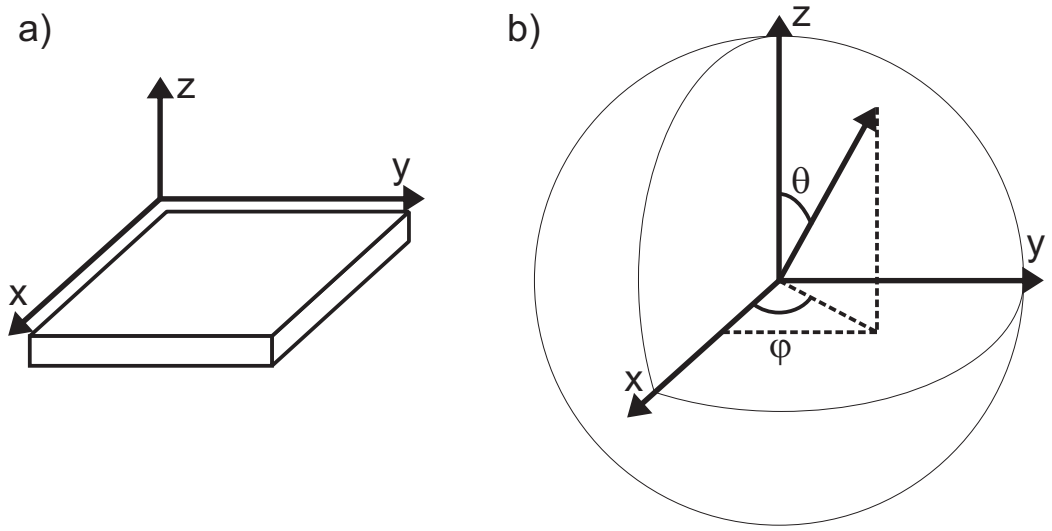

Figure 2.1.: Definition of the Cartesian coordinate system with a thin film in the xy-plane a) and the spherical coordinate system b). The direction in b) is determined by the azimuthal angle φ and the polar angle θ.

ment occurs. By using a Taylor approximation on Eq. 2.6 one gets the energy density [HS98][Bil07]

$$\mathscr{E}_{\mathrm{ex}} = \frac{A}{VM^2} \int \mathrm{d}V \left(\nabla \cdot \mathbf{M}\right)^2, \tag{2.8}$$

in which A is the exchange stiffness constant. A of a material is related to the exchange integral via $A = nJS^2/a$, with the magnitude of the spin S, the lattice constant a and a factor n depending on the crystal structure.

Zeeman energy

The application of an external field **H** leads to an energy contribution due to the interaction of **H** with the magnetization **M**. The resulting energy density is given by

$$\mathscr{E}_{\mathrm{Z}} = -\frac{\mu_0}{V} \int \mathrm{d}V \mathbf{M} \cdot \mathbf{H}. \tag{2.9}$$

The energy has a minimum for parallel **M** and **H**. For a uniform **M** and **H** we get

$$\mathscr{E}_{\mathrm{Z}} = -\mu_0 |\mathbf{M}| \cdot |\mathbf{H}| \cdot \cos\beta, \tag{2.10}$$

with the angle β between **M** and **H**. In spherical coordinates one obtains

$$\mathscr{E}_{\mathrm{Z}} = -\mu_0 |\mathbf{M}| \cdot |\mathbf{H}| \cdot (\cos\theta_M \cos\theta_H + \sin\theta_H \sin\theta_M \cos(\varphi_M - \varphi_H)). \tag{2.11}$$

φ is the azimuthal and θ the polar angle (see Fig. 2.1) of **M** and **H**.

Demagnetization energy

The origin of the demagnetization energy contribution is the long range dipole-dipole interaction between the spins. To calculate the energy one needs the demagnetization field $\mathbf{H}_{\mathrm{dem}}$ which is generated by the divergence of the magnetization. By using the Maxwell equations we find

$$\nabla \cdot \mathbf{B} = \mu_0 \nabla \cdot (\mathbf{M} + \mathbf{H}_{\mathrm{dem}}) = 0 \Rightarrow \nabla \cdot \mathbf{H}_{\mathrm{dem}} = -\nabla \cdot \mathbf{M} \tag{2.12}$$

and for zero current density

$$\nabla \times \mathbf{H}_{\mathrm{dem}} = 0. \tag{2.13}$$

Using Eq. 2.12 and Eq. 2.13 one can use the Green's function approach to calculate $\mathbf{H}_{\mathrm{dem}}$ [BK86][Gus+02]. In general this is an involved calculation but can easily be done for a uniformly magnetized ellipsoid. One can use [Aha06]

$$\mathbf{H}_{\mathrm{dem}} = -\hat{\mathbf{N}}\mathbf{M}, \tag{2.14}$$

with $\hat{\mathbf{N}}$ as the position-independent demagnetizing tensor. Using the proper coordinate system we can write

$$\hat{\mathbf{N}} = \begin{pmatrix} N_x & 0 & 0 \\ 0 & N_y & 0 \\ 0 & 0 & N_z \end{pmatrix}. \tag{2.15}$$

The trace of the tensor fulfills $N_x + N_y + N_z = 1$. For a sphere the elements are $N_x = N_y = N_z = 1/3$. For other shapes the diagonal elements can be calculated analytically. Some results are shown in Table 2.1.

With the demagnetization field $\mathbf{H}_{\mathrm{dem}}$ the energy term can be written as

$$\mathscr{E}_{\mathrm{dem}} = -\frac{\mu_0}{2V} \int_{sample} \mathrm{d}V \mathbf{M} \cdot \mathbf{H}_{\mathrm{dem}}. \tag{2.16}$$

shape	diagonal elements	source
sphere	$N_x = N_y = N_z = 1/3$	[Osb45]
infinitely extended thin film	$N_x = N_y = 0, N_z = 1$	[Kit48]
stripe with ($t << w$), **M** parallel to the stripe, thickness t (z-direction) and width w (x-direction)	$N_y = 0, N_x = \frac{2t}{\pi w}, N_z = 1 - \frac{2t}{\pi w}$.	[DHS01]

Table 2.1.: Diagonal elements of the position-independent demagnetizing tensor.

By using Eq. 2.14 and Eq. 2.16 we express the energy density for a uniformly magnetized ellipsoid in spherical coordinates as

$$\mathscr{E}_{\mathrm{dem}} = -\frac{\mu_0}{2} M_{\mathrm{s}}^2 (N_x \sin^2\theta \cos^2\varphi + N_y \sin^2\theta \sin^2\varphi + N_z \cos^2\theta) \tag{2.17}$$

with M_{s} as the saturation magnetization.

Uniaxial Anisotropy

In materials such as e.g. $RECo_5$ (RE = rare earth) [LM03] or epitaxial Co on a Cu substrat [Zhu05] the energy depends on the orientation of the magnetization **M**. A prominent example for an origin of this effect is the magnetocrystalline anisotropy. There the energy depends on the magnetization direction with respect to specific axes of the crystal. This can for example lead to a uniaxial anisotropy. In this thesis Py ($Ni_{80}Fe_{20}$) and $Co_{20}Fe_{60}B_{20}$ are used. Py has little to no crystalline anisotropy and $Co_{20}Fe_{60}B_{20}$ is amorphous. So in both cases the crystalline anisotropy can be neglected. Another possibility to introduce anisotropy is e. g. the shape anisotropy. For a uniaxial anisotropy the behavior of the energy density a can be described by [Aha06] [AGG96] e.g.

$$\mathscr{E}_{\mathrm{uni}} = -K_{\mathrm{uni}} m_z^2, \tag{2.18}$$

with $m_z = \mathbf{M} \cdot \mathbf{e}_z$ and K_{uni} as the uniaxial anisotropy constant. Depending on the sign of K_{uni} a magnetization along z leads to an energy minima or maxima. Accordingly the z-direction is the easy or hard axis. In many cases the saturation magnetization M_{s} is included into the anisotropy constant. In spherical coordinates (see Fig. 2.1) Eq. 2.18 becomes

$$\mathscr{E}_{\mathrm{uni}} = -K_{\mathrm{uni}} \cos^2 \theta. \tag{2.19}$$

Surface Anisotropy

In thin films another anisotropy effect becomes important, the surface anisotropy. Near a surface the symmetry of the atomic environment gets reduced. Similar to the magnetocrystalline anisotropy the energy density now depends on the direction of the magnetization with respect to the surface normal. It can be described by

$$\mathscr{E}_{\perp} = -\frac{K_{\perp}}{d} m_z^2, \tag{2.20}$$

with $K_{\perp}$ as the surface anisotropy constant, the film thickness d and e_z as the axis perpendicular to the surface. Using spherical coordinates the energy is given by

$$\mathscr{E}_{\perp} = -\frac{K_{\perp}}{d} M_{\mathrm{s}}^2 \cos^2 \theta. \tag{2.21}$$

In bulk material this energy normally can be neglected, but it is important for thin films. The surface anisotropy field can be described by

$$H_{\perp} = -\frac{2K_{\perp}}{\mu_0 M_{\mathrm{s}} d} m_z^2. \tag{2.22}$$

Total Energy

By summing up all energy densities we acquire the total energy density

$$\mathscr{E}_{\mathrm{tot}} = \mathscr{E}_{\mathrm{ex}} + \mathscr{E}_{\mathrm{Z}} + \mathscr{E}_{\mathrm{dem}} + \mathscr{E}_{\mathrm{uni}} + \mathscr{E}_{\perp}. \tag{2.23}$$

To derive the magnetic ground state the density has to be minimized. By using the total energy density the effective magnetic field can be calculated

using

$$H_{\text{eff}} = -\frac{1}{\mu_0}\nabla_{\mathbf{M}}\mathscr{E}_{\text{tot}}. \tag{2.24}$$

2.3. Domains and Domain Walls

In previous sections of this work we assumed that the ferromagnetic ground state is the uniform magnetization. This is only true for small samples below a certain size, depending on the material and shape, or in a high magnetic field. The minimization of the total energy density (see Sec. 2.2) can lead to a competition between the different contributions. Therefore, in order to find the energy minimum complex domain formation can be created. E.g. a uniform magnetization leads to magnetic stray fields at the borders, outside the sample, which increase the overall energy. Hence, in cases without an external magnetic field it can be favorable, from an energetic point of view, to split the uniform magnetization in different magnetic domains. Each magnetic moment in a domain has the same direction, but the directions of the different domains are diverse. As a result the magnetic stray fields are reduced and the overall energy of the state is decreased. The effect of an increasing number of domains on the stray field is sketched in Fig. 2.2 a).

The idea of magnetic domains was first proposed by Weiss 1907 and later confirmed by Barkhausen in 1919 [HA98]. The areas separating different domains are the so called domain walls. In this zone the magnetization rotates from the direction of one adjacent domain to the direction of the other. To perform such a transition there are in general two possibilities. A rotation in and a rotation out of the plane of the domain wall. The transition with the in-plane rotation is the so called Néel wall. This kind of wall is only stable in films with a thickness smaller than the width of the wall [Coe10]. The other type of wall, the so called Bloch wall, is characterized by a rotation of the magnetization out of the wall plane. Figure 2.2 b) is illustrating the difference between the two types of walls. In the normal case Néel walls have a higher energy compared to Block walls [Coe10]. However in case of a film thickness t smaller than the wall width of the wall the magnetostatic energy for the Néel wall is smaller [Coe10]. Considering that the Bloch wall width is reduced in thin films to minimize stray fields one can find the Bloch-Néel crossover for permalloy

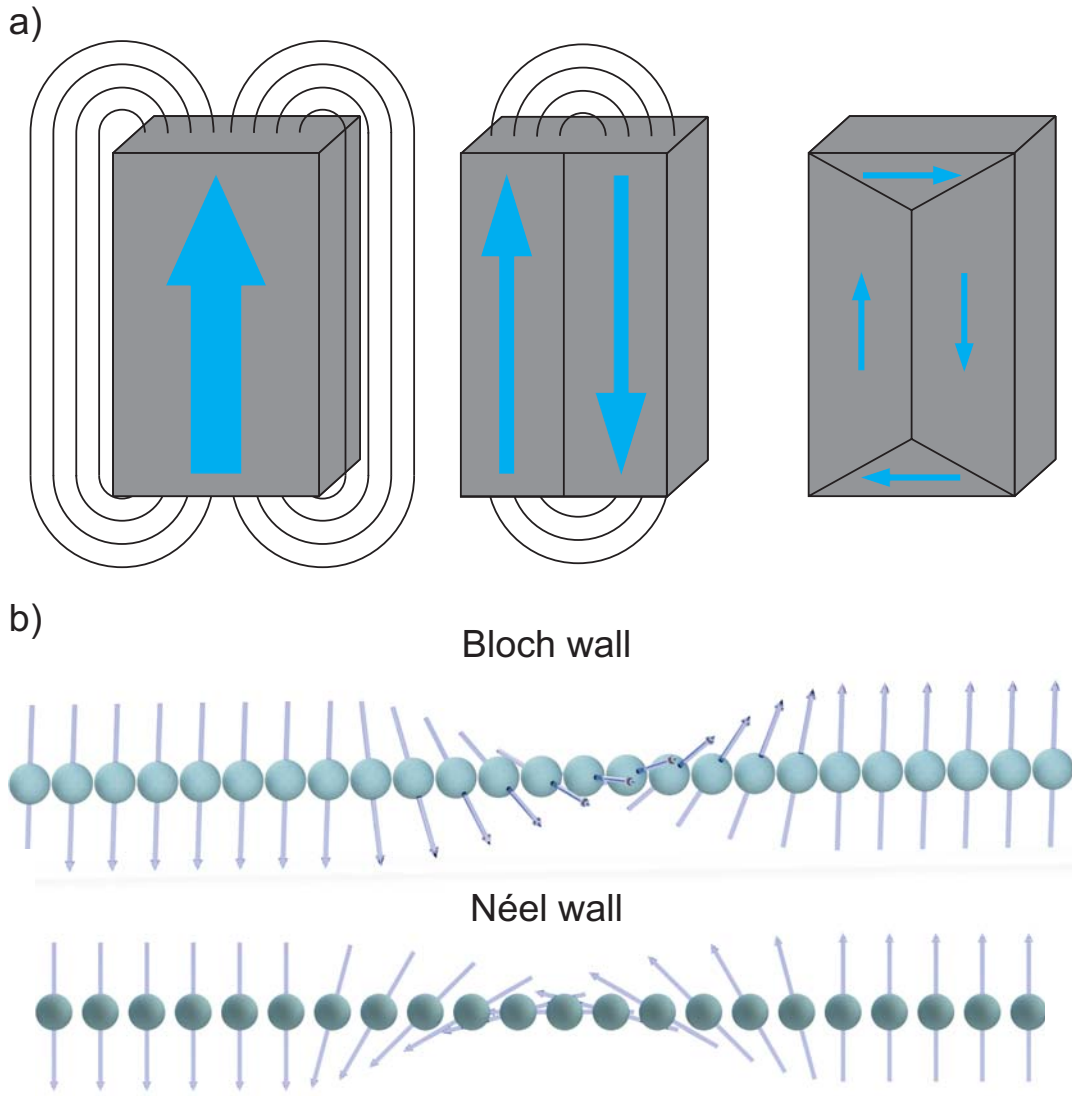

Figure 2.2.: a) Illustration of the magnetic stray field depended on domain configuration. b) Draft of two different type of domain walls. A Bloch wall and a Néel wall.

at a thickness of $t = 60$ nm [Coe10]. A possible combination of Bloch and Néel type is a vortex domain wall. It is characterized by a circulation of magnetization around a Bloch center with a Néel like rotation at the caps [Coe10][MD97]. A detailed description of the origin of domains and domain walls can be found in [Kit49].

2.3.1. Domain Walls in Nanostripes

The shape and layout of magnetic domains also depend on the shape and dimension of the magnetic material. By downscaling a nanostripe there is a point where it is not worthwhile anymore to create domains walls for the reduction of stray fields. The result is a uniform magnetized structure with only one domain. The magnetization lies along the long axis of the stripe which reduces the stray field compared to a magnetization perpendicular to the long axis [Coe10]. Since under normal conditions the magnetization has only the two options parallel and anti-parallel to the stripe axis, it can also be described as a macroscopic Ising spin. The direction of spin can be changed by applying a magnetic field H. The reversal of the magnetization is described in [Coe10]. It starts with the nucleation of a domain wall at one end of the stripe. Then the domain wall is moving though the material from one end to the other reversing the magnetization in the process.

According to [MD97] typically two types of domain walls can form in a thin nanostripe. A Néel-like transverse domain wall and a vortex domain wall. Which one of the two types is formed depends on the width w and the thickness t of the stripe. Following D. McMichael et al. [MD97] the transverse wall has a lower energy for smaller w and t with the critical crossover given by

$$t \cdot w = C l_{\mathrm{ex}}^2 \tag{2.25}$$

with the magnetostatic exchange length $l_{\mathrm{ex}} = \sqrt{A/\mu_0 M_{\mathrm{s}}^2}$ and $C = 128$. In literature the magnetostatic exchange length is also defined such as $\lambda_{\mathrm{ex}} = \sqrt{2A/\mu_0 M_{\mathrm{s}}^2}$ [Abo+13][Coe10]. To distinguish between this two definitions, we are using two different denotations l_{ex} and λ_{ex}.

The velocity of the domain wall depends on the external field. N. L. Schryer et al. [SW74] described the velocity in a 1D model with the assumption that the magnetization only varied perpendicular to the domain wall. Three different regimes were found. In the first regime, the velocity for fields below a critical field, the so called Walker field, without a current

is given by [TP07][A.+07]

$$v = \frac{\gamma \rho_w}{\alpha} H, \tag{2.26}$$

with the gyromagnetic ratio γ, the intrinsic Gilbert damping α and ρ_w as the width of the domain wall. When the field increased beyond the Walker threshold, a second regime was reached and the velocity droped abruptly. The third regime was at an even higher field. There the domain wall velocity depended linearly on the field, given by [TP07][A.+07]

$$v = \gamma \rho_w \frac{\alpha}{1 + \alpha^2} H. \tag{2.27}$$

Compared to Eq. 2.26 the mobility (v/H) is significantly smaller. According to M. Hayashi et al. [Hay+07] the decrease is associated with a periodic change of the domain wall chirality. A transverse wall periodically changes the chirality via a vortex or anti-vortex wall state [Hay+07]. The domain wall width in nanostripes is proportional to the width of the stripe via [Coe10]

$$\rho_w = cw, \tag{2.28}$$

with $c \approx 1$ for the transverse wall and $c \approx 3\pi/4$ for a vortex wall [Coe10].

2.3.2. Domain Walls in Nanotubes

Similar to the stripe configuration one can assume two domain wall types in a ferromagnetic tube with an alignment of the magnetization along its axis: a transverse and a vortex wall. A detailed calculation regarding the energies of the domain walls was performed by Landeros et al. [LN10]. They calculated the energy change due to a domain wall with respect to a homogeneous axial magnetization to be

$$\Delta E = \frac{4\pi r_o^2 (1 - \beta^2) A}{w} \tag{2.29}$$

with the domain wall width [LN10]

$$w = w_v = \sqrt{\frac{1 - \beta^2}{2 \ln(\beta^{-1})}} r_o \tag{2.30}$$

for a vortex wall and [LN10]

$$w = w_t = \sqrt{2}\lambda_{\mathrm{ex}} \tag{2.31}$$

in the case of a transverse wall. The parameters r_0 and $\beta = r/r_0$ are the outer diameter of the tube and the ratio of the inner to the outer diameter, respectively. The energy depends on the dimensions of the tube and the width of the DW. In case of a vortex wall the DW width itself also depends on the tube diameter while a transverse domain wall only depends on the material. By comparing the energies one can determine the criteria [LN10]

$$\frac{r_0}{\lambda_{\mathrm{ex}}} > 2\sqrt{\frac{\ln(\beta^{-1})}{1-\beta^2}}, \tag{2.32}$$

for the creation of a vortex wall. For a further description of DWs in tubes we refer to [LN10] and [Yan+11].

2.4. Dynamic magnetization

The previous sections addressed the static case with the magnetization in its equilibrium state. In the following we investigate the dynamic behavior of the magnetic moments. A magnetic moment in a magnetic field experiences a torque $\boldsymbol{\tau}$ described as [DS09]

$$\boldsymbol{\tau} = \mathbf{m} \times \mathbf{B}. \tag{2.33}$$

In the ground state the magnetic moments align to the effective magnetic field and the torque is zero. Now let's assume the magnetic moment is deflected from its static position. The magnetic moment $\mathbf{m}$ is connected with an angular momentum $\mathbf{J}$ via the relation $\mathbf{m} = \gamma\mathbf{J}$. For an electron $\gamma = g|e|/(2m_e)$ with g as the Landé factor, e and m_e as the charge and mass of an electron. Because the torque is equal to the time rate of change of the angular momentum Eq. 2.33 can be rewritten as

$$\frac{\mathrm{d}\mathbf{m}}{\mathrm{d}t} = \gamma\mathbf{m} \times \mathbf{B}. \tag{2.34}$$

If we assume γ is the same for all magnetic moments in a material, it is possible to sum over all moments and get an equation displaying the mo-

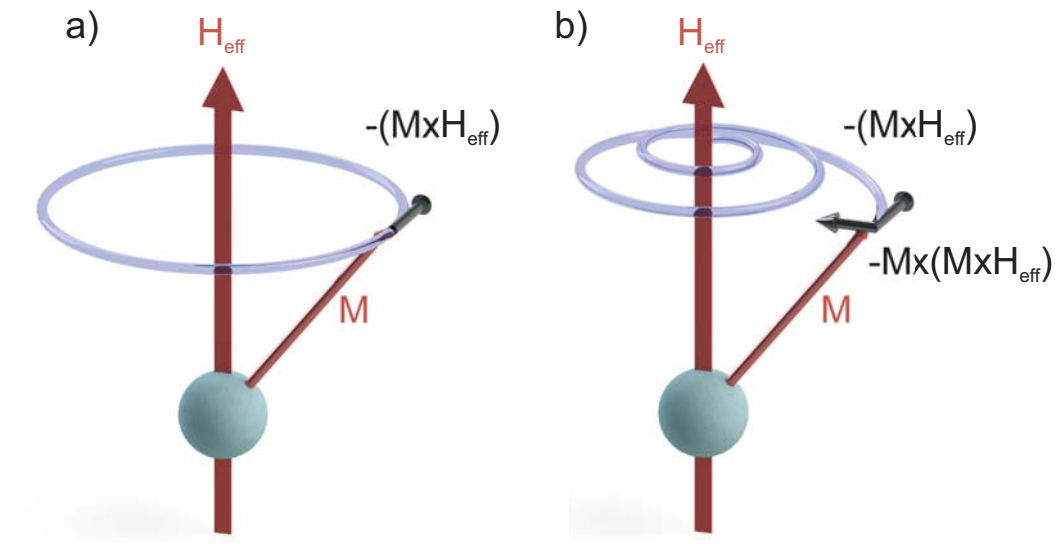

Figure 2.3.: a) Precession of the magnetization around an effective magnetic field H_{eff}. b) Precession of the magnetization with a phenomenological damping term. The damping term leads to a spiral-like motion back to the equilibrium position parallel to H_{eff}. The absolute value of M remains constant.

tion for the net magnetization. For a negatively charged particle (electron) it describes a circular precession counterclockwise around the field-vector. In literature a minus sign is often taken from the γ into the equation to highlight the precession direction. Since this work focus on magnetic moments generated by electrons we follow this convention and state the following formula

$$\frac{\mathrm{d}\mathbf{M}}{\mathrm{d}t} = -\gamma\mu_0\mathbf{M} \times \mathbf{H}_{\text{eff}}, \tag{2.35}$$

first introduced by Landau and Lifschitz (1935) [LL35]. It describes a precessional motion around the effective magnetic field H_{eff} (see Fig. 2.3 a)). Experiments show that the magnetization heads back to the equilibrium position in a finite time period (see Fig. 2.3 b)). Therefore, a damping term was added which represents a force directing towards the field-vector resulting in the Landau-Lifshitz (LL) equation

$$\frac{\mathrm{d}\mathbf{M}}{\mathrm{d}t} = -\gamma\mu_0\mathbf{M} \times \mathbf{H}_{\text{eff}} - \frac{\lambda}{M_{\text{s}}^2}\mathbf{M} \times (\mathbf{M} \times \mathbf{H}_{\text{eff}}), \tag{2.36}$$

with a damping parameter λ. The formula can be used for small damping terms but faces problems with larger damping. This was addressed by Gilbert [Gil04] resulting in the famous Landau-Lifshitz-Gilbert (LLG) equation

$$\frac{\mathrm{d}\mathbf{M}}{\mathrm{d}t} = -\gamma\mu_0\mathbf{M}\times\mathbf{H}_{\mathrm{eff}} + \frac{\alpha}{M_{\mathrm{s}}}\left(\mathbf{M}\times\frac{\mathrm{d}\mathbf{M}}{\mathrm{d}t}\right), \tag{2.37}$$

with α as the phenomenological Gilbert damping term. The damping term directly depends on the rate of change of the magnetization. The result is a viscous liquid like damping behavior. Using substitution and simplification [Gil04] it is possible to rewrite Eq. 2.37 to

$$\frac{\mathrm{d}\mathbf{M}}{\mathrm{d}t} = -\frac{\gamma\mu_0}{1+\alpha^2}\mathbf{M}\times\mathbf{H}_{\mathrm{eff}} - \frac{\gamma\mu_0\alpha}{M_{\mathrm{s}}(1+\alpha^2)}\mathbf{M}\times(\mathbf{M}\times\mathbf{H}_{\mathrm{eff}}). \tag{2.38}$$

Using $\lambda = \frac{\alpha\gamma\mu_0 M_{\mathrm{s}}}{1+\alpha^2}$ and $\gamma^* = \frac{\gamma}{1+\alpha^2}$ we see the LLG was transformed into a form similar to the LL-equation. The only difference is the new gyromagnetic ratio γ^* which depends on α. For the case of small damping $\alpha^2 << 1$ both Eq. 2.36 and Eq. 2.37 are the same, but while LL encounters problems for large damping, LLG can still be used.

2.5. Dynamic susceptibility

With the LLG (see Chap. 2.4) we got a powerful tool to describe the magnetization dynamics. But it is not possible to solve the LLG in a general form. Nevertheless it can be used to solve the problem of an infinite plane film using some assumptions [Gie05]:

- static parts of the external field $\mathbf{H}_{\mathrm{ext}}$ and the magnetization $\mathbf{M}$ in x-direction (homogeneous magnetization)
- constant absolute value of $\mathbf{M}$
- uniform excitation ($k = 0$) in y and z direction with the time dependent component $\exp(i\omega t)$
- no anisotropies beside demagnetization effects
- dynamic parts of field and magnetization with time dependence $\mathbf{h}(t) = \mathbf{h}\exp(i\omega t)$ and $\mathbf{m}(t) = \mathbf{m}\exp(i\omega t)$

- dynamic parts small compared to the static parts ($H_{\mathrm{ext}} >> h, M_{\mathrm{s}} >> m$)

The dynamic component of the magnetization is connected to the dynamic field via the susceptibility by

$$\mathbf{m} = \hat{\chi}(\omega)\mathbf{h} = (\hat{\chi}' - i\hat{\chi}'')\mathbf{h}. \tag{2.39}$$

$\hat{\chi}'$ is the real and $\hat{\chi}''$ the imaginary part. For the demagnetization we are using a general diagonalized tensor. As a result one gets the effective field and the magnetization

$$\mathbf{H}_{\mathrm{eff}} = \begin{pmatrix} H_{\mathrm{ext}} - N_x M_{\mathrm{s}} \\ h_y(t) - N_y m_y(t) \\ h_z(t) - N_z m_z(t) \end{pmatrix}, \mathbf{M} = \begin{pmatrix} M_{\mathrm{s}} \\ m_y(t) \\ m_z(t) \end{pmatrix}. \tag{2.40}$$

Equation 2.40 is now applied to the LLG Eq. 2.37. Since the dynamic parts are assumed to be very small, all nonlinear terms are neglected, resulting in

$$\begin{pmatrix} (\omega_H + (N_y - N_x)\omega_M - i\alpha\omega) & -i\omega \\ i\omega & (\omega_H + (N_z - N_x)\omega_M - i\alpha\omega \end{pmatrix} \begin{pmatrix} m_y \\ m_z \end{pmatrix} = \begin{pmatrix} h_y \\ h_z \end{pmatrix}, \tag{2.41}$$

with $\omega_M = \gamma\mu_0 M$ and $\omega_H = \gamma\mu_0 H_{\mathrm{ext}}$

By using Eq. 2.39 the susceptibility can be obtained. A more detailed description can be found in Ref. [Gie05]. As an example the following equations show the real and imaginary part of the susceptibility for the y-components [Gie05]:

$$\begin{aligned} \chi'_{yy} =& \frac{\omega_M(\omega_{\mathrm{res}}^2 - \omega^2)(\omega_H + (N_z - N_x)\omega_M)}{(\omega_{\mathrm{res}}^2 - \omega^2)^2 + \alpha^2\omega^2[2\omega_H + (N_y + N_z - 2N_x)\omega_M]^2} \\ &+ \frac{\alpha^2\omega^2[2\omega_H + (N_y + N_z - 2N_x)\omega_M]}{(\omega_{\mathrm{res}}^2 - \omega^2)^2 + \alpha^2\omega^2[2\omega_H + (N_y + N_z - 2N_x)\omega_M]^2} \end{aligned} \tag{2.42}$$

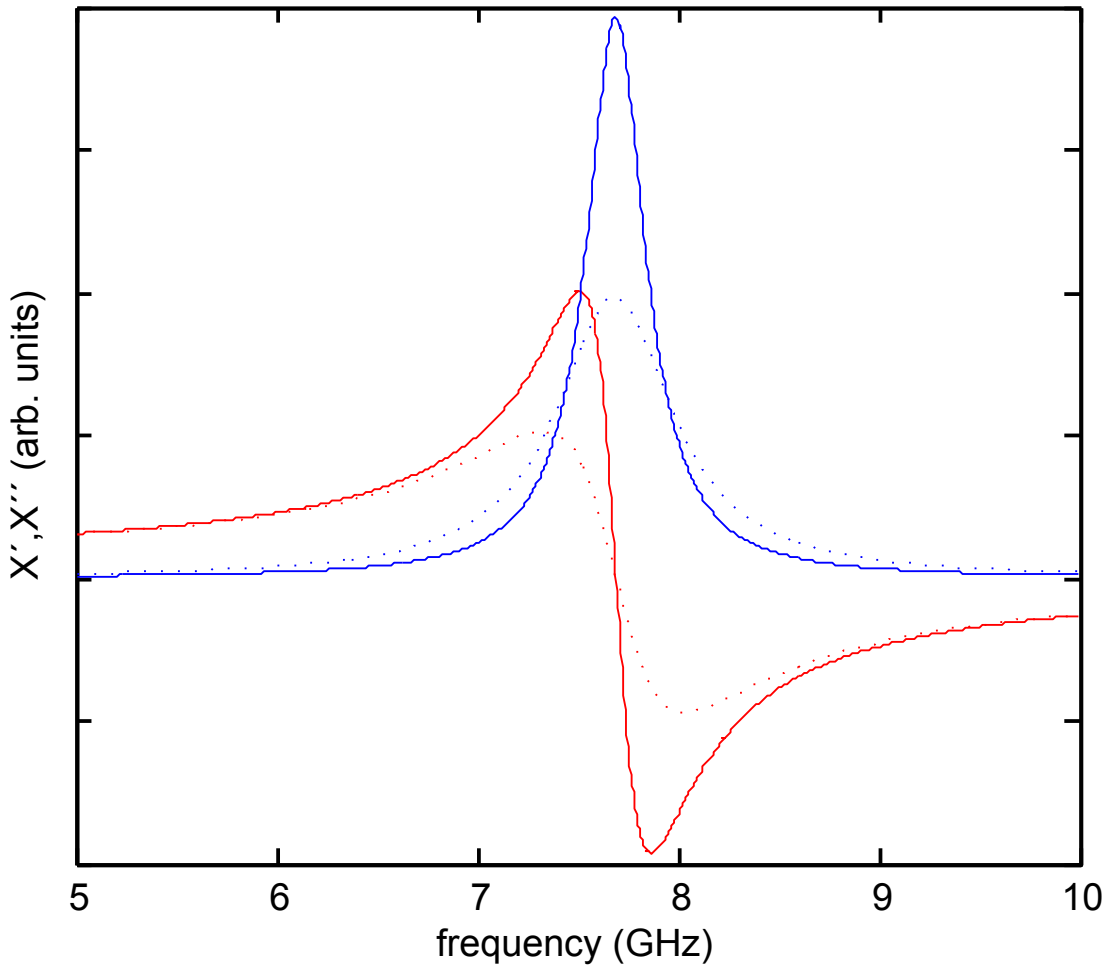

Figure 2.4.: Real part (red) and imaginary part (blue) of the susceptibility χ_{yy}. For the solid line $\alpha = 0.01$ and for the dotted line $\alpha = 0.02$. The used parameters are: $\mu_0 M_\mathrm{s} = 1.81$ T, $\mu_0 H_\mathrm{ext} = 0.1$ T.

$$\chi''_{yy} = \alpha\omega\omega_M \left[\frac{[(\omega_\mathrm{res}^2 - \omega^2)}{(\omega_\mathrm{res}^2 - \omega^2)^2 + \alpha^2\omega^2[2\omega_H + (N_y + N_z - 2N_x)\omega_M]^2} + \frac{(\omega_H + (N_z - N_x)\omega_M)(2\omega_H + (N_y + N_z - 2N_x)\omega_M)}{(\omega_\mathrm{res}^2 - \omega^2)^2 + \alpha^2\omega^2[2\omega_H + (N_y + N_z - 2N_x)\omega_M]^2} \right]. \tag{2.43}$$

ω_res is defined as

$$\omega_\mathrm{res}^2 = (\omega_H + (N_y - N_x)\omega_M)(\omega_H + (N_z - N_x)\omega_M). \tag{2.44}$$

By applying the demagnetization factors $N_z = 1, N_x = N_y = 0$ we obtain the formula for an infinite thin film. χ'_{yy} and χ''_{yy} are plotted for this case in Fig. 2.4 with the saturation magnetization $M_\mathrm{s} = 860$ kA/m ($\mu_0 M_\mathrm{s} = 1.081$ T) (typical value for Permalloy) and an external field of $\mu_0 H_\mathrm{ext} = 100$ mT in x direction. The imaginary part can be approximated with the Lorenz function with a maximum at ω_res. The full width at half maximum (FWHM) is given by [Bil07]

$$\Delta\omega = \alpha(2\omega_H + \omega_M). \tag{2.45}$$

The linewidth can also be gained by determining the FWHM of the magnitude. In this case the value of the FWHM has to be multiplied by a factor of $1/\sqrt{3}$ to arrive at $\Delta\omega$ [DS09][Bra14][Sch13]. An alternative method to obtain the linewidth is to calculate the difference between the maximum and the minimum of the real part χ'_{yy} [Bil07]. The positions of the extrema for the infinite plane film in xy-plane are given by [Bil07]

$$\omega_\mathrm{max} = \omega_\mathrm{res}\sqrt{1 - \frac{\alpha(2\omega_H + \omega_M)}{\omega_\mathrm{res}}}, \tag{2.46}$$

$$\omega_\mathrm{min} = \omega_\mathrm{res}\sqrt{1 + \frac{\alpha(2\omega_H + \omega_M)}{\omega_\mathrm{res}}}. \tag{2.47}$$

For $\Delta\omega << \omega_\mathrm{res}$, which is true for investigated material parameters and a resonance frequency greater than a few hundred MHz, the linewidth $\Delta\omega_{mm} = \omega_\mathrm{min} - \omega_\mathrm{max}$ converges to the linewidth $\Delta\omega$ obtained from the imaginary part [Bil07]. In many cases this method is favorably since it is easier to determine the extrema position compared to measure the exact FWHM $\Delta\omega$.

At the frequency (ω_res) the real part is crossing the zero amplitude. This position/frequency is the so called ferromagnetic resonance (FMR). By rewriting Eq. 2.44 we get

$$f_\mathrm{res} = \frac{\gamma\mu_0}{2\pi}\sqrt{(H_\mathrm{ext} + (N_y - N_x)M_\mathrm{s})(H_\mathrm{ext} + (N_z - N_x)M_\mathrm{s})} \tag{2.48}$$

known as the Kittel formula. By using different demagnetization factors it is possible to determine the FMR for different shapes, but also for different magnetization-directions. In this section we neglected any form of

anisotropy. Nevertheless it is important to note that e.g. for a thin film we have the influence of a surface anisotropy. In this case the magnetization has to be altered. The parameter M_s in 2.48 is replaced by

$$M_\mathrm{eff} = M_\mathrm{s} - \frac{2K_\perp}{d\mu_0 M_\mathrm{s}}. \tag{2.49}$$

2.6. Damping and Linewidth

Damping is an important parameter for spin waves. Equation 2.45 shows that it is a determinant factor for the linewidth of the resonance peak. By conducting field sweeps we also receive a linewidth [HCH85] [Kal+06]

$$\Delta H = \Delta H_0 + \frac{4\pi\alpha f}{\gamma}. \tag{2.50}$$

It depends on two different parts. A frequency independent part ΔH_0 and an intrinsic Gilbert-like term depending on f. ΔH_0 reflects different effects responsible for damping [Bra14][Pat68][Liu+03]:

$$\Delta H_0 = \Delta H_\mathrm{mae} + \Delta H_\mathrm{mos} + \Delta H_\mathrm{inhom} + \Delta H_{\delta k} + \Delta H_\mathrm{2magnon} + ... \tag{2.51}$$

ΔH_mae, and ΔH_inhom are the contributions of the inhomogeneties of the magnetic anisotropy and in the external magnetic field, respectively. ΔH_mos is the contribution of mosaicity which describes the spread of crystal plane orientations. In case of a k-vector distribution $\rho(k)$ instead of a single k-vector the linewidth might broaden as described by $\Delta H_{\delta k}$. The contribution $\Delta H_\mathrm{2magnon}$ occurs because of a two magnon scattering process. Thereby, a magnon is extinguished by a scattering and a new magnon with a different k-vector is created [Bil07]. According to [Kal+06] the linewidths ΔH and Δf are connected by

$$\Delta H = \Delta f \frac{\partial H_\mathrm{Kittel}(f)}{\partial f}; \Delta f = \Delta H \frac{\partial f_\mathrm{Kittel}(H_\mathrm{ext})}{\partial H_\mathrm{ext}}; \tag{2.52}$$

at $k = 0$. The formula was thoroughly discussed by Patton [Pat68] and Kuanr et al. [KCC05].

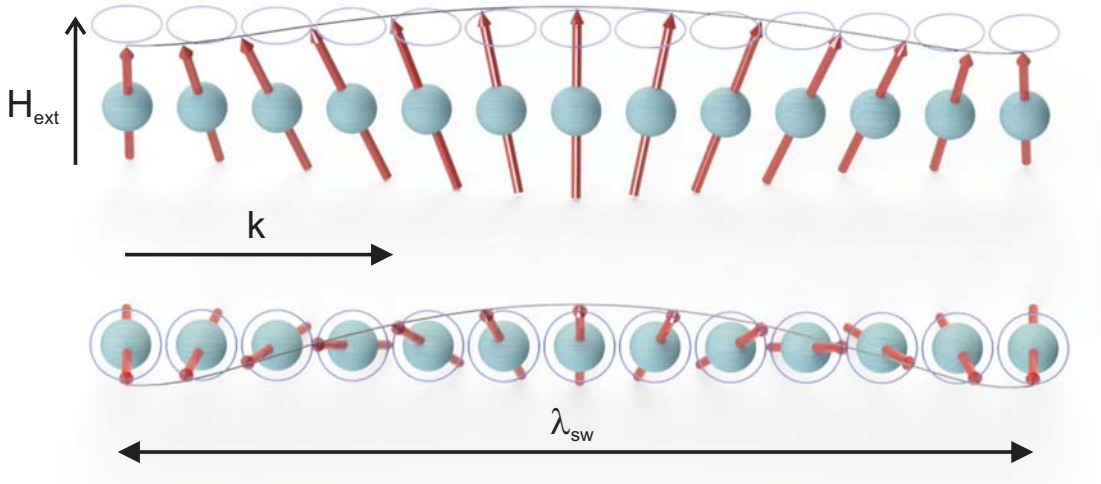

Figure 2.5.: Spin wave with the wavelength λ_{SW} traveling in a one-dimensional ferromagnetic chain. The external bias field is applied perpendicular to the wave vector k.

2.7. Spin Waves

A spin wave denotes a collective excitation of magnetic moments, with the so called magnon as the corresponding quasiparticle. So far we focussed on the uniform excitation were all moments precess in phase. It can be described with an infinitely long spin wave with wave vector $k = 0$. In this section we address spin waves with a finite wavelength. Figure 2.5 shows an illustration of such a wave with a wavelength λ_{SW}. Spin waves with a large wave vector are dominated by the exchange interaction. Therefore, they are called exchange spin waves. On the contrary spin waves with a small wave vector are called dipolar spin waves or magnetostatic waves. Here the exchange interaction can be neglected and the dipolar interaction dominates. The basic equation for magnetostatic waves in homogeneous media is the Walker's equation [DS09]. It can be obtained by starting with the Maxwell equations

$$\nabla \times \mathbf{H} = 0;\ \nabla \cdot \mathbf{B} = 0;\ \nabla \times \mathbf{E} = -\dot{\mathbf{B}}. \tag{2.53}$$

Since for every analytical function, $\nabla \times (\nabla\psi) = 0$ is true we can define a magnetostatic scalar potential

$$\mathbf{H} = -\nabla\psi. \tag{2.54}$$

Using ψ, neglecting the exchange interaction and assuming a bias field along the z-direction we obtain [DS09] [Wal57]

$$(1+\hat{\chi})\left[\frac{\partial^2\psi}{\partial x^2} + \frac{\partial^2\psi}{\partial y^2}\right] + \frac{\partial^2\psi}{\partial z^2} = 0, \tag{2.55}$$

the so called Walker's equation. Here $\hat{\chi}$ is position independent. By assuming $\psi \propto \exp(i\mathrm{k}\cdot\mathrm{r})$ the Walker's equation becomes:

$$(1+\hat{\chi})\left(k_x^2 + k_y^2\right) + k_z^2 = 0. \tag{2.56}$$

Given that $\hat{\chi}$ depends on the frequency (see Sec. 2.5) Eq. 2.56 connects the frequency with the wave vector. A general formalism describing spin waves in a thin film including the exchange interaction was developed by Kalinikos and Slavin [BK86]. For such a film the direction of the bias field and the in-plane direction of k are significant. Therefore, we divide the k-vector in an in-plane component k_ζ and an out-of-plane component k_n. Additionally the in-plane part is further divided into the component $k_\parallel$ parallel and $k_\perp$ perpendicular to the magnetic field. The resulting relation is given by $k^2 = k_\zeta^2 + k_n^2$ and $k_\zeta^2 = k_\parallel^2 + k_\perp^2$. Since we assume an infinitely thin film, waves in the direction perpendicular to the surface are confined by the thickness of film d. Therefore, we can assume a quantization of the component of the wave vector perpendicular to the surface:

$$|k_n| = n\frac{\pi}{d}, n \in \mathbb{N}. \tag{2.57}$$

The dispersion relation (including exchange, without damping) is given by [BK86]

$$\omega_{\mathrm{res}}^2|_n = (\omega_H + \lambda_{\mathrm{ex}}^2\omega_M k^2)[\omega_H + \omega_M(\lambda_{\mathrm{ex}}^2 k^2 + F_{nn})], \tag{2.58}$$

with F_{nn} as the dipolar matrix element. As mentioned above the contribution of the exchange term depends on k. For large k the exchange term $\lambda_{\mathrm{ex}}^2 k^2$ dominates the equation while for small k it can be neglected, leading

to the exchange spin waves and magnetostatic waves, respectively. F_{nn} is given by [BK86]

$$F_{nn} = P_{nn} + \sin^2\theta \left(1 - P_{nn}(1 + \cos^2\varphi) + \omega_M \frac{P_{nn}(1 - P_{nn})\sin^2\varphi}{\omega_H + \lambda_{\mathrm{ex}}^2 \omega_M k^2}\right), \tag{2.59}$$

with the angle φ between the propagating spin wave and the magnetization M and θ the angle between the magnetization and the surface normal. For unpinned surface spins

$$P_{nn} = \frac{k_\zeta^2}{k^2} - \frac{2k_\zeta^3}{k^4 d}\frac{1}{1 + \delta_{0n}}[1 - (-1)^n \exp(-k_\zeta d)], \tag{2.60}$$

with δ_{0n} as a Kronecker delta. The phase velocity v_{p} and group velocity v_{g} for the spin waves are given by

$$v_{\mathrm{g}} = \frac{\partial\omega}{\partial k}, v_{\mathrm{p}} = \frac{\omega}{k}. \tag{2.61}$$

In the following we show three different types of special configurations for magnetostatic waves given by Ref. [DS09]. In all configurations the spin wave vector lies in-plane (parallel to the surface).

- **Magnetostatic Surface Waves (MSSW)** In this configuration the wave vector k is perpendicular to the magnetization while the magnetization lies in the film plane. The result is a wave with the group and the phase velocity pointing in the same direction. The amplitude is the highest at the surface and decays exponentially (surface mode). The dispersion relation is given by [DS09]

  $$\omega_{\mathrm{MSSW}}^2 = \omega_H(\omega_H + \omega_M) + \frac{\omega_M^2}{4}(1 - e^{-2k_\perp d}). \tag{2.62}$$

  The waves were first described by Damon and Eshbach [DE61] and are therefore, known as Damon-Eshbach (DE) modes.

- **Magnetostatic Backward Volume Waves (MSBVW)** As an outstanding characteristic of these waves the group and the phase velocity point in opposing directions and thus are called backward waves. Different to the MSSW the amplitude is distributed over the entire

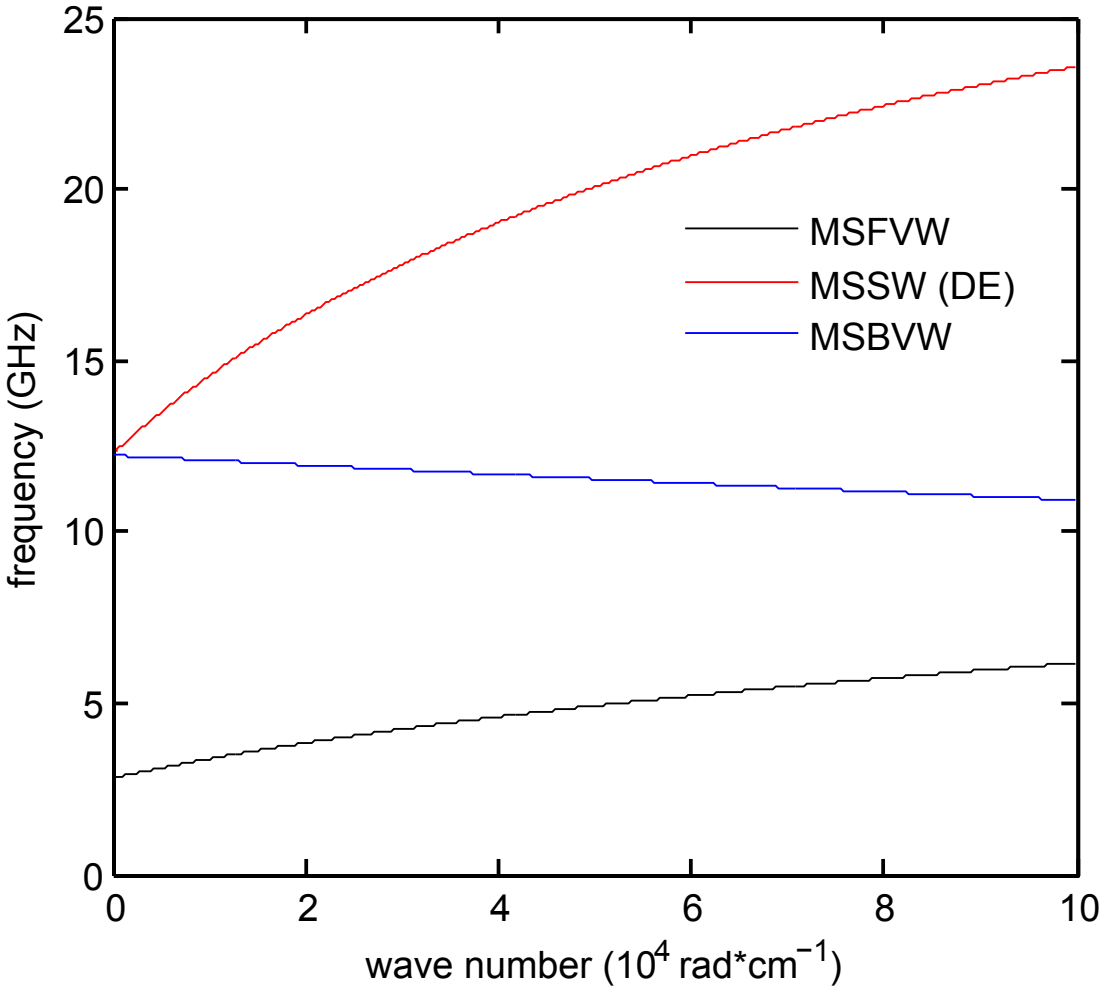

Figure 2.6.: Dispersion relation for the MSSW, MSFVW and MSBVW. The used parameters are: $\mu_0 M_\mathrm{s} = 1.81$ T, $\mu_0 H = 0.1$ T.

volume. The configuration for the MSBVW is a magnetization in-plane and a wave vector parallel to the magnetization. The equation [DS09]

$$\omega^2_{\mathrm{MSBVW}} = \omega_H \left[\omega_H + \omega_M \left(\frac{1 - e^{-k_\parallel d}}{k_\parallel d} \right) \right] \tag{2.63}$$

describes the corresponding dispersion relation.

- **Magnetostatic Forward Volume Waves (MSFVW)** In case of a magnetization perpendicular to the film plane (out-of-plane) MSFVW are generated. The waves are forward waves with an ampli-

tude distributed over the whole volume. The corresponding dispersion relation is [DS09]

$$\omega^2_{\mathrm{MSFVW}} = \omega_H \left[\omega_H + \omega_M \left(1 - \frac{1 - e^{-k_\zeta d}}{k_\zeta d} \right) \right]. \tag{2.64}$$

It is important to note that the direction of k_ζ in the film plane has no influence on the dispersion. For $k_\zeta \to 0$ and for $H_{\mathrm{ext}} \geq M_{\mathrm{s}}$ Eq. 2.64 is simplified to

$$\omega_{MSFVW} = \omega_H = \mu_0 \gamma (H_{\mathrm{ext}} - M_{\mathrm{s}}). \tag{2.65}$$

with a minimum frequency for $H_{\mathrm{ext}} = M_{\mathrm{s}}$. In the case of smaller fields $H_{\mathrm{ext}} < M_{\mathrm{s}}$ the magnetization is in a ground state which continuously changes with the external field.

The dispersion relation of these three configurations can be seen in Fig. 2.6. So far we presented different formulas describing isotropic ferromagnetic thin films. In the presence of a uniaxial anisotropy we follow a different approach. A detailed explanation of the formalism is given in [CG]. It can be very complicated to integrate an arbitrary anisotropy in a dispersion relation for spin waves. However we can use an analytical formula in the case of an in-plane magnetized thin film which fulfills $d \cdot k_\zeta << 1$. It is given in a spherical coordinate system (see Fig. 2.1) by [Hil05]

$$\begin{aligned} \left(\frac{\omega}{\gamma} \right)^2 = & \left(\frac{1}{M_{\mathrm{s}}} \frac{\partial^2 \mathscr{E}_{\mathrm{ext}}}{\partial \theta^2} + H_{\mathrm{ext}} \cos(\varphi - \varphi_H) + \frac{2A}{M_{\mathrm{s}}} k^2 \right. \\ & + 4\pi M_{\mathrm{s}} f' \cdot \left(1 - \frac{1}{2} k_\zeta d \right) \Bigg) \times \left(\frac{1}{M_{\mathrm{s}}} \frac{\partial^2 \mathscr{E}_{\mathrm{ext}}}{\partial \varphi^2} + H_{\mathrm{ext}} \cos(\varphi - \varphi_H) \right. \\ & \left. + \frac{2A}{M_{\mathrm{s}}} k^2 + 2\pi M_{\mathrm{s}} f' k_\zeta d \sin^2(\varphi - \varphi_k) \right) - \frac{1}{M_s^2} \left(\frac{\partial^2 \mathscr{E}_{\mathrm{ext}}}{\partial \theta \partial \varphi} \right)^2 \end{aligned} \tag{2.66}$$

with f' as the demagnetization factor and θ as the polar angle of the magnetization. The azimuthal angles $\varphi, \varphi_H, \varphi_k$ represent the in-plane direction of the magnetization $\mathbf{M}$, the external field $\mathbf{H}_{\mathrm{ext}}$ and the wave vector $\mathbf{k}$. $\mathscr{E}_{\mathrm{ext}}$ is the effective energy density consisting of all anisotropic energy contributions except the demagnetization term [Bra14]. It is important to note

that Eq. 2.66 is using cgs unis, while all previous equations are written in SI units.

A requirement to employ Eq. 2.66 is the knowledge about the direction of the magnetization. In special cases it is justified to assume that the magnetization is aligned with the external magnetic field. However we cannot use this presumption in a system with an uniaxial anisotropy. In this case it is possible to obtain the direction by minimizing the total energy density Eq. 2.23 for θ and φ. With this method and equation Eq. 2.66 it is possible to determine the anisotropy constants from a resonance measurement as described in [Hil05]. The measurement is performed with a fixed $\mathbf{k}$ at external fields with different angels φ_H. The magnetization direction is determined by the energy minimization for each field and finally Eq. 2.66 is used to fit the resonance frequencies by changing the anisotropy constants.

2.8. Wave Interference

Interference describes a phenomenon in which two or more coherent waves superpose. The dynamic magnetization of a propagating SW at position $\mathbf{r}$ can be described mathematically as

$$\mathbf{M}_1 = \mathbf{A}_1 e^{i(\mathbf{k}_1 \cdot \mathbf{r} - \omega_{\mathrm{SW}} t + \phi_1)}, \tag{2.67}$$

with the amplitude $\mathbf{A}$, frequency ω_{SW}, time t and an additional phase ϕ. The term $(\mathbf{k}_1 \cdot \mathbf{r} - \omega_{\mathrm{SW}} t + \phi_1)$ describes the phase of the SW depending on time and position. When two waves with the same frequency ω_{SW} are added they interfere and the result can be written as

$$\mathbf{M}_{\mathrm{total}} = \mathbf{M}_1 + \mathbf{M}_2 = \left(\mathbf{A}_1 e^{i(\mathbf{k}_1 \cdot \mathbf{r} + \phi_1)} + \mathbf{A}_2 e^{i(\mathbf{k}_2 \cdot \mathbf{r} + \phi_2)} \right) e^{-i\omega_{\mathrm{SW}} t}. \tag{2.68}$$

However, in experiments such as the BLS measurements performed in this thesis, the detected quantity is not the amplitude and phase, but the time-

average intensity (following [Opt])

$$I_{\text{total}} = \left\langle |\mathbf{M}|^2 \right\rangle = \langle (\mathbf{M}_1 + \mathbf{M}_2) \cdot (\mathbf{M}_1^* + \mathbf{M}_2^*) \rangle \tag{2.69}$$

$$= \left\langle |\mathbf{M}_1|^2 \right\rangle + \left\langle |\mathbf{M}_2|^2 \right\rangle + \langle \mathbf{M}_1 \cdot \mathbf{M}_2^* \rangle + \langle \mathbf{M}_2 \cdot \mathbf{M}_1^* \rangle \,. \tag{2.70}$$

By utilizing [Opt]

$$\left\langle |\mathbf{M}_1|^2 \right\rangle = I_1, \left\langle |\mathbf{M}_2|^2 \right\rangle = I_2, \tag{2.71}$$

$$\langle \mathbf{M}_1 \cdot \mathbf{M}_2^* \rangle = \langle \mathbf{A}_1 \cdot \mathbf{A}_2^* \rangle \, e^{i[(\mathbf{k}_1 - \mathbf{k}_2) \cdot \mathbf{r} + (\phi_1 - \phi_2)]} \tag{2.72}$$

$$= \sqrt{I_1 I_2} e^{i[(\mathbf{k}_1 - \mathbf{k}_2) \cdot \mathbf{r} + (\phi_1 - \phi_2)]} \tag{2.73}$$

$$\langle \mathbf{M}_2 \cdot \mathbf{M}_1^* \rangle = \langle \mathbf{A}_2 \cdot \mathbf{A}_1^* \rangle \, e^{-i[(\mathbf{k}_1 - \mathbf{k}_2) \cdot \mathbf{r} + (\phi_1 - \phi_2)]} \tag{2.74}$$

$$= \sqrt{I_1 I_2} e^{-i[(\mathbf{k}_1 - \mathbf{k}_2) \cdot \mathbf{r} + (\phi_1 - \phi_2)]} \tag{2.75}$$

and $\cos\rho = \frac{1}{2}\left(e^{i\rho} + e^{-i\rho}\right)$ the intensity can be simplified to [Opt]

$$I_{\text{total}} = I_1 + I_2 + 2\sqrt{I_1 I_2}\cos\rho \tag{2.76}$$

with $\rho = (\mathbf{k}_1 - \mathbf{k}_2) \cdot \mathbf{r} + (\phi_1 - \phi_2)$. Therefore, the total intensity of the two interfering waves depends on the relative phase difference ρ between the SWs.

For the general case with different propagation distances of both waves until they superpose the phase difference can be written as $\rho = \mathbf{k}_1 \cdot \mathrm{r}_1 - \mathbf{k}_2 \cdot \mathbf{r}_2 + (\phi_1 - \phi_2)$. The phase difference can be influenced by different factors. For the special case with $\Phi_1 = \Phi_2$ and $\mathbf{r}_1 = \mathbf{r}_2 = \mathbf{r}$ the phase difference ρ depends on the k-vectors according to $\rho = (\mathbf{k}_1 - \mathbf{k}_2) \cdot \mathbf{r} = \Delta\mathbf{k} \cdot \mathbf{r}$. If the k-vectors are the same for both waves $\mathbf{k}_1 = \mathbf{k}_2 = \mathbf{k}$ the phase depends on the different paths according to $\rho = \mathbf{k} \cdot (\mathbf{r}_1 - \mathbf{r}_2)$. To obtain the relative phase between to waves expected of an experiment performed in this thesis (see Chap. 6) we have to divide the propagation path of the SWs in two. In one segment (seg1) the propagation distance a is equal (see Fig. 2.7). However, the k-vectors are different leading to relative phase of

$$\rho_{\text{seg1}} = (\mathbf{k}_1 - \mathbf{k}_2) \cdot \mathbf{a}. \tag{2.77}$$

In the second segment (seg2) both k-vectors are the same $\mathbf{k}_1 = \mathbf{k}_2 =$

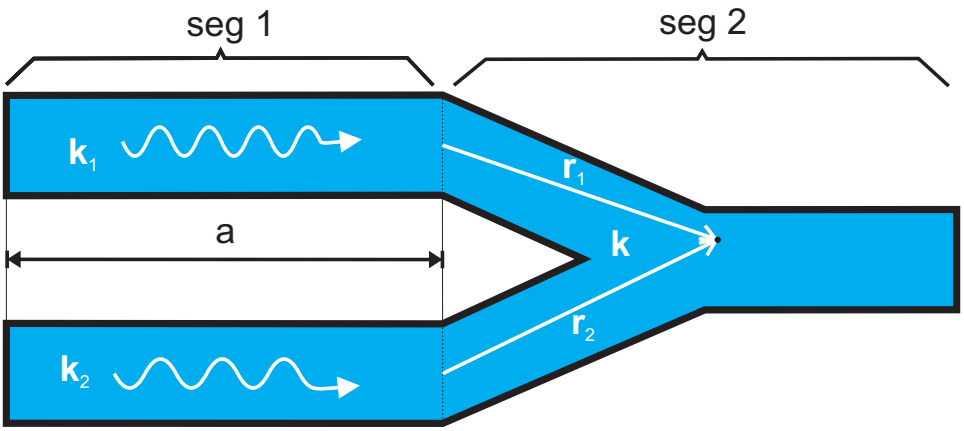

Figure 2.7.: Spin wave interference structure. Different sections of the structure have different properties leading to different k-vectors.

k. Depending on the measurement position we have different propagation distances leading to

$$\rho_{\text{seg2}} = (\mathbf{r}_1 - \mathbf{r}_2) \cdot \mathbf{k}. \tag{2.78}$$

The resulting phase of both segments is

$$\rho = \rho_{\text{seg1}} + \rho_{\text{seg2}} = (\mathbf{k}_1 - \mathbf{k}_2) \cdot \mathbf{a} + (\mathbf{r}_1 - \mathbf{r}_2) \cdot \mathbf{k}. \tag{2.79}$$

With a linear change of the k-vector discrepancy $\Delta\mathbf{k}$ it is possible to change the total intensity of the two interfering waves (cosine dependency). In the case of equal amplitudes $\mathbf{A}_1 = \mathbf{A}_2$ we get $I_1 = I_2 = I$ and the total intensity can change between $4I$ and 0.

2.9. Anisotropic Magnetoresistance

In 1857 W. Thomson [Tho56] discovered that the resistance of iron and nickel depended on the relative orientation of the magnetization direction in the material and the direction of current used to measure the resistance. The effect is the so called anisotropic magnetoresistance (AMR) and its influence on the resistivity ρ can by described by [MP75]

$$\rho(\xi) = \rho_\perp + (\rho_\parallel - \rho_\perp) \cos^2 \xi \tag{2.80}$$

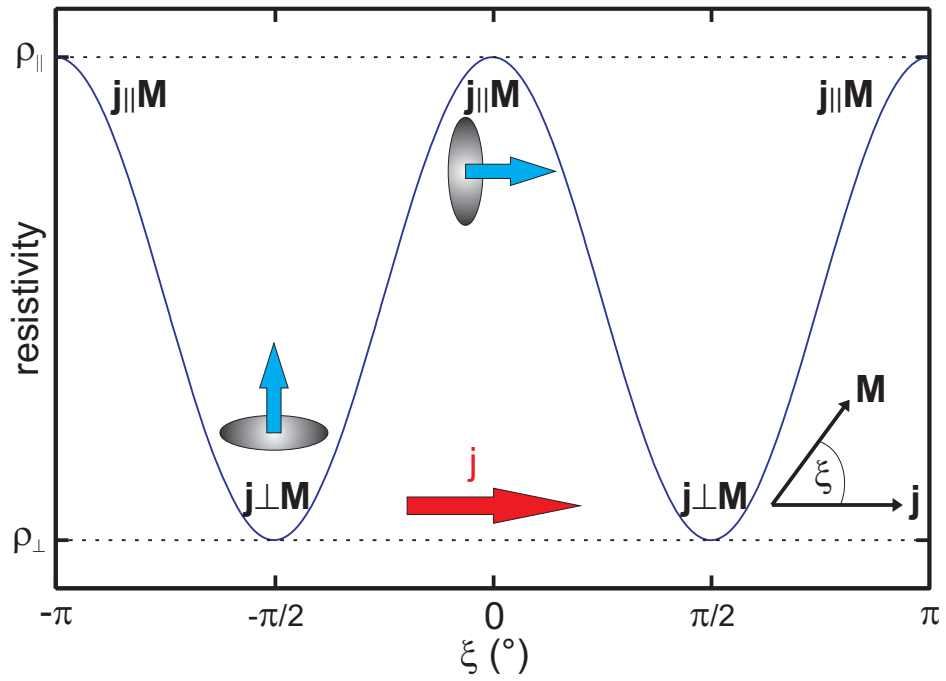

Figure 2.8.: AMR resistivity as a function of the angle ξ between the direction of the current density **j** and the magnetization **M**. The blue arrows and gray ellipsoids represent the direction of the spins/magnetization and the asymmetric orbitals.

with the angle ξ between the direction of the current density **j** and the magnetization **M**. Experiments showed the highest resistivity $\rho_{\parallel}$ for a parallel and the lowest $\rho_{\perp}$ for the perpendicular configuration of **M** and **j** (see Fig. 2.8).

Considering the resistance$R$ Eq. 2.80 can be rewritten to

$$R(t) = R_0 + \Delta R \cos^2(\xi(t)), \tag{2.81}$$

with $R_0 = R_{\perp}$ and $\Delta R = R_{\parallel} - R_{\perp}$.

The origin of the AMR effect arises from the spin-orbit interaction. The charge density distribution and therefore, the scattering cross section of orbitals in 3d-ferromagnets is not isotropi. Since the orientation of the orbitals depends on the spin direction and the resistivity depends on the scattering of the electrons, the change of the angle ξ leads to a variation of the measured resistance [MP75].

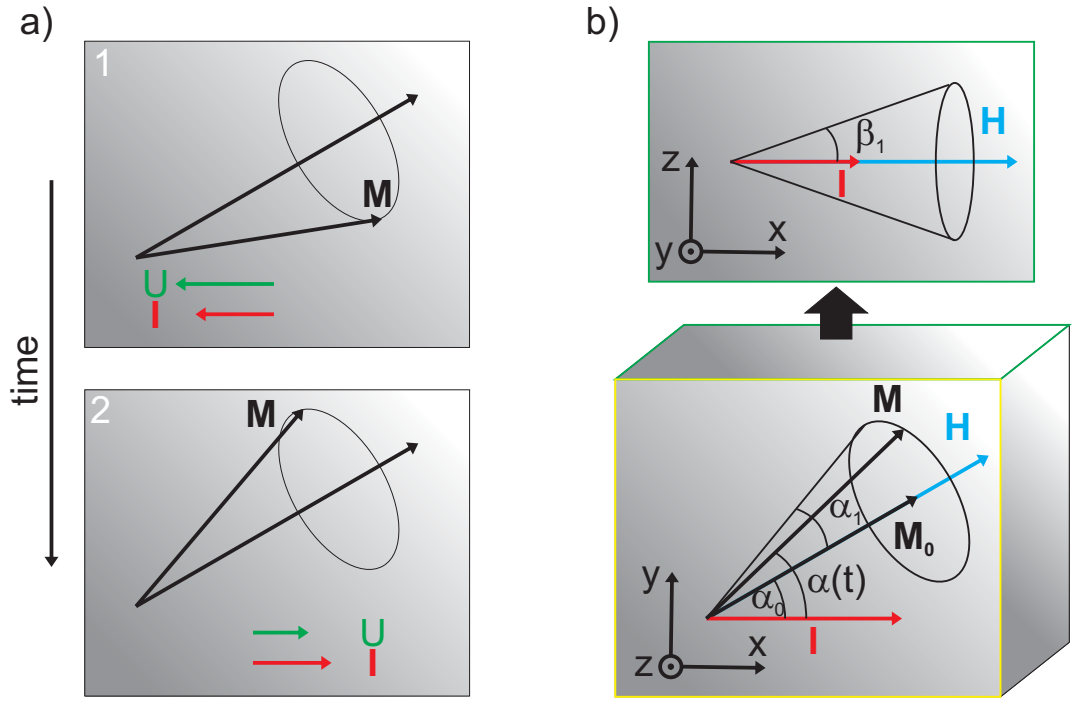

Figure 2.9.: a) Illustration of the non-zero time averaged photovoltage due the AMR effect. Sketches 1 and 2 show two moments (half the time period in between) with the same absolute current values, but opposing signs. Due to different resistance values because of the AMR effect (sketch 1 high, sketch 2 low) the resulting absolute value of the voltage is different. b) Sketch of the magnetization procession around the equilibrium position $\mathbf{M_0}$ with the out-of-plane component (β top) and in-plane component (α bottom) of the angle ξ (not shown) between the magnetization and the direction of the current. Pictures according to [MGH07].

2.10. Spin Rectification

The excitation of the magnetization in a ferromagnetic material leads to various different effects. One is the generation of a dc-voltage/photovoltage due to spin rectification (SR). In the following we follow the work of Mecking et al. [MGH07] and Harder et al. [Har+11]. In general the SR can be explaind by considering Ohms law

$$U(t) = R(t) \cdot I(t), \tag{2.82}$$

connecting the current $I(t)$, the voltage $U(t)$ and the resistance $R(t)$. For a simple example we assume a current $I(t) = I_1 \cos(\omega t)$ and a resistance $R(t) = R^0 + R^1 \cos(\omega t - \Phi)$. By taking the time average (denoted by <>)

we acquire a time independent photovoltage [MGH07]
$U_{MW} = \left\langle R^1 I_1 \cos(\omega t - \Phi)\cos(\omega t)\right\rangle = (R^1 I_1 \cos\Phi)/2$.
In case of a ferromagnetic material the resistance $R(t) = R_0 + \Delta R \cos^2(\xi(t))$ depends on the angle ξ between the magnetization and the direction of the current because of the AMR effect (see Sec. 2.9). R_0 is the resistance minimum and ΔR the maximal change of the resistance due to the AMR effect. The mechanism of the spin rectification due to the AMR effect is depicted in Fig. 2.9 a). Under an rf excitation with an angular frequency ω the magnetization rotates around an equilibrium position $\mathbf{M_0}$ driven by the magnetic field $\mathbf{h} = \mathrm{h}_0 e^{-i\omega t + \Phi}$ according Eq. 2.39. For our example we postulate that $\mathbf{M_0}$ points along the field $\mathbf{H}$ which is applied in the xy-plane of the sample. Together with $\mathbf{h}$ there is also an electrical field component $\mathbf{e} = \mathrm{e}_0 e^{-i\omega t}$ present in the ferromagnetic material, generating an rf current $I(t) = I\cos(\omega t)$ along the x-direction. The phase difference Φ between $\mathbf{e}$ and $\mathbf{h}$ depends on the wave impedance [Har+11]. Therefore, Φ also depends on the frequency ω and the resonance condition [Har+11]. A sketch of the magnetization and the current in a ferromagnetic stripe is depicted in Fig. 2.9 b). As shown we split the angle $\xi(t)$ into the in-plane angle $\alpha(t)$ and an out-of-plane angle $\beta(t)$. Therefore, the precession of ξ can be described with [MGH07]

$$\begin{aligned}\alpha(t) &= \alpha_0 + \alpha_1^t(t) = \alpha_0 + \alpha_1\cos(\omega t - \Phi)\\ \beta(t) &= \beta_1^t(t) = -\beta_1\sin(\omega t - \Phi)\end{aligned} \tag{2.83}$$

and

$$\cos\xi(t) = \cos\alpha(t)\cos\beta(t). \tag{2.84}$$

Using an approximation on $\cos^2(\xi(t))$ to second order in α_1^t and β_1^t leads to [MGH07]

$$\begin{aligned}\cos^2(\xi(t)) \approx \cos^2\alpha_0 &- \alpha_1\sin 2\alpha_0\cos(\omega t - \Phi)\\ &-\alpha_1^2\cos 2\alpha_0\cos^2(\omega t - \Phi)\\ &-\beta_1^2\cos^2\alpha_0\sin^2(\omega t - \Phi)\end{aligned} \tag{2.85}$$

with $(\sin\beta)|_{\beta_1=0} = 0$. By combining Eq. 2.85 with
$U(t) = [R_0 + \Delta R\cos^2\xi(t)][I_1\cos(\omega t)]$ and taking the time average we

acquire the photovoltage [MGH07]

$$U_0 = \langle U(t) \rangle = -I_1 \Delta R \alpha_1 \sin 2\alpha_0 \cos(\Phi)/2, \tag{2.86}$$

by using the relations $\left\langle \sin^2(\omega t - \Phi) \right\rangle = \left\langle \cos^2(\omega t - \Phi) \right\rangle = 1/2$ and $\langle \cos \omega t \cos(\omega t - \Phi) \rangle = \cos(\Phi)/2$. The phase shift angle Φ changes during the resonance condition of the system and therefore, the photovoltage U_0 gets altered which can be measured. A detailed description of this behavior can be found in Ref. [Har+11]. We note that the voltage also depends on the angle α_0 and therefore, on the internal field. A reversal of the field direction is resulting in a change of the sign of the photovoltage.

2.11. Artificial Spin Ice

In this thesis we are performing experiments on artificial honeycomb spin ice structures which are frustrated systems. To get a better understanding of the results this section gives a short introduction of the concept of frustrated systems and gives a brief overview of frustrated systems leading to the invention of artificial spin ice. Finally we explain a model to describe the behavior of an artificial honeycomb spin ice structure.

2.11.1. Geometrically Frustrated Systems

The research on frustrated systems is a topic that has engaged scientists for decades and is still a field of interest. Frustration in physics can occur in systems with competing interactions which cannot be satisfied simultaneously. Instead of a single ground state this leads to a variety of similar low energy states [Blu01] of which the system can choose from. A detailed explanation about frustration in general can be found in [Ram94]. The kind of frustration is defined by its origin. In this thesis we focus on geometrical frustration which corresponds to the disability of a system to reach one unique minimum state due the geometrical layout of its lattice [Zei13] [Blu01]. A prominent example of a geometrically frustrated system (GFS) is shown in Fig. 2.10. It consists of three Ising spins on a triangular lattice with antiferromagnetic interaction between the neighboring spins. Two spins satisfy the interaction by an anti-parallel alignment. After adding a third spin only two out of three interactions can be satisfied (see Fig. 2.10 a)). As depicted in Fig. 2.10 b) this leads to a six-fold degeneratie ground

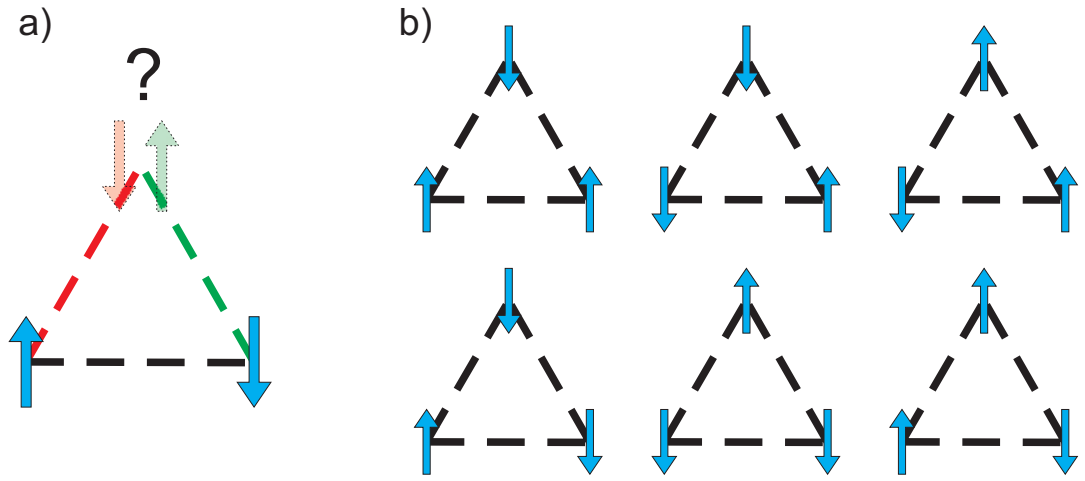

Figure 2.10.: a) Three Ising spins (arrows) arranged in a triangular lattice and connected via an antiferromagnetic interaction (dashed lines). The lattice shows frustration since only one spin can satisfy the interactions of both neighbors. b) 6 degenerated ground states of the triangular lattice.

state. By repeating the triangle structure it's possible to create lattices in 2D and 3D with a large number of degenerate ground states. Because of the large number of states with the same or similar energy, it is possible to change between different states with little energy [Wan07]. Such and other GFSs can be found in different materials or created artificially. Prominent examples for such frustrated systems are water ice, spin ice and artificial spin ice. In the following, the term frustration will refer to the geometrical frustration.

Water Ice

One of the first investigated systems exhibiting frustration was water ice. Experiments showed a residual entropy close to 0 K [GA33]. In the following we will describe the phenomena according to Linus Pauling who first explained it in 1935 [Pau35] using the Bernal-Fowler ice rules [BF33]. Every oxygen atom in an ice crystal is tetrahedrally surrounded by four other oxygen atoms at a distance of 2.76 Å(see Fig. 2.11). Between two neighboring oxygen atoms there lies one hydrogen atom bound to one oxygen atoms by a covalent bond and via a hydrogen bond to the other. Therefore, by looking at an arbitrary representative oxygen atom

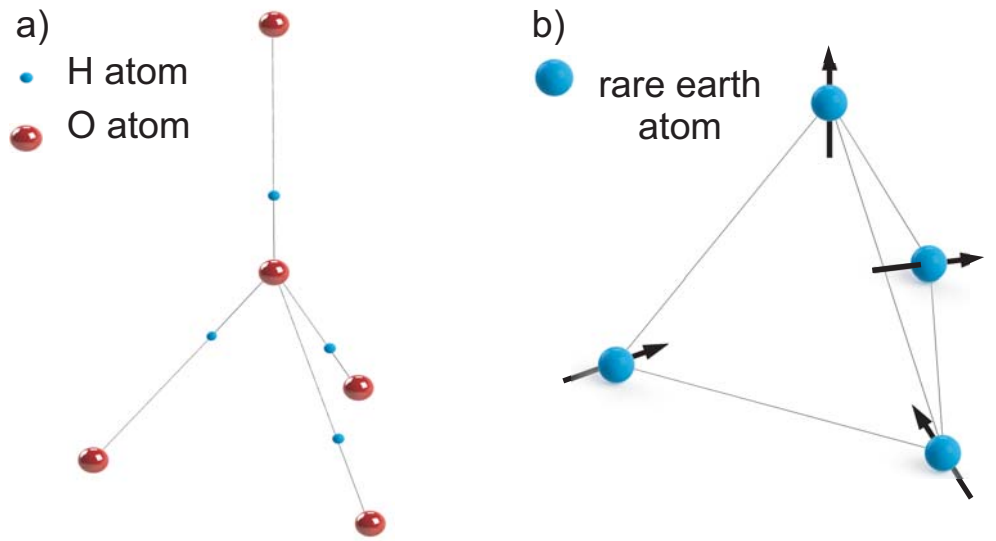

Figure 2.11.: a) Schematic of a water ice structure. The connections between the H- and the O-atomes are depicted by dashed (hydrogen bond) and solid lines (covalent bond). b) Sketch of one tetrahedron of the pyrochlore structure. The black arrows indicate the direction of the magnetic moments.

A, it is surrounded by four hydrogen atoms. Two are connected to A via covalent bonds and are therefore, very close (0.95 Å) to it. The other two hydrogen atoms have covalent bonds to other oxygen atoms and form only a hydrogen bond with atom A. Hence, the distance to these hydrogen atoms is bigger (1.81 Å). The rules describing this arrangement of two strong (close) and two weak (away) bonds are called the ice rules. It is also known as Bernal-Fowler rules named after John Desmond Bernal and Ralph H. Fowler who described it in their work 1933 [BF33]. For one oxygen atom and four surrounding hydrogen atoms there are 16 possible configurations but only 6 of them are obeying the ice rule. This 6 water ice ground states are of equal energy and therefore degenerated. This leads to a residual entropy even close to 0 K and cannot be lifted by long-range ordering [Ram+99]. Pauling calculated the degeneracy using the following assumptions. In a crystal with N water molecules each hydrogen atom has two possible positions in between two oxygen atoms leading to 2^{2N} possible configurations. On the other hand side, in a cell with one oxygen and four hydrogen atoms only 6 of 16 ($6/16 = 3/8$) configurations are allowed. The number of permitted configurations can be calculated ac-

cordingly with $W = 2^{2N}(3/8)^N = (3/2)^N$ [Pau35]. For one molecule H_2O this is leading to an entropy S of [Pau35]

$$S = R\ln(3/2) = 3.37\frac{\mathrm{J}}{\mathrm{molK}} \tag{2.87}$$

with R as the ideal gas constant.

Spin Ice

While water ice is an interesting material due to the finite entropy for a temperature towards zero there occur experimental problems regarding the material. It can melt and the dynamics of hydrogen atoms associated with the degeneracy cannot be investigated independent of the movement of the oxygen atoms [Ram+99]. A class of materials with degeneracy and an access to its dynamics is spin ice [Ram+99]. The term was created by Harris et al. in 1997 [Har+97] whom we are following in the description below. They found a frustration in pyrochlore $Ho_2Ti_2O_7$ similar to water ice. Elemental to the frustration are the magnetic rare earth ions. Those form a pyrochlore lattice which is a system of corner sharing tetrahedrons [Zei13] (see Fig. 2.11). Due to a strong crystalline anisotropy their magnetic moments can only point to or away from the center of the tetrahedron [Wan07] [Ros+00] resulting in an Ising like behavior. Therefore, in a tetrahedron with four Ising spins there are $2^4 = 16$ possible configurations. But not all of them have the same energy and none of them are satisfying all interactions between the spins [Har+97]. The ground state is a configuration with two spins pointing to (in) and two spins pointing away from (out) the center [Har+97]. The two in and two out rule for the system is identical to the ice rule for water ice. Other spin ice materials are for example $Dy_2Ti_2O_7$[Ram+99] or $Ho_2Sn_2O_7$[Mat+00]. The model described so far is reduced to the nearest neighbor interaction between the Ising spins and can explain the general degeneration in spin ice. However, later on the model was extended to include dipole interaction and an antiferromagnetic exchange interaction [HG00]. With the new model it was possible for Bramwell et al. [Bra+01] to get a better approximation to the experimental neutron scattering patterns of $Ho_2Ti_2O_7$.

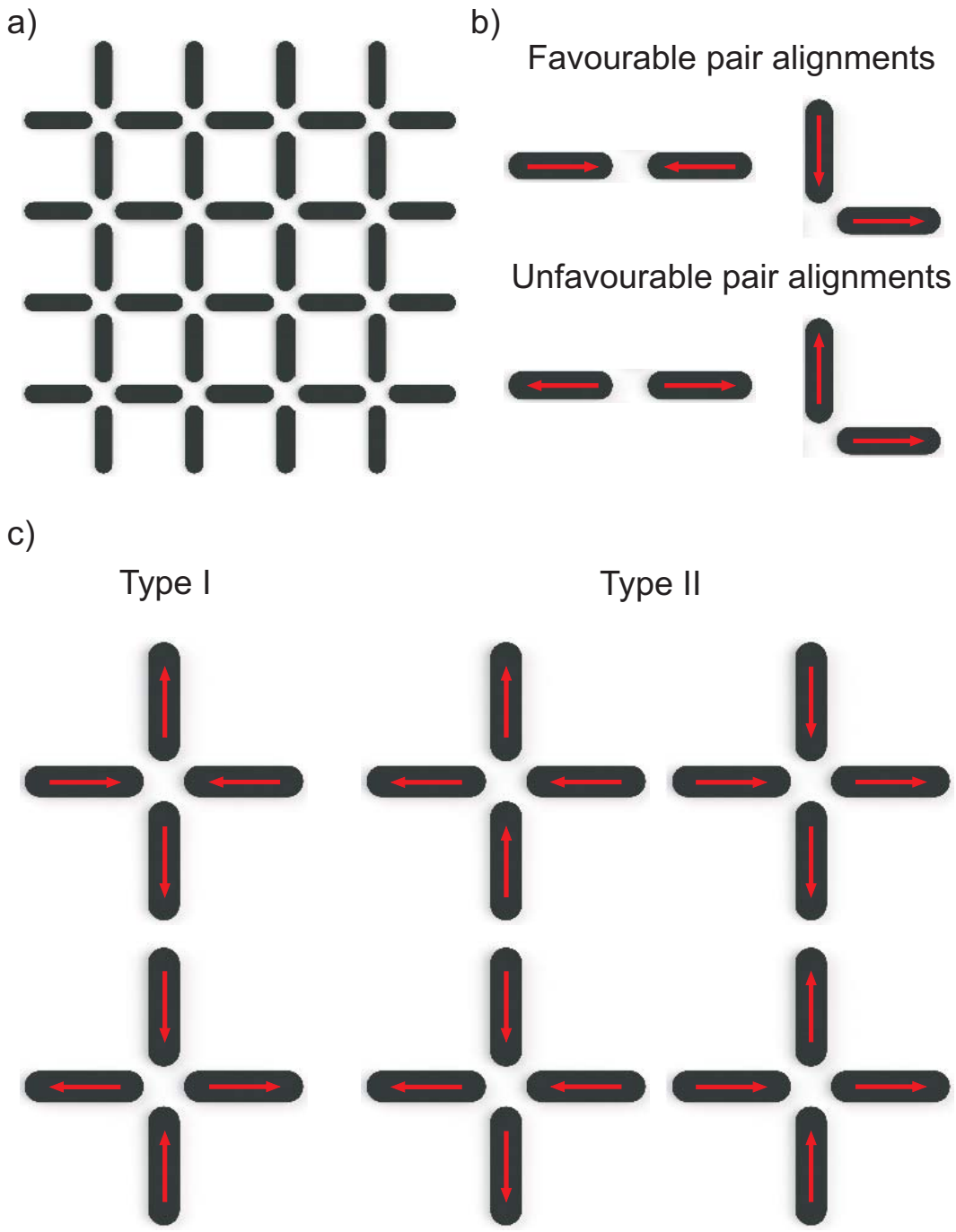

Figure 2.12.: a) Sketch of a square lattice consisting disconnected islands (black bars). b) Energetically favorable and unfavorable configurations for two islands parallel and perpendicular to each other. The red arrows indicate the magnetization direction. c) Configurations fulfilling the spin ice rule divided in type I and type II.

Artificial Spin Ice

While in water and spin ice geometrical frustration is achieved by the internal structure of the material, another way to accomplish this is by the shape of the material. If a ferromagnetic material is confined in a small structure the direction of the magnetization is dominated by the shape anisotropy. This circumstance was used by the Schiffer's group [Wan+06] to create the first 2D artificial spin ice (ASI). It consisted of disconnected elongated islands with the dimensions of 80 nm x 220 nm forming a square lattice as shown in Fig. 2.12a). Due to the shape anisotropy of the islands the magnetization was pointing parallel to the easy axis (along the 220 nm direction) in one of two directions creating an Ising like macro spin. The neighboring islands are interacting via a magnetic field created by the islands. For two islands in line to each other the lowest energy is achieved when the magnetizations of both islands are also in line (see Fig. 2.12 b)). The energetic favorable and unfavorable configuration for two islands with an orientation perpendicular to each other is shown in Fig. 2.12 b). For a vertex with four islands it is not possible to achieve the lowest energy configuration for all pairings. The lowest state is degenerate and can be acquired by the configuration with the magnetization of two islands pointing in and two pointing out of the vertex connecting the four islands which again resembles the ice rule. It is important to point out that states following the ice rule in square lattice can be further divided into states of type I and type II (see Fig. 2.12 c)) and a significant fraction of the structure can violate the ice rule [MM06]. Further information about artificial spin ice in a square lattice can be found in [Wan+06] [Wan07]. Due to the strong magnetic moment of the islands [Wan+06] the frustration is present and the different states of the structure are stable (no thermal fluctuations of the macro spins [She+12]) up to the Curie temperature [Kap+12][Zei13]. Therefore, it is often possible to perform experiments on the system at room temperature. However this also implies that the structure below Curie temperature is not in thermal equilibrium [She+12]. Another advantage of ASI structures beside the room temperature experiments is the possibility of investigating the behavior of a single macro spin and the potential control of the ASI properties by changing its dimensions.

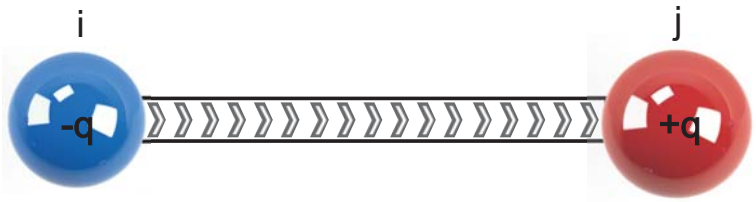

Figure 2.13.: Dumbbell model for a single link. The blue (red) circle at position i (j) is referring to a negative (positive) magnetic charge. The arrows inside the link indicate the magnetization direction.

2.11.2. Continuous Honeycomb Network

The pattern for the artificial spin ice (ASI) which is investigated in this thesis is the connected honeycomb structure. The structure itself is build up by three identical stripes/links rotated by 120° to each other. Since the centers of the links form a kagome lattice, in some cases the pattern is also named kagome ASI [QBC08]. Equal to the square lattice formation the dimensions of the links leads to a strong shape anisotropy resulting in a uniform Ising like behavior of the magnetization in the links, forming a macro spin. While in the first spin ice structure the islands were disconnected, the investigated honeycomb lattice is connected. The ends of each stripe are fused together with ends of two other links with different angles, forming a vertex. To understand the results of the experiments performed on the ASI structures in this thesis, we need to understand the dynamics and properties of a honeycomb structure. A common model to describe them is using the concept of magnetic charges. In the explanation of this concept we are following Ref.[Mel+10] and [She+12].
The basic element the honeycomb ASI consists of is a ferromagnetic stripe. Due to its shape anisotropy we can assume a uniform magnetization and therefore, describe it as a dumbbell with magnetic charges q of opposite signs on its ends. By definition the magnetization between two charges is pointing from the negative to the positive one (see Fig. 2.13). In a stable kagome ASI structure the charges are located in the vertices were the ends of the links are fused together. The value of a vertex charge is acquired by adding over the three joined charges of the links. For the further explanation we label the vertices with a consecutively index. The direction of the magnetization in the macro spin connecting two vertices i and j is

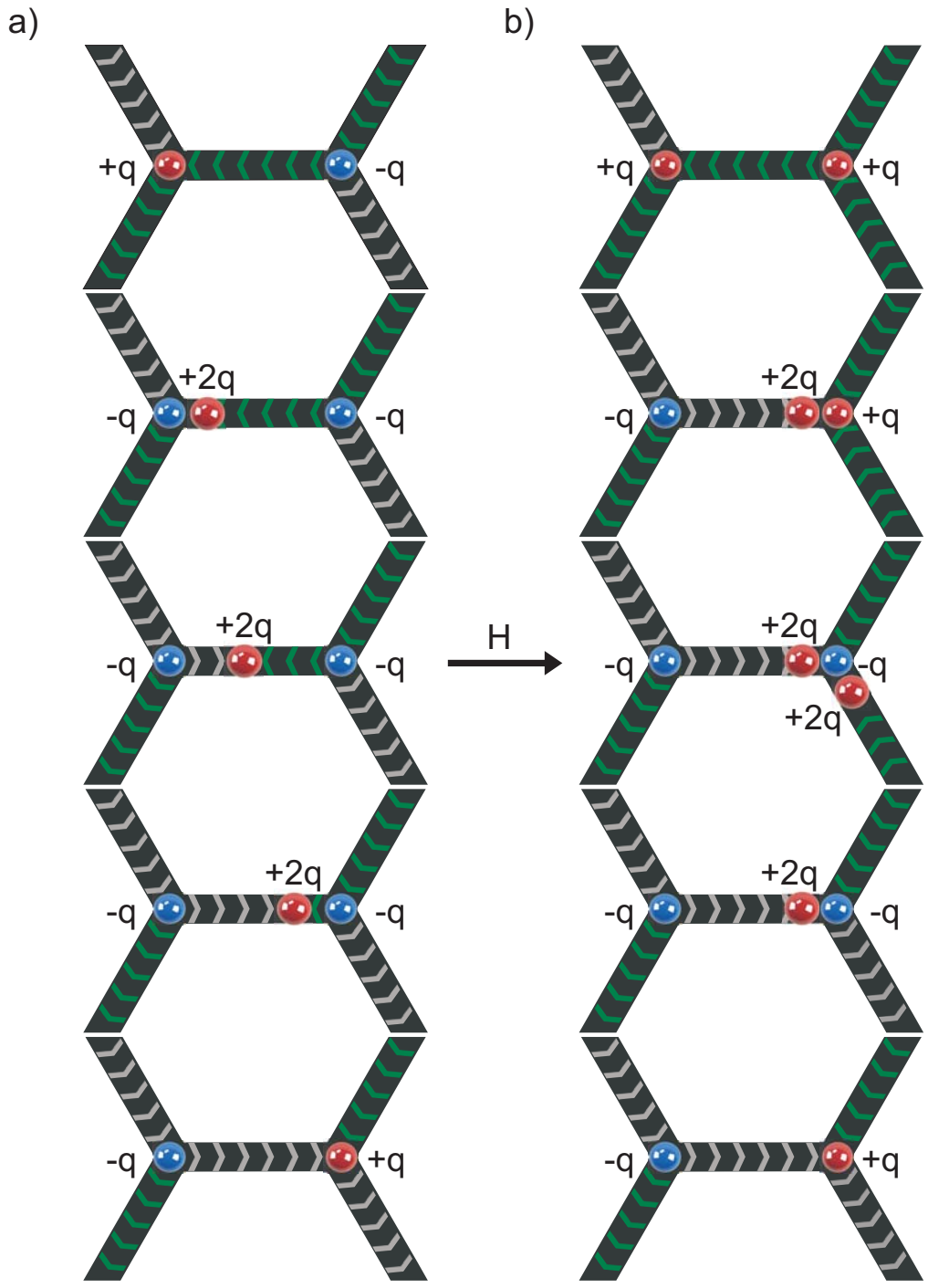

Figure 2.14.: Reversal of a single link in a honeycomb spin ice structure. The blue (red) circles refer to a negative (positive) magnetic charge in units of q. Gray (green) arrows inside the links indicate a magnetization direction to the right (left) side. When the applied field H is high enough, a vertex with charge +q will emit a domain wall with a charge +2q and will subsequently carry the charge -q. The domain wall moves to the second vertex with an opposing a) or equal b) charge. Before the domain wall can get absorbed in b) a second domain wall is emitted from the right vertex in an adjacent link, changing the sign of the vertex charge.

described by an Ising variable $\sigma_{ij} = \pm 1$ with $\sigma_{ij} = -\sigma_{ji}$. The variable σ_{ij} is positive if the magnetization direction is pointing from i to j. As a result we can describe the charge in a vertex i by

$$Q_i = \sum_j \sigma_{ji} q = -\sum_j \sigma_{ij} q. \tag{2.88}$$

The magnetic charge Q_i in the vertex is the magnetic field $\mathbf{H}$ out of the vertex. Since the magnetic induction $\mathbf{B} = \mu_0(\mathbf{H} + \mathbf{M})$ is divergence free Q_i is also equal to the magnetization $\mathbf{M}$ into the vertex [She+12]

$$Q_i = \oint \mathbf{H} \cdot \mathrm{d}\mathbf{A} = -\oint \mathbf{M} \cdot \mathrm{d}\mathbf{A} = -Mtw \sum_j \sigma_{ij} = -q \sum_j \sigma_{ij}. \tag{2.89}$$

Hence q is the magnetic charge in units of Mtw with the absolute value of the magnetization M the width w and the thickness t of the links. For one vertex with 8 different possible configurations of the adjacent links this leads to a possible charge of $Q = \pm 1q$ or $Q = \pm 3q$. Now it is possible to calculate the energy using the energy formula for Coulomb interaction [She+12]

$$E \approx \frac{\mu_0}{8\pi} \sum_{i \neq j} \frac{Q_i Q_j}{|\mathbf{r}_i - \mathbf{r}_j|} + \sum_i \frac{Q_i^2}{2C}, \tag{2.90}$$

with the capacitance C given by the dipolar and exchange coupling of the adjacent spins [CMS08] [She+12]. Careful observation reveals that the second term in Eq. 2.90 will always be positive. Therefore, due to the energy minimization principle it forces the minimization of the magnetic charges. The smallest charge in a vertex is acquired if the magnetization of just two links are pointing in ($Q = +q$) or out ($Q = -q$) which is the ice rule for kagome spin ice [WBL02]. In the following, we will refer to the two links pointing in (out) as majority links and to the one link pointing out (in) as minority link. The charge in a vertex can be altered by flipping a link i. e. changing the magnetization direction of a stripe. Since under normal conditions thermal fluctuations are frozen out [She+12] the transitions between states can be realized by applying an external magnetic field [Mel+10]. The reversal starts by the nucleation of a domain wall in the vertex. The wall can be described by a quasiparticle with a charge of $\pm 2q$. The magnetic field is pulling the domain wall away from the

vertex, through the link reversing the magnetization on its way. Finally the domain wall reaches the vertex on the opposing end of the flipped link and gets absorbed. Figure 2.14 a) is illustrating the reversal for a majority link between two vertices with opposing charges $\pm 1q$. A way to determine the critical field H_c necessary to pull the domain wall away from a vertex is described in [Mel+10]. When a vertex with charge $\pm 1q$ is emitting a domain wall (charge $\pm 2q$) it changes to a vertex with charge $\mp 1q$. The attraction between vertex and domain wall is greatest when the distance between them is equal to the domain wall width a [Mel+10]. This force has to be exceeded by the Zeeman force from the applied field H. Therefore, one gets [Mel+10]

$$F_{\max} = \mu_0 \frac{|Q_i Q_{dw}|}{4\pi a^2} = \mu_0 |Q_{dw}| H \Rightarrow H_c = \frac{|Q_i|}{4\pi a^2} = \frac{Mtw}{4\pi a^2}. \quad (2.91)$$

If the magnetic field is not applied parallel to the link but at an angle θ, we expect a reversal at a field $H = H_c / \cos\theta$ [Mel+10]. However, OOMMF simulations performed by P. Mellado et al. showed an asymmetric dependency of the angle θ [Mel+10]

$$H(\theta) = H_c / \cos(\theta + \alpha) \quad (2.92)$$

with an offset α. The offset angle reproduces the asymmetric distribution of the magnetization in the vertex [Mel+10][She+12]. In the previous part of this section we described the flipping process of a link between two vertices with opposing charges. The case with two equal charges was neglected since by applying the same description of the process used above would lead to a charge $\pm 3q$ which would violate the ice rule. However with the insight of Eq. 2.91 and Eq. 2.92 we can now explain the flipping process with the same charges at the vertices as shown in Fig. 2.14 b). In this case the charges of the domain wall and the second vertex are repelling each other and the domain wall stops at a distance of a. The domain wall on the other hand creates a magnetic field of the strength $2H_c$ resulting in a net field of $3H_c$ in the vertex [Mel+10]. The resulting projected field into the adjacent links is $1.5H_c$ which is high enough to pull a second domain wall from the vertex into the neighboring link. Since the polarity of the vortex charge is now changed, the first domain wall is attracted and absorbed by the vertex. As a consequence it is hard to find

any states violating the ice rule under the assumption that the deviation of the critical fields, for the different links, is small. The attempt to revert a minority link shows a similar result. In this case it is necessary to pull a charge $Q_{dw} = \pm 2q$ from a charge $Q_i = \pm 3q$ which requires a high field of $H = 3H_c$. If the critical field of the neighboring links is about the same, one can assume that the projected field was already big enough to switch one of the majority links first. This changes the minority link to majority and reduces its critical field to H_c enable it to flip. Hence, we are expecting the switching of a minority link only in the combination with a majority link.

3. Experimental techniques and methods

To conduct experiments on ferromagnetic resonance one needs a method to excite spin waves and a technique to detect them. In the following chapter we will describe the different methods used in this thesis and the associated setups.

3.1. All Electrical Spin Wave Spectroscopy

The All Electrical Spin Wave Spectroscopy (AESWS), also known as Propagating spin wave spectroscopy [BOF03], is a method to excite and detect spin waves only using electrical components. In the following we are describing the used setup as well as the mechanism for the spin wave generation and detection.

3.1.1. Vector network analyzer setup

Fig. 3.1 shows a measurement station used for AESWS experiments. The different parts are the following:

- The core part of the system is a vector network analyzer, (VNA) PNA-X N-5242A (two ports) or PNA N-5222A (four ports) from Agilent. Every port of each VNA is capable to generate and detected microwaves at a certain frequency f. The range of f is from 10 MHZ to 26.5 GHz. While all ports are detecting at a certain frequency only one port is emitting a signal at the same frequency. The typical power used in this thesis to generate the microwaves was 0 dBm $(1$ mW).

- An in-plane field is generated by two pairs of opposing electromagnets. Figure. 3.1 shows the four yokes which enhance and guide the field. Each pair of magnets is able to create a magnetic field $|\mu_0 H| = 0$ to100 mT at the sample position in one direction. By adding the fields of the two pairs it is possible to create a resulting field in every in-plane direction.

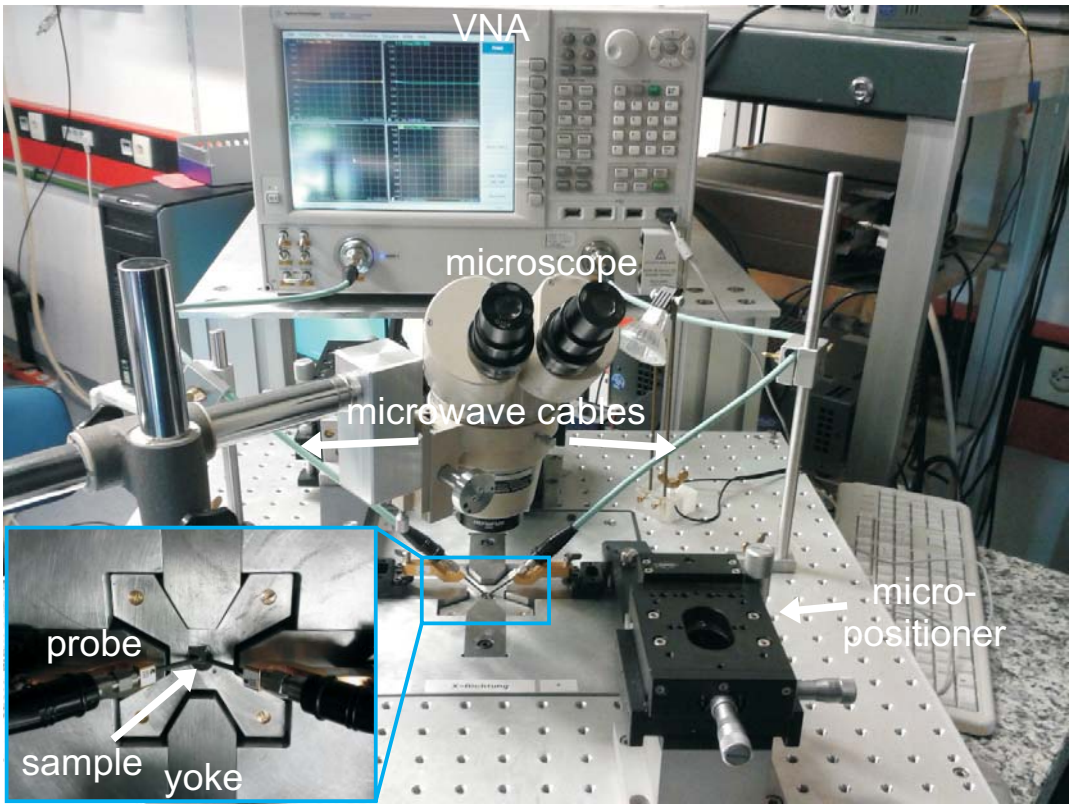

Figure 3.1.: Photograph of an AESWS setup providing a magnetic in-plane field. The sample is connected to the VNA via microwave probes and microwave cables. The probes are moved by the micropositioners. The insert shows a magnification of the sample area. The sample is placed between the yokes generating the in-plane field.

- To detect and control the magnetic field Hall sensors are integrated in the sample holder. They are positioned as close as possible to the tested specimen. They give feedback to the magnet controls and are used to log the actual field.
- To connect the ports of the VNA with the device under test (DUT) we use microwave cables and high frequency probes. Every component is 50 Ω matched to minimize reflection. The probes are consisting of three tips next to each other in one plane. The central tip is connected with the microwave signal, while the outer tips are on ground potential. By using a 3D positioning system the tips can be positioned on top of conduction pads on the DUT to establish a connection.

- In order to protect the setup from surrounding vibrations the setup is mounted on top of a shock absorbing table.

- For the control of the applied bias field and to conduct measurements a PC-program is used. Any possible magnetic field sequence can be planned in advance. The execution and the data acquisition are fully automatic.

VNA calibration

As the name is indicating a VNA (Vector Network Analyzer) is a device built for the investigation of electronic networks. A electronic network is basically a complex electronic system and has, in the most cases, a non-trivial behavior. The VNA is collecting informations about the system by sending a signal into the network and displaying the response signals. Thereby the network is treated as a black box. By changing external parameters as the signal frequency f we can determine the dependancy of the network. In the context of this work we only want information about the DUT. But all the cables and connections guiding the microwave signal to the DUT and even the VNA itself have a frequency depended behavior. The origins of this are basically three sources of errors: systematic, drift and random errors. The non-ideal part of the VNA and the connections are summarized to a so called error network which can be described by error terms. By performing a calibration following [Tec04] it is possible to determine the systematic errors, which are repeatable and stable, and then separate them from the detected signals. Drifting errors can be decreased by redoing the calibration in certain time intervals. The main reason for drifting errors is temperature variation. Since our measurement setup is in a temperature stabilized environment one calibration can be used for a long time. The random errors cannot be predicted and therefore, the calibration has no influence on them. To perform a calibration, we use the calibrations standards short, open, load and through. The method is also known as SOLT [Tec04]. In our case the standards are structures on a substrate with very well-known properties. These properties are summarized and stored in files on the VNA known as cal-kits. By using the microwave probe to establish a connection between the calibration standards, one can determine and remove the systematic error term of the whole error network to the tips of the probe.

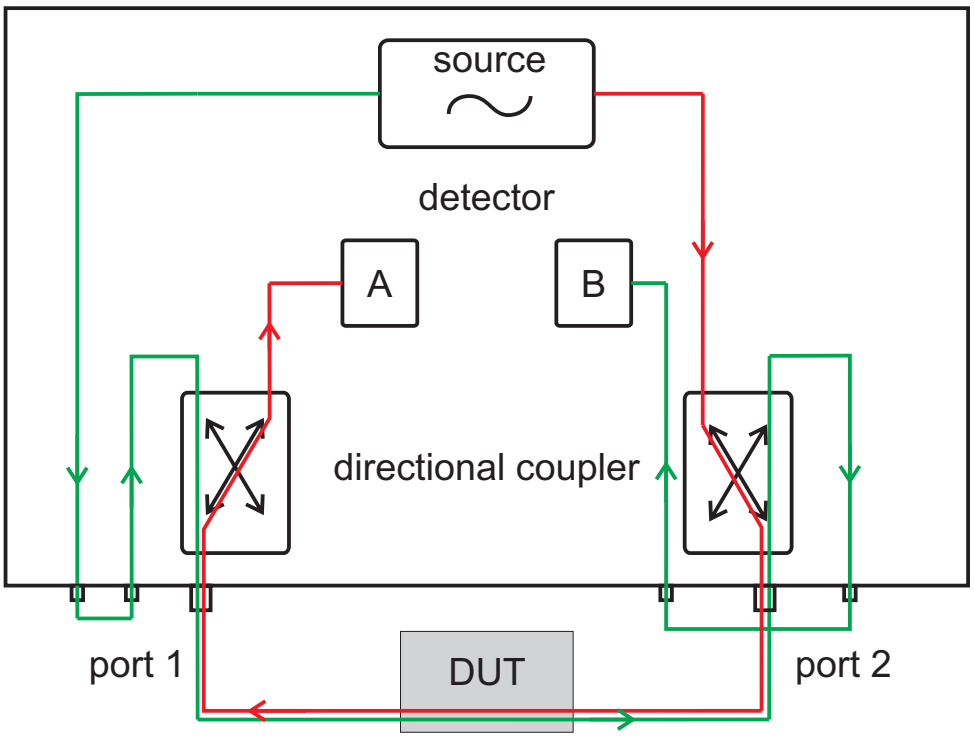

Figure 3.2.: Sketch of a VNA test setup. The green (red) line shows the signal path from port 1 (port 2) to port 2. The setup is configured to increase (decrease) the signal strength for the green (red) path compared to the standard configuration.

VNA sensitivity

The two port VNA PNA-X N-5242A offers the possibility to reroute the signal path to increase the transmission signal. In normal configuration the signal generated by the rf source is guided through the main path of a directional coupler. Then the signal leaves the VNA at a port, gets sent through the DUT and back to the VNA via the other port. Here, the signal is directed by the directional coupler through its coupler path towards the signal detector. However, the signal in the coupler path is decreased by 15 dB. By changing hardware connectors it is possible to reroute the signal as shown in Fig. 3.2. The green path sends a signal coming from port one through the main path of both directional couplers. Therefore, the detected signal is stronger. Following the path from port two to port one (red), the signal gets decreased before entering the DUT and after leaving it. It would

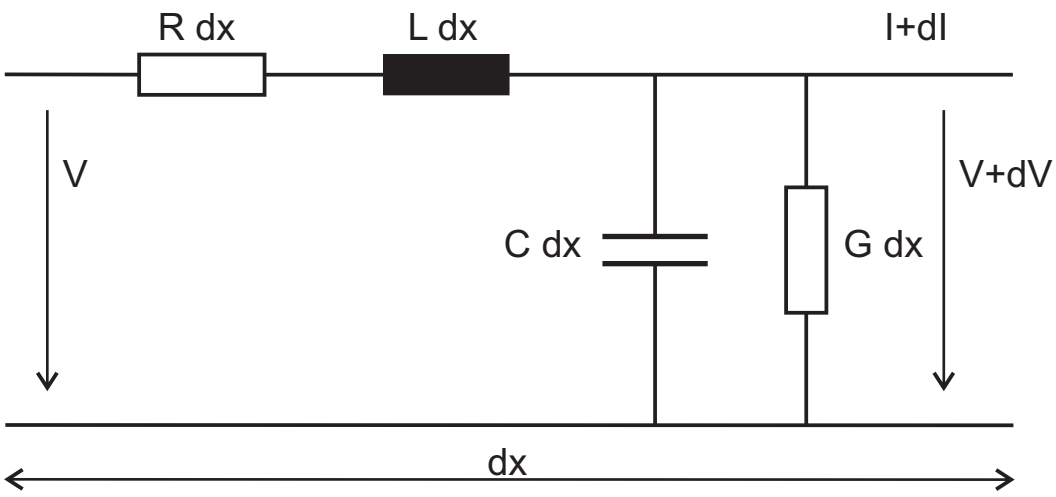

Figure 3.3.: Equivalent network for a section of a microwave circuit with the length dx. The properties of the circuit is defined by the resistance R, inductance L, capacity C and conductance G.

be possible to reroute the signal that way that the signals in both directions would not be deceased after entering the DUT. In this configuration the signal would only decreased before arriving the DUT. To compensate the loss of power it would be possible to increase the power of the source. Unfortunately this would lead to source unleveling which is the reason why this option is not practical.

3.1.2. Characteristic Impedance and Electromagnetic Wave Transmission

In Sec. 2.5 and Sec. 2.7 it was shown that an oscillating magnetic rf field can be used to excite spin waves. By using a rf current such a field can be generated by induction. To guide such a rf current to the DUT (Device Under Test) we need some basic concepts for microwave circuits. A simple example for a circuit are two conducting lines, one signal line and one ground line, separated by a dielectric. The circuit can be divided in a line of serial pieces of infinite small circuits with the length dx. Therefore, dx is small compared to the rf current wavelength λ. An equivalent network for such a piece of circuit is shown in Fig. 3.3. It consists of an ohmic resistor R and an inductance L connected in series. Additionally there is a shunt capacitance C and a shunt conductance G in use. For this concept

we assume Transversal Electric and Magnetic fields (TEM). Only in this special case current and voltage are defined [Bil07]. In the interval dx the voltage is decreased and a part of the current in the signal line is lost to the ground line. The loss can be calculated by

$$dV = -\left(RdxI + Ldx\frac{\partial I}{\partial t}\right) \tag{3.1}$$

$$dI = -\left(GdxV + Cdx\frac{\partial V}{\partial t}\right). \tag{3.2}$$

Since we assume an infinite small dx we can use the differential equations

$$\frac{\partial V}{\partial x} = -\left(RI + L\frac{\partial I}{\partial t}\right) \tag{3.3}$$

$$\frac{\partial I}{\partial x} = -\left(GV + C\frac{\partial V}{\partial t}\right). \tag{3.4}$$

Our signal is provided by the VNA, which generates a signal with a sinusoidal time dependency. Therefore, we assume the time dependency:

$$V(x,t) = \mathrm{Re}(\widetilde{V}(x)\mathrm{e}^{i\omega t}); I(x,t) = \mathrm{Re}(\widetilde{I}(x)\mathrm{e}^{i\omega t}). \tag{3.5}$$

By inserting Eq. 3.5 into Eq. 3.3 , Eq. 3.4 and eliminating t one obtains

$$\frac{\partial \widetilde{V}}{\partial x} = -(R + i\omega L)\widetilde{I} \tag{3.6}$$

$$\frac{\partial \widetilde{I}}{\partial x} = -(G + i\omega C)\widetilde{V}. \tag{3.7}$$

When these two equations are combined we get a formula knowns as the telegrapher's equation [SE43]:

$$\frac{\partial^2 \widetilde{V}}{\partial x^2} = \eta^2 \widetilde{V} \text{ and } \frac{\partial^2 \widetilde{I}}{\partial x^2} = \eta^2 \widetilde{I} \tag{3.8}$$

with the propagation constant $\eta = \sqrt{(R + i\omega L)(G + i\omega C)}$ in units of a wave vector (1/m). The solution of the telegrapher equation is

$$\widetilde{V}(x) = \widetilde{V}^{+}\mathrm{e}^{-\eta x} + \widetilde{V}^{-}\mathrm{e}^{\eta x} \tag{3.9}$$

$$\widetilde{I}(x) = \widetilde{I}^{+}\mathrm{e}^{-\eta x} + \widetilde{I}^{-}\mathrm{e}^{\eta x} \tag{3.10}$$

which describes the superposition of waves traveling in opposite directions. $\widetilde{V}^{+}$, $\widetilde{V}^{-}$, $\widetilde{I}^{+}$ and $\widetilde{I}^{-}$ are integration constants. They are connected by the characteristic impedance

$$Z_c = \frac{\widetilde{V}^{+}}{\widetilde{I}^{+}} = -\frac{\widetilde{V}^{-}}{\widetilde{I}^{-}} = \sqrt{\frac{(R + i\omega L)}{(G + i\omega C)}}. \tag{3.11}$$

For a non-TEM mode Eq. 3.11 can also be used. In this case the voltage and the current have to be replaced by the electrical field E and the magnetic field H [Bil07] [Ell93]. Since η is a complex value we split it into a real and an imaginary part

$$\eta = \alpha + i\beta = \sqrt{(R + i\omega L)(G + i\omega C)}. \tag{3.12}$$

The real part α is the attenuation constant the imaginary part β is a phase constant. This gets illustrated by inserting Eq. 3.9 into Eq. 3.5:

$$V(x,t) = \widetilde{V}^{+}\mathrm{e}^{-\alpha x}\mathrm{e}^{i\omega t - i\beta x} + \widetilde{V}^{-}\mathrm{e}^{\alpha x}\mathrm{e}^{i\omega t + i\beta x}. \tag{3.13}$$

While α reduces the wave amplitude (in traveling direction), β changes the phase depending on the propagation length. Therefore, β can be used to calculate the phase velocity by

$$v_{\mathrm{phase}} = \frac{\omega}{\beta}. \tag{3.14}$$

If the properties of the circuit are constant over the entire lines the signal behaves as described above. If there is a mismatch between different sections we have to consider another effect. Let us assume at position 0 occurs a change in impedance from Z_c to Z_0. By using Eqs. 3.9, 3.10 and

3.11 we can write [Roy]

$$\widetilde{V}^{+}\mathrm{e}^{-\eta x} = \sqrt{Z_c}\frac{1}{2}\left[\frac{\widetilde{V} + Z_c\widetilde{I}}{\sqrt{Z_c}}\right]; \widetilde{V}^{-}\mathrm{e}^{\eta x} = \sqrt{Z_c}\frac{1}{2}\left[\frac{\widetilde{V} - Z_c\widetilde{I}}{\sqrt{Z_c}}\right] \quad (3.15)$$

and the characteristic impedance at position 0 [Ell93]

$$Z_0 = \frac{\widetilde{V}(0)}{\widetilde{I}(0)} = Z_c\frac{\widetilde{V}^{+} + \widetilde{V}^{-}}{\widetilde{V}^{+} - \widetilde{V}^{-}}. \quad (3.16)$$

By rearranging it follows

$$\widetilde{V}^{-} = \frac{(Z_0/Z_c) - 1}{(Z_0/Z_c) + 1}\widetilde{V}^{+}. \quad (3.17)$$

$\widetilde{V}^{-}$ is the amplitude of the voltage wave traveling in the opposite direction. As a consequence, for $Z_0 \neq Z_c$ a part of an incoming wave is reflected at the point of impedance change. The reflection coefficient at this point is defined as [Ell93]

$$\Gamma = \frac{\widetilde{V}^{-}}{\widetilde{V}^{+}} = \frac{(Z_0/Z_c) - 1}{(Z_0/Z_c) + 1}. \quad (3.18)$$

To prevent such reflections reducing the signal it is essential that every component has the same characteristic impedance. Historically the most rf components are adjusted to a wave impedance of $50\ \Omega$.

3.1.3. Scattering Parameters

To analyze high frequency devices it is common practice to compare the original signal with the resulting one. Also at high frequencies it is not possible to easily measure voltage and current directly. Therefore, Scattering parameters S are used which are directly measured by the VNA [Tec04]. A rf device is often treated as a network with a fixed number of gates (ports). On every port it is possible to feed in a signal and to detect one. To describe the signals on port n we use the definition [Roy]:

$$a_n = \frac{1}{2}\frac{V_n + Z_{cn}I_n}{\sqrt{Z_{cn}}}, \quad (3.19)$$

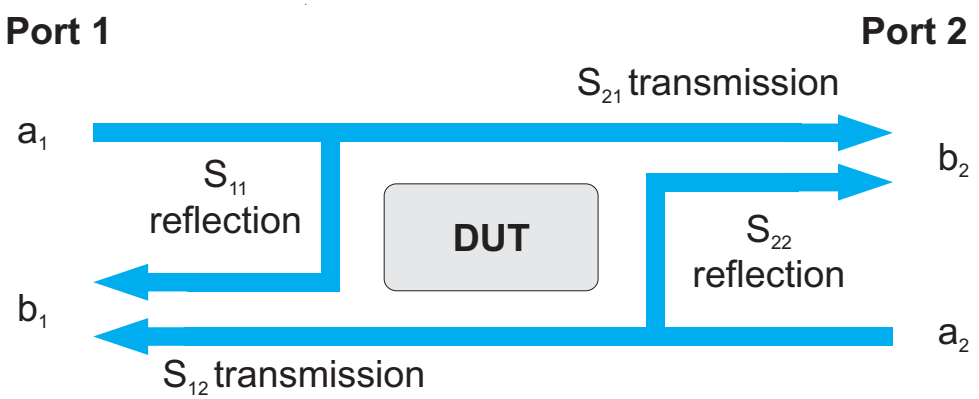

Figure 3.4.: Illustration of a 2 port network representing a DUT. The S-parameter S_{11}, S_{12}, S_{21} and S_{22} describe the relation between all possible incoming signals a and the detected signals b, giving a full description of the network.

for the incoming wave and

$$b_n = \frac{1}{2}\frac{V_n - Z_{cn} I_n}{\sqrt{Z_{cn}}} \tag{3.20}$$

for the detected wave. If we compare Eqs. 3.19 and 3.20 with Eq. 3.15 for a reflected and a transmitted wave we see that a and b are well chosen to present the wave signals at the gates. V_n, I_n and Z_{cn} are the respective voltage, current and characteristic impedance at the particular port. The Scattering parameter S_{mn} is defined by [Dic47]

$$b_m = S_{mn} a_n \rightarrow S_{mn} = \frac{b_m}{a_n} \text{ with } m, n = 1, 2, ... \tag{3.21}$$

Since the reflection coefficient Eq. 3.18 defines a scattering process it is quite obvious why the name for the S-parameter was chosen. The S-parameters and the corresponding signal paths for a two-port system are depicted in Fig. 3.4. The signals a and b on the two ports are connected via the scattering matrix

$$\begin{pmatrix} b_1 \\ b_2 \end{pmatrix} = \begin{pmatrix} S_{11} & S_{21} \\ S_{12} & S_{22} \end{pmatrix} \cdot \begin{pmatrix} a_1 \\ a_2 \end{pmatrix} \tag{3.22}$$

Since the signal described by S_{12} and S_{21} is going through the network, those are also indicated as transmission signal while, we link S_{11} and S_{22} to the reflection signal. It is important to note that the S-parameters are complex values and therefore, a phase sensitive measurement-technique is required.

3.1.4. Electrical Signal Detection

In the AESWS we use Coplanar Wave Guides (CPWs) (see Sec. 3.1.5) to detect spin waves by measuring a voltage induced by the change of magnetic flux. The strength of the voltage can be calculated by using Faraday's law and the reciprocity [Sil+99]. Following F. Giesen [Gie05], we consider two conducting loops, l_1, l_2 enclosing the corresponding areas A_1 and A_2. By sending a current through l_1 a magnetic flux

$$\Phi_2 = \int_{A_2} \mathrm{d}\mathbf{A} \cdot \mathbf{B}_1 \tag{3.23}$$

is induced in l_2. An alternative way to calculate the flux considering the geometries of the two loops and the current is given by:

$$\Phi_2 = L_{21} I_1. \tag{3.24}$$

The induction coefficient L_{21} links the flux in l_2 with a current I_1. The principle of reciprocity states that the two coefficients L_{21} and L_{12} are equal. In the general case it is difficult to calculate the coefficient L for a CPW but using the reciprocity it can be calculated indirectly. Sending a current through a CPW generates a magnetic field $\mathbf{H}(I_{\mathrm{CPW}})$. By using a probe loop l enclosing an area $\mathrm{d}\mathbf{A}$ we get a flux of

$$\mathrm{d}\Phi_l = \mu_0 \mathbf{H}(I_{\mathrm{CPW}}) \cdot \mathrm{d}\mathbf{A} = L_{l,\mathrm{CPW}} I_{\mathrm{CPW}} \tag{3.25}$$

through the loop. $\mathbf{H}(I_{\mathrm{CPW}})$ can be calculated via the law of Biot-Savart. For signal detection we want the flux through the CPW. The result is

$$\mathrm{d}\Phi_{\mathrm{CPW}} = L_{\mathrm{CPW},l} I_l = L_{l,\mathrm{CPW}} I_l = \frac{\mu_0}{I_{\mathrm{CPW}}} \mathbf{H}(I_{\mathrm{CPW}}) \cdot I_l \mathrm{d}\mathbf{A}. \tag{3.26}$$

Since $I_l \mathrm{d}\mathbf{A}$ describes the magnetic moment of the loop, the term can be replaced by the magnetic moment $\mathrm{d}\mathbf{m} = \mathbf{M}\mathrm{d}V$ of a ferromagnetic film

resulting in:

$$\Phi_{\mathrm{CPW}} = \mu_0 \int_{V_s} \mathrm{d}V \frac{\mathbf{H}(I_{\mathrm{CPW}})}{I_{\mathrm{CPW}}} \cdot \mathbf{M} \tag{3.27}$$

with V_s as the volume of the sample.

To calculate the components of the CPW field, electromagnetic simulations (MicrowaveStudio) haven been performed by T. Schwarze on CPWs with similar dimensions as used in this thesis. He found that the field values of the in-plane (xy-plane) components are by an order of magnitude larger compared to the out-of-plane component (z) [Sch13]. Therefore, we neglect the out-of-plane field and assume a field with only in-plane components, perpendicular to the signal line. The field generated by a CPW (signal line along the x-axis) can be approximated by [Neu11]

$$\mathbf{H}(I_{\mathrm{CPW}}) = f(y)\frac{I_{\mathrm{CPW}}}{w}\mathbf{e}_y \tag{3.28}$$

with the inner conductor line w, the unit vector $\mathbf{e}_y$ in y-direction and the normalized spatial field distribution $f(y)$. Therefore, the general equation Eq. 3.27 can be rewritten to

$$\Phi = \frac{\mu_0 t_s l \sin\alpha}{w} \int \mathrm{d}y f(y) M_y(y,t), \tag{3.29}$$

were t_s is the thickness, l the length of the signal line and α the angle between the magnetization and the x-axis. Finally the induced voltage can be calculated with

$$V = -\frac{\mathrm{d}\Phi}{\mathrm{d}t} = \frac{\mu_0 t_s l \sin\alpha}{w} \int \mathrm{d}y f(y) \chi_{\mathrm{tot}}(\omega) \frac{\mathrm{d}h(y,t)}{\mathrm{d}t}. \tag{3.30}$$

χ_{tot} is the susceptibility for all contributing wave vectors k [Cou+04]. It is given by [Neu11][PWB08][VB10]

$$\chi_{\mathrm{tot}}(\omega) = \int \mathrm{d}k \chi(\omega,k)\rho(k)\exp(-ikd). \tag{3.31}$$

$\rho(k)$ is the spin wave excitation distribution given by the CPW and d the traveled distance of the wave. In Eq. 3.30 we see that the measured voltage is proportional to $\chi_{\mathrm{tot}}(w)$. The voltage is also changing the impedance

matrix of the CPW and therefore, because of the relation [DA97] [Hub13] $S_{ij} \leftrightarrow Z_{ij}$ the S-parameters. It is important to note that depending on the CPW and the measurement installation, the measured voltage may be smaller compared to Eq. 3.30 because the induced voltage wave travels in both directions of the signal line [Sil+99]. Hence depending on the measurement setup only a share of the whole signal might be detected. More detailed information about the electrical signal detection can be found in [Gie05], [Sil+99] and [Neu11].

3.1.5. Coplanar Waveguide

To excite spin waves in a ferromagnetic material we use a CPW. It was first demonstrated by C. P. Wen [Wen69] in 1969. The CPW consists of three parallel, conducting lines separated by fixed gaps (see Fig. 3.5 a)). The two outer lines, the so called ground lines with the width w_{g} and the signal line of width w_{s} are separated by a gap of the width w_{gap}. To excite spin waves an rf current is sent through the signal line resulting in a magnetic rf excitation field around the signal line (see Sec. 3.1.4). This structure supports a quasi-TEM mode of propagation [Sim01] and therefore, the description of the electrical signal detection in Sec. 3.1.4 and Sec. 3.1.2 can be applied. Compared to a conventional microstrip line we benefit from some important advantages. The structure is in one plane which simplifies the fabrication (no ground-plate on the backside of the structure). Since the signal line is surrounded by the ground planes, the crosstalk to other structures next to the CPW is strongly reduced [Sim01] [Sch13] [Neu11]. Because the used rf setup is adjusted to an impedance of $50\ \Omega$, the CPW has also to be $50\ \Omega$ matched to maintain the best signal transmission from and into the CPW. For high frequency $\omega L >> R$ is valid and Eq. 3.11 becomes [Bil07]

$$Z_c = \sqrt{\frac{L}{C}}. \tag{3.32}$$

Following [Sim01] the characteristic impedance of a CPW on a dielectric substrate of finite thickness can then be calculated by

$$Z_c = \frac{30\pi}{\sqrt{\epsilon_{\mathrm{eff}}}} \frac{K(k_0')}{K(k_0)}. \tag{3.33}$$

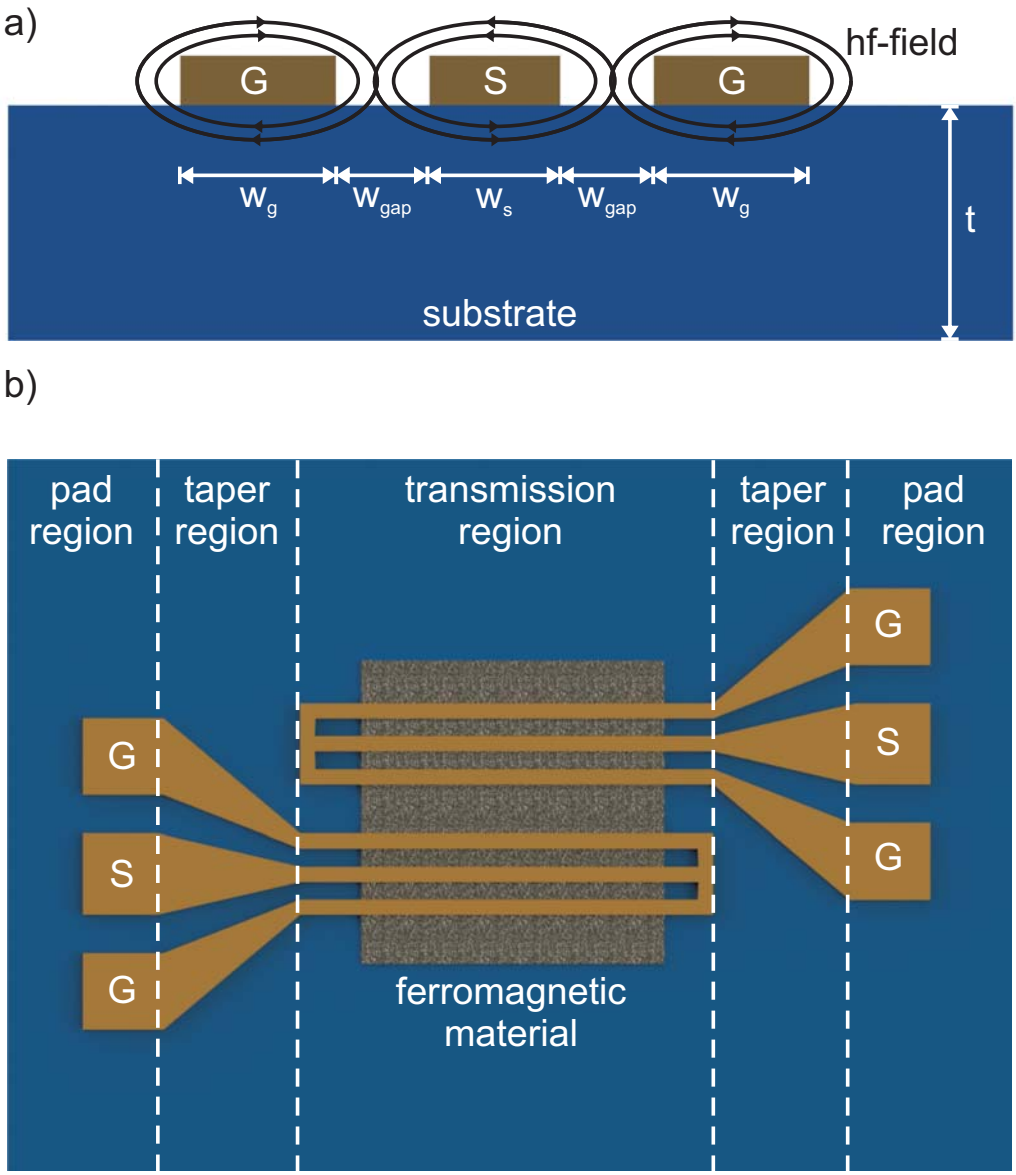

Figure 3.5.: a) Cross section of a CPW. The ground lines (G) with width w_g are separated from the signal line (S) with width w_s by a distance of w_{gap}. An rf current excites an rf field surrounding the CPW lines. b) Top view on two CPWs for transmission measurements. Different parts are separated by white lines.

K is the complete elliptic integral of the first kind. The other parameters are given as

$$\epsilon_{\text{eff}} = 1 + \frac{\epsilon_r - 1}{2} \frac{K(k_1)}{K(k_1')} \frac{K(k_0')}{K(k_0)}. \tag{3.34}$$

ϵ_r is the relative permittivity. The k values are

$$k_0 = \frac{w_{\text{s}}}{w_{\text{s}} + 2w_{\text{gap}}}; k_0' = \sqrt{1 - k_0^2}, \tag{3.35}$$

$$k_1 = \frac{\sinh(\pi w_{\text{s}}/4t)}{\sinh\{[\pi(w_{\text{s}} + 2w_{\text{gap}})]/4t\}}; k_1' = \sqrt{1 - k_1^2}, \tag{3.36}$$

with t as the thickness of the dielectric substrate. We see that the characteristic impedance strongly depends on the ratio of w_{s} and w_{gap}. Hence it is possible to vary the size of the CPW. As long as the ratio is constant the characteristic impedance Z_c stays about the same. This fact was also used to design the contact pads of the CPWs. These pads are necessary to connect the microwave cables from the VNA to the CPW. To establish this connection, high frequency tips are placed on top of the pads. The pads are adjusted to $50\ \Omega$ and the fix gap between the tips. The tapering region (see Fig. 3.5 b)) adjusts the size of the pads to the size of the actual CPW lines in the transmission region.

In this work we use two types of designs. A flip chip and an integrated CPW. The integrated CPW is directly fabricated on top of the DUT. If the DUT contains conducting materials, CPW and DUT are separated by a thin isolation layer. The flip chip CPW is fabricated on a separate chip. The DUT is then flipped and put on top of the flip chip CPW with the magnetic film surface meeting the CPW surface.

For data acquisition it is important to know the excitation profile of the CPW. It can be obtained by simulating the profile of the magnetic excitation field h_y in y-direction (see Sec. 3.1.4), using a electromagnetic simulation (Microwave Studio). According to [Sch13] [Neu11] the other components of the field are relative small and can be neglected. The field h_y changes across the CPW (in y-direction) since the currents in the signal line and the ground lines flow in opposite directions. By performing a Fourier-transformation we get the k dependent excitation profile (see [Sch13] [Neu11] [Yu+13]), which depends on the geometry of the CPW. The spectrum has multiple maxima with a finite width of Δk which en-

ters the resonance linewidth Δf (see Sec. 2.6). For many experiments the first maximum is essential. Two rough approaches to estimate the maximum position can be found in [Cou+04] and [KKS07]. The methods give a good approximation for small signal lines. But for large w_s the deviation from the exact simulations gets quite significant [Sch13]. Therefore, in this work we use k-vectors extracted from electromagnetic simulation.

3.1.6. Measuring Protocol and Data Treatment

In the actual AESWS measurement we detect the S-parameters of the DUT while sweeping the frequency at a chosen range. After each sweep the applied external magnetic field is changed and the measurement repeated. The result is the response of DUT depending of frequency and field.

By using a calibration (see Sec. 3.1.1) we can limit the signal measured with the VNA to the DUT beyond the contact tips. But this signal still includes changes of the CPW impedance without a magnetic resonance. The impedance alteration can arise from temperature changes but also a frequency dependency of the CPW impedance. All the changes sum up to a magnet field independent background signal which can be bigger than the signal originate from the magnetic resonance. To remove the background and to increase the signal contrast we use two methods.

For the first method the experimental routine is divided into two parts. The reference part and the actual measurement part. The background is independent of the external magnetic field. Hence in the reference part we choose a magnetic field configuration different from the measuring part. That way the expected magnetic resonance frequencies are different from the frequencies of the measuring part. In an ideal case we excite only spin waves of frequencies outside the measured frequency range, leading to a reference dataset only showing a background signal. If that is not possible we try to avoid a superposition of resonances in the two different parts (reference and measurement) and choose a configuration with a weak magnetic signal in the reference measurement. In the second part the normal measurement is performed as described above. Finally the reference sweep is subtracted (linear components) from all measurements sweeps removing the background signal.

$$\Delta S = S_{Meas} - S_{ref} \tag{3.37}$$

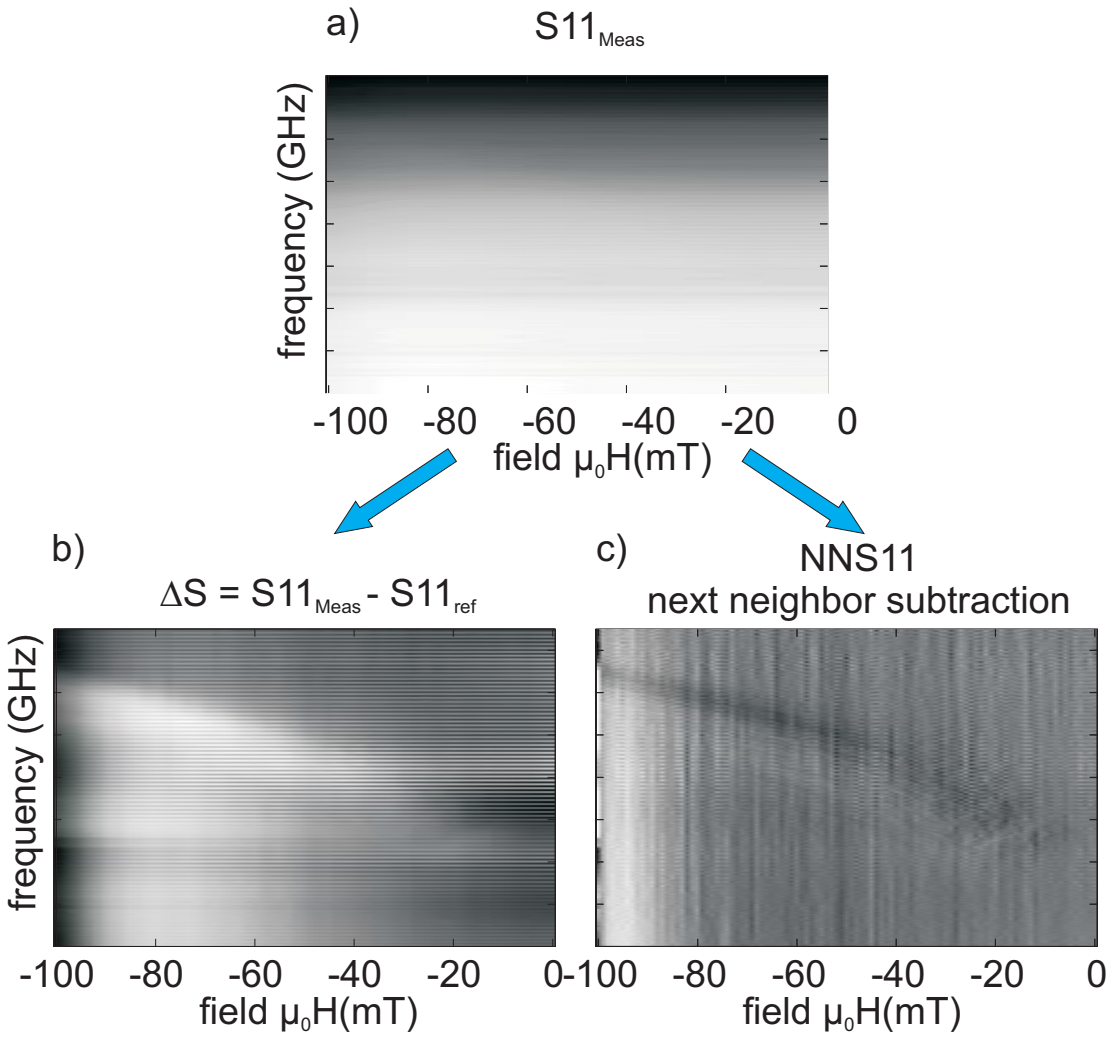

Figure 3.6.: a) depicts the real part of the scattering parameter S11, received by an AESWS measurement on a ferromagnetic sample. By subtracting a reference measurement b) or performing next neighbor subtraction c) the contrast of the resonance signal gets increased.

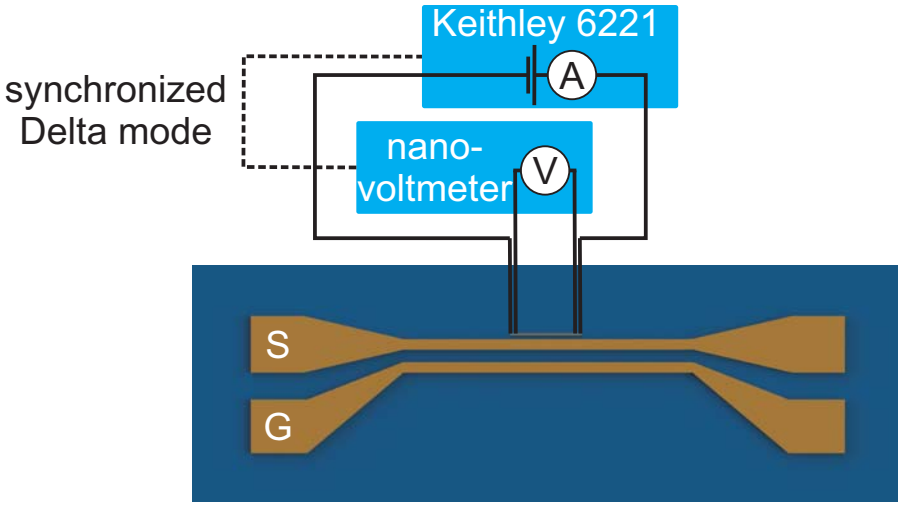

Figure 3.7.: Sketch of the resistance measurement setup with delta-mode measurement technique. Black solid lines represent current leads to a nanotube (gray thick line) near a CPW (signal line S and ground line G). Dashed lines represent links between devices for communication between them.

In an ideal case the spin wave signal is pronounced. The effect of the protocol is shown in Fig. 3.6 b).

The second method is denoted by next neighbor subtraction (NNS). The measurement is first performed as described above. Then, after all spectra were taken, the data are processed as follows:
Spectrum taken at step number $x - 1$ is subtracted from the spectrum at x. Sweep x is subtracted from sweep $x + 1$ and so on. From each measurement the neighboring sweep is subtracted. The result does not reflect the signal strength depending on frequency and field, but the change of the signal from magnetic field x to field $x + 1$. This method can significantly increase the contrast of weak signals and also suppresses background signals which are is slowly changing over time during the measurement. The result of the methods can be seen in Fig. 3.6 c).

3.2. Resistance Measurement

In the course of the work the resistance measurement was utilized to measure the effect of the anisotropic magnetoresistance (AMR). Since the change of the resistance due to the AMR is usually relative small we used the four probe configuration to connect the DUT with a Keithley 2182

nanovoltmeter and a Keithley 6221 current source as shown in Fig. 3.7. The Keithley 6221 sent a current I through the DUT (in case of Fig. 3.7 a nanotube), while the Keithley 2182 measured the voltage U. Finally the resistance of the DUT was determined via $R = \frac{U}{I}$. For an improvement of the signal to noise ratio the current source and the nanovoltmeter were linked and utilizing the delta-mode as described in Sec. 3.4

3.3. Electrical Detected Ferromagnetic Resonance (EDFMR)

A challenge in the investigation of ferromagnetic nanotubes (Nts) is the small magnetic moment of the sample. To ensure an adequate signal strength a great number of potential methods, used to examine magnetic properties, require a minimal magnetic moment. In many cases the amount of magnetic material of a single Nt is just too small to resolve its signal. A measurement on an assemble of tubes can be possible, however the variation of dimensions, properties and positions amongst the tubes often leads to a strong broadening of the signal. A method capable to perform measurements on individual Nts is the electrically detected ferromagnetic resonance (EDFMR). Similar to the AESWS the EDFMR is a technique for the detection of ferromagnetic resonance using only electrical components and effects. The difference is the method for the detection of the SW signal. While the AESWS is using a CPW for the signal detection (see Sec. 3.1) EDFMR is utilizing a resistance/voltage measurement whose results gets influenced by the SWs in the ferromagnetic material.

3.3.1. EDFMR Setup

The setup is very similar to the one already described in Sec. 3.1.1. To set the external field and contact the DUT we used the same in-plane field system, and movable high frequency probes. Instead of the VNA, the SW signal was generated with a microwave generator Agilent N5183A, providing a frequency range of 100 kHz to 20 GHz and a maximum output power of 15 dBm. To excite the magnetic moments within the DUT the generator is connected to an asymmetric CPW. Its functionality is similar to a normal CPW. An rf current within the signal line is generating an rf magnetic field which excites magnetic moments. However, instead of ferromagnetic material underneath the CPW the samples (in the framework

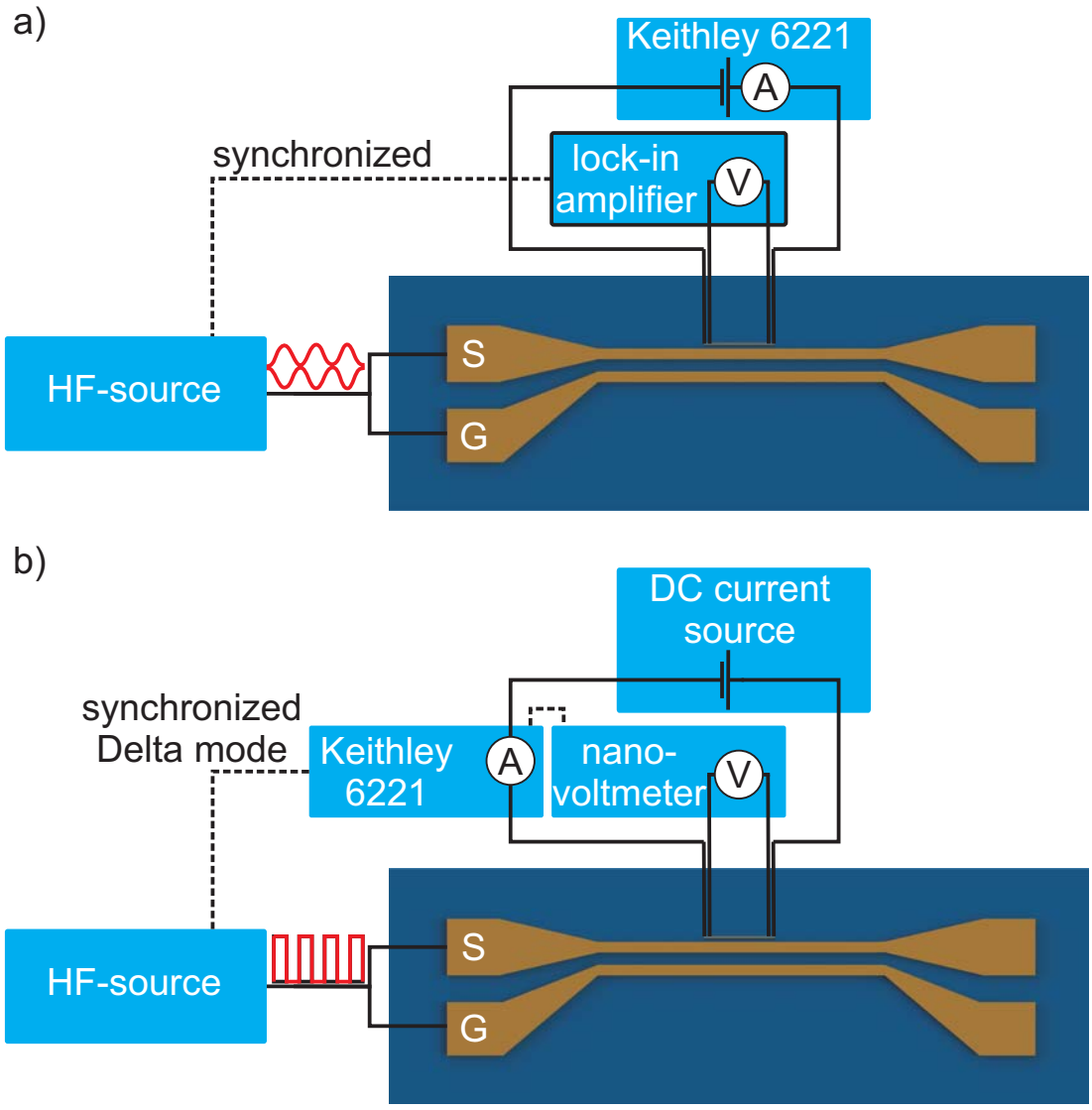

Figure 3.8.: Sketch of the EDFMR setup with lock-in (a)) and delta-mode (b)) measurement technique. Black solid lines represent current lines connected to a nanotube (gray thick line) near a CPW (signal line S and ground line G). Dashed lines represent links between devices for communication between them.

of this thesis ferromagnetic tubes) are placed next to the signal line and therefore, the CPW dimensions have no influence on the k-vector of SWs within the tubes. To minimize the gap between tube and signal line and thus acquire a strong field at the tube one ground line was removed leading to the asymmetry of the structure. For the signal detection we were using two different installations.
FMR Log-In: In this measurement mode a Stanford Research 830 lock-in amplifier is combined together with a Keithley 6221 current source (see Fig. 3.8 a)). By modulating the amplitude of the rf signal from the microwave generator, with a signal from the lock-in amplifier one can use the lock-in technique to enhance the signal to noise ratio. A detailed explanation of the lock-in technique can be found in [Srs].
FMR Delta-Mode: This type of installation is including a Keithley 2182 nanovoltmeter, a Keithley 6221 current source and a DC current source constructed by a E10 technician Thomas Rapp (see Fig. 3.8b)). The Keithley 6221 current source is utilized for the determination of the current through the sample and it provides a rectangular signal which is used for the delta-mode voltage measurement as explained in Sec. 3.4. The rectangular signal is controlling the microwave generator output, switching between on and off while the Keithley 2182 nanovoltmeter is measuring the voltage.

3.4. Delta-Mode

The delta-mode is a method to decrease the influence of static and slow changing external signals which overlay the requested signal. The basic idea is to change a parameter affecting the desired signal and remove the share of the measured signal that is not affected by the change. To realize this concept the delta-mode protocol is using a rectangular reference signal, switching one parameter from a defined high to a low value back and forth and also triggering a measurement device. In case of the FMR measurements the reference signal is switching the rf signal output between on (high) and off (low). For the resistance measurement Sec. 3.2 the applied current through the sample is changing between $+|I|$ (high) and $-|I|$ (low) with $|I|$ as the absolute value of the set current. During the high and the low of the rectangular signal the measurement device is acquiring one value in each case. For the following explanation these val-

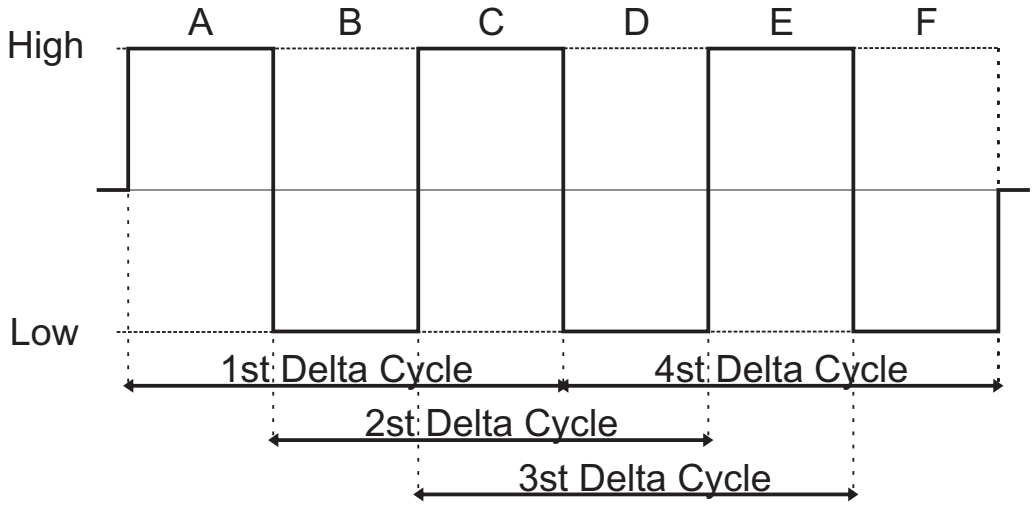

Figure 3.9.: Switching of a parameter between a high and a low value in the delta mode. Three high/lows are combined to a delta cycle.

ues are labeled with A, B, C, ... as shown in Fig. 3.9. To acquire one data point three of those values are used following [K62]

$$\text{value} = \frac{A - 2B + C}{4} \cdot (-1)^0 \tag{3.38}$$

for the first Delta Cycle. To decrease the signal of the background noise it is common to average over several cycles. To consider the changing sign of the even and odd cycles, each values gets multiplied by a factor of $(-1)^{(n-1)}$ with n as the cycle number.

3.5. Brillouin Light Scattering

In the previous sections we presented the methods of the AESWS and EDFMR technique. The signal those provide is the sum over the entire response of the spin excitation either underneath the CPW or in the ferromagnetic material between two electrical contacts. However, in some cases it is beneficial to probe only a smaller specific area. A method providing this possibility is the Brillouin light scattering (BLS)-measurement. It enables us to map the spin excitation at any uncovered positon of the sample with a high resolution. AESWS transmission measurements (S12 and S21) between two CPWs on ASI samples, used in this thesis, didn't

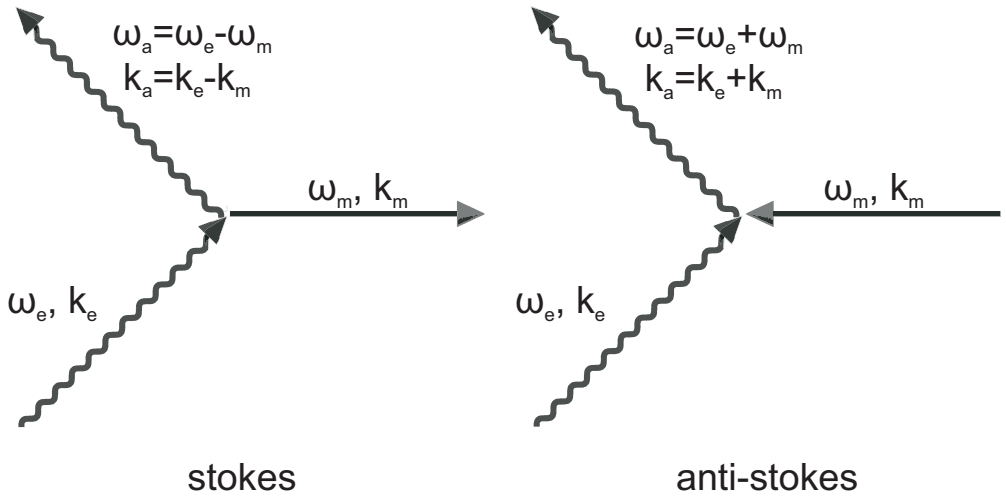

Figure 3.10.: Illustration of the scattering process of a photon (wavy line) on a spin wave excitation (magnon (straight line)). On the left a stokes process is depicted (creation of a magnon), on the right an anti-stokes process (annihilation of a magnon).

show any signal (see Sec. 5.4). Since the CPW positions are fixed due to the preparation and need a minimum distance between each other, we used a BLS to detect the spin wave amplitude in CPW area.

Also we had the intention to detect and if possible control interfering SWs on the Y-structure samples. Since we expected that the signal strength is depending on the position, we needed a method providing the possibility to probe the sample with a high spatial resolution and the possibility to change the measurement position. Hence, for those measurements we used the BLS setup, which is providing these traits.

Brillouin light scattering (BLS) is a method to examine spin waves (magnons) using optical photons. By investigating a spin wave in the spatial regime we detect a periodic change in the phase of the oscillation of the magnetic moments. This can also be interpreted as a phase grating moving with the speed of the spin wave. Due to spin-orbit coupling this grating can be "seen" by light in many materials [Hil00]. In a classical picture the light gets Bragg-reflected. Thereby, the frequency of the light is Doppler-shifted by the spin wave frequency. This process can also be described by an inelastic scattering of photons on magnons, the quasiparticles of the spin wave [Hil05] [Hil00]. A sketch of the process is depicted in Fig. 3.10. During the scattering a magnon is created (stokes-process)

or annihilated (anti-stokes-process). The change of energy and k-vector of the photon can be described by

$$\hbar\omega_a = \hbar\omega_e \pm \hbar\omega_m \tag{3.39}$$

$$\hbar k_a = \hbar k_e \pm \hbar k_m \tag{3.40}$$

with k_e, ω_e as the k-vector and frequency of the incoming photon, and k_a, ω_a for the scattered photon. ω_m and k_m are describing the magnon. As a result we can identify the frequency of the magnon via determination of the photon frequency change $\Delta\omega = \omega_m$. A more detailed description can be found in [Hil00].

3.5.1. Experimental BLS Setup

The BLS setup was built up with the help of the group of Sergej O. Demokritov from the university of Münster. It was designed following Ref. [Dem+08]. A schematic overview can be seen in Fig. 3.11. For a source of coherent light we use a solid state laser with a wavelength of 532 nm. To decrease the divergence of the photons, the beam is expanded and collimated. The laser light is now split up in a measurement and a reference beam.

The reference beam is guided directly to a Fabry-P*é*rot-interferometer (FPI) where it is used to calibrate the FPI for $\Delta\omega = 0$ and to align the mirrors of the FPI (see Sec. 3.5.2). The other part of the beam is passing a polarizer generating a beam of linear polarized light which is guided through a polarizing beam splitter to a micro-focus-stage. The stage consists of a microscope objective and a sample stage. For the stage we are using a XYZ-Piezo scanner moveable in 3-dimesions with an accuracy better than 10 nm [Pi2]. Around the stage two permanent magnets are mounted on threaded control rods to generate an in-plane field in one dimension. The field strength at the sample position can be controlled changing the distance of the magnets. The polarized laser light is focused on the surface of the device under test (DUT) where it is reflected under an angle of $180°$. The spot size of the laser beam at the DUT is about 250 to 300 nm. The precise focusing is achieved by changing the distance of the sample to the microscope objective with the piezo stage.

Due to the reflection of the light by Brillouin-scattering on magnons its polarization is rotated by $90°$. Therefore, after the reflected light is guided back to the polarizing beam splitter, the photons, carrying the information

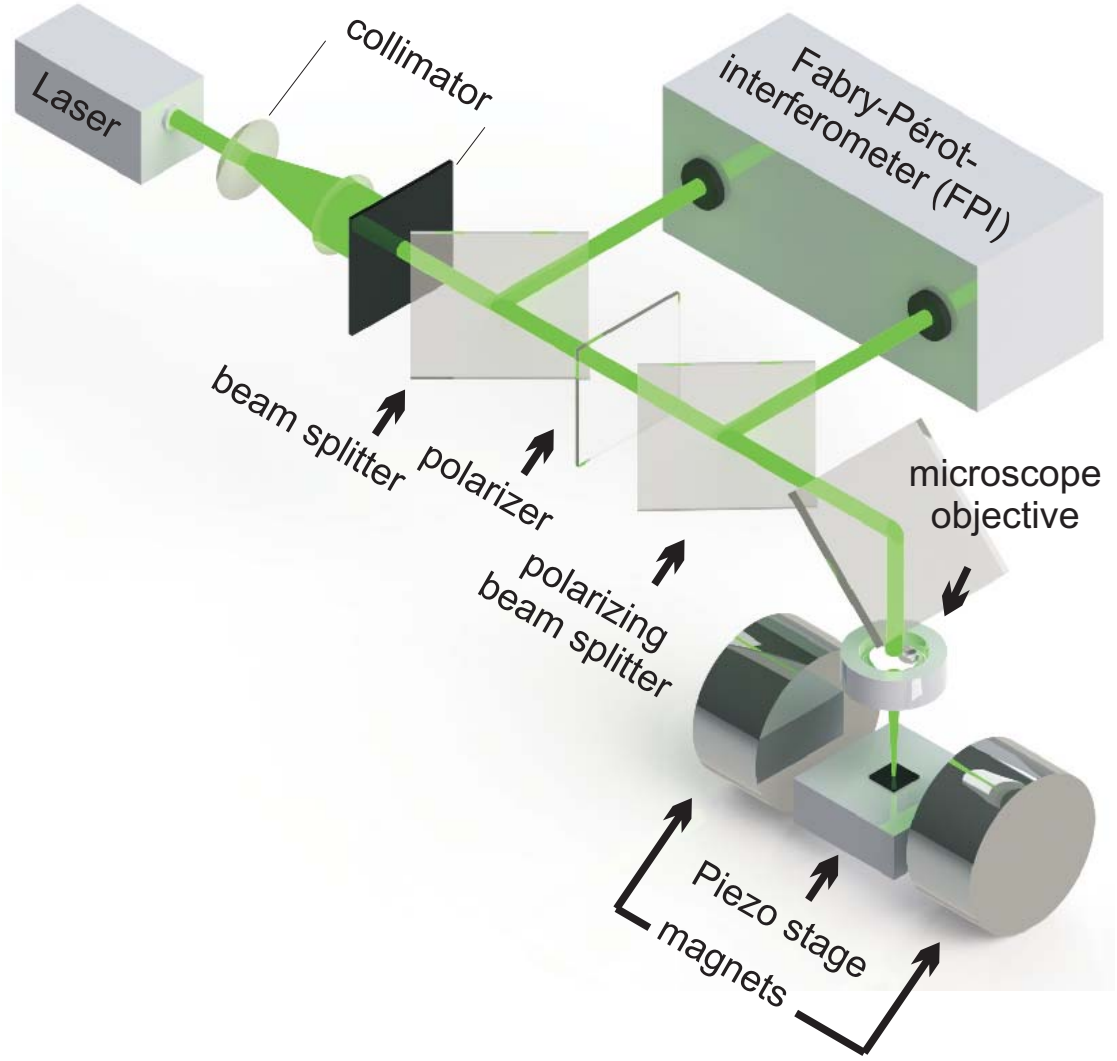

Figure 3.11.: Schematic representation of the optical path of the BLS setup.

about the magnons, are now guided to the FPI. There the FPI is selecting a signal part with a specific frequency/wavelength and is sending the corresponding light to a photon counter (Ultra High Sensitivity CPM Photon Counting Module). The number of photons per unit of time is associated with the signal strength.

By changing the selected wavelength we obtain the signal strength depending on the frequency. Since we expect only signals arising from Brilloin light scattering of magnons, due to their altered polarisation, this allows us to determine the frequency of the magnons using Eq. 3.39. Similar to the AESWS measurement we are exciting SWs using a CPW. Due to the dimensions of the BLS setup, it is not possible to contact the CPW to the microwave signal lines via microwave probes (see Sec. 3.1). Therefore, we are using a GHz connector mounted on the sample holder linked to 2D pad structure similar to the CPW. Both components are optimized to 50 Ω. The final connection to the CPW on the sample is realized by setting Al bonds using a wire bonder. This last part is not optimized for 50 Ω leading to a reduction of the signal reaching the ferromagnetic structure. However, for the BLS measurement this can get compensated by increasing the signal power of the GHz source.

3.5.2. Fabry-Pérot-interferometer

To get information about spin waves with a BLS setup we need to determine the frequency difference between incident light and the inelastic scattered light (see Sec. 3.5). Typically the phase velocity of magnons is very small compared to the velocity of light. That means the change of frequency after BLS is very small:

$$\omega_m = \mathbf{v}_m \cdot k << c \cdot k = \omega_{light} \Rightarrow \omega_{light} \pm \omega_m \approx \omega_{light}. \tag{3.41}$$

Therefore, we need a device to determine the frequency with a very high accuracy and resolution. For this purpose our BLS setup is using a Tandem Fabry-Perot Interferometer (TFPI) produced by JRS Scientific Instruments (J. R. Sandercock). A single Fabry-Perot Interferometer (FPI) is illustrated in Fig. 3.12. It consist of two parallel mirrors with a high reflectivity at a changeable distance d. The transmission is described by

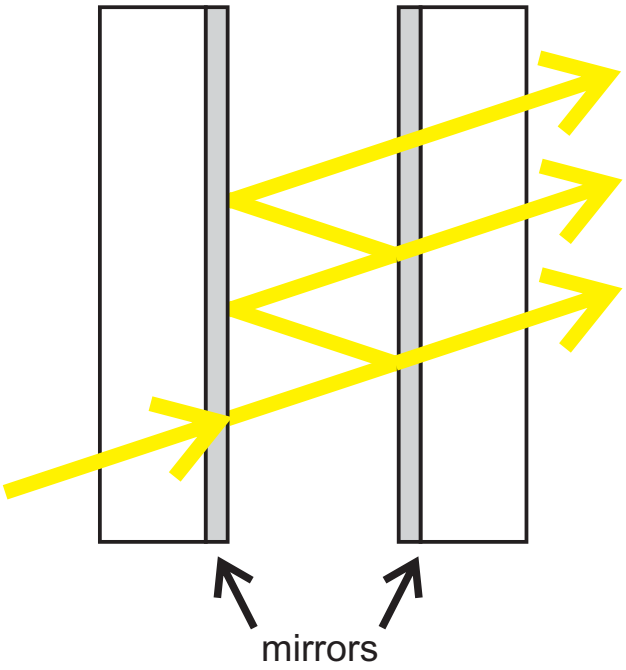

Figure 3.12.: Schematic representation of a Fabry-Pérot-interferometer. The yellow arrows represent beams of light fulfilling the resonance conditions of the interferometer.

[Tfp][Jac60][Dil+81]

$$I = \left(\frac{T}{1-R}\right)^2 \frac{1}{1+\left(\frac{4R}{(1-R)^2}\sin^2(2\pi d\sigma)\right.} \tag{3.42}$$

with R, T and σ as the reflection, transmission coefficient of the mirrors and the wavenumber $\sigma = 1/\lambda$ of the interfering light. The highest possible transmission of Eq. 3.42 is given by[Jac60]

$$I_0 = \left(\frac{T}{1-R}\right)^2 = \left(1 - \frac{A}{1-R}\right)^2. \tag{3.43}$$

$A = 1 - T - R$ is the absorption coefficient of the mirrors. Maximum transmission is achieved if the condition for positive interference

$$d = \frac{1}{2}m\lambda = \frac{1}{2}\frac{m}{\sigma} \Rightarrow \sigma = \frac{1}{2}\frac{m}{d}, \tag{3.44}$$

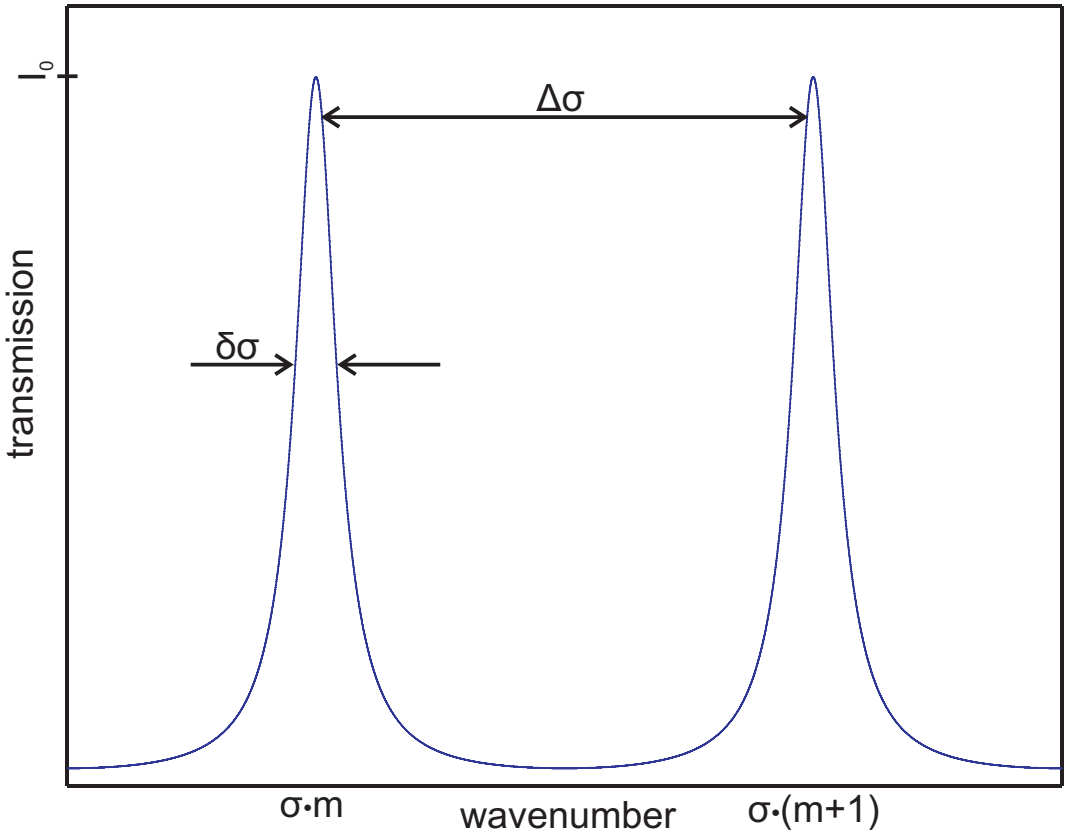

Figure 3.13.: Schematic intensity profile of the transmitted signal for a FPI at a fixed distance.

with m being an integer, is fulfilled. The distance of two peaks with $m_1, m_2 \in \mathbb{N}; m_2 = m_1 \pm 1$ is $\Delta\sigma = \frac{1}{2d}$. The width $\delta\sigma$ of each peak is given by the reflecting finesse [Tfp][Jac60]

$$F = \pi \frac{\sqrt{R}}{1-R} = \frac{\Delta\sigma}{\delta\sigma}. \tag{3.45}$$

Fig. 3.13 is displaying the transmission profile for two m at a fixed distance d. The FPI is acting like a band-pass filter transmitting only the waves fulfilling the resonance-condition. However not only one wavelength is transmitted but all wavelengths satisfying the condition Eq. 3.44. As a result it is only possible to interpret the spectrum if the wavenumbers of the light lie entirely within the spread $< \Delta\sigma$. For this reason, $\Delta\sigma$ is called the Free Spectral Range (FSR) of the interferometer. A possible way to

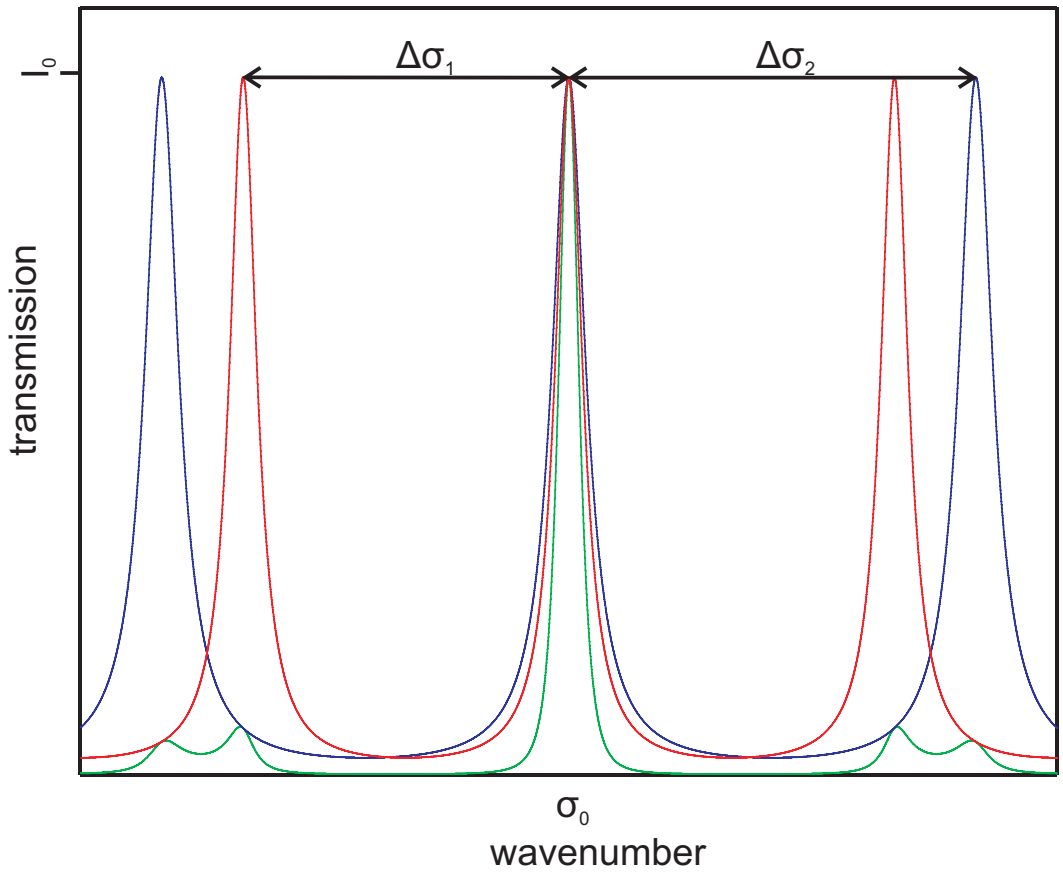

Figure 3.14.: Schematic intensity profiles of transmitted signals. The red and blue lines are representing two single FPIs with different distances. d_1 and d_2 are adjusted for transmission of wavenumber σ_0 through both FPIs. Green shows the transmission profile of the two FPIs in series. The serial connection of the FPIs leads to suppression of neighboring transmission peaks.

increase the FSR would be to decrease the mirror distance d. But according to Eq. 3.45 this would also decrease the spectral resolution.

Tandem-Fabry-Pérot-Interferometer

A way to increase the FSR without decreasing the spectral resolution is to put two FPI in series. The resulting transmission profile is given by [Dil+81]

$$I = I_{01}\frac{1}{1+(\frac{4F_1^2}{\pi^2}\sin^2(2\pi d_1\sigma)} \cdot I_{02}\frac{1}{1+(\frac{4F_2^2}{\pi^2}\sin^2(2\pi d_2\sigma)}, \qquad (3.46)$$

where the indices $1, 2$ indicate the FPI 1 and 2 respectively. For a wave to pass the two interferometers it must meet the condition Eq. 3.44 for both FPIs:

$$d_1 = \frac{1}{2}m\lambda; d_2 = \frac{1}{2}n\lambda. \tag{3.47}$$

The variables m and n are integers. If d_1, d_2 are different, also the distances $\Delta\sigma$ to the neighboring transmission peaks are different. Only after several orders the peaks overlap again. By multiplying the two transmission signals the peaks which are not overlapping are strongly suppressed. An illustration of this effect can be seen in Fig. 3.14. The red and blue lines show the transmission profile of two different FPIs. We can see the signal for σ_0 and the next neighboring transmission peaks. The green line shows the multiplication of the two signals according to Eq. 3.46. The neighboring peaks are strongly suppressed. This effect can be enhanced by sending the light through the TFIP several times. In the present TFIP the light is guided though each FPI three times (see Fig. 3.15). Therefore, it is also labeled as a (3+3) TFPI. As a result the FSR is enlarged several times while the resolution $\delta\sigma$ remains similar [Tfp]. The challenge for this technique is the simultaneous change of d_1 and d_2 in order to continuously sweep σ_0.

Assume d_1, d_2, m and n are set to meet the conditions Eq. 3.47 for a wavelength λ_0. If the wavelength is now shifted by $\Delta\lambda$ the mirror distances have to be adjusted according to [LAS81]

$$\Delta\lambda = 2\frac{\Delta d_1}{m} = 2\frac{\Delta d_2}{n}, \tag{3.48}$$

to transmit the new wavelength. By combining Eq. 3.47 and Eq. 3.48 we acquire the relation

$$\frac{\Delta d_2}{\Delta d_1} = \frac{d_2}{d_1}. \tag{3.49}$$

If the movement of two mirrors is fulfilling Eq. 3.49 it is possible to continuously scan the wavelength. This can be done by exactly controlling the movements of each mirror with piezoelectric elements. However, it is very difficult to correct disruptions of the alignment like offset voltages on the piezos or thermal dilatation effects. A different approach was implemented in the used TFPI build by JRS Scientific Instruments. One mirror of each FPI is fixed to a moving stage while the other two are mounted at

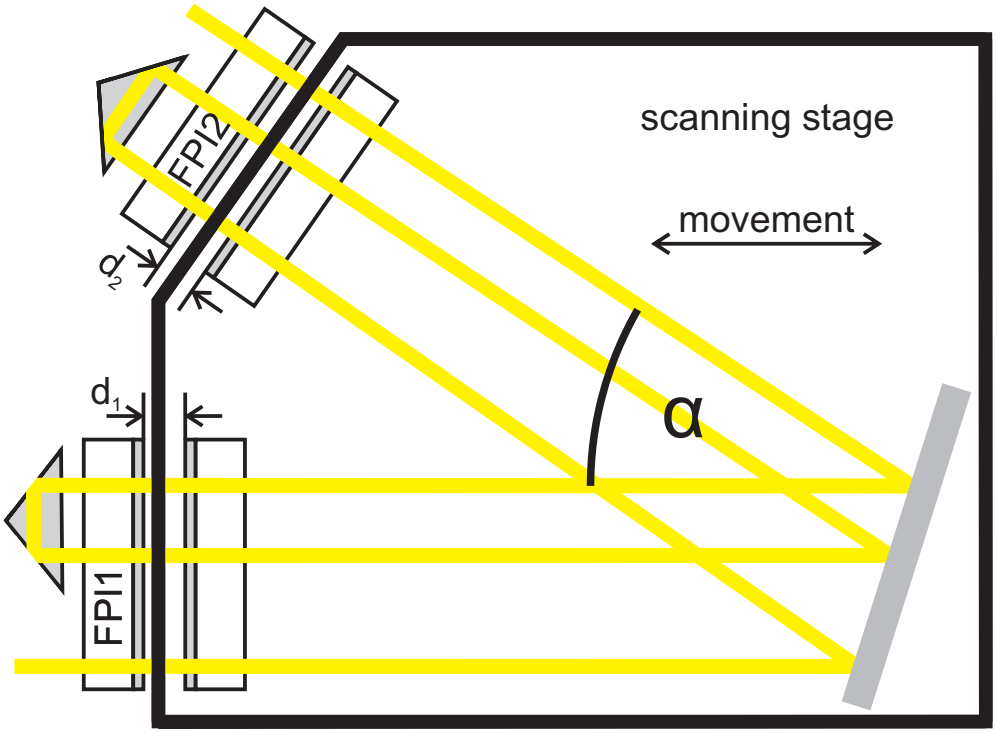

Figure 3.15.: Schematic representation of a Tandem-Fabry-Pérot-interferometer. The light is guided through FPI1 and FPI2 three times. One mirror of each FPI is mounted on a stage moving parallel to the axis of FPI1.

a fixed position on the setup-table. The stage is moved by piezo elements. The orientation of one FPI is rotated by an angle α (see Fig. 3.15). Since the two mirrors are on the same stage the movement is synchronous and follows the relation[Tfp]

$$d_2 = d_1 \cos\alpha, \Delta d_2 = \Delta d_1 \cos\alpha \tag{3.50}$$

which is fulfilling Eq. 3.49. The reference beam described in Sec. 3.5.1 is used to set d_1 and d_2 for the transmission of the σ_0. Since the parallelism of the mirrors is very important it can also be controlled by piezo elements. The distances and the parallelism is optimized by maximizing the transmitted reference signal in a window around σ_0. During the operation of the BLS this is done on every sweep. The optimization window around σ_0 is set by the user according to the intended measurement. For the maximization process the FPI is switching from the measurement signal (see Sec. 3.5.1) to the ref. signal with the help of ultra-fast shutters.

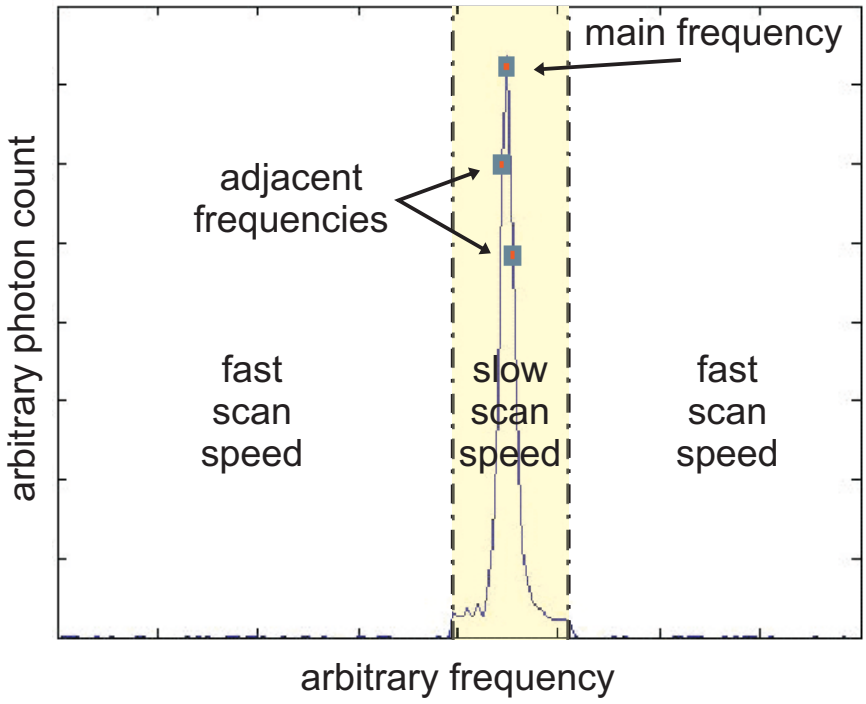

Figure 3.16.: Example of the result of a single BLS sweep with a SW excited at the main frequency. The adjacent frequencies are still part of the exited signal. Number of the counted photons depends on the scan speed.

The whole routine is insuring a stable operation despite effects like thermal dilatation.

3.5.3. Data Acquisition

The signal strength of a SW is measured by the BLS via the number of photons counted at a specific frequency (see Sec. 3.5.1). Due to the setup this number is linked to the time, how long photons are counted and therefore the sweep speed of the TFPI. Since BLS measurements are very time consuming and for the calibration and optimization a full sweep of the FPI is required, the used control program utilizes two velocities. The fast one for the frequencies that are not required those data are not required and a slow one for the frequency range essential for the experiment. Comparing single sweeps show that the number of photon counts at the same frequency under the same circumstances still show a noticeable fluctuation. However, increasing the measuring time by decreasing the scan speed would also increase the time between the optimizations of the mirrors and therefore,

decrease the quality of the FPI. The solution is to sum up the measured count of a multiplicity of sweeps. Additionally we are not only showing the numbers of one frequency, but also add the counts of the two adjacent once (see Fig. 3.16). Due to the finite FWHM, these frequencies still refer to the same SW. With this method the effect of random fluctuations gets reduced since the number of relevant measurements gets multiplied by three, without increasing the measurement time.

In some experiments we were also using DC currents to influence the excited SWs in the BLS measurements. In this case the currents have been generated with a YOKOGAWA 7651 Programmable DC Source (source 1) and a KEITHLEY 2401 SourceMeter (source 2). To prevent a change of the structure temperature during the experiment, all BLS measurements have been delayed for at least 5 minutes after setting a current value through the sample.

4. Sample Preparation

In this chapter we explain the fabrication of artificial honeycomb spin ice arrays made of Py and CoFeB as well as the steps for the creation of investigated Y-structures and ferromagnetic nanotubes. First we specify the different fabrication techniques used and then address the specific preparation of the samples. Detailed recipes for each process can be found in the appendix.

4.1. Lithography

In the framework of this thesis lithography was used to transfer a desired pattern to a resist. Resist in the structured areas got removed while in other areas the resist remained, resulting in the creation of the desired formation. For this purpose we utilized two different methods.

4.1.1. Optical Lithography

For optical lithography the sample gets cleaned and then coated with an UV-light sensitive resist. The sample and an optical mask are brought into soft contact. Then UV-light irradiates on the sample through the mask. This step is followed by a development of the resist with a fitting chemical developer. The parts of the resist which got illuminated are removed by the developer, while the parts covered by the optical mask are not affected. This patterned resist can be used in further steps e.g. lift-off. With this method it is possible to create large areas of patterned resist in a very short time. The accuracy for the positioning can be estimated to be around 5 µm. We are using the optical lithography for large structures with a minimum structure size of 2 µm

4.1.2. Electron Beam Lithography

Electron beam lithography (EBL) is a dynamic lithography technique. Similar to the optical lithography the sample gets coated with a resist, sensitive

to accelerated electrons. A beam of such electrons is created with a scanning electron microscope (SEM). In the used SEM from RAITH a voltage of up to 30 kV accelerates the electrons. Apertures, magnetic and electric lens systems guide the electrons and focus the beam on the sample. Utilizing a shutter mechanism the beam can be blocked and released. A software controls the beam to write arbitrarily structures on the resist. The electrons change the chemical properties of the resist and by using a developer the exposed areas of the resist are removed. Choosing the right parameters and resist enables the creation of nm-size structures using this method. While the EBL is well suitable for small structures there are some limitations for large structures. The number of position steps of the beam is limited. Therefore, by choosing a write field (area which is covered by the beam with only deflecting the beam), its field size is limiting the minimal step size for the writing process. The write field size itself is limited by the maximal deflection range of the beam. Structures bigger then the chosen write field are divided into multiple write fields and the sample is moved by the stage from one write field to the next. This process is also known as stitching. The accuracy of the stage is smaller than the step size of the electron beam. The result is a possible mismatch between the stitched areas.

4.2. Lift-Off and Material Deposition

The lift-off is a technique to transfer a structure from a resist to a deposited film. The structure in the resist is generated by using e.g. lithography Sec. 4.1. When a film of the chosen material is deposited on top of the sample a part of the material settles on top of the resist while at the locations where the resist was removed due to structuring, the material can directly settle on the substrate. When the sample is put into a liquid solvent the resist dissolves and the material covering it floats in the liquid while the material directly deposited on the substrate is not influenced. By using ultrasonic or a stream of liquid the floating material gets severed from the sticking material leaving only the settled film in the structured areas behind. This process of removing the material is called lift-off. To facilitate the separation one can generate an undercut at the resist edges. When the deposition direction is only perpendicular to the sample surface no material settles on the edges and therefore, the floating parts and the fixed parts are not con-

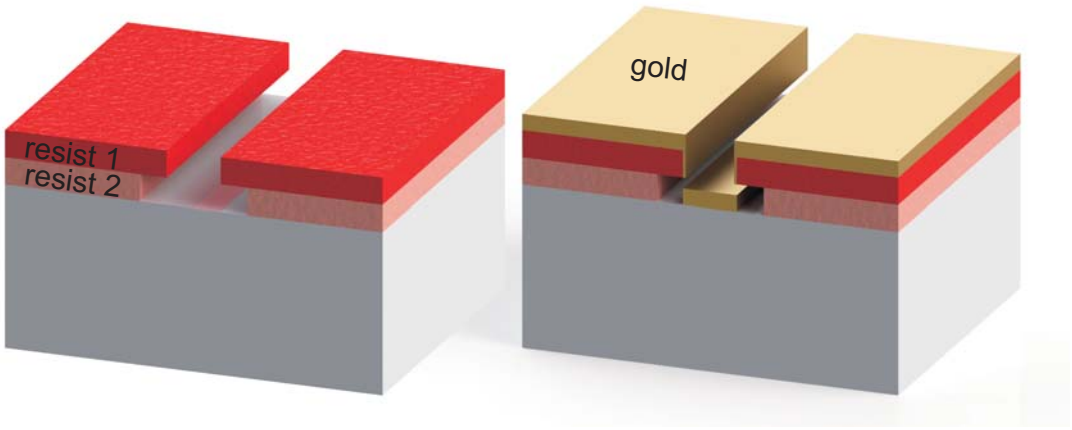

Figure 4.1.: The left side shows structured double layer resist. Due to the higher sensitivity more of resist 2 was removed. The right side illustrates the double layer resist after a gold deposition. The undercut leads to a disconnection of the material on top of the resist and the material on the sample.

nected in the first place. For the lithography techniques described in Sec. 4.1, one way to create an undercut is to use two different resists (double layer resist). The bottom resist has a higher sensitivity compared to the top resist and hence more of the bottom resist gets removed during the development leading to an undercut. Figure. 4.1 shows the effect of an undercut generated by using a double layer resist. For the deposition we utilize two different kinds of techniques.

- **Evaporation deposition** is a method which is conducted in a vacuum. Using an electron beam or a current, the selected material gets evaporated into the vacuum and then condensates on the target surface generating a film. The deposition acquired with this method is unidirectional.

- **Magnetron sputtering** [KA00]. An inert gas (e.g. Ar or Xe) is channeled into a vacuum chamber where the gas gets ionized. An electrical field applied between the substrate (anode) and a target (cathode) accelerates the ions (cation) toward the target. The ions collide with the target and remove (sputter) target atoms/molecules. A share of this atoms/molecules travel to the substrate where they condensate and form a film. During the collision also secondary

electrons are emitted which may create new gas ions maintaining the plasma [KA00]. To enhance the probability to generate new ions magnetron sputtering uses a magnetic field to confine the electrons in an area near the target. This leads to a higher concentration of ions in this area and therefore, to a higher sputtering rate. The magnetic field is generated by permanent magnets with one pole at the center and the other pole at the rim around the target.

In this thesis we use the magnetron sputtering to deposit CoFeB and the evaporation deposition for Py, Au and Cr.

4.3. Artificial Honeycomb Spin Ice

As the first step the ground substrate (GaAs (001)) gets cleaned with acetone and isopropanol. Using optical lithography and the lift-off technique we create alignment markers made of a dual layer with 4.5 nm Cr and 120 nm Au. These markers are used to align the artificial spin ice structures and the CPWs. The honeycomb structure is created using electron beam lithography. The exposure of a pattern with that many elements can be very time consuming. Therefore, we don't write areas with a defined width to create the elements of the ASI (links). Instead every link is generated by a single pixel line. The width can be controlled by the dose of the electron beam. This decreases the writing time by more than a factor 100. The development of the resist is followed by covering of the sample with Py (using evaporation deposition) or CoFeB (using magnetron sputtering). After a lift-off the entire sample gets capped with 10 nm of isolating Al_2O_3 created with atomic layer deposition (ALD). The concept of the ALD is described in Sec. 4.5.1. On top of the isolation layer we fabricate CPWs using electron beam lithography, evaporation deposition (4.5 nm Cr, 120 nm Au) and lift-off.

Fabrication Challenges

The main challenge in the fabrication of artificial spin ice structures is the lift-off. In the used evaporation chamber we can set an angle between the deposition source and the sample with an accuracy of $\sim 1^\circ$. Even with an undercut this can lead to metal deposition on one sidewall of the resist inside the structured areas. If this material is connected to the main structure

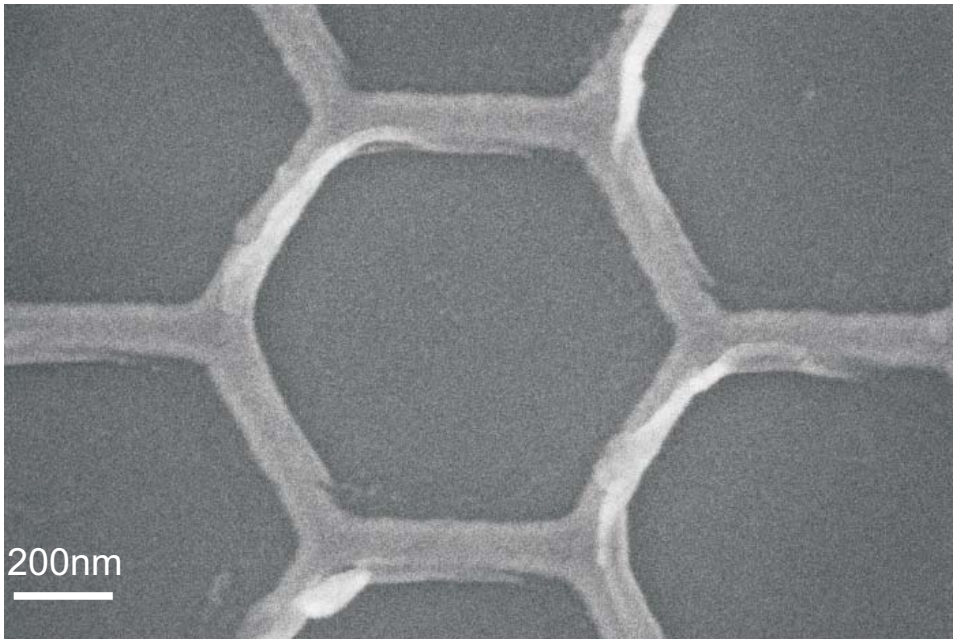

Figure 4.2.: SEM image of the sample SI7_2_1. The links at an angle of 60 ° are covered by arrears of the material deposited on the right side wall.

small parts may stick to the sample after the lift-off. The result can be seen in Fig. 4.2. It shows a SEM picture of sample SI7_2_1. We can see arrears on top of the structure due to a material deposition on the right resist sidewalls. For the magnon sputtering all sidewalls of the resist are covered with the deposited material since the deposition direction is not unidirectional which is increasing the effect. A possible countermeasure is a higher resist system. Unfortunately due to the small structure size a thicker resist is also decreasing the amount of material reaching the substrate. Another counteraction is using ultrasonic to remove the floating metal parts connected to the main structure. By increasing the vibrations strength and time more of the remaining parts of the floating material get removed. The downside of this method is that the ultrasonic can also damage the main structure. As a result one has to find a compromise between the different factors to maximize the quality of the artificial spin ice structure.

4.4. Y-Structure

Before any preparation steps the ground substrate (GaAs (001)) gets cleaned with acetone and isopropanol. Using optical lithography and the lift-off

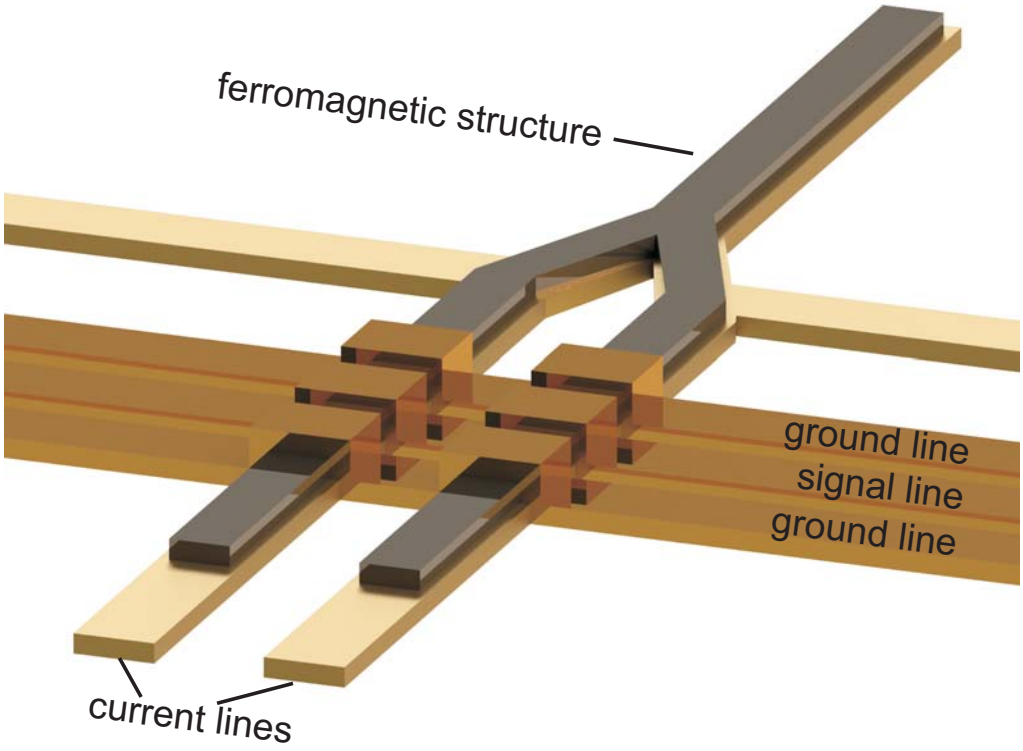

Figure 4.3.: Sketch of the SW interferometer Y-structure. It displays the layer composition of current lines, ferromagnetic structure and CPW.

technique we create alignment markers made of 4.5 nm Cr and 120 nm Au to create a general coordinate system. The actual structure is created by a combination of electron beam lithography, evaporation, sputtering and ALD. Its shape is sketched in Fig. 4.3 and gets explained in Sec. 6.1. As a first step we create the structure of the current lines with EBL and evaporation of Cr (4.5 nm) and Au (100 nm) followed by a lift-off. Simultaneously we are also creating additional smaller markers in the same process as the current lines. These are used in further steps to enable a more accurate alignment of the following structures. After the lift-off the entire sample gets evaporated with a layer of 1.5 nm Al. The sample is then exposed to the Air at room temperature for two days, to ensure a oxidation of the Al layer. On top of this layer we grow additional 60 nm of Al_2O_3 using the ALD. The structure for the ferromagnetic material is put on top of the current line structure using the new EBL markers. Again we use the EBL, sputtering of CoFeB (30 nm) and lift-off to create it. These

steps are followed by the creation of 10 nm Al_2O_3, covering the sample, using the ALD. The final structure is a CPW across the two paths of the Y-structure isolated to the ferromagnetic material by the previous Al_2O_3 layer. It gets prepared using EBL evaporation (4.5 nm Cr and 120 nm) and a lift-off. Since the structure under the CPW is higher than the thickness of the CPW, we are slewing the sample back and forth around 20° to ensure the CPW is connected over the edges of the structure underneath. Beside the showed structure in Fig. 6.1 the current lines end in contacted pads similar to the CPWs. After the mounting of the DUT on a sample holder we use a wire bonder to connect these pads of the Au structure to further electrical contacts outside the DUT. Thereby the wire bonder links one end of a thin Al wire through the isolation layers to the gold layer and the other end to the electrical contacts.

4.5. Ferromagnetic Nanotubes

The bases of the ferromagnetic nanotubes are non-ferromagnetic GaAs nanowires. Those were produced by D. Rüffer from the ÉCOLE POLYTECHNIQUE FÉDÉRALE DE LAUSANNE (EPFL) using the Vapor-Liquide-Solid growth mechanism [WE64]. A detailed description of the growing process can be found in his work [Rüf14]. Instead of fabricating a hollow structure, we coat the nanowire with a ferromagnetic material (Ni and CoFeB) to create a magnetically hollow tube similar to other ferromagnetic-shell nanowire systems [Zha+04] [Rud+09]. The coating technique depends on the chosen material.

4.5.1. Ni Tubes (Atomic Layer Deposition)

The Ni shell around the GaAs cores was created by T. Schwarze and R. Huber from the TU Munich using Atomic Layer Deposition (ALD).

The concept of the ALD was developed in the 1970s for the deposition of thin films from a gaseous phase [SA77]. Its concept can be described as follows. A gaseous precursor is injected into a reaction chamber holding a sample and gets adsorbed on the surfaces including the accessible surfaces of the sample. When the surface is saturated, the chamber gets purged with N_2 leaving only the adsorbed precursor behind. With the injection of a second precursor into the chamber a chemical reaction between the two precursors gets initiated and continues until the entire remaining material

of the first precursor got consumed. Since the reaction is limited by the amount of the adsorbed material it is also called a self-limiting or self-terminated process. Afterwards the chamber gets purged again and it is possible to inject additionally precursors or repeat the previous process. As a result of the successive steps we receive an isotropic and homogeneous growth of a film[Sun92][LR02][Geo10].

The Ni tubes are created by using the materials Nickelocene ($Ni(C_5H_5)_2$ or $NiCp_2$) and Ozone (O_3). Using these two precursors it is possible to grow a shell of NiO with a defined thickness around the nanowires. By including reduction steps the O in the NiO can get removed increasing the metallic component of the film. However, this also can give rise to a non-homogeneous film due to Ostwald ripening [Ost00] during the reduction [Hub13]. A further description of the used process and the minimization of the effects of the Ostwald ripening can be found in [Hub13].

4.5.2. CoFeB Tubes (Sputtering)

For the CoFeB tubes we use the magnetron sputtering technique to coat the GaAs nanowires in the ferromagnetic material. However, this method does not provide a homogeneous growth in all direction, as does the ALD. Especial at surfaces facing away from the CoFeB source the growth rate is reduced significantly compared to surfaces with a normal pointing towards the source. To avoid this problem we rotate the sample with a motor to assure that the time average of the growth rate is the same on every side. Since we don't prepare single tubes, but cover arrays of wires simultaneously we have to consider a screening effect. Outer wires cast a material "shadow" on the wires behind them leading to an unequal growth distribution depending on the position of the wires. To reduce this effect we don't use a deposition angle of 90° (see Fig. 4.4 b) left) between the long axis of the wire and the axis from the sample to the CoFeB source, but at a different angle (150°) instead (see Fig. 4.4 b) left). A schematic sketch of the rotation setup is illustrated in Fig. 4.4 a).

4.5.3. Tube Preparation for EDFMR Measurements

The coated GaAs nanowires are grown with a random spatial distribution and normal to the surface of the sample [Rüf14]. Therefore, it is necessary to transfer the tubes to another substrate in order to apply electrical

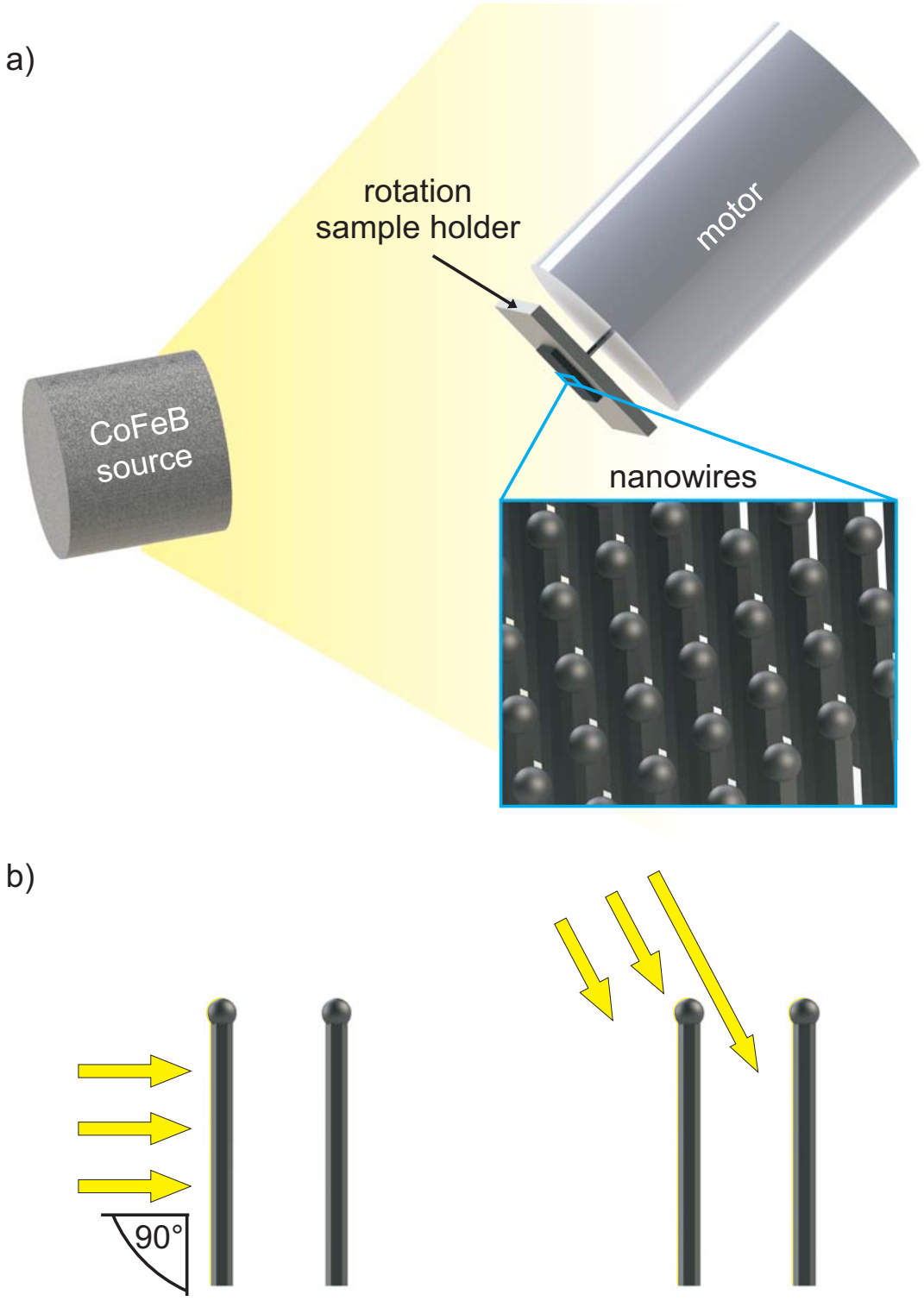

Figure 4.4.: a) Sketch of a setup for CoFeB magnetron sputtering during the rotation of a wire sample. b) yellow arrows indicate the direction of the material deposition. At a deposition angle of 90° one nanowire is screening the second one, preventing a material deposition. A different angle (right) enables the deposition on both wires.

contacts and CPW structures needed for the planned experiments. The correlated processes were developed and realized by D. Rüffer from EPFL. As a first step the nanotubes have to be removed from the original substrate. Therefore, the original substrate gets placed into isopropanol. Using ultrasonic, the tubes get released from the substrate and float freely in the liquid. With the help of e.g. a pipette the solution is now transferred to a set wafer. After drying, the nanotubes get into direct contact with the wafer surface and get attached to it at a random position and in-plane orientation. Before the tube transfer the used wave has been prepared with encoded markers. These markers and the nanotubes can be detected using an optical microscope. A novel developed software is detecting the nanotubes in the optical image and with help of the encoded markers it determines the exact position and orientation of the tubes. Using the two extremal points of the tubes, the software also creates a pattern for the CPW structure and contacts which can be used for the EBL process. The contacts are generated after the development of the EBL resist by magnetron sputtering of 5 nm Ti and 100 nm Au followed by a lift-off. To increase the adhesion between the metals and the surface of the wafer a pre sputtering in-situ rf etching gets performed. To link the contacts to electronic connections outside the sample, the contact structure ends in connection pads. These enable us to utilize a wire bonder to link the components with a thin Al wire. The CPW structure is generated in a second step. The pattern is transferred to the structure using EBL followed by the electron beam evaporation of 5 nm Ti and 120 nm Au and a lift-off. A detailed description of the fabrication can be found in [Rüf14].

5. Artificial Spin Ice

5.1. Sample Characterization

For experiments on connected honeycomb ASI (see Fig. 5.1) several samples, made of Py ($Ni_{80}Fe_{20}$) and CoFeB ($Co_{20}Fe_{60}B_{20}$), were produced. In this section we give a brief description about the structure of the used samples and some additional information. The basic elements of a connected honeycomb structure are three equal magnetic thin stripes/nanobars rotated 120° to each other. For a better distinction depending on the direction, we refer to these stripes also as link 1 (0°), link 2 (120°) and link 3 (-120°). To determine the dimensions of the links, we used two methods. For the length of a bar, which is defined by the distance between the centers of the vertices enclosing the link, we utilized SEM-imaging. The width and thickness of the sample were measured with the help of AFM (Atomic Force Microscopy). An example of a line scan over one link can be seen in Fig. 5.2. For the width we declare the value at the half thickness of the bar (FWHM). The dimensions of the investigated spin ice samples are listed in Table 5.1. Each value in Table 5.1 was generated by averaging over the width, height or length at the center of three different nanobars. All samples were produced on an undoped (001) GaAs substrate using lithography and lift-off techniques (see Chap. 4). Due to the fabrication progress (see Sec. 4.3 and Sec. 4.1.2) the arrays are divided into uniform squares of equal size. In each sample except SIB1 the squares have the dimension 194.5 µm in x-direction and 100 µm in y-direction. The distance between two neighboring squares is 5.5 µm. For SIB1 the dimensions are 100 µm x 100 µm with a distance of 1 µm. The saturation magnetization of the used Py was determined by S. Neusser to be of $M_s = 830$ kA/m [Neu11]. For the used CoFeB T. Schwarze found a value of $M_s = 1440$ kA/m [Sch13]. On top of the spin-ice structure the sample is coated with 10 nm of Al_2O_3. The alumina acts as an isolation layer between the magnetic material and the CPW. If not mentioned otherwise we use two integrated parallel CPWs with a signal line width of 2.1 µm. The distance between the two signal lines is 15.5 µm (see Fig. 5.1).

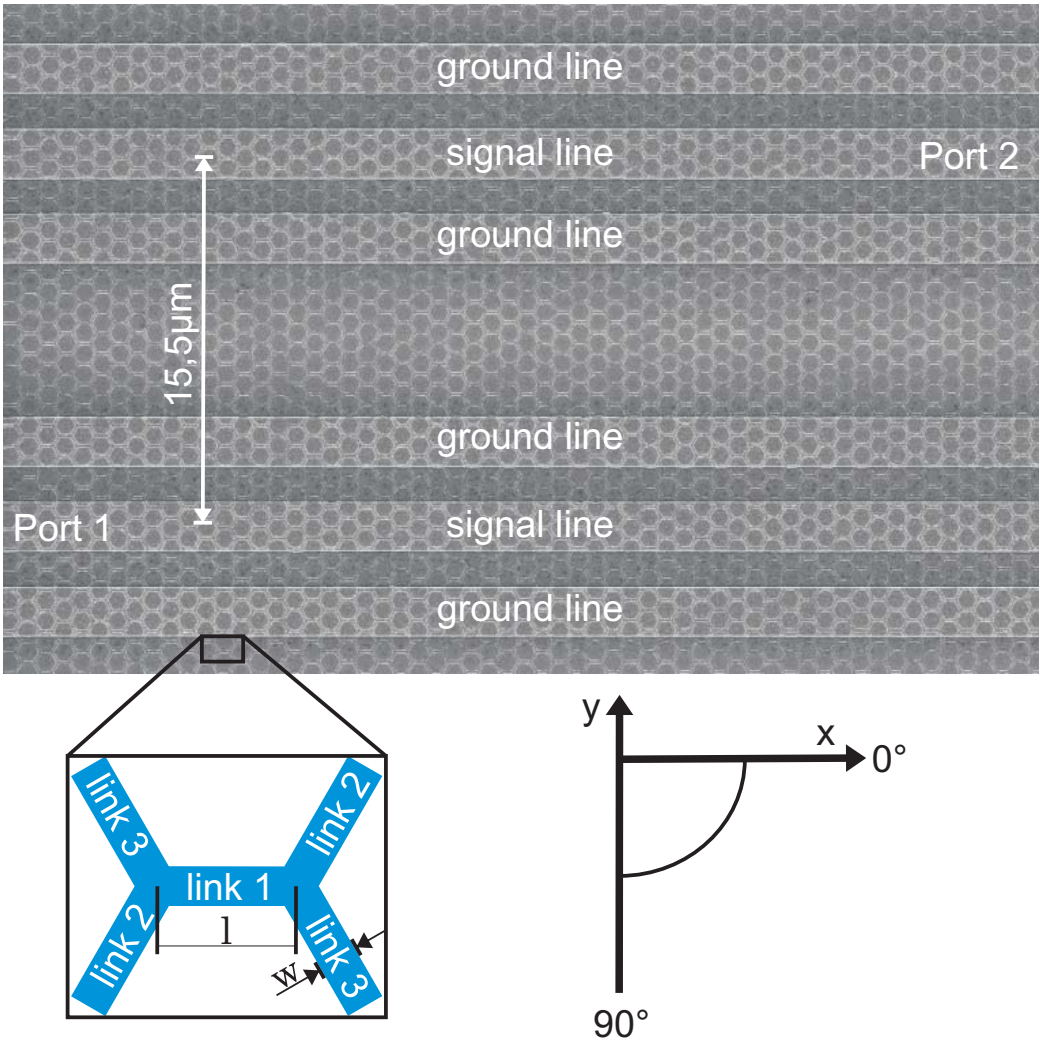

Figure 5.1.: SEM-picture of the CoFeB sample SI8_1_1. Link 1 and the integrated CPWs are aligned along 0°. Link 2 lies along 120° link 3 along -120°.

As described in Sec. 2.3.1 we expect two different types of domain walls (DWs) in the nanobars. A Néel-like transverse wall or a vortex wall. With Eq. 2.25 we can predict the transverse wall type for a Py sample with a thickness of 30 nm to occur for a width smaller than 65 nm. The exchange length l_{ex} was calculated to be 3.9 nm by using an exchange stiffness constant of $1.3 \cdot 10^{-11}$ J/m [MD97] and $M_{\mathrm{s}} = 830$ kA/m. Hence looking at Table 5.1 we assume the DWs propagating in the investigated samples are of the vortex type. With this information it is possible to calculate the minimum DW speed with Eq. 2.27. The smallest external field is 1 mT.

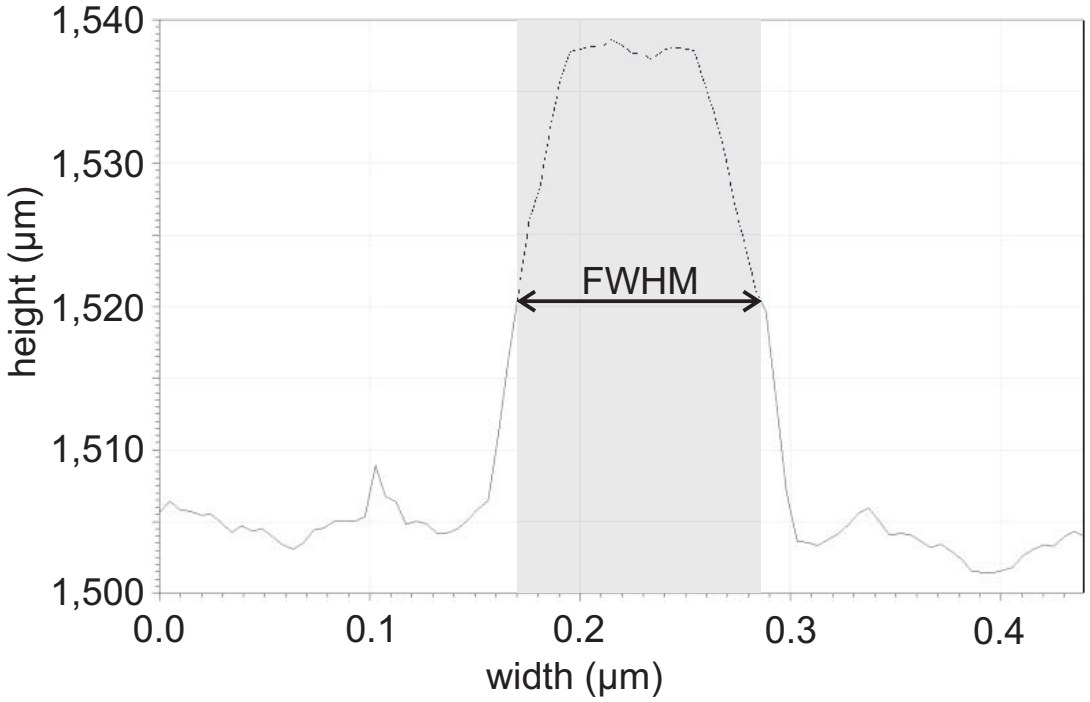

Figure 5.2.: Line scan of a AFM measurement over a nanobar of sample SI7_1_2. The width of the bar is determined at the half height of the bar.

The Gilbert damping was determined by S. Neusser by investigating a thin plane film to be $\alpha = 0.0045$ [Neu11]. Therefore, the velocity of a DW for an array with a stripe width $w = 110$ nm is $v = 3.3$ cm/s. The actual speed should be higher because we don't expect 1 mT to be beyond the Walker field. Since due to the protocol the measurement is delayed for a few seconds after the external magnetic field is set, and the limited size of the array, we can assume that all measurements are performed at a static configuration of the magnetization.

5.2. Magnetic Force Microscopy

We performed magnetic force microscopy (MFM) on sample SI7_1_2 as a representative for the produced honeycomb samples (a detailed description of MFM can be found in [MW87][Har99][Rug+90]). Its dimension can be found in Table 5.1. Before the measurement, an external field $\mu_0 H = +100$ mT was applied along 0° (the x-axis). Thereafter the magnetic field was reduced to $\mu_0 H = 0$ mT and the sample transferred to the MFM-

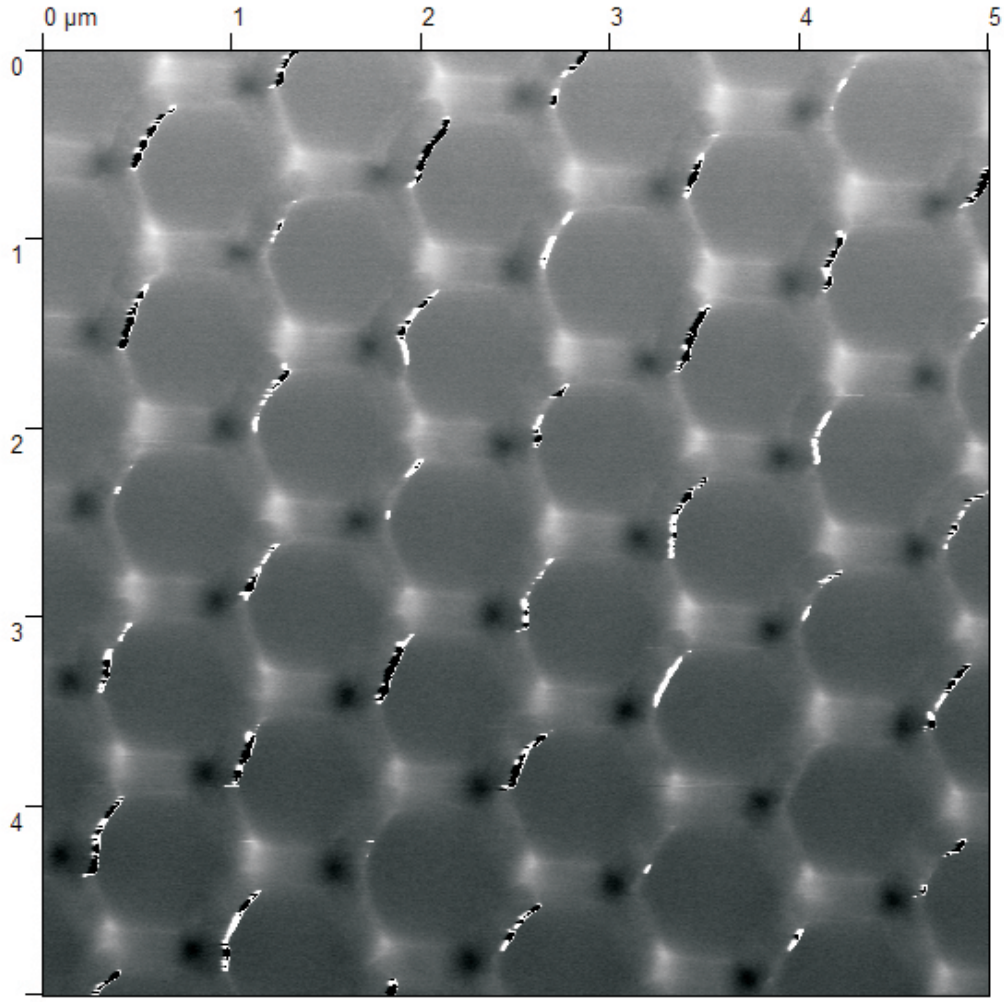

Figure 5.3.: MFM measurement on sample SI7_1_2. Before the measurement, a magnetic field $\mu_0 H = +100$ mT was applied along link 1 (x-axis) and then reduced to $\mu_0 H = 0$ mT. Dark and light contrast indicates magnetic stray fields.

Sample	Length	Thickness	Width	Material
SI1_1_1	500±10 nm	31±2 nm	179±5 nm	Py
SI7_1_2	500±10 nm	34±2 nm	111±5 nm	Py
SI12_2_1	500±10 nm	30±2 nm	110±5 nm	Py
SI13_1_3	500±10 nm	30±2 nm	115±5 nm	Py
SI8_1_1	500±10 nm	36±2 nm	240±10 nm	CoFeB
SIB1	500±10 nm	37±2 nm	239±5 nm	Py

Table 5.1.: Material and dimensions of nanobars in the investigated structures.

setup.

While the signal is sensitive to magnetic stray fields we also get a contribution from the height profile of the sample. Therefore, the measurement shows a combination of an AFM and a pure MFM signal. The scan was performed at an area of 5 µm x 5 µm at a scan speed of 5 µm/s with a resolution of 512pt x 512pt.

The result is depicted in Fig. 5.3. We can clearly see the signals generated by the fields of the DWs located in the vertices. The stray fields are indicated with black or white depending on the field direction. Therefore, the white (black) color corresponds to a positive (negative) magnetic charge in the vertices (see Sec. 2.11.2). Every positive charge is surrounded by negative charges and vice versa. Beside the fields at the DWs in the intersections of the stripes there are no stray fields in links 1 and 3. However we observe strong magnetic stray fields at the right rim of links 2. Figure. 4.2 shows that at this position the investigated sample is covered by remains of the material that was deposited on the right side walls of the resist (see Sec. 4.3). Those ferromagnetic remains have an arbitrary shape, which implies that the magnetization direction can differ from the magnetization in the associated link creating the observed stray fields.

5.3. Simulation

As a complementary method, we are using results of micromagnetic simulations. Those were performed by Dr. Vinayak Bhat from the TU München using the Object Oriented MicroMagnetic Framework (OOMMF) (see also [DP99]).

For the simulated structure we used a honeycomb ASI with dimensions

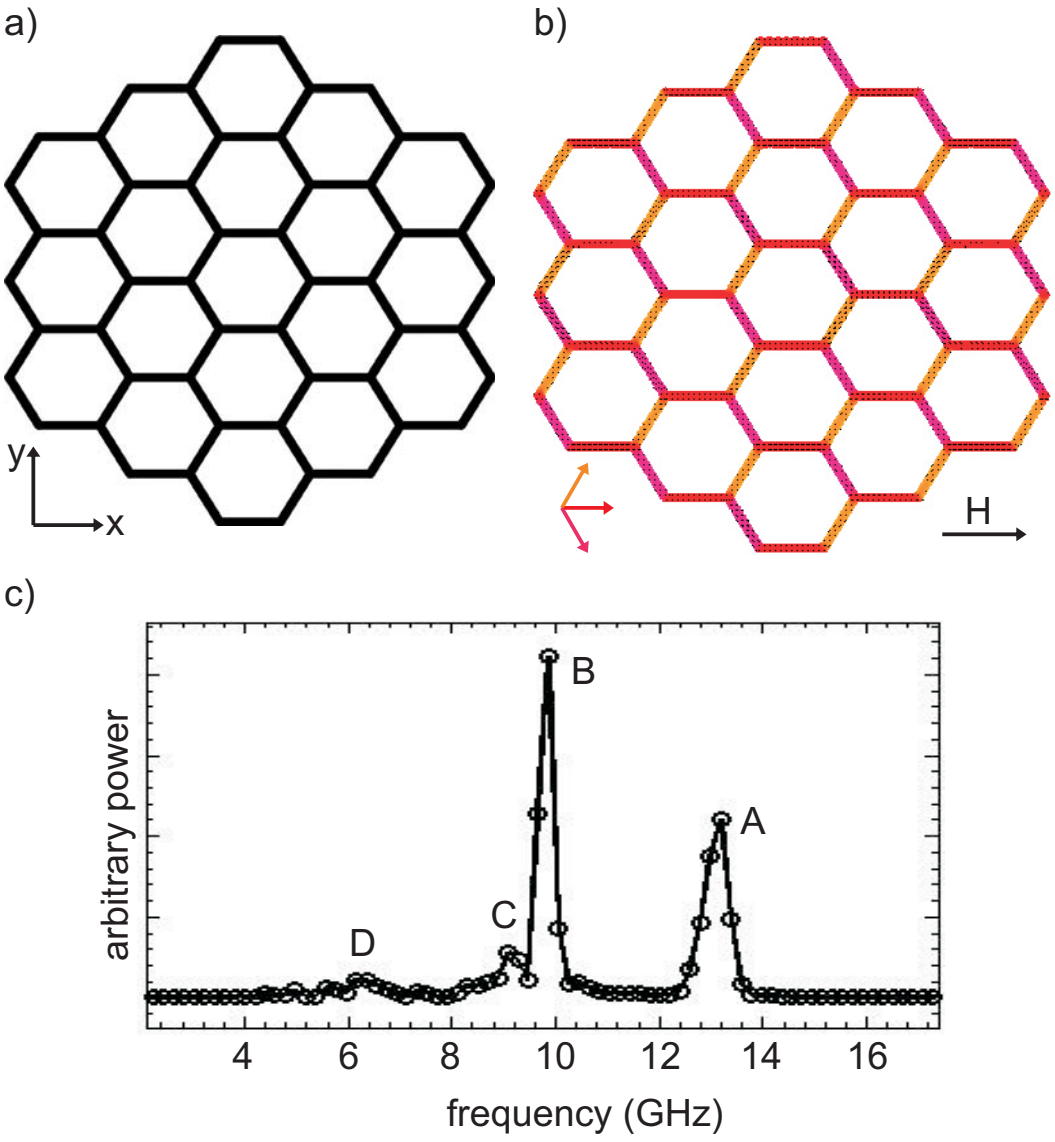

Figure 5.4.: a) depicts the structure used in the simulation. Black indicates ferromagnetic material, white no material. b) shows the magnetization configuration at a applied magnetic DC field $H = 1000$ Oe along the x direction. The different colors refer to different magnetization directions. c) plots the absorbed power summed over all unit cells depending on the frequency. Frequencies A, B, C and D indicate maxima in the plot.

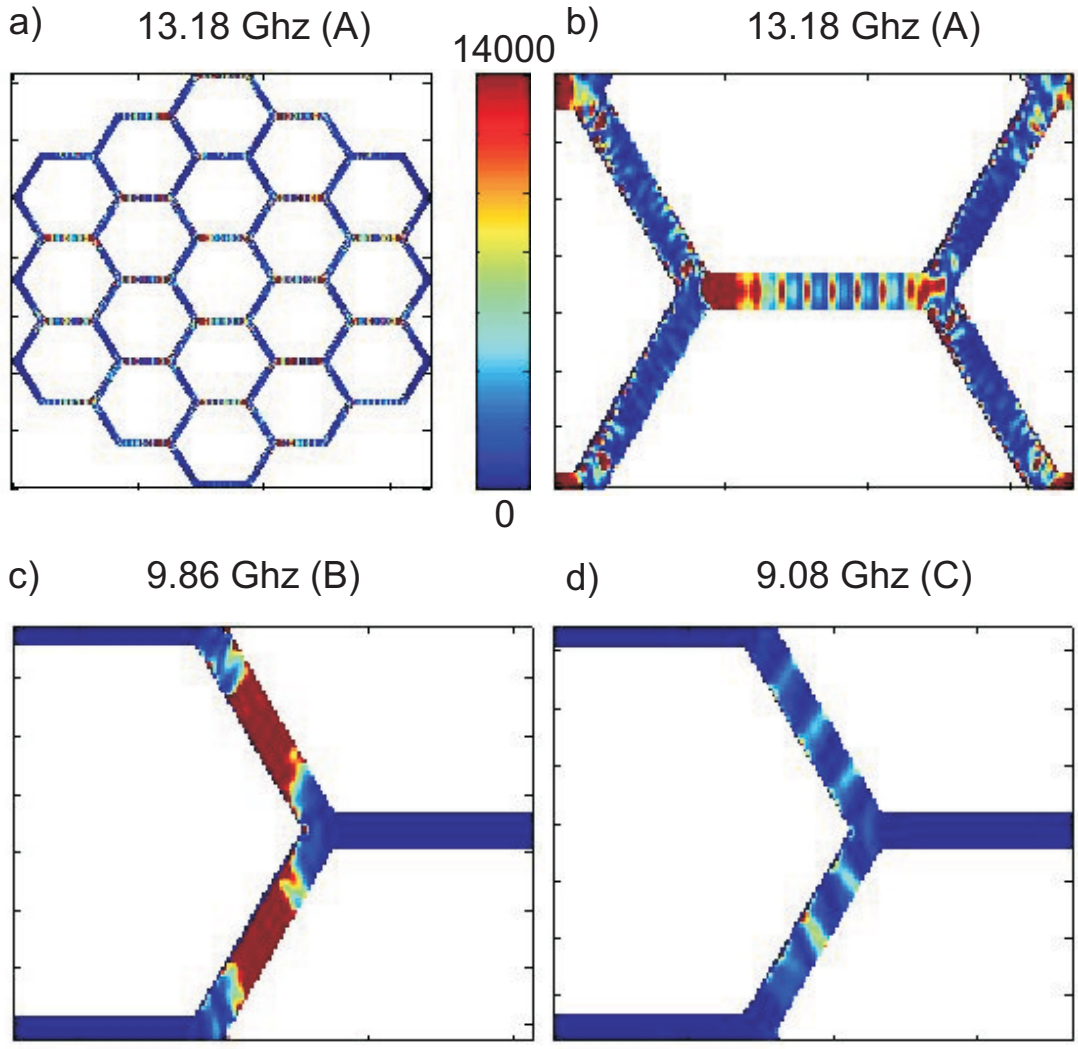

Figure 5.5.: a) shows the power map of the entire lattice at frequency A. b), c), d) show a magnified part of the power map at a excited region near the center of the lattice at frequency A, B, C. The color code in arbitrary units, is the same for all four maps.

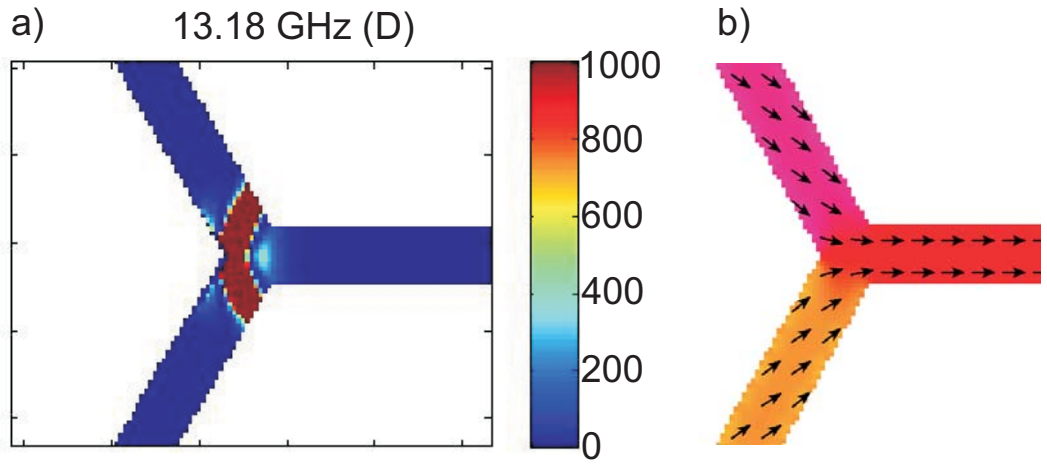

Figure 5.6.: a) shows a excited part of the power map at frequency D color coded in arbitrary units. b) shows the magnetization configuration of the same area. The black arrows indicate the direction of the magnetization.

chosen similar to experimental samples. The distance between two adjacent vertices, the width of a link and thickness of the structure were 500 nm, 130 nm and 25 nm. For the material parameter we used the exchange stiffness constant $A = 1.3 \cdot 10^{11}$ J/m, the gyromagnetic ratio $\gamma = 1.9 \cdot 10^{9}$ HzT^{-1}, the saturation magnetization $M_{\mathrm{s}} = 7 \cdot 10^{5}$ Am^{-1} [Wan07], and a damping coefficient $\alpha = 0.001$, to match Py. The unit cell was chosen to be $10 \times 10 \times 25$ nm^3. Since the processing power of the used computer is limited, we were not able to perform the simulations on a structure with a number of links equal to the experimental samples. Therefore, the simulated structure was reduced to a sub lattice as shown in Fig. 5.4 a).

The first step in in the simulation was the application of a magnetic in-plane field $H = 1000$ Oe. In this configuration the OOMMF code was calculating the ground state for the honeycomb lattice by minimizing the total energy in the ferromagnetic system. The resulting magnetization configuration is shown in Fig. 5.4 b). In a second step we applied a Gaussian magnetic out-of-plane field pulse with an amplitude maxima of 200 Oe and a FWHM 2.5 ps. Finally the dynamic response was recorded by logging the magnetization vector for each unit cell. This was done 256 times with a step size of 20 ps.

By performing a FFT on the magnetization of the unit cells along the timeline, one obtains the resonance spectrum of the system. The absorbed

power in each unit cell, which represents the excitation strength of the magnetization, is obtained by squaring the amplitude of the FFT. The result of this method can be seen in Fig. 5.4 c). It shows the power summed over all unit cells of the structure. We identify two prominent peaks at frequency A and B, and two smaller ones at frequency C and D. By looking at the absorbed power depending on the position, we can connect the resonant frequencies A, B, C and D with the excitation of specific areas in the simulated lattice.

In Fig. 5.5 we see the absorbed power at three different frequencies. Figure. 5.5 a) shows the power distribution for the entire lattices at the frequency A. The excitation of the magnetization is mainly concentrated in the links parallel to the x-axis (link 1). One can also see that the power distribution is changing at the edges compared to the center of the lattes. We attribute the deviation at the rim of the lattice to the influence of boundary effects. Therefore, we are now focusing on the structure at the center of the honeycomb structure.

Figure 5.5 b) displays a magnified part of the power map located at a link 1 near the middle of the structure. In the excited region the power is not distributed evenly, but shows a periodic variation in its strength. The oscillation of power is equivalent to an oscillation of the magnetization motion amplitude and therefore, indicates to a standing spin wave with nods (anti-nods) at regions with low (high) power.

A different behavior can be seen for the resonance frequency B in Fig. 5.5 c). There the signal intensity is focused in link 2 and 3. In both links we see strong uniform excitation over a large area at the center of the segments, which strength is decreasing towards the vertices.

Finally 5.5 d) shows the excitation for the frequency C. In this case we also see an excitation in link 2 and 3 but in contrast to the frequency B we see a periodic change of the absorbed energy in the material. It is also striking that the excitation strength for frequency C is small compared to the excitation in B and A.

Comparing the excitation between frequency C and D we discover that the absorbed power in D is even smaller than in C. An excited region at frequency D is shown in Fig. 5.6 a). In this case the magnetization is excited in the vertices following an arc. By comparing the excited region with the magnetization of this area (see Fig. 5.6 b)) we see that the absorbed power is concentrated in the unit cells describing the DW forming between the three magnetization directions in links 1 2 and 3.

5.4. AESWS

5.4.1. Field Sweep

In the following we provide an overview of the magnetic field dependency of the broad band resonance measurements on honeycomb ASI structures. We focus on the fields in the switching regime of the system (see Sec. 2.11.2) and show data with applied in-plane fields in the range of ± 100 mT. A measurement on sample SI7_1_2 is displayed in Fig. 5.7. It is a representative measurement the S22 (a) and S12 (c) data. Both data sets were processed with the next neighbor subtraction (NNS) starting at small fields (see Sec. 3.1.6) to maximize the contrast. Resonance modes are identified by a change in color toward black or white compared to the uniform gray background. The colors black and white in the resonances modes are a result of the NNS method. White (black) indicates an enhancement (decrement) of the signal strength at a fixed frequency compared to the adjacent lower field. Gray demonstrates no change of signal strength. In some cases vertical lines along fixed fields appear in the results, indicating a strong signal. Their origins are disturbances during the experiment and cannot be reproduced by repeating it. Therefore, those will not be part of the discussion.

The measurement begins at a field $\mu_0 H = -100$ mT along the 0° direction. Starting from there the field value was increased to $\mu_0 H = 100$ mT in steps of 1 mT. The transmission signal (S12 see Fig. 5.7 b)) shows no evidence of a resonance signal. This is true for all measured ASI structures produced in the course of this thesis. The reflection signal (S22 see Fig. 5.7 a)) shows one prominent mode (blue rectangle) with a width of ≈ 1 GHz. Starting with a frequency of 10.7 GHz (center of the mode) at a field of -100 mT it decreases with increasing magnetic field value. This trend goes on until a critical field of $\mu_0 H = 26$ mT (labeled with an arrow) at a frequency of 5.9 GHz. From this point on the strength of this branch is reduced till a point at $\mu_0 H = 33$ mT were it vanishes. Simultaneous it reappears in the very same field sector at a frequency of 8.3 GHz. The vanishing and reappearing can also be described by a shift of the resonance frequency to a higher frequency value. Instead of decreasing, now the resonance frequency is increasing with the absolute field, to a value of 10.7 GHz at a field of $\mu_0 H = 100$ mT.

Additional to the prominent branch we observe a secondary mode with

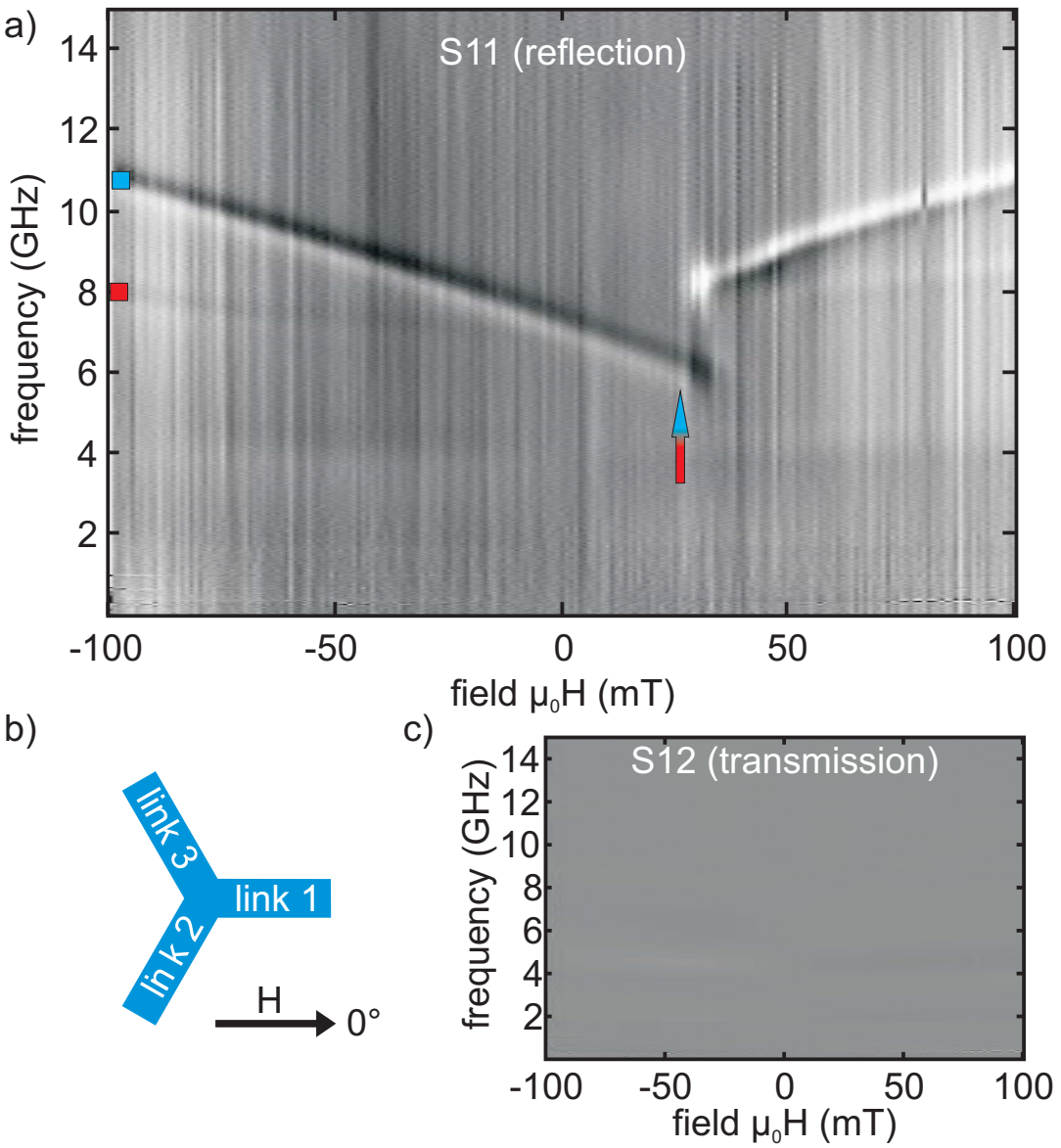

Figure 5.7.: Color-coded NNS (processed with next neighbor subtraction) reflection a) and transport c) FMR data taken from sample SI7_1_2 at an external field angle of 0°. The dark and light contrast marks the resonance modes. Blue and red rectangles indicate two different modes at an external field value of -100 mT. Blue/red arrows mark the associated critical field. b) Indicates the direction of the field relative to the link directions.

a weak signal strength compared to the first one. Starting with 8.6 GHz at field $\mu_0 H = -100$ mT (red rectangle) the frequency is decreasing with an increase of the absolute field value similar to mode one. While both modes respond to an increasing field value, till the critical field, with a decreasing resonance frequency, the slop of the secondary mode is smaller. However, in the area where the two modes might or might not cross the amplitude of the lower branch is reduced to the point where it cannot be identified anymore. It is reappearing above the critical field value. Equal to the prominent branch its resonance frequency is shifted up and is now increasing with the field. The resonance frequency at $\mu_0 H = 100$ mT is 8.6 GHz.

The same measurement was also performed on several other samples with different dimensions. All of them showed the same behavior as described above although in some cases the secondary mode couldn't be identified. The resulting critical field, and maximum frequencies of the prominent mode are listed in Table 5.2.

Sample	$\mu_0 H_{\mathrm{crit}}$	$\mu_0 \Delta H_{\mathrm{crit}}$	**Max f at $\mu_0 H = 100$ mT**
SI1_1_1	26 mT	6 mT	9.5 GHz
SI7_1_2	26 mT	7 mT	10.7 GHz
SI12_2_1	51 mT	4 mT	13.1 GHz
SI13_1_3	41 mT	5 mT	11.7 GHz
SIB1	36 mT	11 mT	12.6 GHz

Table 5.2.: The critical field, its width and the maximum frequency of the prominent mode, in the measured field area. The external during the measurement was applied along 0°.

All these samples were made of Py. Additional to them we also produced a CoFeB sample (SI8_1_1) and performed the same measurement (see Fig. 5.8). Again we observe one mode following the same general behavior as the Py samples. By comparing the frequencies, we note that the values of the visible mode in the measurement on the CoFeB sample are lower compared to the frequency values from the samples made of Py.

During the entire measurements on the different samples the external field was applied along the x-direction with an angle of 0°. For a further investigation of the resonance behavior we also performed field sweeps at

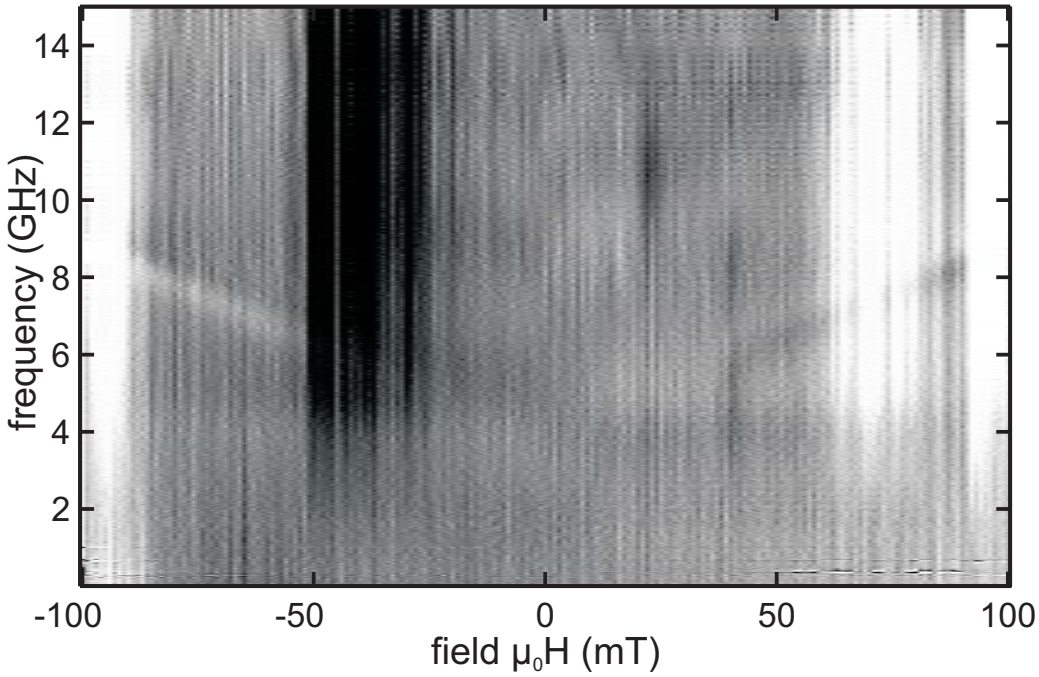

Figure 5.8.: FMR data taken from CoFeB sample SI8_1_1 at an external field angle of 0°.

different angles. To assure equal starting configurations for all measurements we applied an external field of -100 mT along 0° direction, followed by a reduction to 0 mT. Beginning from this resulting magnetic setup we performed field sweep under different angles up to a field value of 100 mT.

The results for sample SI7_1_2 treated with the NNS method for some selected angles are displayed in Fig. 5.9. The measurement at angle 20° shows a frequency shift of the mode similar to the 0° sweep. However, the frequency of the second mode (indicated with red), after the shift, is higher and its slope at larger field values is more steep compared to the 0° data. On the other hand side, the change of the external field angle to 20° is also leading to a smaller frequency shift of the prominent mode (indicated with blue) and a reduction of its slope at higher field values. With a the further rotation of the angle the slop and frequency values of both modes are changing following a trend that can also be observed in the angle sweep measurements shown in Sec. 5.4.2 and discuss in Sec. 5.6.

Additionally starting at an angle of around 60° the critical fields for both modes separate, leading to a frequency shift of the red mode followed by a shift for the blue mode at a higher field value. With increasing angle

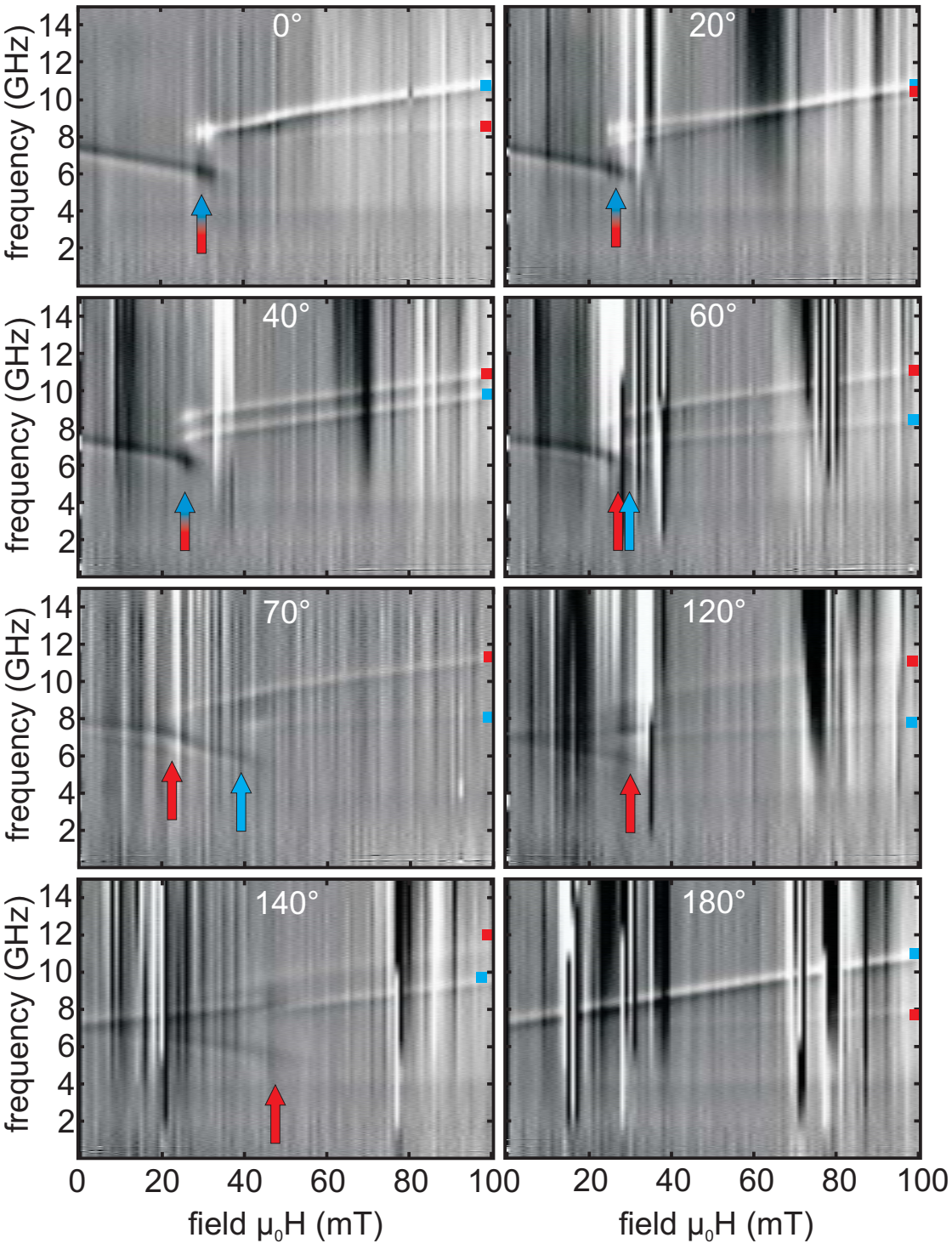

Figure 5.9.: FMR data taken from sample SI7_1_2 at different external field angles. Blue and red rectangles indicate two different modes at an external field value of -100 mT. Blue and red arrows mark the associated critical field.

also the critical field values are increased. In the data with a field angle of 120° and 140°, the frequency shift of the blue mode is not observed in the measured field sector anymore, while the critical field of the red mode was shifted to higher values. The data at an angle of 180° can be seen in Fig. 5.9. It shows the two branches without sudden jumps (shifts) of the resonance frequency.

A different approach was used with sample SIB. Instead of using an integrated CPW, the ASI sample was placed on top of flip chip CPWs to excite magnetic material (see Fig. 5.10). This enabled us to align the ground and signal lines and therefore the AC-field to any direction relative to the directions of the links.

The field sweep measurements on a flip chip CPW with a signal line width of 160 µm are shown in Fig. 5.10. In this experiments the external field was always at an angle of 0° as was the direction of the CPW lines. Before each field sweep, the sample was saturated with a field of -100 mT at 0°. The ASI placed on top of the structure was rotated counterclockwise by the specified angle, starting from 0° (equal to the integrated CPW configuration see Fig. 5.1). For a more convenient differentiation of observed modes we placed markers in different colors on top of them to highlight their course (see Fig. 5.10).

The measurement at 0° shows one prominent mode (blue) starting at 12.5 GHz. As expected it follows the same general behavior as the strong mode of the other samples with an external field direction of 0°. The rotation of the sample leads to a decrease of its maximum frequency similar to the rotation of the external field. This was expected since a rotation of the structure leads to a different external field orientation relative to the links.

Additionally we identify another mode (green) starting at a frequency of 9.5 GHz decreasing to ≈0 GHz at 0 mT and going up again to a frequency of 9.5 GHz at 100 mT resembling the behavior of the Kittel formula. We attribute this mode to some unpatterned Py thin film on the edge of the GaAs substrate. In some positions of the sample this remains are excited by the CPW leading to the signal of the Kittel mode which is therefore, independent of the ASI.

Further comparison to the field sweeps with changing field angle reveals a new effect due to the rotation of the AC-field orientation. With increasing discrepancy between the directions of link 1 and the signal lines the strength of the ASI mode (blue) is decreasing. At an angle of 50° and 60° the original ASI mode signal is hardly recognizable. However, at these

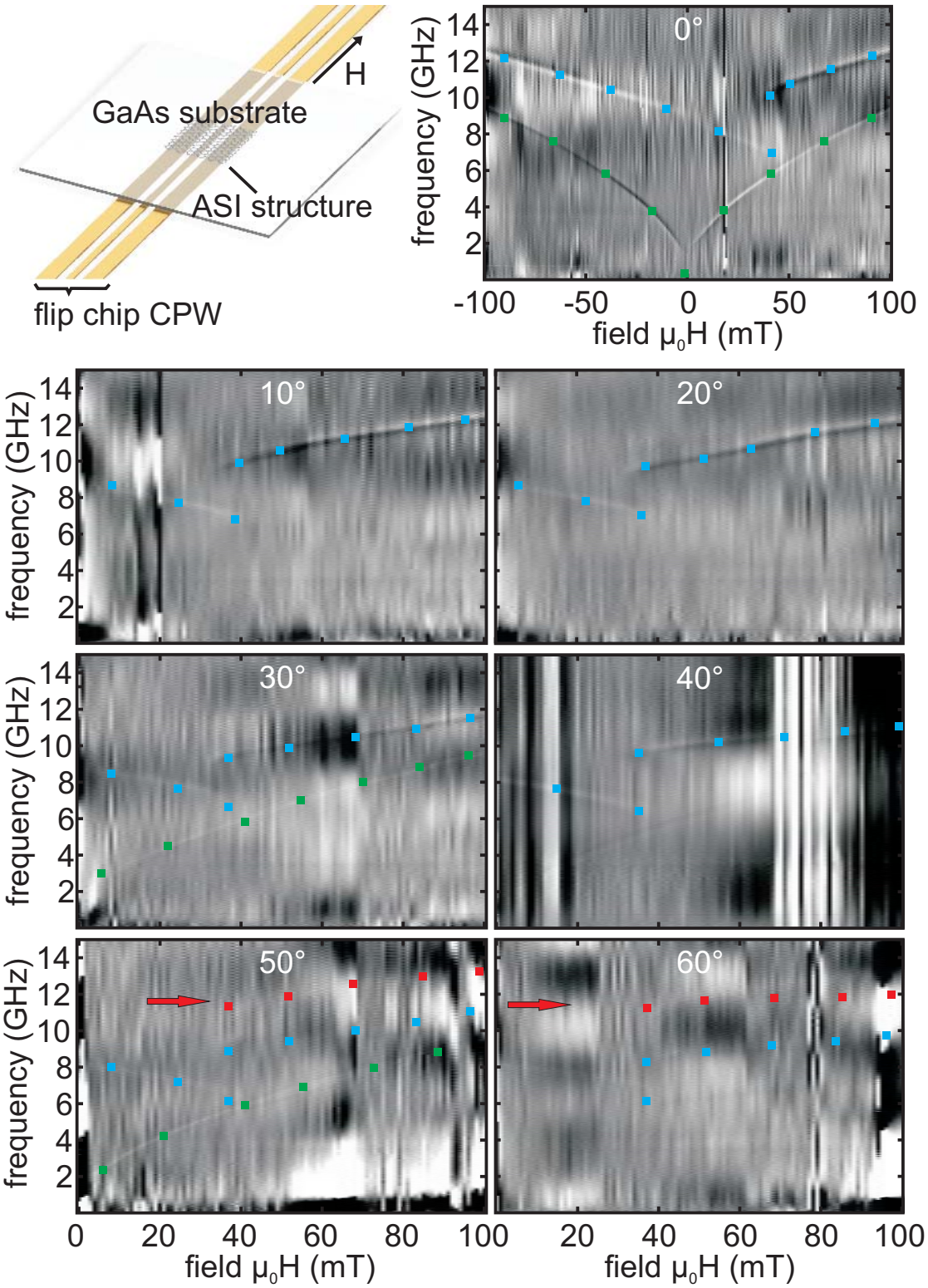

Figure 5.10.: FMR data taken from sample SIB at different sample angles positions. Colored squares highlight the course of the different modes. Red arrows indicate the first observation of a additionally mode.

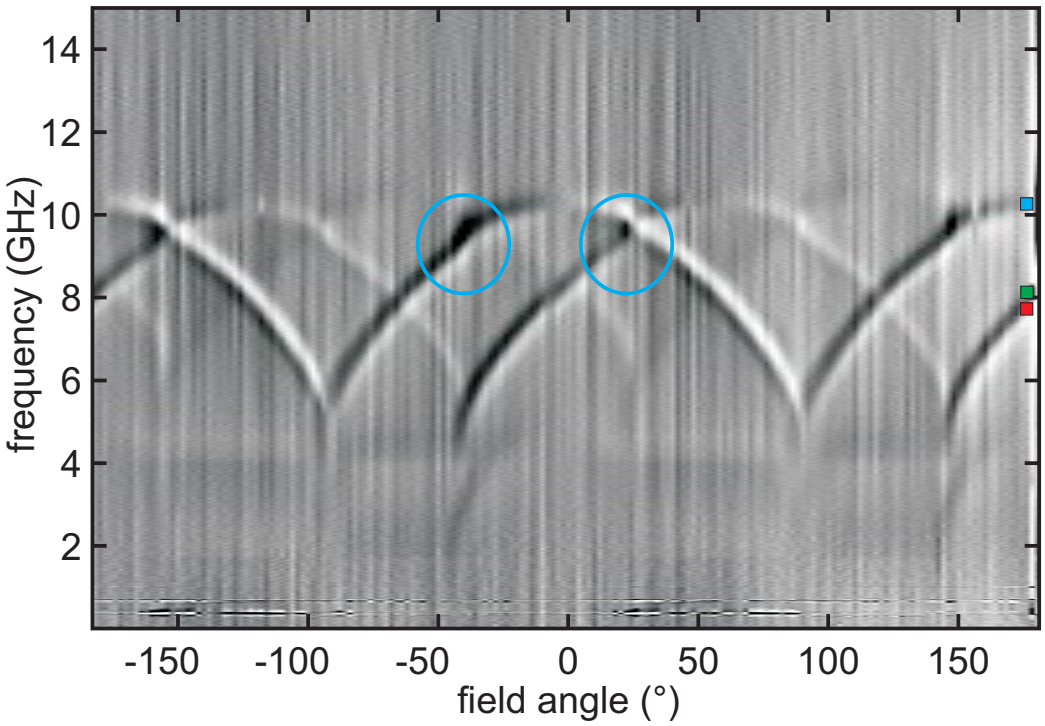

Figure 5.11.: Angle dependend FMR data taken from sample SI7_1_2 at an external field value of 80 mT. Blue, green and red rectangles indicate three different modes at an external field angle of 180°. The blue circles highlight frequency shifts in the blue mode at the same position as minima of the red and green modes.

angles, hints of a new mode (red) at a higher frequency appear (see red arrows in Fig. 5.10 at 50° and 60°).

5.4.2. Angle Sweeps

Additional to the field sweeps we also performed angle sweeps. In that case the AESWS measurement was used to obtain the ferromagnetic resonance signal of the ASI structures during the rotation of an external field with a fixed absolute value. The measurements started at an external field angle of 180° with a field value of 80 mT. It was rotated to smaller angles in 2° steps.

Figure 5.11 displays the result of a measurement on sample SI7_1_2. It shows three different modes residing between 4-12 GHz. The strongest one starts at a frequency of 10.3 GHz (indicated with a blue rectangle). It follows an arc down to a minimum frequency of 4.5 GHz at 86°. At this

angle the frequency is shifted up by ≈0.5 GHz and then starts to increase again up to a local maximum with 10.3 GHz at 0°. From this point to -180° the course of the mode is repeating the previous one. The second (red) mode follows the same general behavior as the blue mode. However, it is shifted by about -60° compared to the first branch and therefore it has a smaller frequency (7.9 GHz) at the starting point (180°). Its signal strength is weaker than the blue but still stronger than the third (green) mode which is only slightly above the noise level. The green branch also shows the general behavior as the blue mode but is shifted by +60° relative to it.

Important features that all three modes share are additional shifts (discontinuities in the measured resonance frequency) in the frequency (highlighted for the blue mode by circles) beside the shift at the frequency minimums. Comparing all three modes it gets revealed that shifts occur always at an angle were another mode is at a minimum frequency.

A further feature of this dataset is at a frequency below 4 GHz. We resolve a weak mode at around 150° and -40°. These two branches can be followed only over a small angle regime.

The applied field value of 80 mT is very big compared to the critical field for sample SI7_1_2 found in the 0° field sweep (see Table 5.2). Therefore, we also present the same measurement on sample SI13_1_3 (see Fig. 5.12) which has a higher critical field value. Overall we get a similar behavior to the measurements on sample SI7_1_2, but there are also notable differences.

We can only identify two, compared to three, modes and their positions are different. While the arc between two minima in the measurement on SI7_1_2 is almost symmetric, this isn't the case for sample SI13_1_3. The main reason for this is the increased frequency shift at the minima. While in the previous measurement we only detected a small increase of the frequency, now it is shifted from 6.3 GHz to 8.5 GHz. This trend could be seen in many different measurements on different samples (not shown in this thesis). If the external field value gets closer to the critical field we observe a bigger frequency shift relative to the overall frequency variation. If the absolute applied field value is below the critical field we don't see a shift at all. The positions and the change of the frequency Δf at the minima are listed in Table 5.3. Since in some measurements not all three modes are clearly visible the table holds only the data from modes with a clear signal.

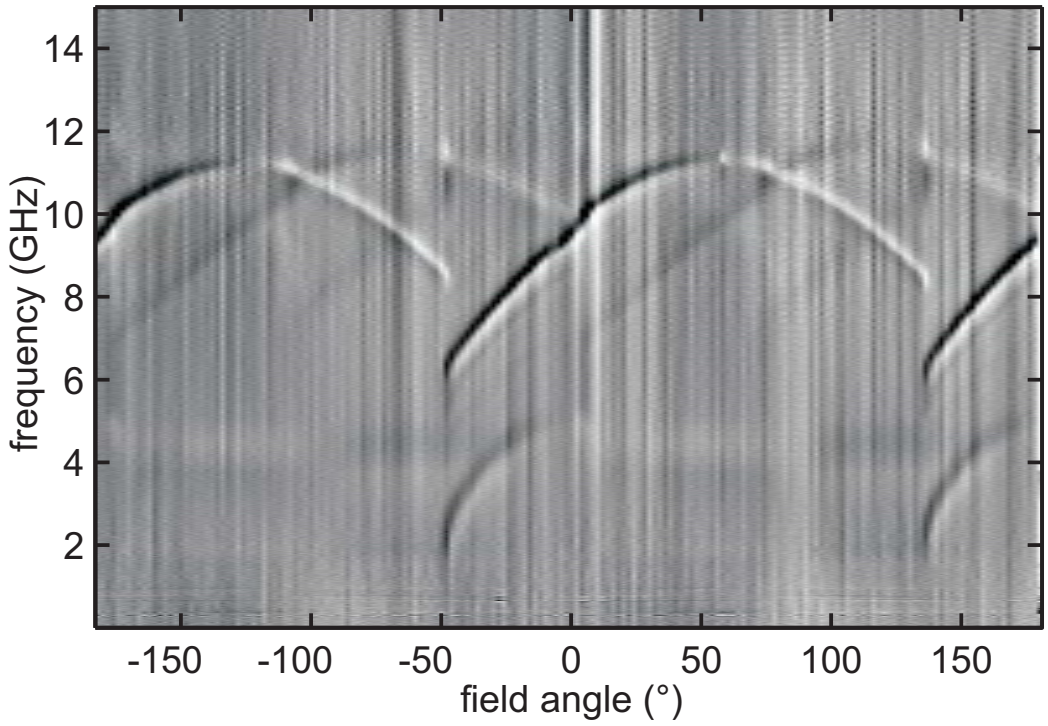

Figure 5.12.: Angle dependend FMR data taken from sample SI13_1_3 at an external field value of 80 mT.

Below the 4 GHz line in the dataset of sample SI13_1_3 we see again the beginning of a mode near the minima position of the strongest ASI mode. By this data it is not clear if the mode only appears at certain angles or if the signal at other angles is only weaker. A Sample with strong signal strength in the low frequency part of the measurement is SI8_1_1 made of CoFeB (see Fig. 5.13). It shows one prominent mode with six local minima (132°, 78°, 26°, -38°, -102° and -166°) at a frequency of 4.1 GHz. Between each minima the mode follows an arc with a maximum at 7.7 GHz. The signal strength of the mode is changing with the angle. The strongest parts of the signal are highlighted with a blue frame around the area.

Above the prominent mode we recognize signals at higher frequencies. However, due to the very weak signal it is not possible to clearly distinguish them from the noise, over the whole angle scan.

Sample	$\text{angle}_{\text{min1}}$	$\text{angle}_{\text{min2}}$	Δf
SI1_1_1 (1)	60°	-122°	≈1 GHz
SI1_1_1 (2)	114°	-68°	≈1 GHz
SI7_1_2 (1)	86°	-98°	≈0.5 GHz
SI7_1_2 (2)	144°	-42°	≈0.5 GHz
SI12_2_1 (1)	64°	-118°	2.5 GHz
SI12_2_1 (2)	6°	-174°	2.5 GHz
SI13_1_3	136°	-48°	2.2 GHz

Table 5.3.: Minima positions for different samples and modes in angle sweep measurements with a fixed external field value of 80 mT. Last column displays the frequency shift at these positions.

5.5. BLS measurement

The measurement was performed on sample SI7_1_2 at a fixed frequency of 9.5 GHz and a power of 10 dBm. The external magnetic field is applied along the CPW. To determine the resonance conditions we used results of previous conducted AESWS measurements and a BLS-field sweep. The highest photon count, which is proportion to the spin wave signal strength at frequency 9.5 GHz, was found at a field of $\mu_0 H = 55$ mT. At fixed field and resonance frequency the number of counted photons depends on the spin wave strength and the amount of ferromagnetic material underneath the lase spot.

Since the ASI-structure cannot be recognized in the BLS microscope we chose three lines with a distance of 0.4 µm to each other for the scan area (see Fig. 5.14 a)). Together these three lines cover the most part of one ASI period in x-direction. The starting points are at the boarder of the signal line of the CPW. From there the position of the BLS laser was shifted up (y-direction) 60 times by 0.1 µm steps. On each position we performed 400 measurements and summed over the counted photons at the resonance frequency. Figure 5.14 b) shows the results of the measurements.

All three measurements at the starting point show relative high signal strength. We attribute the difference in the signal strength to different measurement positions in the ASI unit cell. By changing the position and increasing the distance from the start we see a fast decrease of the signal strength on all three measurements. Additional we detect a local minimum

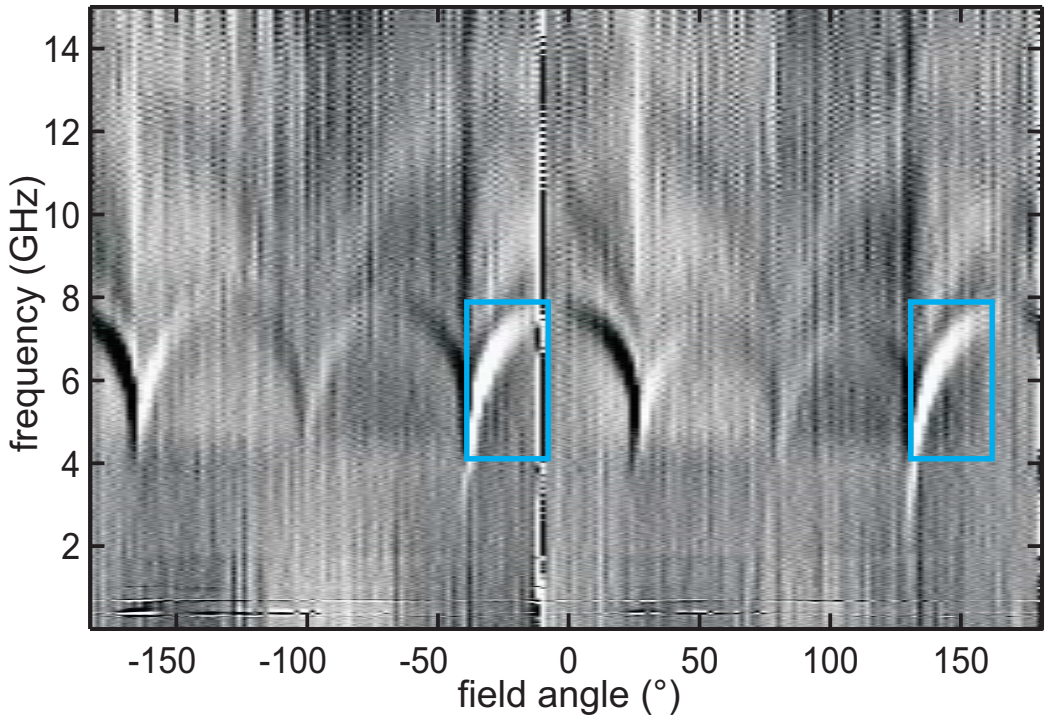

Figure 5.13.: Angle dependend FMR data taken from CoFeB sample SI8_1_1 at an external field value of 80 mT. The two areas with the highest signal strength are highlighted with a blue frame

and maximum in measurement one (red) and two (green) and a shoulder in the third (blue) measurement. At a distance of around 0.8 µm the signal of all three measurements is in the order of the noise level. This is also true for the remaining steps to a distance of 6 µm.

5.6. Interpretation

In the previous section we presented a wide range of different measurements which give information about the investigated system. For all this methods, beside the MFM measurement, one key element is the ferromagnetic resonance, which is depending, among other things, on the k-vector of the exited spin waves (SWs). For an infinite thin film the k-vector is determined by the geometry of the CPW due to the spatial variation of the AC field. The SW gets excited underneath the CPW from where it starts to propagate through the film. If the behavior of the SWs is still the same as in a plane film gets reveal by the BLS measurement (see Sec. 5.5).

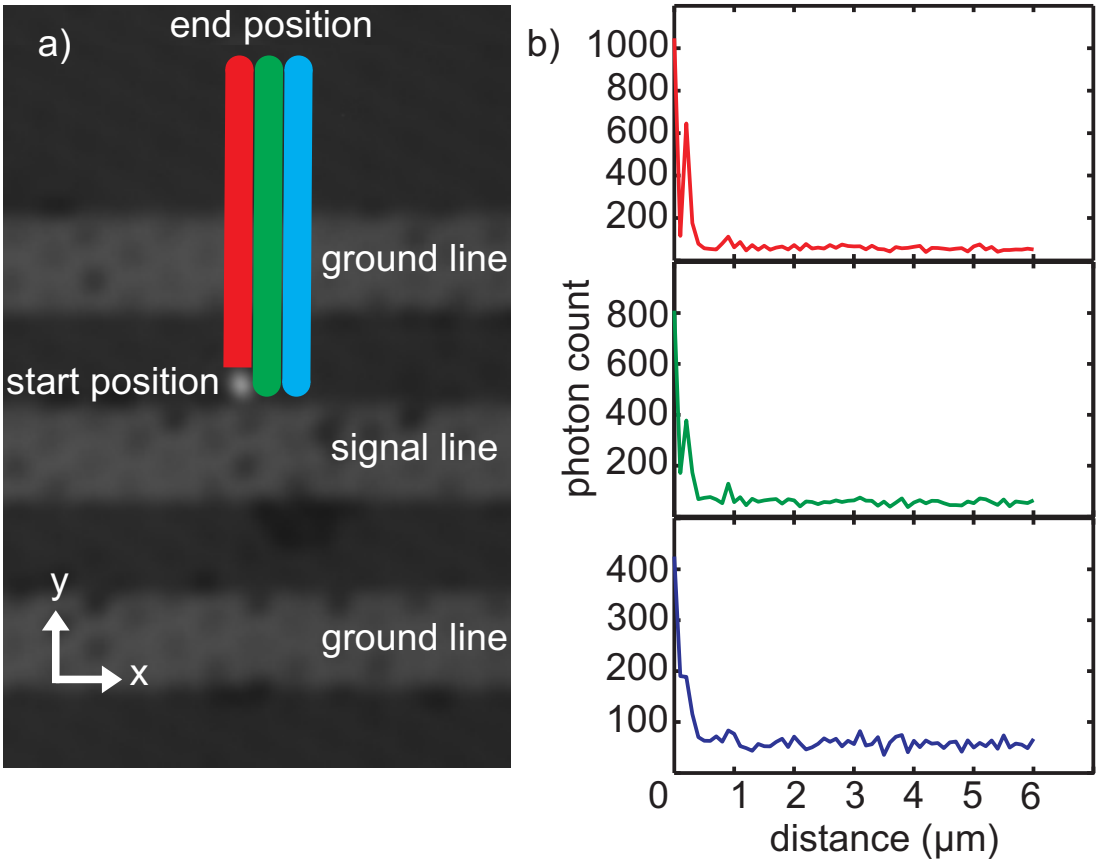

Figure 5.14.: a) Shows a microscope picture of the measured honeycomb ASI sample SI7_1_2. The three lines (red, green, and blue) mark the measurement areas for three different measurements. At the starting position of measurement one (red) we see the laser spot of the BLS setup. The three light horizontal areas are the ground and signal lines of the CPW. The BLS area scan was performed at $\mu_0 H = 55$ mT and an associated resonance frequency $f = 9.5$ GHz. b) shows the number of counted photons at resonance frequency depending on the distance to the start positions.

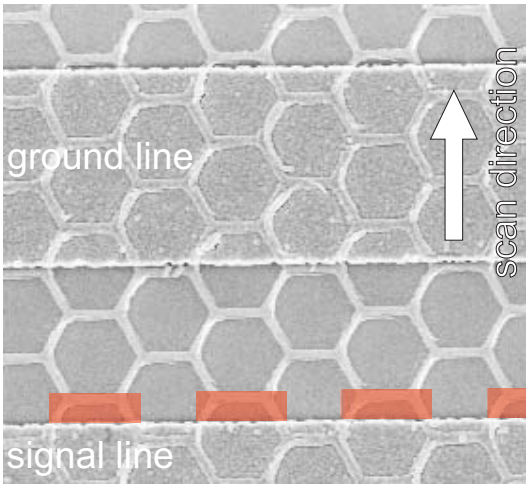

Figure 5.15.: SEM picture of sample SI7_1_2. Red areas mark regions with ferromagnetic material near the signal line.

The measurements one (red), two (green) and three (blue) (see Fig. 5.14) show a strong signal at the edge of the signal line which is declining very fast. Since the signal not only depends on the strength of the SW but also on the probed ferromagnetic surface size, we see a variation of the signal. The ASI structure of the probed samples SI7_1_2 at the CPW is displayed in Fig. 5.15. Unfortunately we cannot exactly track the laser position relative to the spin ice lattice, because its structure is not clearly visible in the microscope image of the BLS setup (see Fig. 5.14 a)). However, since we got a strong signal near the signal line, the laser starting positions has to cover ferromagnetic material. Those possible areas are marked in Fig. 5.15 with red squares. Measurement three has significant lower signal strength at the start, compared to the other measurements one and two. Therefore, we can assume that the start position of measurement three has only a small overlap with the red areas.

By moving the laser spot over the sample, the share of ferromagnetic material underneath it is changing. The variation during the decrement can be attributed to structure of the ASI sample. Past a distance of 800 nm we only detect the background noise, but no SWs independent of the amount of probed ferromagnetic material. This is also true for the area around and beyond the ground line of the CPW. The area underneath the CPW lines cannot be detected since laser light is not reaching the ferromagnetic material. Based on these results we can make the following conclusion. The ex-

citation of spins mainly takes place underneath the CPW lines. An excitation underneath the ground lines is expected, but since the current through those lines is smaller, compared to the signal line, those stray fields might be too small to create a detectable signal in the ferromagnetic structures next to them.

Propagating SWs, if present are decaying within a small distance, which explains the none existing signal in all AESWS transport measurements (S12, S21). In the probed ASI samples the single elements are smaller than the CPW line width and therefore, only see a fraction of the AC field scenery. As a result the dimension of the CPW has no influence on the k-vector of the SWs.

This can also be observed in the simulations (see Sec. 5.3). In those we used a uniform AC-field to excite the magnetization of the structure, which is a convenient process due to the relative small size of the ASI elements compared to the CPW lines in the experiments. The calculations assumed a magnetic pulse with homogenous amplitude over the entire structure. Still it led to a local stimulation of certain areas. Depending on the frequency the excited areas are confined to a selected group of links or the vertices between them.

A further inspection of the stimulated regions reveals a diverse distribution of the signal strength in the links. At frequency A, link 1 reveals a periodic variation of the power along the link axis (see Fig. 5.5 b)). This is an indication for a standing spin wave with a nonzero k-vector. We also observe standing SWs in link 2 and 3 for the frequency B (see Fig. 5.5 c)). However the number of maxima in one link, and therefore the k-vector, is different compared to link 1 at frequency A. At a third frequency (C see Fig. 5.5 d)) we got again a SW excitation at a new k-vector. The values of the resulting k-vectors from the simulation are about $4{\cdot}10^7\ \frac{1}{m}$,$1{\cdot}10^6\ \frac{1}{m}$ and $4 \cdot 10^6\ \frac{1}{m}$ at the frequencies A, B and C. However compared to frequency A and B the signal at C is very weak.

One question is arising. Why do we observe diverse behavior in different kind of the nanobars? The dimensions of the links and whose excitation fields were virtually identical. The difference was established by the external field leading to diverse internal fields and magnetization configurations in the different kind of links. As a result we get one prominent mode for each kind of link at a specific frequency and k-vector, depending on the relative orientation and strength of the external field. For the special case of a field along the angle 0° we find the same relative orientation of the

external field to both link 2 and 3. This was leading to the simultaneously stimulation of the two links at the same frequency. Therefore, we expect a separation of the mode at frequency B into two modes with a change of the external field angle.

Exactly this behavior was observed in the angle sweeps. The measurement on SI7_1_2 (see Fig. 5.11) shows three modes, one for each kind of links. Their frequency behaviors are identical and only an effective shift of $\approx \pm 60°$ discriminates them. The effective 60° shift instead of the geometrical 120° is a result of the twofold symmetry modes due to the shape of the nanobars. Additional to these modes the simulation showed that additional k-vectors might get stimulated. However, the strength of this additional mods in the simulation (see Fig. 5.4 frequency C) are significantly weaker compared to the strong modes. This trend seems not to change for other external field configurations since, in the case of excitation of other modes at different k-vectors, they were too small to be detected in the AESWS measurements.

Regarding the strength of the modes we expect the same absorbed power for each kind of link for the same relative external field. However, this isn't the case in the actual AESWS experiments. There we observe a significant difference in the strength of different modes. One reason for this effect is the relative orientation of the AC field vector to the magnetization direction. The torque from a magnetic field on a magnetic moment, leading to the excitation, is given by Eq. 2.33. A magnetization in AC-field direction leads to no torque and therefore, to no excitation. As described in Sec. 2.11.2 we basically assume a uniform magnetization along the long axis the nanobars. According to the Biot-Savart law the AC field is pointing in-plane perpendicular to the signal line. The resulting angle between the AC-field and the magnetization in the links is different for each link and therefore, leads to different excitation strength. The consequence of this effect can be seen in field sweeps on SIB (see Fig. 5.10). By changing the angle between the links and the CPW lines we observe a change in signal strength.

While this effect is certainly a reason for the difference, it cannot explain all discrepancies in the mode strengths. In the angle sweep on SI7_1_2 the signal line is along the link 1 direction. Therefore, the torque on link 2 and 3 should be equal, but we still see a huge difference between them. Another indication for an additional effect can be found in angle sweeps on SIB1 (see appendix A.3). The mode associated with link 1 is the most prominent

mode independent of the angle between the links and the signal line. The answer is provided by a SEM picture of the sample SI7_1_2 (see Fig. 4.2). In the fabrication process ferromagnetic residuals can stick to the actual ASI structure and join to the links. The residuals are locally changing the width thickness and therefore, the internal fields of parts of the nanobars. This is changing resonance conditions for every affected nanobar, which is leading to a broadening of the measured mode and hence, decreasing its maximum strength. The effect has also been observed by S. Neusser et al. in [NBG08]. Because of the sample mounting during the evaporation (see Sec. 4.3) there is a increased probability that a particular kind of link gets covered. E.g. in case of sample SI7_1_2 nearly every link 2 is fractionally covered at its right rim (see Fig. 4.2 and 5.3) leading to a reduction of its mode signal strength.

Regarding the angle sweeps on SIB1 we already mentioned that it is possible to assign one mode to one special kind of links. In order to do this we use a framework established with the charge model in Sec. 2.11.2. Due to the strong anisotropy/demagnetization the magnetization is parallel or antiparallel to the long axis of the nanobars, and all field components except the field along the long axis of the stripe gets strongly reduced. Hence, in an angle scan the biggest internal field is found at an external field along the link. According to section Sec. 2.7, with a constant magnetization, SW k-vector and field configuration, the resonance frequency increases with a higher internal magnetic field. Therefore, at fix absolute external field value, we expect a maximum frequency at an applied field direction along the stripe.

A closer inspection of Eq. 2.66 reveals that this is only true for a magnetization along the field. For the shown angle sweeps this has been ensured with a big enough field value. However, while the simulations indicate that the k-vector (set due to the stripe dimensions) direction is always along the links, it also shows that the k-vector might change with the external field angle. Therefore, we need another method to ensure the correct affiliation of modes and links.

This can be accomplished by locating the position of the switching angle (minima). With the assumption of an Ising spin like behavior of the magnetization, it is changing its sign at this specific angles. The result is a sudden change (shift) in the resonance frequency, which was observed in both, field and angle sweeps. The measurement on SI7_1_2 begins in the magnetization configuration displayed in Fig. 5.16 at 180°. By rotat-

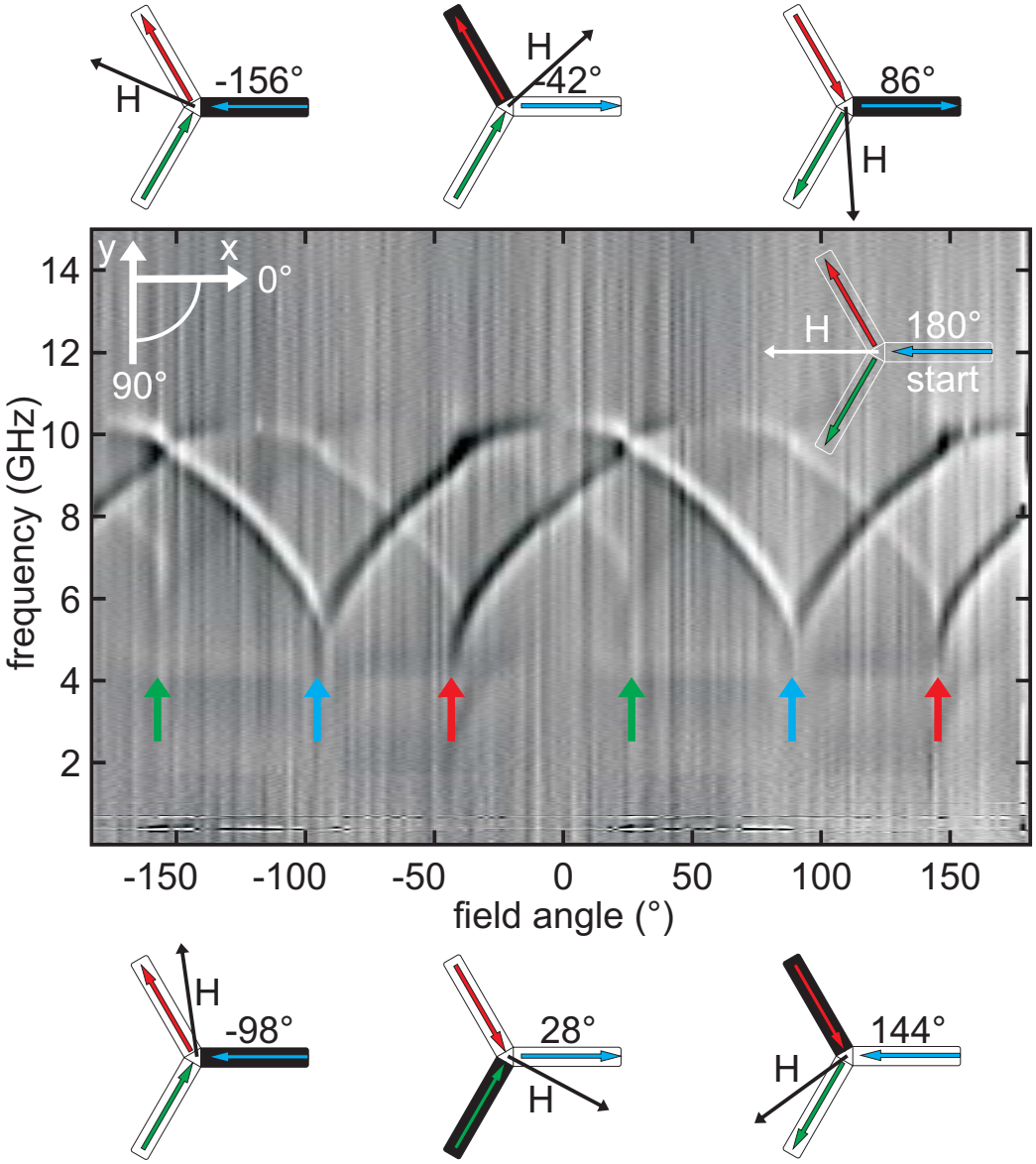

Figure 5.16.: AESWS angle sweep with an external field value of 80 mT at sample SI7_1_2. The blue, red and green arrows indicate the position of the magnetization in the associated links. The sketches of three connected links display the magnetization directions at different angles. A black link indicates the switching of its magnetization at the specific angle. White links remain unchanged.

ing the field and comparing the magnetization of the links it is possible to determine which link is switching and hence relate the modes to the kind of links (see Fig. 5.16). Evaluation of all angle sweeps indicates that our first assumption, that the modes excited in one kind of link is highest if a magnetic field with a fix value is aligned along the associated link and its magnetization, might be correct, despite a change of the SW k-vector during the field rotation.

The information about the affiliation of the modes can be transferred to the field sweep measurements, which enables us to compare the critical field values with the values predicted by the magnetic charge model. Following Eq. 2.91 the theoretically predicted critical field for sample SI7_1_2 is $\mu_0 H_{\mathrm{crit}} \approx 8$ mT. Many papers utilizing this equation use the stripe width w for the DW width a, which is justified for a transverse wall. However, since we are expecting a vortex wall (see Sec.5.1) we multiplied the used stripe width with a factor of $3\pi/4$ (see Sec. 2.28). In the field sweep measurement displayed in Fig. 5.7 the prominent mode belongs to link 1. Due to the starting configuration this kind of link is a minority link and therefore, we expect a switching of the magnetization at a field (switching field/critical field) around $\mu_0 2H_{\mathrm{crit}} = 16$ mT (see 2.11.2). The measured value from the AESWS is considerably higher. Other samples show an even bigger discrepancy. According to Eqs. 2.28 and 2.91 the critical field is proportional to t/w. Comparing the measured critical fields in Table 5.1 with the dimensions in Table 5.2 we see that this relation is also not fulfilled.

To understand the deviation of the experiment from the theoretical model one has to realize that the model was designed to explain the simulated behavior in a perfect honeycomb ASI structure. Due to the preparation the actual measured samples exhibit different discrepancies compared to a perfect sample. This is including random local variations of width and thickness of the stripes, and an overall edge roughness. A local variation of stripe dimensions could lead to a changed switching field of the affected stripe [US04]. However, since the average values of the stripes size are the same for the whole structure, this can only lead to an enlargement of the critical field width $\mu_0 \Delta H_{\mathrm{crit}}$, and cannot explain the high critical field value.

The edge roughness on the other hand could lead to an enhancement of the critical field. Bryan et al.[BAC04] showed that the switching of the magnetization in Py submicrometer nanostructures is influenced by the

edge roughness. A higher roughness increases the field necessary to switch the magnetization. As a possible explanation they suggest that the higher critical field may be a result of pinning of the DW due to the edge roughness. So while a field might be strong enough to separate the DW charge from the vertex charge (see Sec. 2.11.2) an even higher field is required to overcome the pining effect. If this is indeed the reason for the high critical field, it is required to find the same average roughness over the entire sample. This is expected to be true, since preparation parameter affecting the roughness are the same for each kind of link. Local variations of the roughness should lead to a broadening of the signal.

The pinning of DWs is also explaining a discovery we observe in the field sweeps under different external field angles (see Fig. 5.9). Contrary to prediction in Sec. 2.11.2 the switching field value is not affected by the field angle until it is reaching $\approx 60°$. Evidence suggests there are two critical field strength values. One value to create an unpinned (free) DW in the vertex, and one value to pull the DW from the vertex, through the nanobar. At least the second one depends on the angle of the external field leading to the change of the critical field value at higher angles compared to the link direction. For small angles the first critical field, due to pinning, is determining the switching behavior. By changing the external field angle the share of the field pulling the magnetic charge from the vertex is getting smaller. Starting at an angle of $\approx 60°$ the share pulling the DW, at an external field value fulfilling the first critical field condition, is to small to pull the wall through the link. As a result the switching occurs at a higher field value. For an angle bigger than 90° the field component along the link is pointing in the magnetization direction and therefore, the magnetization cannot be switched anymore, independent of the applied field strength. The magnetization however, can still get influenced.

The previous theory assumed that the magnetization is always pointing parallel or antiparallel to the long axis of a link. The origin of this behavior is a uniaxial anisotropy due to the shape of the nanobars. Nevertheless, since the anisotropy constant has a finite value it is energetic beneficially to rotate the direction of the magnetization towards the external field. The rate of rotation depends on the relative strength of the external field and the anisotropy constant. This effect can be observed in angle sweeps on samples with different anisotropy, or at different external field values. The energy due to the uniaxial anisotropy is described by Eq. 2.19 with a maximum at a magnetization perpendicular to the easy axis. Since during the

switching progress the magnetization has to rotate over this configuration this energy maximum is representing a barrier which has to be overcome with a high enough applied external field. Therefore, it is justified to assume a high critical field and a high anisotropy are related. In samples with a smaller anisotropy the rotation of the external field leads to distinct rotation of the magnetization, hence decreases the magnetization component along the long axis of the link. In the switching process only this component is changing its sign. So with the rotation of the magnetization from the easy axis its change in the switching process gets decreased. By comparing the angle sweeps on sample SI7_1_2 (see Fig. 5.11 (low critical field)) and SI13_1_3 (see Fig. 5.12 (high critical field)) we find a significant difference at the frequency shift due to this effect.

To determine the anisotropy constant we are using Eq. 2.66. For the field direction we are choosing 0°. In this special case the magnetization direction in the link before and after the switching event is constant. By fitting the k-vector and anisotropy on the results of measurements on sample SI7_1_2, we obtain the values $k = 3.4 \cdot 10^7 \frac{1}{\mathrm{m}}$ and $\mathrm{K_{uni}} = 39 \frac{\mathrm{kJ}}{\mathrm{m^3}}$. The resulting fit, is displayed in the appendix (see Fig. A.1). The field value for the change of the magnetization direction was chosen according to the measurement result. At this field value and angle we expect a switching of all three kinds of links due to the ice rule see Sec. 2.11.2). However, since the sample exhibits local variations of is parameter, not all links are switching at the same field.

The process starts by the nucleation of single DWs switching one or more connected links, forming chains of switched links. With increasing field strength more and more links reach their critical field and change the magnetization. A detailed description of this process can be found in [Zei13][Mel+10] and [She+12]. The result is a finite width of the critical field ΔH_{crit}, which is an indicator for the homogeneity of the sample. While in the field sweep at 0° all three links are switching at once, the angle sweeps fixed absolute field value show a switching of individual kind of links. If the modes of the different links are observed not separately but together, the latter case reveals a further effect. At the switching angle of one mode the other modes exhibit also a change in the resonance frequency (e. g. see Fig. 5.11). This is a crucial finding because it implies that the resonance frequency of one link does not only depend on its own parameters (magnetization, internal field, et cetera), but also on the parameters of its neighboring links. Due to the field history in our experiments

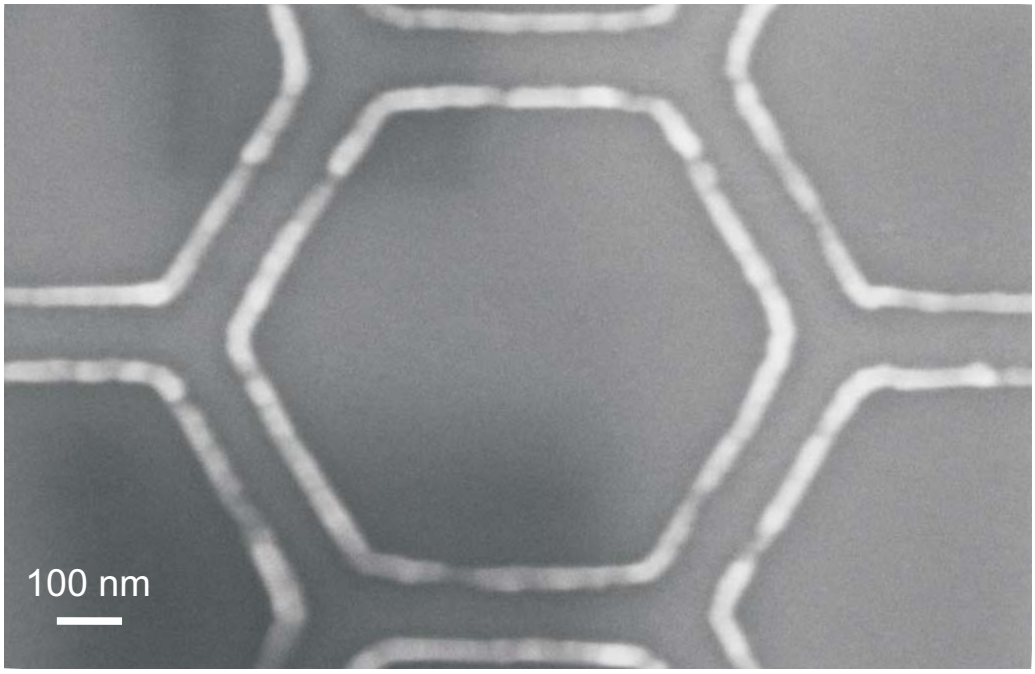

Figure 5.17.: SEM picture of sample SI8_1_1.

the magnetization configuration of all three kinds of links are always the same over the entire sample (at least we could not detect any deviations). In other experiments however, it is possible to have local variations of the configuration at one sample. With the exact knowledge of the resonance frequency behavior it is possible to identify the different configurations.

The majority of the samples are made of Permalloy. Only sample (SI8_1_1) is made of CoFeB. The field sweep of the sample displays the same general behavior as the other samples. However, the angle sweeps shows a different result. Instead of strong modes at higher frequency and a hint of a mode in lower frequencies the behavior is reversed. It displays hints of modes at higher frequencies, even higher than in the strong modes in the Py samples, and a strong mode at lower frequency. By looking at the SEM picture of the sample (Fig. 5.17) we see a high rim of magnetic material on all edges of the sample. Following the conclusions from the Py measurements this should lead, among other things, to a broadening of the modes associated with the different kind of links and decreases those strength. Keeping this in mind we assume that the hints of modes at high frequencies are the remains of the signal of the stimulation in the links.

To find the source of the prominent mode in the angle sweep on SI8_1_1

we have to look at the simulations. They displayed one mode at a low frequency those origins are not from the links, but the vertices of the structure. If the vertex is the source of the signal, we expect a sixfold symmetry of the signal due to the geometry of the vertices. And indeed, we find a sixfold repetition of the same signal development over the 360° angle rotation. The minima positions show a random deviation from the expected 60° repetition, however this can be attributed to the high edge roughness. As explained above the rough edges can lead to a pinning of the magnetization and therefore, restrain a free rotation of the DW in the vertex.

Looking at the signal strength of the mode we see a strong variation depending on the angle. Comparing the strongest parts of the mode (see blue squares in Fig. 5.13) with the measurements on other samples (see Fig. 5.11, 5.12) we notice that the strong parts of the mode from SI8_1_1 and the hints of modes in the other samples are alike in sharp and position. Hence it is justified to assume that all samples can get exited in different links, and the vertices. Unequal imperfections in different samples lead to a weakening of the signal of specific modes and therefore, different measurements show different signal-to-noise ratios. The relative strong signal from the vertex in sample SI8_1_1 compared to the other samples is very likely a result of a bigger vertex area (more ferromagnetic material gets excited) compared to most other samples. The sample with a similar vertex size SIB could also show a good vertex signal, but due to the flip chip measurement technique used at this sample the general signal strength is weaker compared to the measurements with integrated CPWs. Hence we don't observe the weak vertex signal in its datasets.

5.7. Local Critical Field Reduction by Laser Induced Heating

An essential characteristic of ASI is the switching of the magnetization direction in the links. Hence it is a crucial interest to influence or control it. A possibility is to use a specific external field sequence. Since the field affects all links this method might modify the configuration of the whole sample.

A way to achieve more control is to introduce reversal pads [Zei13]. Due to a large width the magnetization in the pad switches at a lower field compared to the links. From the pads a DW moves into the attached link

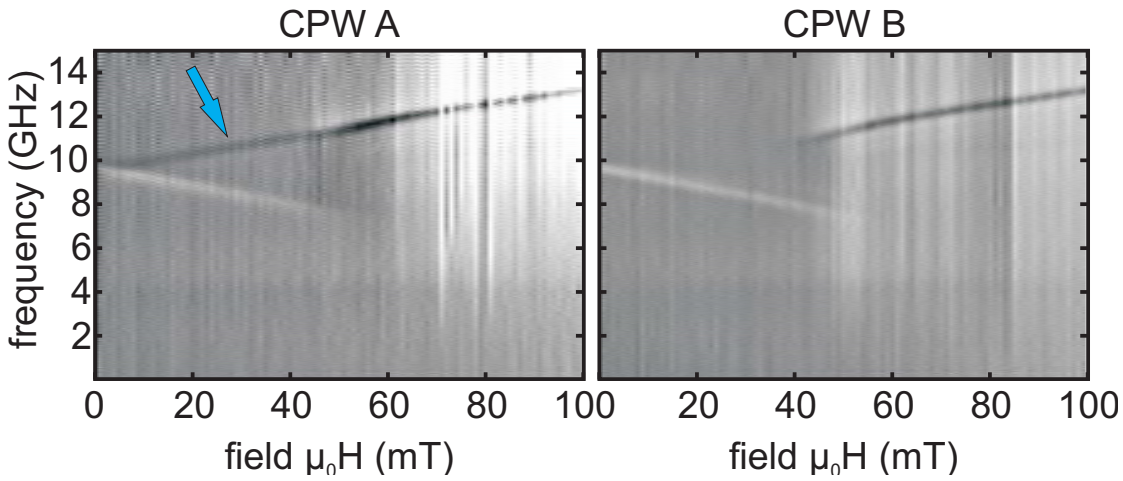

Figure 5.18.: Color-coded NNS (processed with next neighbor subtraction) reflection FMR data taken from sample SI5 from CPW A and B at an external field angle of 0°. The dark and light contrast marks the resonance modes. The blue arrow indicates an additional mode compared to the measurement from CPW B.

reversing it and starting a reversal process until the DW gets pined. However, this method has limits and once prepared it is hard to remove the pads without destroying the sample.

In the following we present a method to locally switch the magnetization in links without changing the structure of the sample. The experiments were conducted on the ASI sample SI5. The nominal length, thickness and material of its links are 500 nm, 30 nm and Py, respectively. Two nominally identical CPWs (A and B) on the DUT have been used to excite and detect spin waves. They are characterized by the same dimensions and spacing as the CPWs described in Sec. 5.1. Measurements with both of them show an identical behavior as was expected and described in Sec. 5.4.

In the experiment we proceeded according to a following protocol. First an external field was applied at an angle of 0° and a value of -100 mT. Than the value was ramped to 0 mT followed by an increment to a value of +42 mT. While the sample was exposed to the magnetic field we used a laser to heat one third of the ASI underneath CPW A. The laser had a spot size of about 0.5 μm [Bra14] and a power of 28 mW. Afterward the external field was reduced to zero and the sample was transferred to the AESWS setup were we performed a field sweep at an angle of 0° from a value of 0 mT to 100 mT. During the sweep we measured the S-parameter

S11 (reflection on CPW A) and S22 (reflection on CPW B). The result is shown in Fig. 5.18.

The data from CPW B shows the same behavior as the date taken without laser heating. The measurement on CPW A on the other hand shows an additional mode ranging from 0 mT to the switching field. Using the results from Sec.5.4 and Sec. 5.6 we identify the new mode marked by a blue arrow with the mode from links with a magnetization switched in the direction of the external field. Therefore, we can make the following conclusion.

Due to the heating M_s of the ferromagnetic material got reduced [Rou+15]. This reduced the shape anisotropy energy and accordingly decreased the switching field. This enabled a switching of the heated elements of the SI at a field of 42 mT which is below the switching field at room temperature. Since only one third of the SI underneath the CPW was heated we get a contribution to the signal of both, switch and not switch links. The signal of CPW B on the other hand, only exhibits signals from not switch links. The heat diffusion from one CPW to its neighbor was not enough to decrease the critical field below 42 mT. Consequently the local laser heating is a method to decrease the critical switching field of a confined are. An additional advantage of this technique is its reversibility. Subsequent experiments without laser heating showed that when the material has cooled down the critical field is changing back to its original value.

5.8. Conclusion

In summary we showed the behavior of excited SWs in honeycomb ASI structures using several techniques. A key feature of the results is the selective excitation of different parts of the ASI lattice at different frequencies and magnetic configurations. It allowed us to gain magnetic information not only about the entire structure but also about specific parts of the honeycomb. We also discovered that it is not enough to only consider a single vertex and the three adjoined links to describe the dynamic properties in the ASI. The magnetization directions of adjacent links influence the SW excitation frequency of a selected link. Therefore, it is necessary to consider at least two neighboring vertices and those adjoined links to describe the magnetic properties at the link embedded between the two vertices. For the experiments on the real ASIs we saw, if the exciting CPW dimensions

are large enough, that the k-vector of SWs is determined by the dimensions of the ASI. We also observed the influence of possible deviations between theoretically perfect and real samples. Sample imperfections not only had an effect on the measured AESWS signal, but also showed an influence on the switching behavior of the link magnetization which is critical for AESWS measurements and important for other experiments as well. Further experiments should focus on the exact influence of the roughness of the material as well as the influence of neighboring links on the embedded segment. For the realization of such experiments we also demonstrated a method to change the magnetic configuration of ASI parts by locally heating the structure with a laser. With a laser spot small enough this method should enable us to create every possible configuration of the link magnetization in the ASI. The understanding of the influence of sample imperfections and the interplay between the links is not only crucial to improve the sample quality but is also necessary to improve the models describing the ASI.

6. Spin Wave Interference

Interference is a prominent and very important phenomenon in which two waves superpose to form a resultant wave of greater or lower amplitude. It is an essential part of experiments such as the famous Michelson-Morley experiment performed in 1887 disproving the theory of the luminiferous ether. With the experiments on Y-shaped structures (Y-structures) we are introducing samples that enable us to observe interference of two spin waves (SWs) and offer a certain control of the waves via an electrical current.

6.1. Characterization

Sample	a	b	c	d	e
BLSinter2	6.0 µm	2.8 µm	0.9 µm	2.1 µm	11.2 µm
BLSinter4	6.8 µm	2.0 µm	1.2 µm	2.6 µm	11.7 µm
Sample	f	g	h	i	
BLSinter2	35.0 µm	30.0 µm	13.8 µm	3.8 µm	
BLSinter4	33.4 µm	30.0 µm	14.9 µm	2.1 µm	

Table 6.1.: Nominal dimensions of the investigated Y-structures.

For the following experiments the goal was to create a structure with the possibility to directly observe interference of coherent SWs from two sources and influence those with an electrical current. In setups that show interference on other kinds of waves (e.g. light) a common practice is to split up a package of identical waves into two. One of the packages is altered compared to the other one and then both are reunited to observe interference. This concept could also be transferred to SWs by preparing a SW guide that is divided into two paths and combined to one again as shown in Fig. 6.1 a). However, assuming a uniform external field, the signal strength of a SW gets decreased when guided through a SW guide bend [Vog+12]. In the SW guide displayed in Fig. 6.1 a) the SWs are

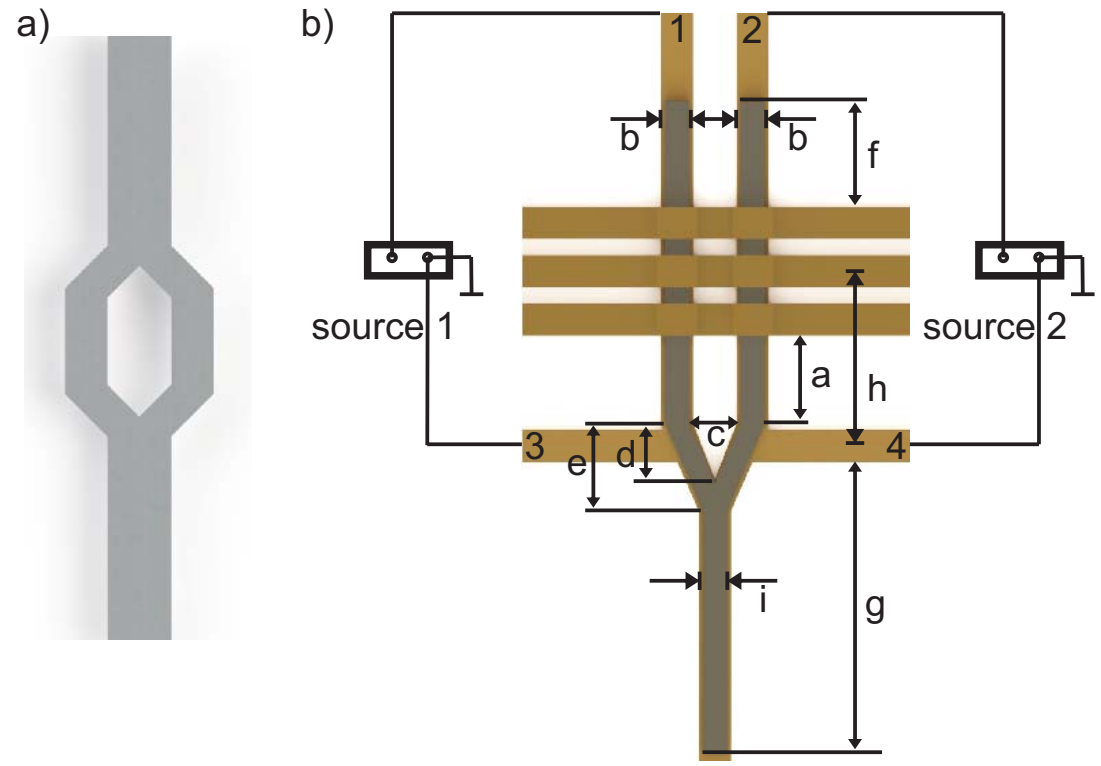

Figure 6.1.: Sketch of a possible a) and used b) SW interferometer structure. The labels a-i represent the relevant lengths/distances of the ferromagnetic structure and CPW. The numbers 1-4 label the contacts of the current lines/structure. Source 1 and 2 represent the current sources connected to the current lines.

guided through two bends resulting in a significant decrease of SW signal strength. Additionally C. S. Davies et al. showed that a misalignment of the external field relative to the structure could lead to an unequal splitting of the SWs into the different paths [Dav+15].

To avoid these difficulties we are using a Y-like shaped structure as illustrated in Fig. 6.1 b). The dimensions of the two Y-samples investigated in the framework of this thesis are listed in Table 6.1. The geometry of the samples reduces the number of bend areas and therefore, the decrease of the amplitude is reduced. Instead of one we excite two SWs, with a fixed phase relation between the SWs, in the two separated paths of the structure with a CPW prepared across them (see Sec. 4.4). In the following we will also refer to this parts of the structure as path 1 and 2 (left and right in Fig. 6.1 b)). The width of signal and ground lines of the CPW are 2.1 µm with an edge to edge gap of 1.5 µm between them. The resulting main

excitation of k-vectors is around a maxima at $k = 0.92$ rad/µm [Yu+13].

To alter the SWs in the different paths of sample BLS2 we utilize a method also used by V. E. Demidov et al. [DUD09]. By putting the ferromagnetic structure on top of a conducting line it is possible to change the resonance conditions for SWs via a current. The implementation of the current lines is depicted in Fig. 6.1 b) and 4.3. It is covered by a layer of oxidized aluminum and Al_2O_3 (not shown in Fig. 4.3, see Sec. 4.4) to ensure isolation between the current line and the SW guide on top of it. By sending a current I through one path of the current lines with width w and thickness t, it is creating a uniform field with strength of about

$$H_I = \frac{I}{2(w+t)}, \tag{6.1}$$

close to the gold surface, changing the local external field and therefore, the resonance conditions in the ferromagnetic material (see [DUD09]). Since it is possible to send different currents through the two paths we acquire SWs with the same frequency but different wave lengths. With a fixed distance h this should lead to a phase difference at the position where the SWs meet depending on the difference of the local fields. To set the current we use two source meters (see Sec. 3.5.3) connected to the contacts 1,3 (path 1) and 2,4 (path 2). One connector of each current source is connected to its counterpart via ground (see Fig. 6.1 b)). Experiments on others samples (not included in this thesis) showed that we were able to apply a current of ± 30 mA without damaging the structure.

To grant a plain surface for the ferromagnetic material without any steps, the gold of the current lines is underneath the entire ferromagnetic structure, independent if the gold is needed for applying a current or not. Additionally the width of the gold lines is larger than the ferromagnetic stripes, to reduce the edge effects of the magnetic field due to an applied current through the gold or misalignment of the structures (see Sec. 4.4). However, despite the use of additional markers (see Sec. 4.4) the ferromagnetic structure of sample BLS2 was shifted horizontally (to the left in Fig. 6.4), so that an about 250 nm wide stripe of the material was not on top of the current lines.

6.2. BLS Measurements

The presented data give an overview of the signal distribution in two selected Y-structure samples, depending on the probe position, applied field and currents through the current lines. To label the different probe positions for the BLS laser on the DUT we use three terms, area, section and position.

Measurements in areas were always performed at a fixed field, current and only the position was changed in constant steps in two spatial dimensions. The correspondent measurement locations are restricted to the squares marked in the location maps (see Fig. 6.2 a) and 6.4) and can be individually addressed by coordinates (x, y) within the area (x (y): number of steps horizontally (vertically) necessary to reach the measurement location).

Sections on the other hand, refer to measurements in which the location of the BLS laser was only changed in one direction (also fixed step size). The measurements were performed on locations along the thick section lines in the location maps. In contrary to the area scans, measurements in sections involve variation of the applied current and location.

Positions mark the location for measurements without moving the laser spot. Similar to the sections, other parameters (field or current) were changed during the measurement. The different positions are marked with circles.

For the external field we use two permanent magnets (see Sec. 3.5). The position of the sample was chosen to apply the external field along the lines of the CPW.

6.2.1. Sample BLS4

The different locations of the measurements are marked in Fig. 6.2 a). At every spatial point we performed 200 sweeps of the Tandem-Fabry-Pérot-Interferometer (TFPIs) (see Sec. 3.5.3). To excite SWs with the CPW, a frequency of 8 GHz and power of 10 dBm had been chosen. As the first step we performed a field sweep at position 1 to maximize the signal strength/intensity (see Fig. 6.2 b)). At this position the direction of the SW k-vector points in the opposite direction compared to all other experiments on sample BLS4. Hence, for the measurement at position 1 the direction of the applied external field was reversed. According to the results of the field

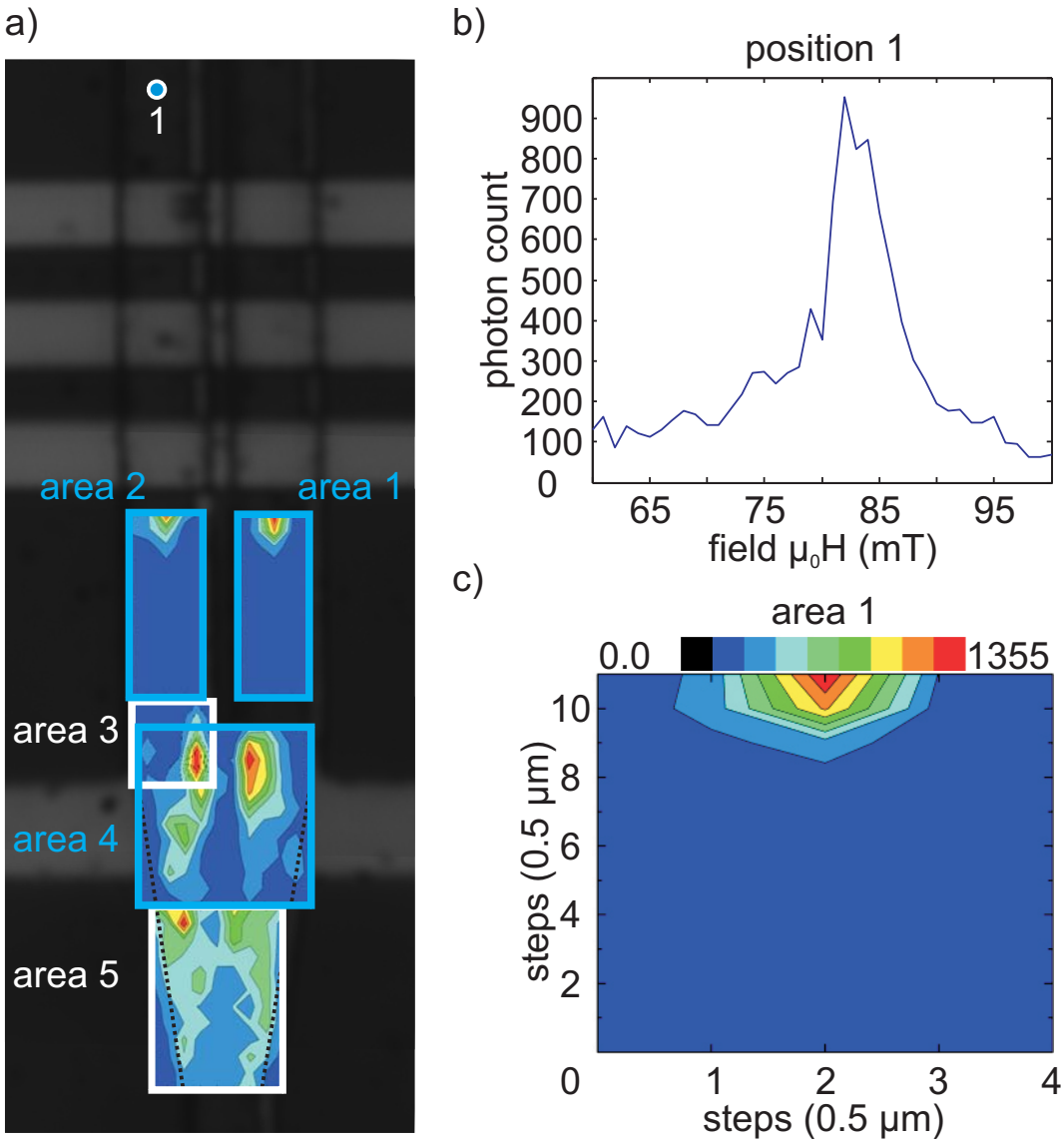

Figure 6.2.: a) Positions (circles), and different areas (squares of two colors, white and blue for a better differentiation of overlapping areas) for the measurements on sample BLS4 in a microscope picture. The color code of each area displayed in the map is different. The dotted line in the map indicates the edge of the ferromagnetic material. The field scan at pos 1 b) and the scan at area 1 c) were performed at 8.0 GHz. The photon count at the locations in area 1 c) is color-coded. The external field for the area scan c) was $\mu_0 H = 84$ mT.

sweep the following BLS measurements on this sample were performed at an external field strength of 84 mT.

Two experiments were conducted in area 1 and 2 (see Fig. 6.2 c) and 6.3). These areas cover the two separated paths (1 and 2) in which the SWs get excited. Both areas show a similar spatial signal strength distribution. The strongest signal of the SW can be found close to the CPW in the middle of the ferromagnetic path. Starting from this position the signal strength decreases significantly within two spatial steps to the side (1.0 μm) or three steps down (1.5 μm). The remaining measurement points show a very weak signal compared to the maximum value.

The measurement below area 2 was continued with area 3 (see Fig. 6.3). The signal at the top part of area 3 shows the same strength as the bottom part of area 2. By moving the BLS laser spot further down we detect an increase of the signal strength in the lower right part of the area at (4,1) and (4,2).

The same maximum is also covered by area 4 at location (4,9). Additionally we now observe a second prominent maxima at (7,9). Starting from these maxima the spatial map shows two vertical channels of higher signal strength compared to the background signal. We also observe two local maxima within the channel on the left. The two channels themselves are separated by a region of low signal strength.

A similar distribution is shown in area 5. The general trend is a reduction of the signal strength with increasing distance of the measured location to the CPWs. Within this development we see several local maxima and similar to area 4 a separation into two channels. However, the separation is not as distinct as the one in area 4.

6.2.2. Sample BLS2

The main purpose for sample BLS2 was the individual manipulation of two phase coherent spin waves by changing the local magnetic field via an electrical current and the observation of its influence on the spin wave signal distribution. Therefore, we performed several measurements in different locations on the sample (see location map in Fig. 6.4 a)). We also conducted one measurement without an applied current in area 1 equal to the measurements on sample BLS4 (see Sec. 6.2.1). For this and all other measurements the excitation frequency was chosen to be 9.5 GHz with a power of 25 dBm. For the applied external field we chose $\mu_0 H = 72$ mT.

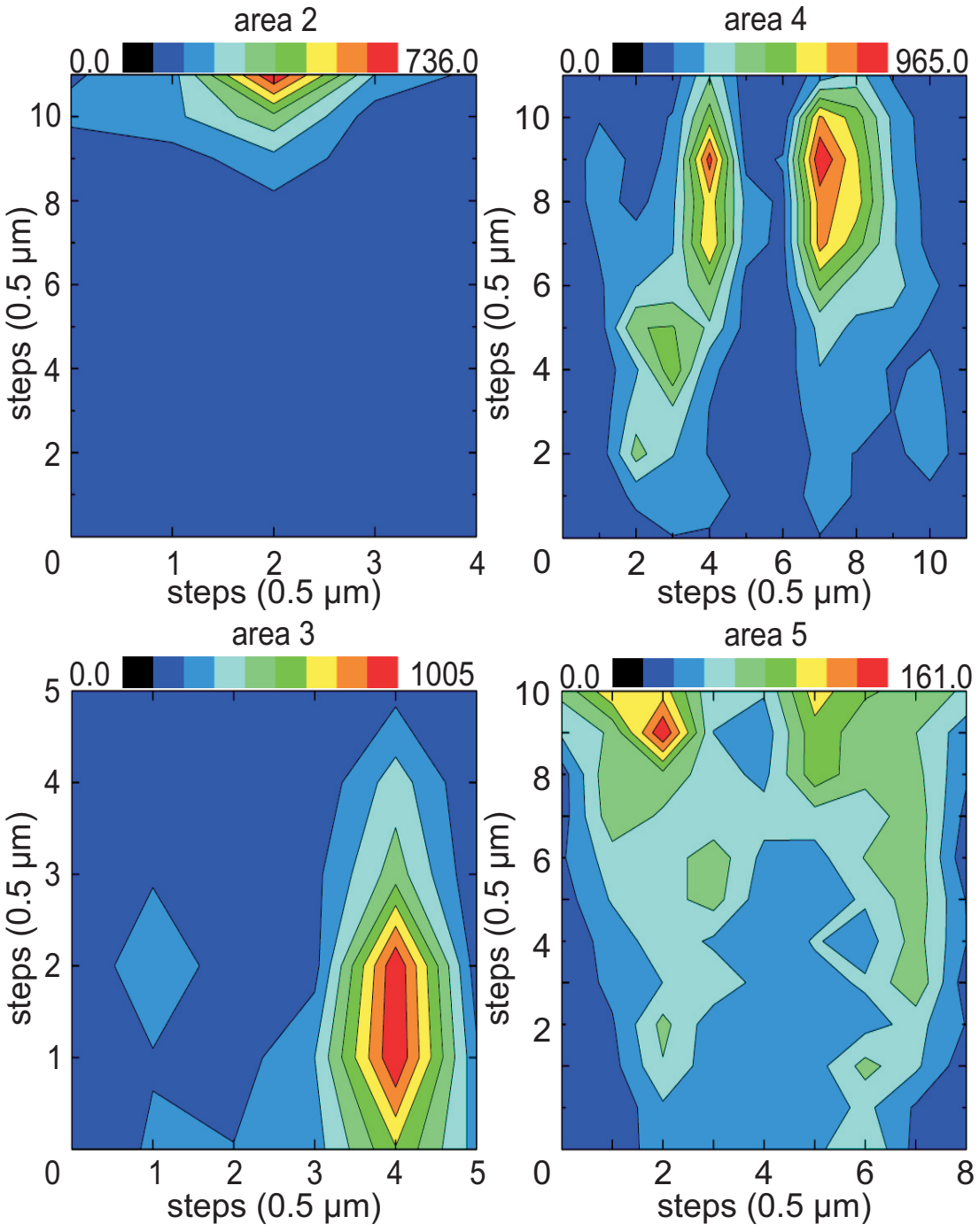

Figure 6.3.: Color-coded signal strength distribution of different areas at an external field of $\mu_0 H = 84$ mT, at a frequency of 8 GHz.

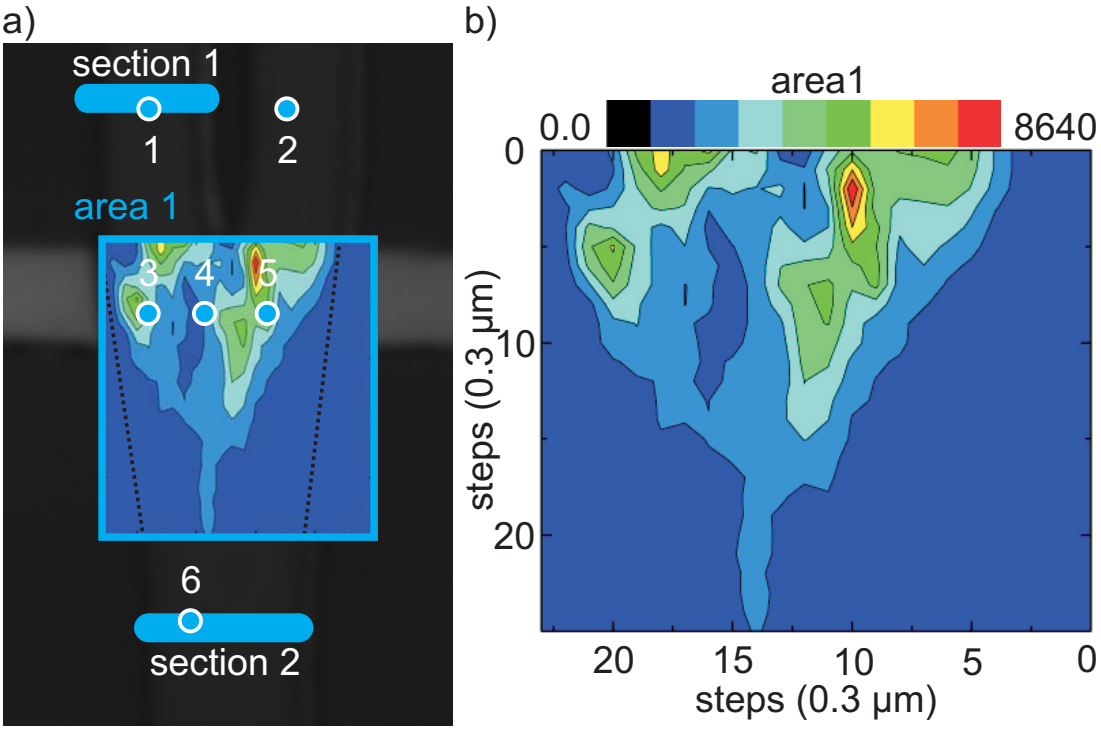

Figure 6.4.: a) shows the different positions (circle), area (square) and sections (line) for the measurements on sample BLS2 in a microscope picture. The dotted line in the map indicates the edge of the ferromagnetic material. The color-coded signal strength distribution of area 1 at an external field of $\mu_0 H = 72$ mT, at a frequency of 9.5 GHz is displayed in b).

The value was determined by maximizing the signal strength depending on the field (not shown) similar to the method applied to sample BLS4.

On every location of the measurements in area 1 200 sweeps of the TF-PIs have been performed. Its spatial signal strength distribution is depicted in Fig. 6.4 b). It shows two prominent maxima close to the position of the two separated paths (1 and 2) in which the SWs get excited by the CPW. Starting from these points the distribution displays two regions with a higher signal strength spreading to the lower left side of the area. The regions form two channels, partially separated by a region of low signal strength. In each of those channels we detect a second local maximum. While the left channel is vanishing on the edge of the sample, we see a small region of increased signal strength reaching from the right channel into the lower part of the sample.

For the following experiments a current with a value up to $I = \pm 30$ mA

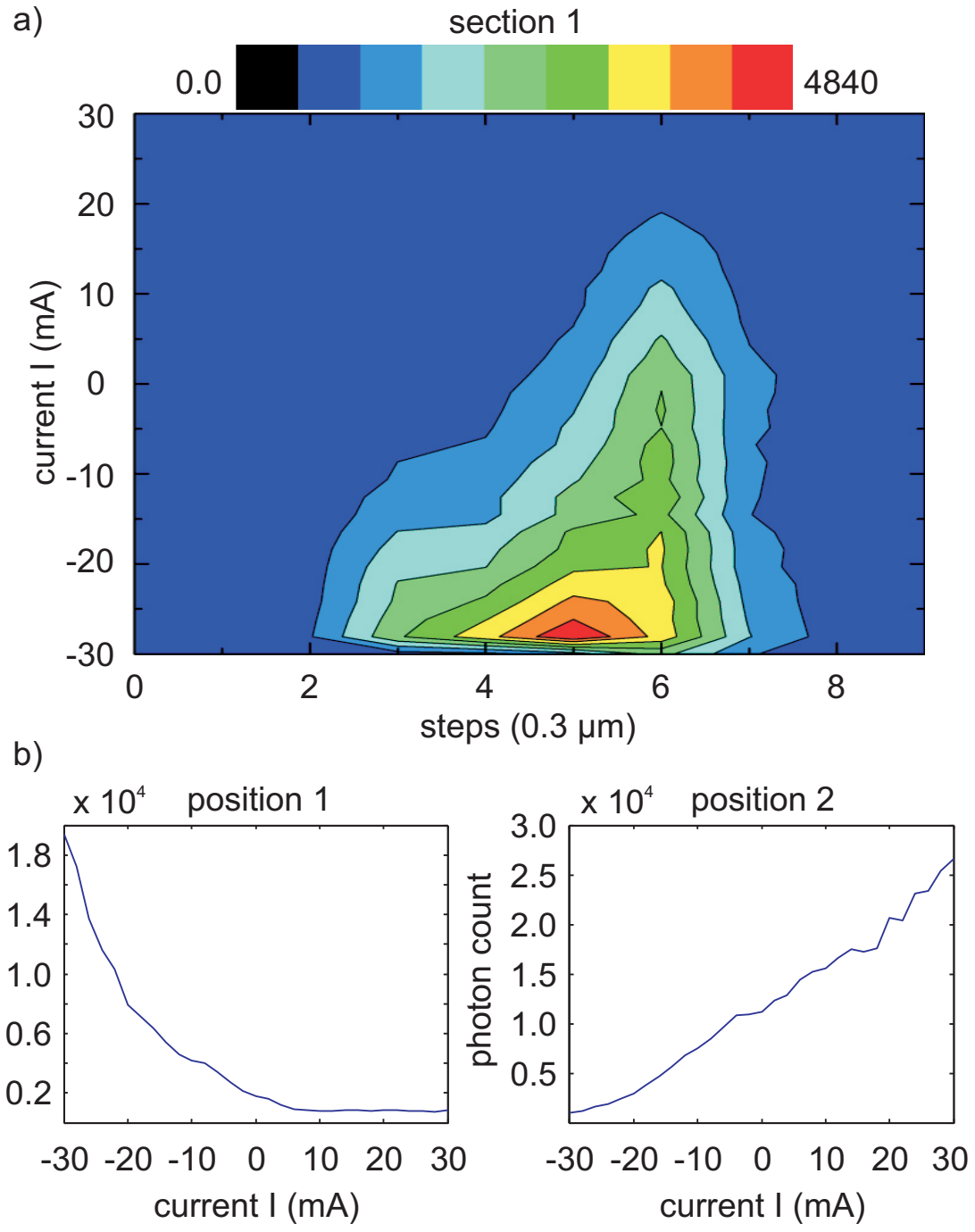

Figure 6.5.: Signal strength distribution of section 1 a) (color-coded), position 1 b) and 2 c) depending on a current at an external field of $\mu_0 H = 72$ mT, at a frequency of 9.5 GHz.

(step width 2 mA) was sent through the two paths of the current lines. According to Eq. 6.1 the maximum amount of 30 mA provides $\mu_0 H = 6.7$ mT in the sample plane. To generate a large difference between the two SW paths, we simultaneously sent two currents with opposing signs through the lines. For simplification of the notation we only specify the current generated by source 1 sent from contact 1 to contact 3 (path 1 see Fig. 6.1 b)). The current sent from contact 2 to contact 4 (source 2) has always the same absolute value, but the opposing sign.

A measurement depending on the current was conducted in section 1. Similar to area 1 we also performed 200 TFPI sweeps for every measurement point. The maximum signal is obtained at a current of $I = -30$ mA in the middle of the section. Changing the probed location to the left or the right decreases the signal strength (see Fig. 6.5). Increasing the current up to +30 mA decreases the signal until it reaches the level of the background noise. The strength and shape of signal does not only depend on the current value, but also the spatial position in the section. As a general behavior, all positons show a decrement of the signal strength while changing the current value from -30 mA to +30 mA.

The same trend can also be observed in the measurement on position 1 (see Fig. 6.5 b)). To obtain the measurement data at this and the other positions (2-6) we performed 500 TFPI sweeps. For position 1 the data shows a maximum of the signal at a current of $I = -30$ mA and a nonlinear decrement till a current of $I = +10$ mA. At higher currents it is not possible anymore to distinguish the signal from the background noise. Compared to position 1 the sign of the slope of the signal from position 2 is reversed. The maxima can be found at a current of +30 mA and decreases with the current value. Also, compared to position 1, the value of the maximum signal strength is higher and the signal does not reach the noise level.

A complete different course of the signal can be found in the data obtained from position 3-6 (see Fig. 6.6). Position 3 shows a maximum at a current of $I = -22$ mA. Starting from this point the signal strength decreases till a minimum at a current of $I = +6$ mA. At higher current values the signal starts to increase again, ending in a local maximum at $I = +30$ mA.

At position 4 we observe a maximum at a current of $I = 0$ mA. Changing the current in positive or negative direction leads to a reduction of the signal. It is striking that the signal course isn't as smooth as the measure-

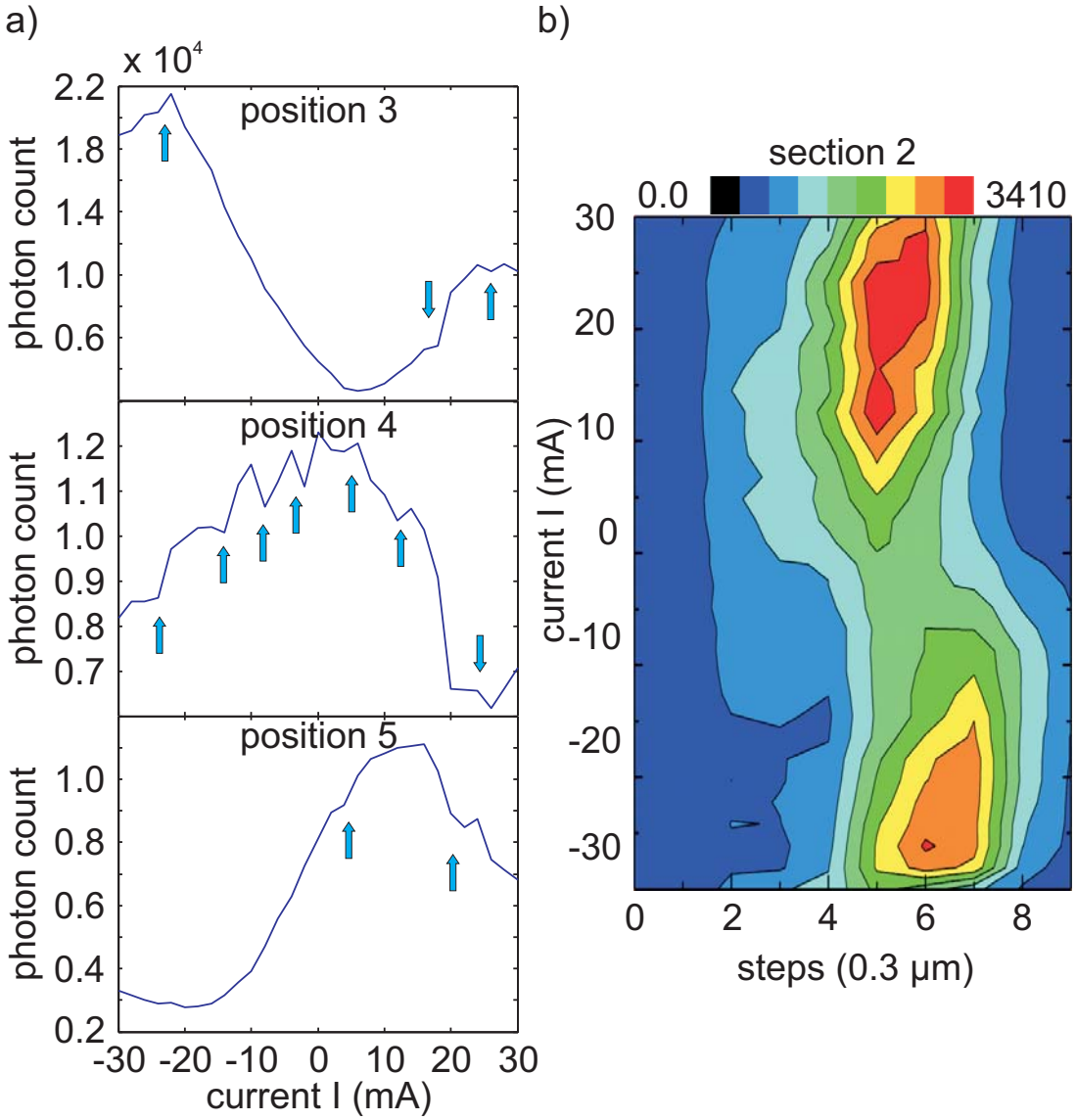

Figure 6.6.: Signal strength at position 3, 4, 5 a) and color-coded at section 2 b) depending on a current at an external field of $\mu_0 H = 72$ mT, at a frequency of 9.5 GHz. Blue arrows indicate minor signal changes within the main oscillation.

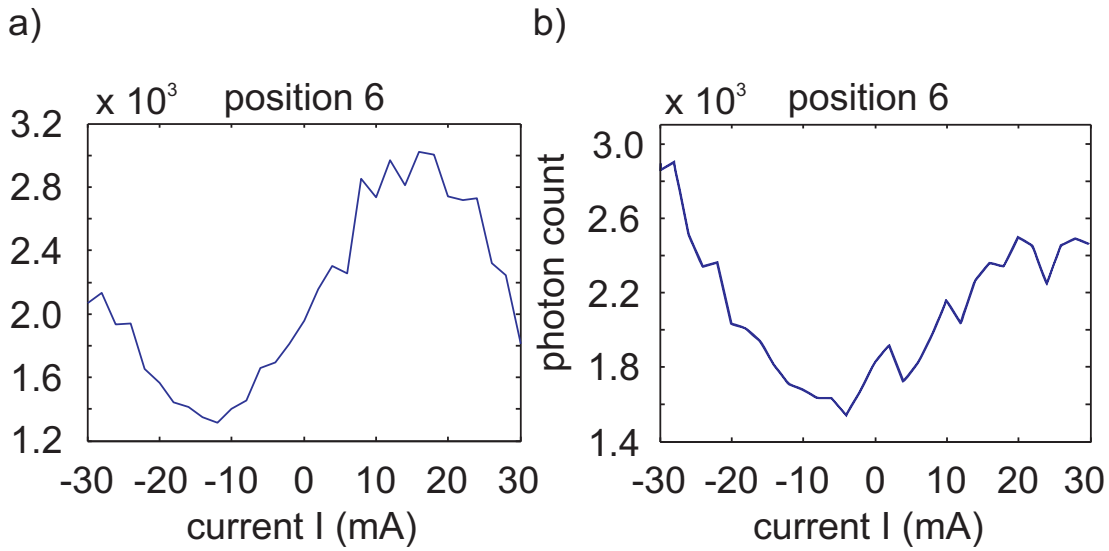

Figure 6.7.: Signal strength at position 6 with a changing current in both a) (path 1 and 2) or only one b) (path 1) path of the Y-structure, at an external field of $\mu_0 H = 72$ mT, at a frequency of 9.5 GHz.

ments on the other positions.

We also took data at position number 5. The data shows a maximum of the signal strength at a current of $I = +12$ mA. Going to smaller current values the signal shows a minimum at $I = -18$ mA. A further decrement of the current value again leads to an increment of the signal.

A strong dependence of the signal strength and the used current is also observed in the data taken at section 2 (see Fig. 6.6 b)). At each data point 490 TFPI sweeps have been performed. In the resulting signal map we observe two maxima near a current of $I = \pm 30$ mA. The minimal signal is found for a current, around $I = 0$ mA. The exact associated current to the minimum and maxima is depending on the location of the measurement. While in general the strongest signal can be found around the center of the section, we also see that the signal distribution over the different spatial locations is changing with the current.

Two further measurements are displayed in Fig. 6.7. Both have been performed on position 6 which is partly overlapping with section 2. The data of the first current sweep (see Fig. 6.7 a)) shows the same behavior as observed in section 2. Two maxima of different heights at $I = -30$ mA and $I = +16$ mA are separated by a minimum. For a current value above

$I = +16$ mA the signal strength drops again. The second measurement on position 6 was performed with a different current setup compared to the other experiments. During the sweep, the current in path 2 (contacts 2,4) was constant at $I = 0$ mA and only the current in path 1 got changed. The result is displayed in Fig. 6.7 b). It shows a minimum around $I = -4$ mA. Starting from there the signal strength increases with a current change in positive of negative direction till the maxima current values $I = \pm 30$ mA.

6.3. Interpretation

The measured signals are the result of two sets of SWs, which have been combined in the Y-shaped wave guide structure. An essential part of the experiment is the generation of two coherent SWs. This was achieved via an rf excitation field irradiated by a CPW across the two paths (1 and 2) of the structure. While one can assume that the excitation field distribution across the paths (horizontal direction in the Figures of this chapter) is uniform, this is not the case for the excited SWs in the paths. By examining the measurement in area 1 and 2 on sample BLS 4 (see Fig. 6.2) and section 1 on sample BLS2 (see Fig. 6.5 a)) we observe a strong variation of the signal strength with a maximum of the excited signal near the center of the path. The same profile was observed and explained by Demidov et al.[Dem+08]. The internal field of the sample edges is strongly reduced, due to demagnetizing effects. As a result the field varies over the width of the structure. The external field was chosen so that a maximum excitation is obtained in the center of the paths. Since the internal field on the sides and therefore, the resonance conditions are different, the SW amplitude is reduced. This effect has to be considered in measurements at the edges of the ferromagnetic structure.

In addition to the signal variation in the horizontal direction the data from area 1 on sample BLS4 also shows a strong decrease down to the noise level along the vertical axis. The same was also observed in the other path in area 2 (see Fig. 6.3). We see that the SW signal can be detected again after a certain distance and reaches nearly its former strength, by adding the results of the experiments in area 3 and 4 (see Fig. 6.3). A variation of the signal strength distribution along a SW wave guide was also observed by Demidov et al. [Dem+07] [Dem+09] and Büttner et al. [But+98]. According to these publications the modulation is the

result of the simultaneous excitation of different k-vectors. The interference between these SWs leads to an interference pattern with a spatial period $l = 2\pi/\Delta k$ depending on the discrepancy between the k-vectors [Dem+07]. The distance l between the signal maximum in area 2 and area 3 is about 7 µm which equates a $\Delta k = 0.9 \cdot 10^6$ rad/µm. As mentions above the field was chosen to excite the maximum signal strength. According to the excitation spectrum for the used CPW shown in the work of Yu et. Al [Yu+13] the maximum is obtained at a k-vector of $k = 0.92$ rad/µm. The intensities of additional modes with k-vectors $k = 0.92 \pm 0.9$ rad/µm are significantly smaller compared maximum excitation. Therefore, the interference between those SWs cannot lead to the signal decrease to the noise level (see Eq. 2.76), which was observed between the two spatial signal maxima in area 2 and 3. We also note that, unlike the measurements illustrated in this thesis (area 1 and 2), the signal intensity, of measurements presented in the works of Demidov et al. [Dem+07] [Dem+09] and Büttner et al. [But+98], integrated over the cross section of the SW guide does not decrease to the noise level. While the simultaneous excitation of different k-vectors might occur in the samples measured in this thesis it seems that its influence is small compared to other effects determining the spatial SW intensity distribution.

An explanation for the strong intensity variation along the SW guide in the two paths is the generation of standing SWs. A SW leaving one path can get reflected at the edges of the tapering area of the sample. When a part of the SW gets reflected back into the path, this leads to a standing wave and therefore, to a decrement of the signal in specific areas of the path.

The same effect can also explain the signal distribution in area 4 (see Fig. 6.3). The combination of the two SWs from the two paths and a multitude of reflected SWs create a strong variation of the signal strength due to interference of the waves. Another possible explanation of the signal map would be corresponding defects in the ferromagnetic material. However, SEM pictures (not shown in this thesis) didn't reveal any hints of such imperfections. Additionally similar signal distribution could also be found in the tapering regions of other samples (e.g. BLS2 see Fig. 6.4 b)).

Comparing the signal distribution of the tapering area in sample BLS4 and BLS2 we detected two separated areas with a higher overall signal strength forming channels in both samples. The channels in area 4 of sample BLS4 lead straight down away from the CPW. Sample BLS2 area 1

displays two diagonally channels spreading down and to the left. As already mentioned we attribute the appearance of several local maxima in this region to the interference of different SWs. So it is only natural to assume that the region of low signal strength between the two channels is also a result of interfering SWs. Due to the shift of the ferromagnetic structure relative to the current lines to one side in sample BLS2 (see Sec. 6.1) the structure of the ferromagnetic material on top of the current lines is not symmetric anymore, leading to the asymmetric interference pattern in the sample as seen in Fig. 6.4 b).

Considering the previous results it is justified to assume that the coherence length of the SWs is sufficient so that the interacting SWs in the probed regions have a phase relation.

The assumption of interference as the dominating factor in the spatial SW signal distribution gets supported by the current sweeps on BLS2. In these measurements the currents in the current paths have two effects on the SWs. The first one is the Joule heating of the structure and therefore, a change of M_s [Rou+15] in the affected material. The second is the local change of the magnetic field in the paths. Both effects lead to a change of the resonance and propagation properties of the SWs. In Sec. 6.1 it is already explained how the second effect can be used to change the phase of the SWs in the two paths and influence the interference in the sample. In addition to the phase shift, the change of resonance conditions can also lead to a change of the excited SW amplitude since the excitation frequency is fixed.

For measurements with a current in two paths the absolute current value is the same in both of them and therefore, an identical Joule heating is expected. In this case the heating results in an identical variation of the SW amplitudes and no phase shift between the SWs. The phase shift is acquired by the opposing signs of the currents and the resulting difference in the local fields of the two paths. Nevertheless, it is important to estimate how much the two effects affect the phase of an individual SW in the used structures. Thus current sweeps have been performed at locations within the two paths of the structure. There it is expected that the measurement signal is mainly influenced by respectively only one SW. In both paths a signal (intensity) maximum was observed at a current of -30 mA in the associated path. Figure 6.5 (measurement at position 2) shows a maximum at $I = +30$ mA. However, since the current in path 2 has the opposite sign of the specified current (see Sec. 6.2.2) the maximum was measured at a

current of $I = -30$ mA through the path. The change of the current to $I = +30$ mA leads to a decrease of the signal strength.

The Joule heating is the same for a positive and a negative current. Hence, the influence of the heating leads to a symmetric signal contribution around $I = 0$ mA. The actual measurements shown in Fig. 6.5, do not indicate a symmetric component in the data. Therefore, we assume that the additional field due to the current is the dominating force behind the signal change of the SWs.

Beside the general change of the signal strength, the measurement in section 1 (see Fig. 6.5 a)) displays a shift in the horizontal position of the SW signal maximum during the current sweep. As already explained above, the local internal field changes near the edges [Dem+08]. Since the current changes the internal field, the location of maximal signal excitation shifts with the current.

While the signal in the two paths (position 1, 2 and section 1) is mainly determined by one SW, one expects an influence of both SWs in current sweeps at the other locations (position 3, 4, 5, 6, area 1 and section 2). In this case the phase difference between the two SWs depends on their propagation distance and therefore, on the measurement position. As explained in Sec. 6.1 the phase shift generated due to the current sweep depends on the propagation distance of the SWs through the wave guide region affected by the current. Because of the circuitry the current density is strongly reduced beyond the paths and hence, it is justified to assume that in these regions the influence of the current can be neglected. Therefore, beyond the paths, the total shift of the SW phase during a current sweep is independent of the measurement position.

The relative phase shift due to the magnetic field can be estimated by using Eq. 2.58 (in Damon-Eshbach configuration). When the resonance frequency is given (9.5 GHz) the excitation k-vector linearly depends on the internal magnetic field. With $M_\mathrm{s} = 1440$ kA/m [Sch13], $A = 2.8 \cdot 10^{-11}$ J/m [Bil+06] for CoFeB and a film thickness of 30 nm the k-vector changes with $-4 \cdot 10^4$ (rad/m)·mT^{-1}. The field in each path produced by the current has a extremum of ± 6.7 mT (see Sec. 6.2.2) and influences the SWs over a distance of about $a = 6.8$ µm. As a result the phase of the SWs at a position beholden the paths changes by about 1.2π (see Fig. 6.8) during a current sweep from ∓ 30 mA to ± 30 mA. For current sweeps in both paths the relative phase shift between SWs from the two paths should change by about 2.4π during the sweep.

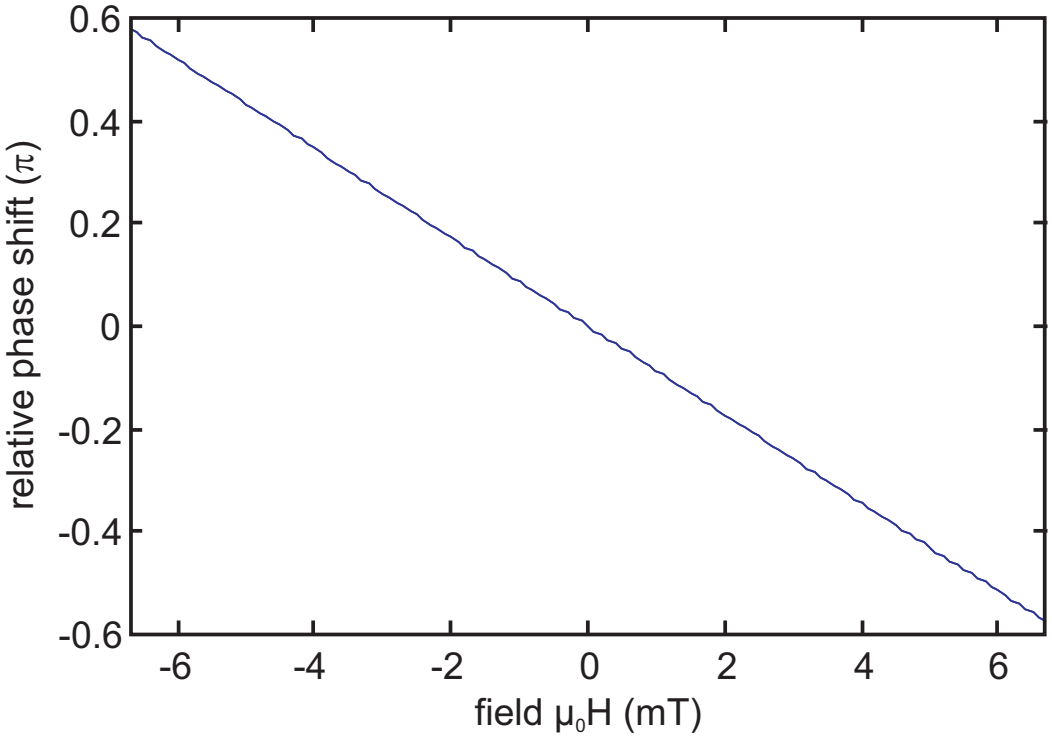

Figure 6.8.: Relative phase shift of SWs after a distance of 6.8 µm depending on the field perpendicular to the SWs (DE configuration) calculated with excited k-vectors depending on the field at a frequency of 9.5 GHz . The k-vector dependency has been calculated with Eq. 2.58 using $M_s = 1440$ kA/m [Sch13], $A = 2.8 \cdot 10^{-11}$ J/m [Bil+06] for CoFeB and a film thickness of 30 nm.

The data of position 4, 5, 6 reflect this behavior. All of them show the expected cosine dependency (see Sec. 2.8) and contain about one period of a cosine wave (see Fig. 6.6 a)) with different starting points, which is in good agreement with the estimation above.

Depending on the horizontal position we observe a clear shift of the maxima and minima positions within the three measurements. A phase shift between two identical sinusoidal SWs with identical amplitudes leads to a cosine change of the amplitude of the resulting interference signal (see Sec. 2.8). Discrepancy to perfect cosine oscillations in our measurements (intensity), seems to be a result of the different amplitudes of the two SWs at the probed location (due to different SW propagation distances) and the distinct amplitude dependency of the applied current. Beside the influence of the two main SWs, coming directly from the two paths, we also expect additional reflected SWs contributing to the interference signal, leading

to additional minor signal changes within the main oscillation (see blue arrows in Fig. 6.6 a)).

Furthermore to the discussed measurements we also performed current sweeps in the part of the structure beyond the tapering in section 2 (see Fig. 6.6 b)) and position 6 (see Fig. 6.7). The data from section 2 at fixed positions and changing current show again similarity with a cosine wave

The first measurement on position 6 (see Fig. 6.7 a)) shows the same behavior as expected from the results in section 2. For the second measurement (see Fig. 6.7 b)) only the current in the left path (path 1) was swept. We still see a variation of the signal similar to the measurement with changing currents in both paths, which is again supporting the assumption of interference as the main source of the observed effects. By comparing the sweeps with two (see Fig. 6.7 a)) and one (see Fig. 6.7 b)) changing currents, the signal shows a similar strength, but a less pronounced variation of the signal with only one current. This is expected since the phase shift within the ± 30 mA for two currents should be doubled compared to only one current.

6.4. Conclusion

By changing the local field of restricted regions with an electrical current we controlled the amplitude of two superimposed SWs. We attribute the signal variation to a current-controlled phase shift between SWs generated in two separated branches of the Y-junction. Measurements in the path regions of the wave guide could show that the phase change due to the electrical current is mainly the result of the magnetic field by the current. Further experiments should aim to increase the possible range of the phase change by either increasing the current density in the current paths or extend the distance in which the SWs are influenced by the magnetic field of the current. Optimizing this structure and the control of a SW amplitude might be used to create SW logic devices.

7. Ferromagnetic Nano Tubes

The ferromagnetic nanotube (Nt) has become an object of great interest for both fundamental research and applications. Theory predicts a suppression of the Walker breakdown, due to its hollow structure, enabling a domain wall speed [LN10] [Yan+11], possibly high enough to generate Cherenkov-type spin wave excitations [Yan+13] [Yan+11]. In the following chapter we present measurements on such a ferromagnetic hollow structure, created by coating a GaAs nanowire wire with a ferromagnetic material. The measurements haven been performed by T. Stückler (TUM) in the course of his Master thesis under the supervision of F. Heimbach (TUM) and close cooperation with D. Rüffer (EPFL).

7.1. Sample Characterization

The experiments described in this chapter were performed on four contacted individual Nts (see Fig. 7.1 a)) whose fabrication is described in Sec. 4.5. Two of them were made of Ni while the other two were made of CoFeB. SEM pictures of a CoFeB tube is shown in Fig. 7.1 b). Compared to Ni tubes (see [Ruf+12]) we notice a significant difference in the roughness of the ferromagnetic materials. The high roughness of the Ni tube is attributed to tension effects occuring in the reduction process during and after the ALD growth (see Sec. 4.5.1).

The core element of each tube is a GaAs nanowire. It can be easily identified in the center of a dark field TEM image (see Fig. 7.1 c)) provided by Kovács et al. from the Ernst Ruska-Centre for Microscopy and Spectroscopy with Electrons and Peter Grünberg Institute, Forschungszentrum Jülich. The image was acquired from a slice of a CoFeB nanotube. The ferromagnetic material in the picture is represented by the light color around the GaAs core. Between the CoFeB and the core we notice a thin rim of dark color around the GaAs. This seems to be an indication of an oxide layer.

Due to the structure and fabrication of the GaAs wire (see [Rüf14]) the tube has a hexagonal cross-section and exhibits a spherical element (nano-

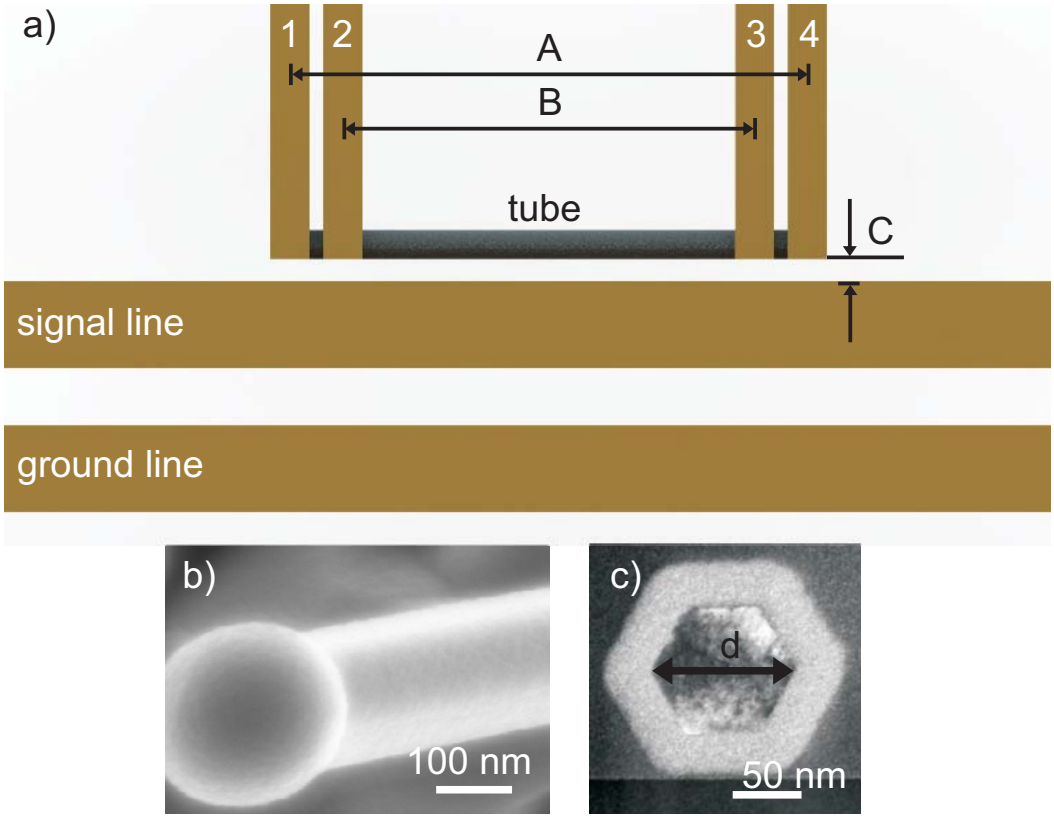

Figure 7.1.: a) Sketch of the installation of the Nt samples. A, B, C represent the relevant distances in the structure. b) SEM picture of CoFeB tube. A dark field TEM image of the cross section of a CoFeB tube with a GaAs core is displayed in c). The transmission electron microscopy (TEM) image c) was provided by Kovács et al. [MDB], Ernst Ruska-Centre for Microscopy and Spectroscopy with Electrons and Peter Grünberg Institute, Forschungszentrum Jülich.

droplet) on one end of the wire (see Fig. 7.1). For the CoFeB nanotubes the dimensions of the GaAs wire defined the inner radius of the tube. In case of the Ni tubes we used an ALD process to increase the inner radius by coating the GaAs wire with an Al_2O_3 layer before the actual Ni coating.

For the measurements two sets of contacts have been prepared on both ends of each wire (1 and 4 for applying a current through the tube; 2 and 3 for the voltage measurement along the tube (see Fig. 7.1)). The separation between them depended on the length of the wires. The dimensions, material and lengths (see Fig. 7.1 a)) of the investigated wires are listed in Table 7.1. With this information it is possible to estimate the type of DW forming in the tubes. The saturation magnetization was determined

Sample	N1-40	N2-40	C-20	C-30
Material	Ni	Ni	CoFeB	CoFeB
Thickness in nm	40	40	20	30
Inner diameter d in nm	300	310	140	130
Total length in µm	20.72	16.53	11.45	11.95
A in µm	18.72	14.53	9.45	9.95
B in µm	15.72	11.53	6.45	6.95

Table 7.1.: Dimensions of the investigated Nts. For lengths A and B see Fig. 7.1.

with cantilever magnetometry on single tubes by D. P. Weber et al., to be $M_\mathrm{s} = 375 \pm 70$ kA/m for Ni [Web+12] and $M_\mathrm{s} = 870 \pm 30$ kA/m [Web14] for CoFeB. The saturation magnetization for Ni was in good agreement with published values for bulk Ni [KM05]. However, the value for CoFeB was significantly smaller compared to values reported for thin films [Sch13]. If the discrepancy resulted from the rotation during the fabrication is still under investigation. For the exchange stiffness we assumed $A = 7.2 \cdot 10^{-12}$ J/m [Boa05] for Ni and $A = 2.8 \cdot 10^{-11}$ J/m [Bil+06] for CoFeB. Utilizing Eq. 2.32 we estimated that all four Nts should form vortex DWs. To excite the magnetic moments within the tube we implemented an asymmetric CPW (see Sec. 3.3) with the Nt placed close to the signal line. The distance C between the tube and the signal line of the asymmetric CPW was about 350-400 nm for all tubes.

An important parameter for the measurements on the tubes is the angle between the external magnetic field and the long axis of the tubes which also represents the direction of the current density **j**. Since the samples were placed within the setup by hand, we performed measurements to confirm the angle orientation of the Nts relative to the 0° axis of the external field. Therefor, the resistance was measured (see Sec. 3.2) during the rotation of an external field with the absolute field value of 100 mT. This kind of measurement was only performed on CoFeB tubes. Data are displayed in Fig. 7.2. Despite the shape anisotropy, the applied external field led to a partial rotation of the magnetization. Therefore, the AMR effect (see Sec. 2.9) led to a change of the resistance depending on the orientation of the magnetization to the direction of the current. The extrema of the plots are used to determine the field angles along and perpendicular to the tube axis.

For the following measurements on the CoFeB tubes (C-20 and C-30)

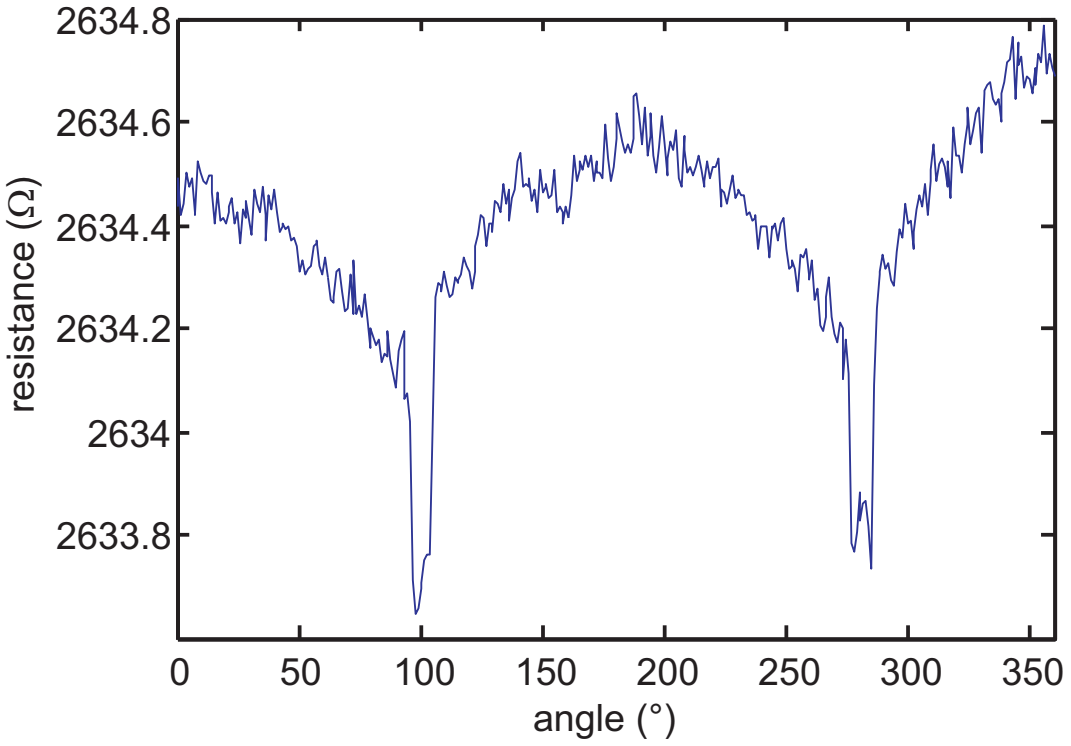

Figure 7.2.: Resistance measurement on a CoFeB Nt depending on the angle of the external magnetic field with an absolute field value of 100 mT.

the information of the angle position was used to set the angle along the tube to 0°. Comparing the angle position acquired by visual control and the angle gained from the angle transport measurement on several CoFeB tubes showed a discrepancy of about 3°. We assumed that the misalignment between the 0° direction of the magnetic field and the axis of the Ni-tube was similar.

7.2. Transport Measurement

Figure 7.3 shows data from a CoFeB Nt with the external field applied in the direction of the tube axis and changed in steps of 0.5 mT. Each resistance value was generated by averaging over three data points. The entire experiment was performed at room temperature. Starting at a field value of $\mu_0 H = -100$ mT the up sweep provides a constant resistance $R_{\max} = 5621.7\ \Omega$ with increasing field. Beginning at a value of $\mu_0 H_s = -13.5$ mT the resistance drops till a field $\mu_0 H_{\min} = 6.5$ mT to the re-

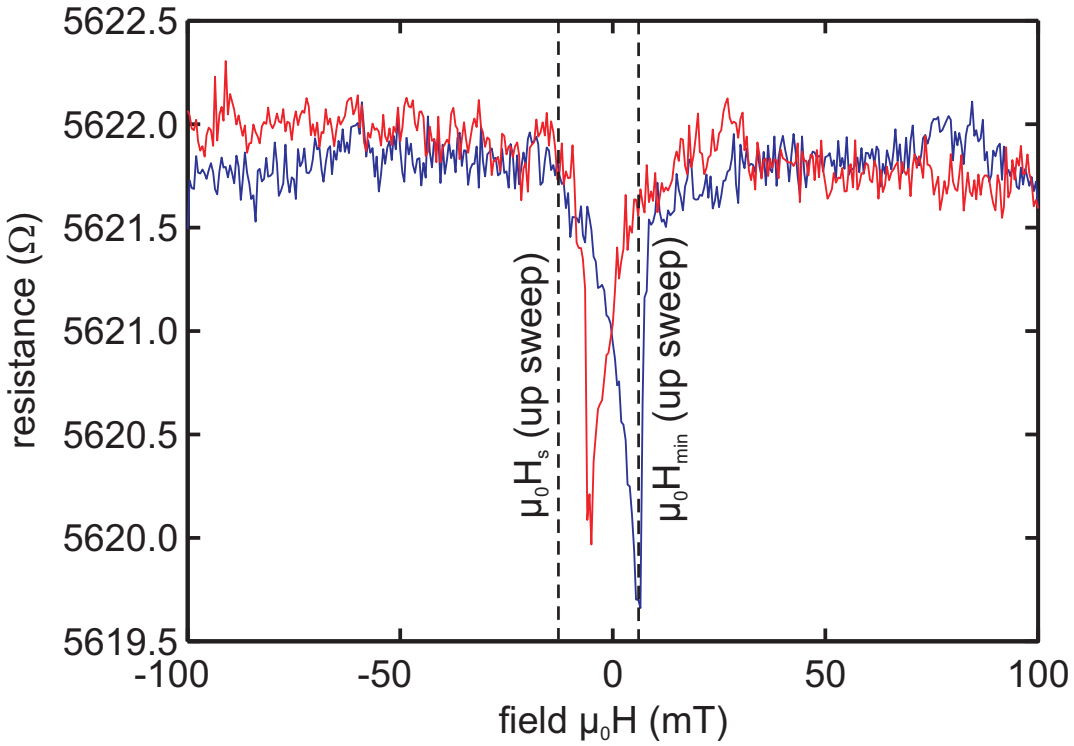

Figure 7.3.: Field sweep measurement down (red) and up (blue) on the CoFeB Nt C-20 with an applied external magnetic field along the tube axis.The current amounted to 1 μA.

sistance $R_{\min}$. From there the resistance jumps back, close to its original value $R_{\max}$, within a few field steps. With a further increment of the field the resistance reaches its maximum $R_{\max}$ at around $\mu_0 H = 27.5$ mT and stays there till the final field value of $\mu_0 H = 100$ mT. The down sweep displays a very similar trend. Compared to the up sweep it is mirrored on the $\mu_0 H = 0$ mT axis. The characteristic values extracted from data of the four Nts are summarized in Table 7.2.

7.3. Electrically detected ferromagnetic resonance

A measurement at a set excitation frequency of 4.3 GHz was performed in the FMR Log-In setup configuration described in 3.3.1 on tube N1-40. During the measurement the external field was applied along the tube axis and swept from -100 mT to 100 mT. The experiment was repeated several times for different DC-currents through the tube. The results are displayed in Fig. 7.4. The general trends of the different sweeps show the same be-

	up sweep			
Sample	$R_{\max}$	$R_{\min}$	$\mu_0 H_{\mathrm{s}}$	$\mu_0 H_{\min}$
N1-40	181.88 Ω	181.21 Ω	-21 mT	10 mT
N2-40	94.71 Ω	94.19 Ω	-20 mT	8 mT
C-20	5621.7 Ω	5619.6 Ω	-13.5 mT	6.5 mT
C-30	2531.8 Ω	2531.4 Ω	-3 mT	11.5 mT
	down sweep			
Sample	$R_{\max}$	$R_{\min}$	$\mu_0 H_{\mathrm{s}}$	$\mu_0 H_{\min}$
N1-40	181.73 Ω	181.08 Ω	20 mT	-11.5 mT
N2-40	94.69 Ω	94.15 Ω	20 mT	-8 mT
C-20	5621.7 Ω	5619.9 Ω	14 mT	-5 mT
C-30	2531.7 Ω	2531.4 Ω	3.5 mT	-8.5 mT

Table 7.2.: Characteristic values of the field sweep transport measurements on Nts.

havior. Starting at $\mu_0 H = -100$ mT the detected voltage increased with the external applied field to a local maximum at around $\mu_0 H = -40$ mT. A further field increment led to a decrease of the voltage. This behavior continued till a field value of approximately $\mu_0 H = 40$ mT where the measurement displays a local minimum. From there the voltage values increased again. On top of the general trend of the voltage we encounter several dips and peaks. The position, shape and amplitude of these features were similar for different current values through the tube. The only exception is in a field range from about $\mu_0 H = 0$ mT to $\mu_0 H = 20$ mT where the trend varied in every measurement. Further comparison shows an offset voltage separating the different field sweeps. The offset voltage depended on the current through the Nt with about $0.23 \cdot 10^{-6}$ V per -0.5 µA.

While this measurement has been conducted with the Lock-In methode, the following EDFMR measurements have been realized with the FMR Delta-Mode (see Sec. 3.3.1) since it provided a better signal to noise ratio. The field was swept along the tube axis from -100 mT to 100 mT in 0.5 mT steps at a constant excitation frequency with an applied current of $I = 0$. From the data of such a measurement (also entitled trace) we subtracted an individual offset $(U_{\max} + U_{\min})/2$ with $U_{\max}$ ($U_{\min}$) as the maximal (minimal) voltage value of the original trace. After removing the offset,

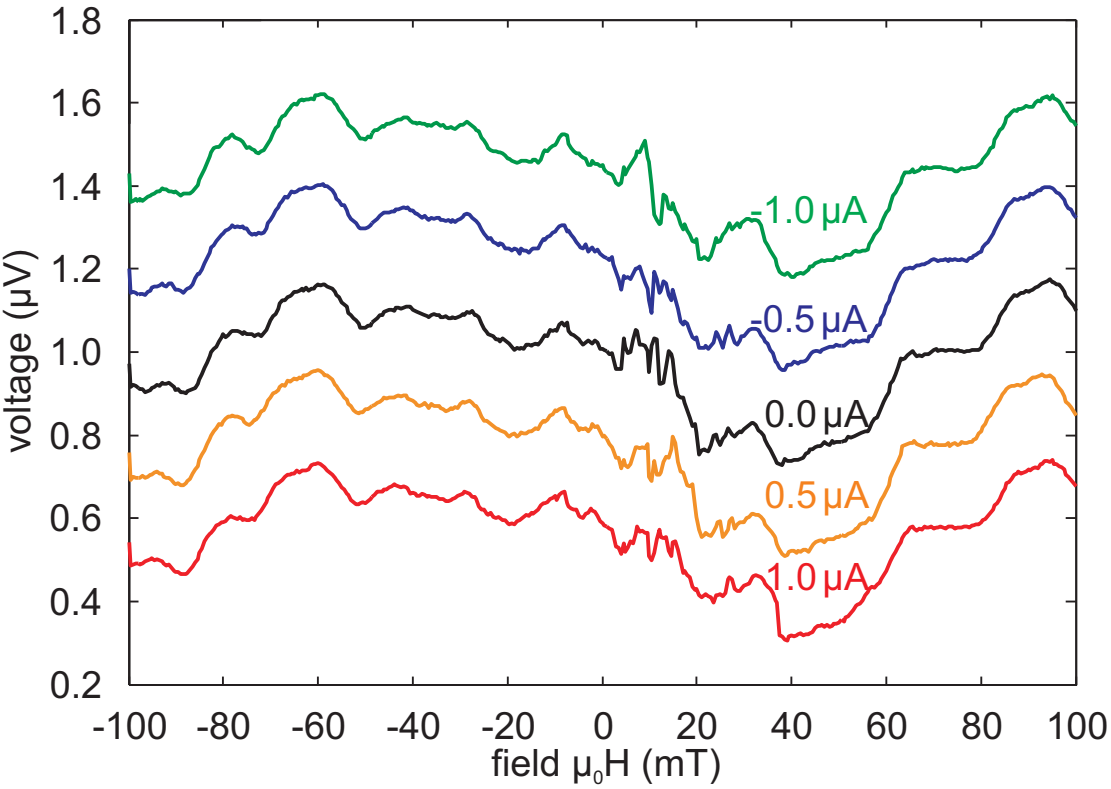

Figure 7.4.: Voltages detected for an up sweep at different current values through the tube N1-40. The Nt was irradiated at a frequency of 4.3 GHz with the external field aligned along the tube axis.

the trace got normalized by dividing the data with the half peak-to-peak amplitude $(U_{\max} - U_{\min})/2$. By changing the excitation frequency value in 100 MHz steps and repeating the measurement we acquire 2D EDFMR plots. The plots for the four tubes are displayed in Fig. 7.5. The signal strength is color coded and due to normalization always between -1 and 1.

Attributing the measured signal to spin rectification (see Sec. 2.10 and 7.4), the voltage is a measure of a variation of the phase angle Φ between the electrical rf field **e** and the magnetic rf field **h** in the magnetic material. Φ is expected to vary when sweeping through a ferromagnetic resonance [Har+11] and therefore, we can identify ferromagnetic resonance modes in the 2D plots.

For N2-40 one of such modes starts at a field value of -100 mT and a frequency of 3.9 GHz. From -100 mT to -24 mT the frequency of the mode decreases to 100 MHz, the minimal value of the measurement. At frequen-

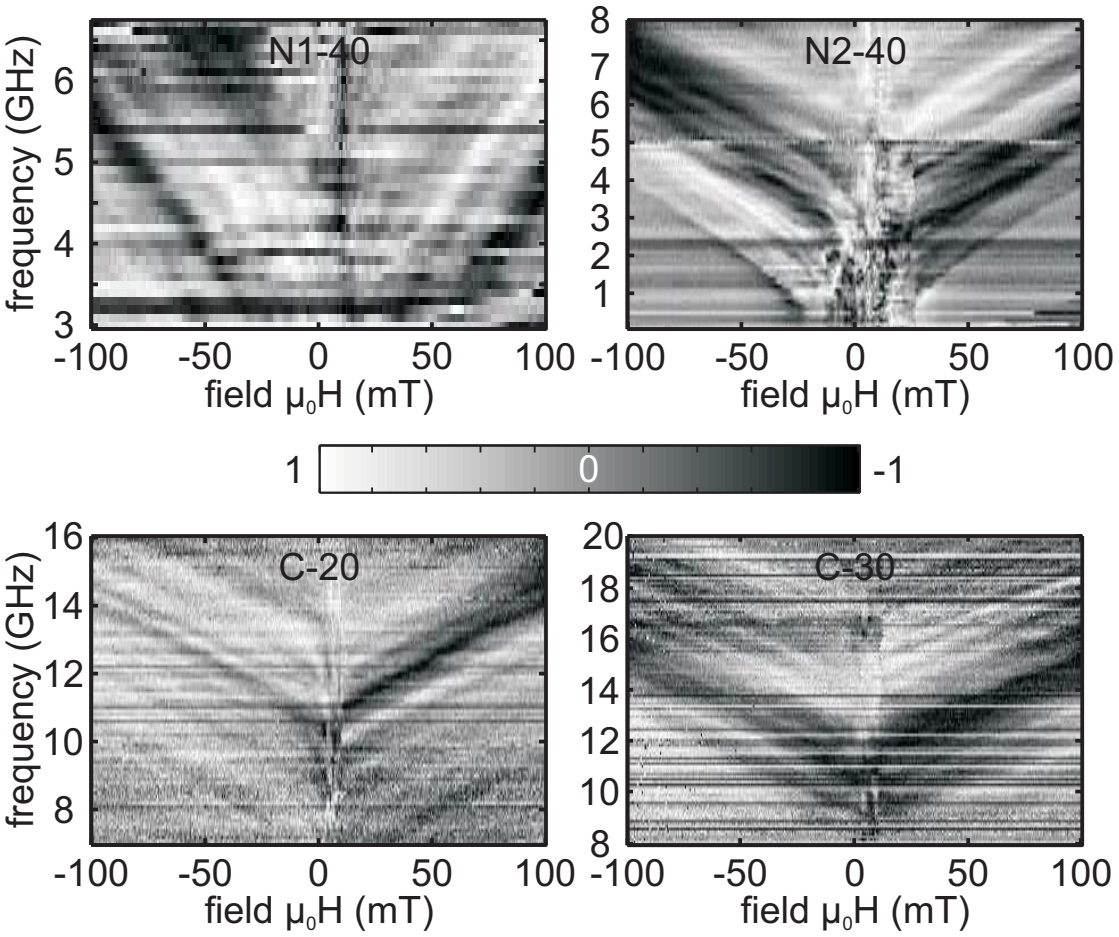

Figure 7.5.: 2D plots of EDFMR measurements of different tubes. The individual off set at constant frequencies was removed and the change of the remaining signal normalized and color coded to values between 1 and -1.

cies above this mode we also observe ferromagnetic resonance excitation. We detect several modes with slopes slightly changing with higher excitation frequencies. The mode which starts at 8 GHz for -100 mT is still strong. We see weak modes existing at even higher frequencies. Close to a field value of 0 mT all modes end in a field range with a strong signal variation which seems to be random, like a noise signal. At field values exceeding this field range at positive field values the modes are reappearing again. Similar to negative fields the lowest mode raises with the absolute field value till a frequency of 3.9 GHz at 100 mT. Comparing the modes in the negative and the positive field regimes we see that in many cases the signs of the signal, representing the associated modes, are reversed.

The experiments on the other tubes show similar results. In case of the CoFeB tubes the signal strength is weaker compared to the Ni tubes and the observed resonance modes start a higher frequency. The lowest mode at -100 mT was resolved at 10.2 GHz (C-20) and 13.3 GHz (C-30). Finally we note that the field regions with random variation of the signal are smaller in the 2D plots of the CoFeB tubes compared to the Ni samples.

7.4. Interpretation

The understanding of the magnetization reversal within NTs is an essential part necessary to describe the magnetic behavior of the Nts. Due to the AMR effect (see Sec. 2.9) one method to achieve this goal is to capitalize on the change of the electrical tube resistance during the reversals. For the following discussion we assume a current direction along the tube axis. Starting at an absolute field value of 100 mT the resistance remains constant (within the limits of the instrument noise level) when the external field was decreased, which indicates the presence of a stable magnetic state. According to calculations of Landeros et al. [Lan+09] the equilibrium state of tubes presented in this thesis is a mixed state. In this case the middle part of the tube shows a uniform magnetization along the tube axis. To decrease the stray fields the magnetization on the ends of the tube forms a vortex state. Measurements on Nts performed by D. Rüffer [Rüf14] support this assumption. However, the resistance in the AMR measurement and therefore, the average direction of the investigated magnetization is constant over a relatively large part of the applied field range. Hence we assume a uniform magnetization along the external magnetic field in the examined tube section between the electrical contacts. As expect from the theory of AMR we found the highest resistance in this configuration (magnetization parallel/antiparallel to the current direction). Beginning at the field $\mu_0 H_\mathrm{s}$ before reaching a field of zero the resistance along the tube starts to decrease. While the uniform magnetization along the tube seems to be the preferred saturated state (with a high enough external field along the magnetization direction), the drop of the resistance indicates a deviation from this configuration. In the field range of $\mu_0 H_\mathrm{s} \leq \mu_0 H \leq 0$, the magnetization direction gets tilted away from the tube axis, because of an anisotropy. Further decrease of the external field shows initiation of the actual reversal process in the Nts. According to a theoretical model pre-

sented by Landeros at al. [Lan+07] the reversal occurs via the nucleation of a DW which moves through the tube from one end to the other, switching the magnetization direction during this process. However, observation of such reversal process is difficult, due to the speed of the DW, and the relative long intervals during and between the measurement steps, since the resistance along the tubes axis should be the same before and after the reversal. Nevertheless we see a further decrement of the resistance along the tube axis. This can be referred to two possible effects.

A feasible explanation is the nucleation of DWs. Because of the surface roughness and defects in the tube the DWs cannot move freely and are pinned in the tube. This leads to a magnetic state in which different sections in the tube exhibit opposing magnetization directions, separated by pinned DWs. The portion of the tube occupied by the DWs can be approximated by considering the change of the resistance ΔR. The maximal resistance change from the parallel to the perpendicular magnetization configuration relative to the current direction at room temperature on tubes produced with the same method as the tubes examined in this work has been reported by D. Rüffer et al. [Rüf+14]. The reported values are $\Delta R \approx 1.4\%$ for Ni tubes, $\Delta R \approx 0.11\%$ for CoFeB tubes with a thickness of 20 nm and $\Delta R \approx 0.08\%$ for a 30 nm thick CoFeB shell. The percental change denoted in the paper was determined with respect to the minimal resistance. Since this value is unknown for the tubes used in this thesis we converted the values with respect to $R_{\max}$according

$$\Delta R = \frac{R_{\max} - R_{\min}}{R_{\max}}, \tag{7.1}$$

and the relative resistivity to be

$$\frac{\rho(\xi)}{\rho_{\max}} = \frac{\rho_{\max} - (\rho_{\max} - \rho_{\min}) \sin^2 \xi}{\rho_{\max}} = 1 - \Delta R \sin^2 \xi. \tag{7.2}$$

However, because the maximal and the minimal resistance are very close to each other, the changes of the values of resistance due to the conversion mentioned above are in the range of the assumed error and therefore, remain unchanged.

In the measurement on sample N1-40 the resistance changed from $R_{\max}$ to $R_{\min}$ by about 0.04%. Assuming we have a uniform rotation of the mag-

netization within the DWs from $\xi = 0°$ to $180°$ the relative resistivity in a DW segment of the tube is decreased by $0.5\Delta R$ compared to the maximum value. To obtain a change of 0.04% about 53% of the tubes have to be occupied by a DW, if we assume that the only magnetic moments tilted away from the tube axis can be found in the DWs. It is important to note that this is a rough approximation and its main purpose is to illustrate the influence of DWs and the required combined size of the DW areas. The percental occupation of the tube by DWs for the down sweep and the other tubes is summarized in Table 7.3. However, the values needed to explain

	forth sweep			
	N1-40	**N2-40**	**C-20**	**C-30**
Max. share of DWs	53%	78%	68%	39%
Max. angle rotation	31°	39°	36°	26°
	back sweep			
	N1-40	**N2-40**	**C-20**	**C-30**
Max. share of DWs	51%	81%	58%	30%
Max. angle rotation	30°	40°	33°	23°

Table 7.3.: Values to explain the resistance change in the AMR measurements, with only an occupation of the tube with DWs, or a rotation of the magnetization angle relative to the applied current direction.

the resistance change in the AMR measurements with only pined DWs within the tubes are very large. In most cases more than half of the entire tube had to be occupied by DWs, which is unlikely. Also we see a sudden jump in the resistance at higher fields. This would imply that nearly all DWs would be unpinned at the same field value, traveling through the tube and vanish. While it is possible, it is much more likely that the resistance would change back to its maximum value with a slope similar found in the decrease to its minimum.

Another explanation for the resistance drop in the AMR experiment is that the magnetization gets tilted away from the tube axis. Since we already detected a rotation of the magnetization away from the tube axis at $\mu_0 H = 0$ we can expect a further rotation with an inversion of the applied field direction. Assuming a uniform rotation we can calculate the necessary angle ξ with Eq. 7.2. The values for the different sweeps and

tubes can be found in Table 7.3. When the external magnetic field is high enough ($\mu_0 H_{\min} < \mu_0 H$) a DW forms, travels through the tube and reverses the magnetization. This gets supported by the measured data that shows the already mentioned jump at $\mu_0 H_{\min}$ back, close to the maximum resistance. The anisotropy responsible for the rotation of the magnetization away from the tube axis at small field also prevents an orientation of the magnetization parallel to the current directly after the reversal. With an increment of the absolute field value the magnetization gets tilted towards the tube axis until we reach the maximum resistance.

After taking into account the values and the trend of the measurements we conclude that the uniform rotation of the magnetization is the prime reason for the AMR resistance change. An additional pinning of DWs within the tubes is possible but is not clearly observed in the experimental data.

The same development of the magnetization occurs during the field sweeps in the EDFMR measurements. For the analysis of the data it is important to know the origin of the EDFMR signals. For this purpose we performed field sweeps on N1-40 at a fixed excitation frequency and different bias currents through the tube (see Fig. 7.4). From the comparison with 2D EDFMR plots (see Fig.7.5) we attribute the dips and peaks on top of the general trend to resonance modes in the ferromagnetic material. The striking point in Fig. 7.4 is that the current has no influence on the position of the modes or signal strength. This implies that the observed signal is not the result of a changing resistance during the resonance condition, also including the influence of the AMR-effect due to the changed excitation angle during the resonance. Hence, the detected signals have to be the result of a direct voltage generation.

The only field region where we observe a variation in the signals is from -10 mT to 30 mT. By comparing this region with the transport measurements in 7.2 one can infer that this is within the reversal region of the tube. While on average the reversal passes through the same macroscopic magnetic states, the microscopic magnetic stats in the tube vary every time the magnetization of the tube gets switched leading to a different EDFMR signal. Beyond this field regime the tube exhibits a uniform magnetization, which in turn leads to a high reproducibility of the measured signal.

Another feature that we would like to point out is the offset voltage observed in the data. Due to modulation of the rf signal and a Lock-In technique DC-signals should be suppressed. And indeed by considering

the resistance values in Table 7.2 and the currents I through the sample we note that the voltage difference between the different measurement traces in Fig. 7.4 is nearly three orders of magnitude smaller than expected. This suppression is also the reason why the voltage change for $I \neq 0$, during the reversal of the magnetization due to the AMR-effect is not observed. Nevertheless the EDFMR signal for $I = 0$ and, considering the equal voltage shifts between the traces because of the different current values, also the other traces are shifted by an offset voltage. Measurements on different tubes with an applied current of 0 µA (not displayed in this thesis) show that the offset voltage is depending on the excitation frequency. The origin of this voltage is still under investigation.

We have removed the offset from the presented 2D EDFMR plots as it has no influence on the position or shape of the signal associated with ferromagnetic resonance modes (see Fig. 7.5). First we determined the minimal and maximal value and then subtracted the offset $(U_{\max} + U_{\min})/2$ from each data point for each trace. Subsequently, the data for each trace are normalized, to acquire a uniform contrast. We now concentrate on the modes in the uniform magnetization states as the exact magnetic states during the reversal are unknown. This EDFMR dataset provides us with the final hint about the source of the voltage depending on the ferromagnetic modes. Without the offset we see that the voltage signal of several modes changes with the reversal of the external magnetic field. This feature suggests spin rectification to be the origin of the photovoltage.

In the 2D plots acquired from Ni and CoFeB tubes (see Fig. 7.5) we observe a multitude of resonance modes. Comparing the linewidth of the modes in the tubes with modes in plane films (see e.g. [Hub13] for Ni and [Sch13] for CoFeB) we see that the line width in tubes is significant smaller, which implies that the tubes might act as a cavity for the SWs. Therefore, we assume that many of the observed modes are associated with azimuthal SWs. To form a standing SW around the circumference, the SW has to fulfill the condition

$$n\lambda = \pi d_t \Leftrightarrow k = \frac{2n}{d_t}, n \in \mathbb{N}, \tag{7.3}$$

with wavelength λ, the diameter of the tube d_t and an integer n. To fit the modes we use the dispersion relation equation Eq. 2.66 for a thin film. To determine the k-vectors Eq. 7.3 was utilized with d_t of the nonmagnetic

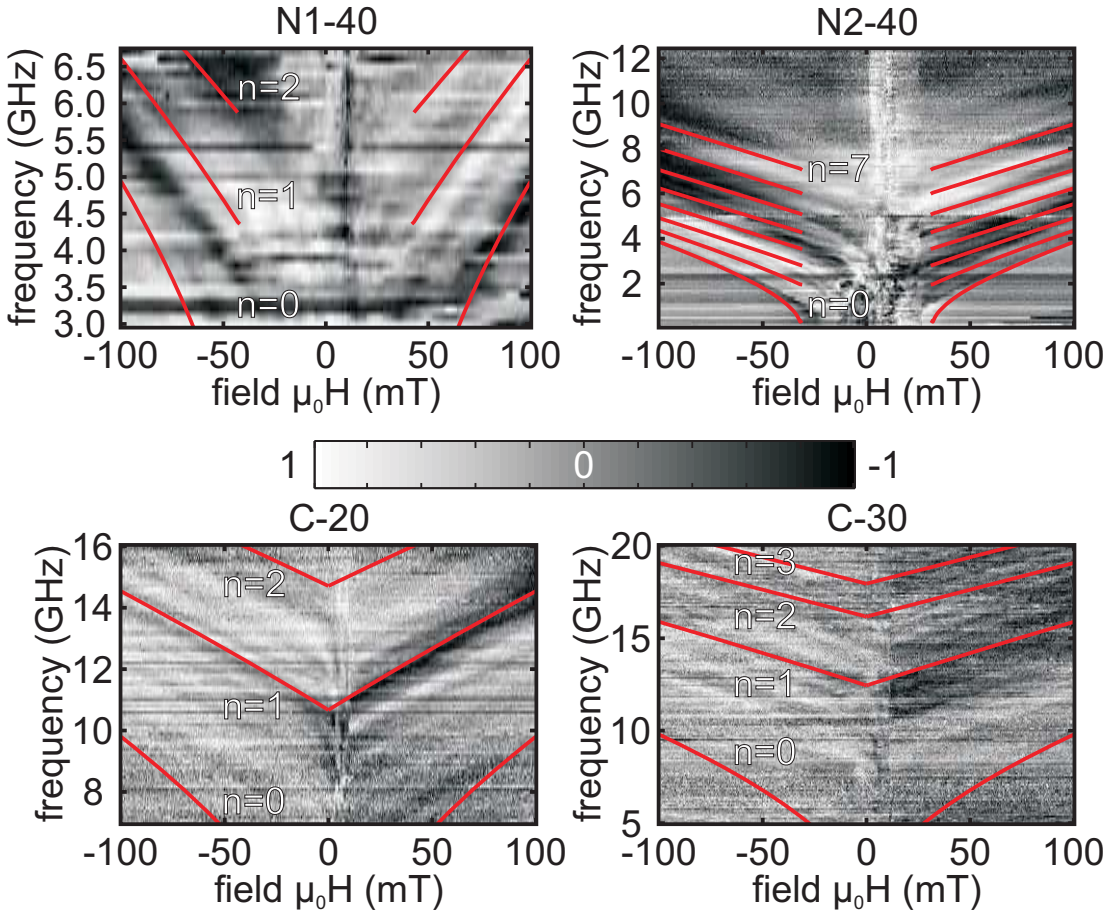

Figure 7.6.: Colorcoded EDFMR 2D plots with fitting curves (red). The used fitting parameters are $M_s = 375$ kA/m, $K = 8000$ J/m^3 for N1-40, $M_s = 157$ kA/m, $K = 2500$ J/m^3 for N2-40, $M_s = 870$ kA/m, $K = 0$ J/m^3 for C-20 and C30.

core diameter d plus the thickness of the ferromagnetic tube (see Table 7.1), ignoring the hexagonal shape. The fits are displayed in Fig. 7.6. In case of the CoFeB tubes we used the parameters as described in Sec. 7.1 neglecting any magnetic anisotropy. Eigenfrequencies and their field dependencies are in very good agreement with the detected modes. For a magnetization along the tube axis and a k-vector around the tube the lowest resonance frequency is acquired for the uniform excitation ($n = 0$).

However, the 2D plot of the Ni tubes displays modes below the mode calculated with n$= 0$. To model the low-frequency mode we additionally allow for an anisotropy. This is justified since we already assumed its influence in the AMR measurements. The anisotropy leads to a rotation

of the magnetization away from the tube axis at small field values, beside the general change of the resonance frequency. Therefore, we limit the calculation to large fields where we expect the magnetization to be along the tube axis. By adding an anisotropy of $K = 8000$ J/m^3 perpendicular to the applied field direction we can fit the lowest mode on sample N1-40. To fit the data from tube N2-40 additional adjustments were necessary. With the additional anisotropy the resonance frequency of the uniform mode could be reduced, however the field dependence of the mode didn't fit. To model this, the effective saturation magnetization was reduced. The actual fit on N2-40 used an anisotropy constant $K = 2500$ J/m^3 and an effective saturation magnetization of 157 kA/m. The value of the effective magnetization is significantly lower than the value measured by D. Weber et al. in [Web+12]. The origin of this discrepancy has yet to be resolved. The anisotropy needed to fit the Ni tubes is very likely the result of stress within the ferromagnetic material. The values for the anisotropy constants obtained from the fits are within the possible range given by J. M. D. Coey for stress as the source of the anisotropy [Coe10]. We expect stress in the Ni tubes [Hub13] due to the reduction of the Ni (see Sec. 4.5.1).

7.5. Conclusion

In this chapter the properties and magnetic states of ferromagnetic tubes were investigated. We were able to get an insight in to the magnetization configuration at high fields and during the magnetization reversal, utilizing different measurement techniques. The findings of the experiments suggested the spin rectification as the source of the EDFMR signal and excluded the influence of a change of the resistivity during resonance conditions. The rectification signal was used to detect a multitude of SW modes. The assumption of standing azimuthal SWs with and without an anisotropy in the tube enabled us to fit a share of the modes. Further measurements should aim at increasing the signal strength in the EDFMR experiments to get a better contrast between the detected modes and limit the experiments to smaller sections within the tube to decrease possible effects due to parameter variations along the tube, and to determine the influence of the finite tube length at the ends of the tubes.

8. Summary and Outlook

In this thesis we have studied the magnetic behavior and SW phenomena in three different types of structures. Honeycomb ASI, Y-shaped interferometer structures and ferromagnetic nanotubes have been produced utilizing different preparation techniques and investigated by various measurement methods.

The ASI structures were produced using EBL. A key element of the fabrication is a double layer resist and a general optimization of the lift-off process including all relevant parameters. We were able to create honeycomb ASI networks made of Py and CoFeB, obeying the ice rule, and to excite SWs in the structure. Micromagnetic simulations showed that depending on the frequency and external magnetic field SWs are excited in different components of the ASI structure enabling us observe the magnetization behavior in these parts. We found a switching of different kinds of links in field range depending of the investigated sample. In contrary to a theoretic dumbbell model based on micromagnetic simulations (see Sec. 2.11.2 and [Mel+10]) we observed that the switching does not only depend on the dimensions of the ASI network, but is very likely also depending on the roughness of the sample. In future experiments it might be reasonable to examine the exact correlation of switching depending on the roughness and the shape of the vertices in the network. According to the switching behavior we were able to assign the SW modes to the corresponding parts of the ASI. As a key feature we evidenced that the resonance frequency in one type of network component does not only depend on its own magnetic state, but also in the magnetization of the adjoined segments. Therefore it is not sufficient to consider three connected links (of different types) as a unit cell to describe the ASI behavior. A unit cell should at least include one link with all four adjoining links. Finally we used a focused laser beam to locally heat the ferromagnetic material decreasing the field strength required to switch the magnetization in the links. This enabled us to switch the magnetization of restricted area of the ASI system without altering the sample (e.g. by preparing reversal pads). This technique might be used to create specific magnetization configuration within the network.

Utilizing the BLS technique on a microscopic Y-shaped magnonic waveguide we were able to investigate the special SW power distribution within the ferromagnetic structure. We observed that the distribution depends on interference between the SWs. Using EBL and an alignment system we created a multi-stack system enabling us to change the local field of specific parts of the SW guide using an electrical current. Utilizing the local field variation we were able to change the phase difference between two coherent SWs and control the strength of the resulting interference signal. A further optimized structure could be used as a "SW intensity regulator", controlling the SW strength with an electrical current without influencing the SW source. Also the insight gained from the structure optimization could be utilized in the realization of spin logic devices based on SW interference. E. g. by setting the phase shift to π the Y-structure can work as a XOR element.

As a third structure we produced ferromagnetic nanotubes by coating GaAs nanowires with a ferromagnetic material. Using an ALD and reduction process it was possible to create a Ni coating, while the rotation of the sample during a sputtering process allowed the creation of CoFeB tubes. Transport measurements during the sweeping of the external field gave an insight in the reversal process of the magnetization within the ferromagnetic tube, as well as the magnetic state at high external fields along the tube axis. The results of the EDFMR measurements on different tubes showed a multitude of different modes with considerable smaller linewidth compared to measurements on thin films of the same material. Using the assumption of a standing SW around the tube and anisotropy we were able to fit a share of the modes. By preparing more contacts over different segments of the tube and optimization of the measurement to increase the signal strength it might be possible to assign the different modes to different sections of the tube. This would lead to a better understanding of the exact behavior of the magnetization within the tube. Another possibility to detect SWs in specific areas of the tube might be to locally change the external field using e.g. an electrical current. While we used only tubes made of Ni and CoFeB the method of rotating the sample during material deposition allows the production of tubes made from a variety of different materials. For this purpose and to increase the quality of the tubes future experiments should also focus on the influence of the fabrication parameter as the deposition rate and the rotation speed on the properties of the tubes.

A. Appendix

A.1. Recipe

1. standard cleaning:
   - bathing of the sample for 1 min in aceton
   - rinsing the sample with fresh aceton and putting the sample in a second aceton bath for 1 min
   - rinsing the sample with fresh aceton and putting the sample in a isopropanol bath for 1 min
   - rinsing the sample with fresh isopropanol and dry the sample with N_2.
2. Treatment of optical sensitive resist
   - standard cleaning of the sample
   - spin-coating of the sample with LOR-3A (4500 rpm for 60 sek)
   - baking the sample at 180°C for 60 sek
   - spin-coating of the sample with S1813 G2 (6000 rpm for 40 sek)
   - baking the sample at 115°C for 60 sek
   - exposure to UV-light for 3.5 sek at a power of 11 mW/cm^2.
   - development of the structure with an optical developer MF-26A for 25 sek.
3. Treatment of electron beam sensitive resist
   - standard cleaning of the sample
   - spin-coating of the sample with AR 639.10 50k or AR 639.04 50k (6000 rpm for 120 sek)
   - baking the sample at 160°C for 120 sek
   - spin-coating of the sample with AR 679.04 950k (6000 rpm for 120 sek)

- baking the sample at 160°C for 120 sek
- exposure of the sample to an electron acceleration voltage of 20kV and a dose of 150-180 µC/cm^2 for areas and 1750 µC/cm for lines. The used aperture size was 10 µm in general and 60 µm for the pad structure of CPWs
- development of the structure with AR-600 56 for 60 sek.

4. evaporation
   - background pressure: $p \approx 1.0 \cdot 10^{-7}$mbar
   - rate: 1.5 Å/s (Au); 0.5Å/s (Py); 0.3Å/s (Cr)
5. magnetron sputtering
   - background pressure: $p \approx 2.5 \cdot 10^{-7}$mbar
   - working pressure: $p_{\mathrm{work}} \approx 3.5$ mbar
   - power: 400 W
   - Xe flow: 1 sccm
   - rate: 0.9 nm/s

A.1.1. ALD Recipes

The ALD recipes are defined with [Mar+11]

$$C \times [(t_1|t_2) + (t_3|t_4)], \tag{A.1}$$

where t_1 and t_3 are the exposure times for precursor 1 and 2, t_2 and t_4 are the associated purge times after the exposure pulses. C is the number of cycles defining the film thickness.
Al_2O_3:

$$C \times [(0.1\ \mathrm{s}|8.0\ \mathrm{s}) + (0.1\ \mathrm{s}|12.0\ \mathrm{s})], \tag{A.2}$$

with TMAl (precursor 1) and H_2O (precursor 2) at a chamber temperature of 100°C.
Ni with In Situ Reduction

$$C \times [(0.8\ \mathrm{s}|4\ \mathrm{s}) + (10.0\ \mathrm{s}|10.0\ \mathrm{s}) + (16.0\ \mathrm{s}|20.0\ \mathrm{s})], \tag{A.3}$$

with $NiCp_2$ (precursor 1),O_3 (precursor 2) and H_2 (precursor 3) at a chamber temperature of 300°C [Hub13].

A.2. Additional Measurement Data

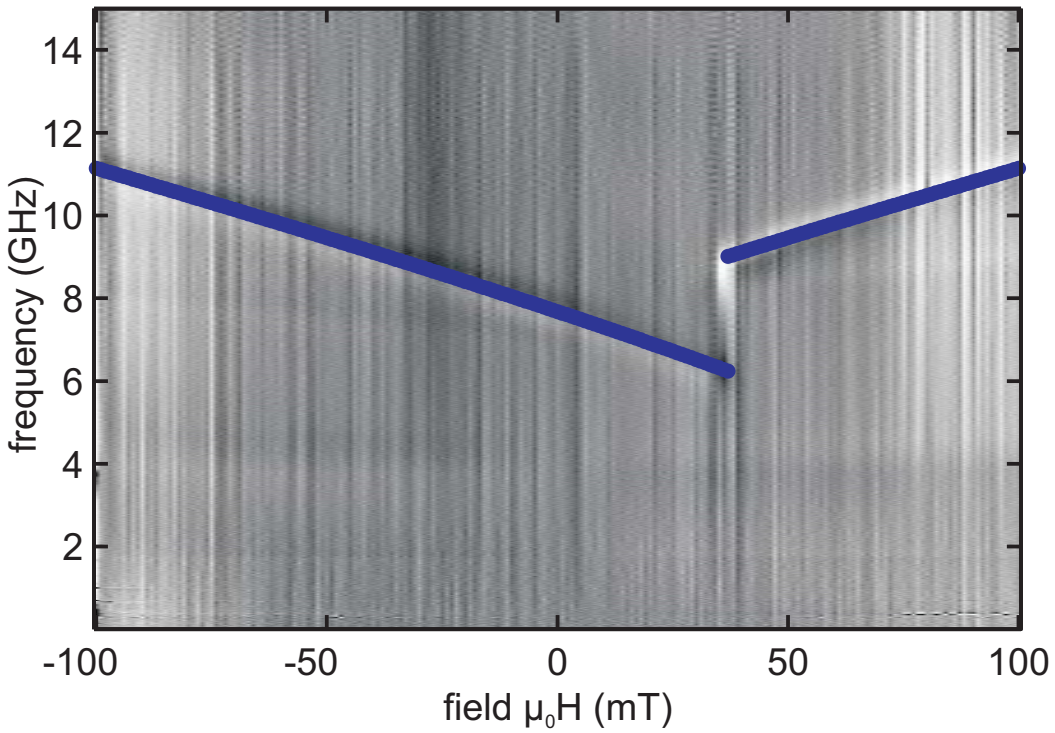

Figure A.1.: AESWS field sweep on sample SI7_1_2 at an external field angle 0°. The mode was fitted with Eq. 2.66. The used constants were $M_\mathrm{s} = 860$ kA/m, thickness $t = 34$ nm, $\mathrm{K}_\perp = 510^{-3}$J/m^3, $\theta = 90^\circ$; $\varphi_H = 0^\circ$; $\gamma = 28.4$ GHz/T, $A = 1310^{-7}$ erg/cm. The magnetization is assumed to be in-plane with $\varphi_k = 180^\circ$ at the start (-100 mT) and $\varphi_k = 0^\circ$ after the switching. By fitting the equation to the actual date we obtain the values $k = 3.4 \cdot 10^7 \frac{1}{\mathrm{m}}$ and $\mathrm{K}_\mathrm{uni} = 39 \frac{\mathrm{kJ}}{\mathrm{m}^3}$.

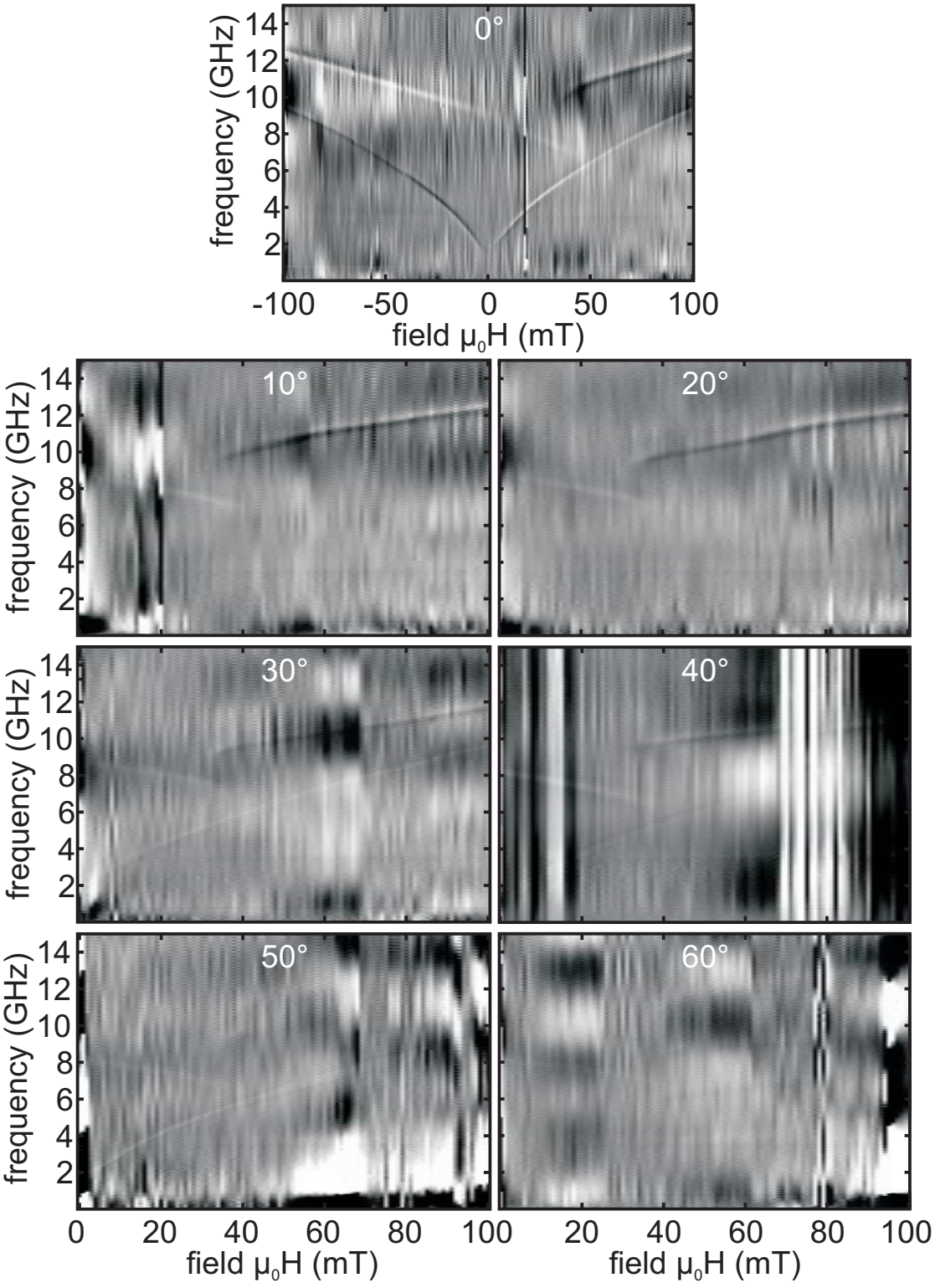

Figure A.2.: FMR data taken from sample SIB at different sample angles positions on top of a flip chip CPW.

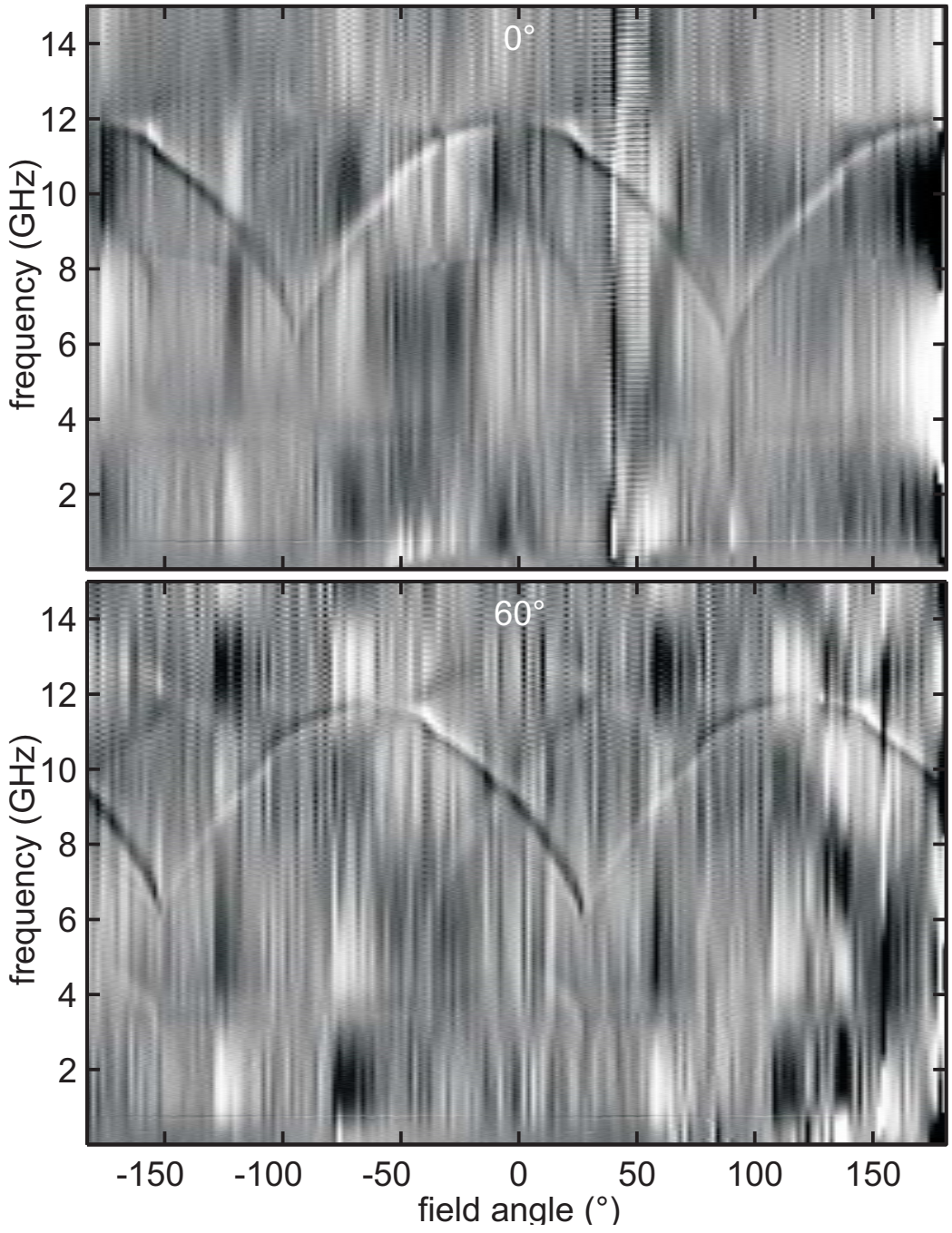

Figure A.3.: Two AESWS angle sweep on sample SIB1 with a flip chip CPW (signal line width 160μm).The orientation of link 1 is 0° and 60°.

Bibliography

[A.+07] Mougin A. et al. “Domain wall mobility, stability and Walker breakdown in magnetic nanowires”. In: *EPL (Europhysics Letters)* 78.5 (June 2007). DOI:10.1209/0295-5075/78/57007, pp. 57007–57012.

[Abo+13] G. S. Abo et al. “Definition of Magnetic Exchange Length”. In: *IEEE Transactions on Magnetics* 49.8 (Aug. 2013), pp. 4937–4939. ISSN: 0018-9464. DOI: 10.1109/TMAG.2013.2258028.

[AGG96] Gennadii A. Melkov Alexander G. Gurevich. *Magnetization Oscillations and Waves*. CRC Press, 1996.

[Aha06] A. Aharoni. *Introduction to the Theory of Ferromagnetism*. New York: Oxford University Press, 2006.

[BAC04] M. T. Bryan, D. Atkinson, and R. P. Cowburn. “Experimental study of the influence of edge roughness on magnetization switching in Permalloy nanostructures”. In: *Applied Physics Letters* 85.16 (2004), pp. 3510–3512. DOI: http://dx.doi.org/10.1063/1.1806566. URL: http://scitation.aip.org/content/aip/journal/apl/85/16/10.1063/1.1806566.

[BF33] J. D. Bernal and R. H. Fowler. “A Theory of Water and Ionic Solution, with Particular Reference to Hydrogen and Hydroxyl Ions”. In: *The Journal of Chemical Physics* 1.8 (1933), pp. 515–548. DOI: http://dx.doi.org/10.1063/1.1749327. URL: http://scitation.aip.org/content/aip/journal/jcp/1/8/10.1063/1.1749327.

[Bil+06] C. Bilzer et al. “Study of the dynamic magnetic properties of soft CoFeB films”. In: *Journal of Applied Physics* 100.5, 053903 (2006). DOI: http://dx.doi.org/10.1063/1.2337165. URL: http://scitation.aip.org/content/aip/journal/jap/100/5/10.1063/1.2337165.

[Bil07] Claus Bilzer. “Microwave susceptibility of thin ferromagnetic films: metrology and insight into magnetization dynamics”. PhD thesis. Université Paris-sud 11, 2007.

[BK86] A. Slavin B. Kalinikos. “Theory of dipole-exchange spin wave spectrum for ferromagnetic films with mixed exchange boundary conditions”. In: *J. Phys. C* 19.35 (1986), pp. 7013–7033.

[Blu01] S. Blundell. *Magnetism in Condensed Matter*. Oxford University Press, Oxford, 2001.

[Boa05] R. P. Boardman. "Computer simulation studies of magnetic nanostructures". PhD thesis. University of Southampton Faculty of Engineering, Science and Mathematics School of Engineering Sciences, 2005.

[BOF03] Matthieu Bailleul, Dominik Olligs, and Claude Fermon. "Propagating spin wave spectroscopy in a permalloy film: A quantitative analysis". In: *Applied Physics Letters* 83.5 (2003), pp. 972–974. DOI: http://dx.doi.org/10.1063/1.1597745. URL: http://scitation.aip.org/content/aip/journal/apl/83/5/10.1063/1.1597745.

[Bra+01] S. T. Bramwell et al. "Spin Correlations in $Ho_2Ti_2O_7$: A Dipolar Spin Ice System". In: *Phys. Rev. Lett.* 87 (4 2001), p. 047205. DOI: 10.1103/PhysRevLett.87.047205. URL: http://link.aps.org/doi/10.1103/PhysRevLett.87.047205.

[Bra14] Florian Brandl. "Thermal effects in laser-heated freestanding permalloy and multiferroic hybrid structures forming magnonic grating couplers and prototype spin wave multiplexers". PhD thesis. TECHNISCHE UNIVERSITÄT MÜNCHEN, July 2014.

[But+98] O. Buttner et al. "Mode beating of spin wave beams in ferrimagnetic $Lu_{2.04}Bi_{0.96}Fe_5O_{12}$ films". In: *IEEE Transactions on Magnetics* 34.4 (1998), pp. 1381–1383. ISSN: 0018-9464. DOI: 10.1109/20.706555.

[BW87] J D Bryngelson and P G Wolynes. "Spin glasses and the statistical mechanics of protein folding". In: *Proceedings of the National Academy of Sciences* 84.21 (1987), pp. 7524–7528. eprint: http://www.pnas.org/content/84/21/7524.full.pdf. URL: http://www.pnas.org/content/84/21/7524.abstract.

[CG] M. Cardona and G. Güntherodt. *Light Scattering in Solids VII: Crystal-Field and Magnetic Excitations*. Ed. by 2000. Springer-Verlag GmbH.

[CMS08] C. Castelnovo, R. Moessner, and S. L. Sondhi. "Magnetic monopoles in spin ice". In: *Nature* 451.7174 (Jan. 2008), pp. 42–45. ISSN: 0028-0836. URL: http://dx.doi.org/10.1038/nature06433.

[Coe10] J.M.D. Coey. *Magnetism and Magnetic Materials*. Cambridge, UK: Cambridge University Press, 2010.

[Cou+04] G. Counil et al. “Spin wave contributions to the high-frequency magnetic response of thin films obtained with inductive methods”. In: *Journal of Applied Physics* 95.10 (2004), pp. 5646–5652. DOI: http://dx.doi.org/10.1063/1.1697641. URL: http://scitation.aip.org/content/aip/journal/jap/95/10/10.1063/1.1697641.

[DA97] J. Gruszynski D. Anderson L. Smith. *S-Parameter Techniques for Faster, More Accurate Network Design*. Test & Measurement Application Note 95-1. Hewlett Packard. 1997.

[Dav+15] C. S. Davies et al. “Field-controlled phase-rectified magnonic multiplexer”. In: *Open Research Exeter (ORE)* (2015). DOI: 10.1109/TMAG.2015.2447010.

[DE61] R.W. Damon and J.R. Eshbach. “Magnetostatic modes of a ferromagnet slab”. In: *Journal of Physics and Chemistry of Solids* 19 (1961), pp. 308 –320. ISSN: 0022-3697. DOI: http://dx.doi.org/10.1016/0022-3697(61)90041-5. URL: http://www.sciencedirect.com/science/article/pii/0022369761900415.

[Dem+07] Vladislav E. Demidov et al. “Self-focusing of spin waves in Permalloy microstripes”. In: *Applied Physics Letters* 91.25, 252504 (2007). DOI: http://dx.doi.org/10.1063/1.2825421. URL: http://scitation.aip.org/content/aip/journal/apl/91/25/10.1063/1.2825421.

[Dem+08] Vladislav E. Demidov et al. “Nano-optics with spin waves at microwave frequencies”. In: *Applied Physics Letters* 92.23, 232503 (2008). DOI: http://dx.doi.org/10.1063/1.2945000. URL: http://scitation.aip.org/content/aip/journal/apl/92/23/10.1063/1.2945000.

[Dem+09] Vladislav E. Demidov et al. “Excitation of microwaveguide modes by a stripe antenna”. In: *Applied Physics Letters* 95.11, 112509 (2009). DOI: http://dx.doi.org/10.1063/1.3231875. URL: http://scitation.aip.org/content/aip/journal/apl/95/11/10.1063/1.3231875.

[DHS01] S. Demokritov, B. Hillebrands, and A. Slavin. “Brillouin light scattering studies of confined spin waves: linear and nonlinear confinement”. In: *Physics Reports* 348.6 (2001), pp. 441 –489. ISSN: 0370-1573. DOI: http://dx.doi.org/10.1016/S0370-1573(00)00116-2. URL: http://www.sciencedirect.com/science/article/pii/S0370157300001162.

[Dic47] R. H. Dicke. "A Computational Method Applicable to Microwave Networks". In: *Journal of Applied Physics* 18.10 (1947), pp. 873–878. DOI: http://dx.doi.org/10.1063/1.1697561. URL: http://scitation.aip.org/content/aip/journal/jap/18/10/10.1063/1.1697561.

[Dil+81] J. G. Dil et al. "Tandem multipass Fabry-Perot interferometer for Brillouin scattering". In: *APPLIED OPTICS* 20.8 (Apr. 1981), pp. 1374–1381.

[DP99] M. J. Donahue and D. G. Porter. *Interagency Report NISTIR 6376*. National Institute of Standards and Technology. Gaithersburg, Sept. 1999.

[DS09] P. Anil D. Stancil. *Spin Waves Theory and Applications*. Springer, 2009.

[DUD09] Vladislav E. Demidov, Sergei Urazhdin, and Sergej O. Demokritov. "Control of spin-wave phase and wavelength by electric current on the microscopic scale". In: *Applied Physics Letters* 95.26, 262509 (2009). DOI: http://dx.doi.org/10.1063/1.3279152. URL: http://scitation.aip.org/content/aip/journal/apl/95/26/10.1063/1.3279152.

[Ell93] Robert S. Elliott. *An Introduction to GUIDED WAVES and MICROWAVE CIRCUITS*. Prentice-Hall, Inc, 1993.

[Far+14] Alan Farhan et al. "Thermally induced magnetic relaxation in building blocks of artificial kagome spin ice". In: *Phys. Rev. B* 89 (21 June 2014), p. 214405. DOI: 10.1103/PhysRevB.89.214405. URL: http://link.aps.org/doi/10.1103/PhysRevB.89.214405.

[GA33] W. F. Giauque and Muriel F. Ashley. "Molecular Rotation in Ice at 10° K. Free Energy of Formation and Entropy of Water". In: *Phys. Rev.* 43 (1 Jan. 1933), pp. 81–82. DOI: 10.1103/PhysRev.43.81.2. URL: http://link.aps.org/doi/10.1103/PhysRev.43.81.2.

[Geo10] Steven M. George. "Atomic Layer Deposition: An Overview". In: *Chemical Reviews* 110.1 (2010). PMID: 19947596, pp. 111–131. DOI: 10.1021/cr900056b. eprint: http://dx.doi.org/10.1021/cr900056b. URL: http://dx.doi.org/10.1021/cr900056b.

[Gie05] F. Giesen. "Magnetization Dynamics of Nanostructured Ferromagnetic Rings and Rectangular Elements". Dissertation. Universität Hamburg, 2005.

[Gil04] T.L. Gilbert. "A phenomenological theory of damping in ferromagnetic materials". In: *Magnetics, IEEE Transactions on* 40.6 (Nov. 2004), pp. 3443–3449. ISSN: 0018-9464. DOI: 10.1109/TMAG.2004.836740.

[Gus+02] K. Yu. Guslienko et al. "Effective dipolar boundary conditions for dynamic magnetization in thin magnetic stripes". In: *Phys. Rev. B* 66 (13 Oct. 2002), p. 132402. DOI: 10.1103/PhysRevB.66.132402. URL: http://link.aps.org/doi/10.1103/PhysRevB.66.132402.

[HA98] Schäfer Rudolf Hubert Alex. *Magnetic Domains The Analysis of Magnetic Microstructures*. Springer, 1998.

[Har+11] M. Harder et al. "Analysis of the line shape of electrically detected ferromagnetic resonance". In: *Phys. Rev. B* 84 (5 Aug. 2011), p. 054423. DOI: 10.1103/PhysRevB.84.054423. URL: http://link.aps.org/doi/10.1103/PhysRevB.84.054423.

[Har+97] M. J. Harris et al. "Geometrical Frustration in the Ferromagnetic Pyrochlore $Ho_2Ti_2O_7$". In: *Phys. Rev. Lett.* 79 (13 Sept. 1997), pp. 2554–2557. DOI: 10.1103/PhysRevLett.79.2554. URL: http://link.aps.org/doi/10.1103/PhysRevLett.79.2554.

[Har99] U. Hartmann. "MAGNETIC FORCE MICROSCOPY". In: *Annual Review of Materials Science* 29.1 (1999), pp. 53–87. DOI: 10.1146/annurev.matsci.29.1.53. eprint: http://dx.doi.org/10.1146/annurev.matsci.29.1.53. URL: http://dx.doi.org/10.1146/annurev.matsci.29.1.53.

[Hay+07] Masamitsu Hayashi et al. "Direct observation of the coherent precession of magnetic domain walls propagating along permalloy nanowires". In: *Nat Phys* 3.1 (Jan. 2007), pp. 21–25. ISSN: 1745-2473. URL: http://dx.doi.org/10.1038/nphys464.

[HCH85] B. Heinrich, J. F. Cochran, and R. Hasegawa. "FMR linebroadening in metals due to two-magnon scattering". In: *Journal of Applied Physics* 57.8 (1985), pp. 3690–3692. DOI: http://dx.doi.org/10.1063/1.334991. URL: http://scitation.aip.org/content/aip/journal/jap/57/8/10.1063/1.334991.

[HG00] Byron C. den Hertog and Michel J. P. Gingras. "Dipolar Interactions and Origin of Spin Ice in Ising Pyrochlore Magnets". In: *Phys. Rev. Lett.* 84 (15 Apr. 2000), pp. 3430–3433. DOI: 10.1103/PhysRevLett.84.3430. URL: http://link.aps.org/doi/10.1103/PhysRevLett.84.3430.

[Hil00] Burkard Hillebrands. “Brillouin light scattering from layered magnetic structures”. English. In: *Light Scattering in Solids VII*. Ed. by Manuel Cardona and Gernot Güntherodt. Vol. 75. Topics in Applied Physics. Springer Berlin Heidelberg, 2000, pp. 174–289. ISBN: 978-3-540-66075-0. DOI: 10.1007/BFb0103386. URL: http://dx.doi.org/10.1007/BFb0103386.

[Hil05] B. Hillebrands. “Brillouin light scattering spectroscopy”. English. In: *Modern Techniques for Characterizing Magnetic Materials*. Ed. by Yimei Zhu. Springer US, 2005, pp. 543–578. ISBN: 978-1-4020-8007-4. DOI: 10.1007/0-387-23395-4_14. URL: http://dx.doi.org/10.1007/0-387-23395-4_14.

[HS98] A. Hubert and R. Schaefer. *Magnetic Domains - The Analysis of Magnetic Microstructures*. Springer, 1998.

[Hub13] Rupert Huber. “Control of Spin Waves on the Nanoscale in One-Dimensional Magnonic Crystals and Atomic Layer Deposition of Metallic Ferromagnets for Second Generation of Nanomaterials”. PhD thesis. Technische Universität München, 2013.

[Itr] *ITRS: International Technology Roadmap for Semiconductors*. Tech. rep. 2014.

[Jac60] P Jacquinot. “New developments in interference spectroscopy”. In: *Reports on Progress in Physics* 23.1 (1960), p. 267. URL: http://stacks.iop.org/0034-4885/23/i=1/a=305.

[K62] *Model 6220 DC Current Source Model 6221 AC and DC Current Source*. Keithley. June 2005.

[KA00] P.J Kelly and R.D Arnell. “Magnetron sputtering: a review of recent developments and applications”. In: *Vacuum* 56.3 (2000), pp. 159 –172. ISSN: 0042-207X. DOI: http://dx.doi.org/10.1016/S0042-207X(99)00189-X. URL: http://www.sciencedirect.com/science/article/pii/S0042207X9900189X.

[Kal+06] Sangita S. Kalarickal et al. “Ferromagnetic resonance linewidth in metallic thin films: Comparison of measurement methods”. In: *Journal of Applied Physics* 99.9, 093909 (2006). DOI: http://dx.doi.org/10.1063/1.2197087. URL: http://scitation.aip.org/content/aip/journal/jap/99/9/10.1063/1.2197087.

[Kap+12] Vassilios Kapaklis et al. “Melting artificial spin ice”. In: *New Journal of Physics* 14.3 (2012), p. 035009. URL: http://stacks.iop.org/1367-2630/14/i=3/a=035009.

[KBW10] Alexander Khitun, Mingqiang Bao, and Kang L Wang. "Magnonic logic circuits". In: *Journal of Physics D: Applied Physics* 43.26 (2010), p. 264005. URL: http://stacks.iop.org/0022-3727/43/i=26/a=264005.

[KCC05] Bijoy Kuanr, R. E. Camley, and Z. Celinski. "Narrowing of the frequency-linewidth in structured magnetic strips: Experiment and theory". In: *Applied Physics Letters* 87.1, 012502 (2005). DOI: http://dx.doi.org/10.1063/1.1968433. URL: http://scitation.aip.org/content/aip/journal/apl/87/1/10.1063/1.1968433.

[Kit48] Charles Kittel. "On the Theory of Ferromagnetic Resonance Absorption". In: *Phys. Rev.* 73 (2 Jan. 1948), pp. 155–161. DOI: 10.1103/PhysRev.73.155. URL: http://link.aps.org/doi/10.1103/PhysRev.73.155.

[Kit49] Charles Kittel. "Physical Theory of Ferromagnetic Domains". In: *Rev. Mod. Phys.* 21 (4 Oct. 1949), pp. 541–583. DOI: 10.1103/RevModPhys.21.541. URL: http://link.aps.org/doi/10.1103/RevModPhys.21.541.

[Kit66] C. Kittel. *Introduction to Solid State Physics*. Wiley, New York, 1966.

[KKS07] K. J. Kennewell, M. Kostylev, and R. L. Stamps. "Calculation of spin wave mode response induced by a coplanar microwave line". In: *Journal of Applied Physics* 101.9, 09D107 (2007). DOI: http://dx.doi.org/10.1063/1.2710068. URL: http://scitation.aip.org/content/aip/journal/jap/101/9/10.1063/1.2710068.

[KM05] Charles Kittel and Paul McEuen. *Introduction to Solid State Physics*. Ed. by 8. John Wiley & Sons, Inc, 2005.

[Kos+05] M. P. Kostylev et al. "Spin-wave logical gates". In: *Applied Physics Letters* 87.15, 153501 (2005). DOI: http://dx.doi.org/10.1063/1.2089147. URL: http://scitation.aip.org/content/aip/journal/apl/87/15/10.1063/1.2089147.

[Lan+07] P. Landeros et al. "Reversal modes in magnetic nanotubes". In: *Applied Physics Letters* 90.10, 102501 (2007). DOI: http://dx.doi.org/10.1063/1.2437655. URL: http://scitation.aip.org/content/aip/journal/apl/90/10/10.1063/1.2437655.

[Lan+09] P. Landeros et al. "Equilibrium states and vortex domain wall nucleation in ferromagnetic nanotubes". In: *Phys. Rev. B* 79 (2 Jan. 2009), p. 024404. DOI: 10.1103/PhysRevB.79.024404. URL: http://link.aps.org/doi/10.1103/PhysRevB.79.024404.

[LAS81] S. M. Lindsay, M. W. Anderson, and J. R. Sandercock. "Construction and alignment of a high performance multipass vernier tandem Fabry-Perot interferometer". In: *Review of Scientific Instruments* 52.10 (1981), pp. 1478–1486. DOI: http://dx.doi.org/10.1063/1.1136479. URL: http://scitation.aip.org/content/aip/journal/rsi/52/10/10.1063/1.1136479.

[Liu+03] Xiaomin Liu et al. "High-frequency behavior of electrodeposited Fe-Co-Ni alloys". In: *Magnetics, IEEE Transactions on* 39.5 (Sept. 2003), pp. 2362–2364. DOI: 10.1109/TMAG.2003.815450.

[LL35] E. Lifshits L. Landau. "Theory of the dispersion of magnetic permeability in ferromagnetic bodies". In: *Physikalische Zeitschrift der Sowjetunion* 8 (1935), p. 153.

[LM03] P. Larson and I. I. Mazin. "Magnetic properties of $SmCo_5$ and YCo_5". In: *Journal of Applied Physics* 93.10 (2003), pp. 6888–6890. DOI: http://dx.doi.org/10.1063/1.1556154. URL: http://scitation.aip.org/content/aip/journal/jap/93/10/10.1063/1.1556154.

[LN10] P. Landeros and Álvaro S. Núnez. "Domain wall motion on magnetic nanotubes". In: *Journal of Applied Physics* 108.3, 033917 (2010). DOI: http://dx.doi.org/10.1063/1.3466747. URL: http://scitation.aip.org/content/aip/journal/jap/108/3/10.1063/1.3466747.

[LR02] Markku Leskelä and Mikko Ritala. "Atomic layer deposition (ALD): from precursors to thin film structures". In: *Thin Solid Films* 409.1 (2002). Proceedings of the 2nd Asian Conference on Chemical Vapour Depostion, pp. 138 –146. ISSN: 0040-6090. DOI: http://dx.doi.org/10.1016/S0040-6090(02)00117-7. URL: http://www.sciencedirect.com/science/article/pii/S0040609002001177.

[Mar+11] Alex B. F. Martinson et al. "Atomic Layer Deposition of Fe_2O_3 Using Ferrocene and Ozone". In: *The Journal of Physical Chemistry C* 115.10 (2011), pp. 4333–4339. DOI: 10.1021/jp110203x. eprint: http://dx.doi.org/10.1021/jp110203x. URL: http://dx.doi.org/10.1021/jp110203x.

[Mat+00] K Matsuhira et al. "Low temperature magnetic properties of frustrated pyrochlore ferromagnets Ho 2 Sn 2 O 7 and Ho 2 Ti 2 O 7". In: *Journal of Physics: Condensed Matter* 12.40 (2000), p. L649. URL: http://stacks.iop.org/0953-8984/12/i=40/a=103.

[MD97] R.D. McMichael and M.J. Donahue. “Head to head domain wall structures in thin magnetic strips”. In: *Magnetics, IEEE Transactions on* 33.5 (Sept. 1997), pp. 4167–4169. ISSN: 0018-9464. DOI: 10.1109/20.619698.

[MDB] A. Kovács D. Meertens and R. E. Dunin-Borkowski. *personal communication*.

[Mel+10] Paula Mellado et al. “Dynamics of Magnetic Charges in Artificial Spin Ice”. In: *Phys. Rev. Lett.* 105 (18 Oct. 2010), p. 187206. DOI: 10.1103/PhysRevLett.105.187206. URL: http://link.aps.org/doi/10.1103/PhysRevLett.105.187206.

[MGH07] N. Mecking, Y. S. Gui, and C.-M. Hu. “Microwave photovoltage and photoresistance effects in ferromagnetic microstrips”. In: *Phys. Rev. B* 76 (22 Dec. 2007), p. 224430. DOI: 10.1103/PhysRevB.76.224430. URL: http://link.aps.org/doi/10.1103/PhysRevB.76.224430.

[MM06] G. Möller and R. Moessner. “Artificial Square Ice and Related Dipolar Nanoarrays”. In: *Phys. Rev. Lett.* 96 (23 June 2006), p. 237202. DOI: 10.1103/PhysRevLett.96.237202. URL: http://link.aps.org/doi/10.1103/PhysRevLett.96.237202.

[MP75] T.R. McGuire and R.I. Potter. “Anisotropic magnetoresistance in ferromagnetic 3d alloys”. In: *Magnetics, IEEE Transactions on* 11.4 (July 1975), pp. 1018–1038. ISSN: 0018-9464. DOI: 10.1109/TMAG.1975.1058782.

[MW87] Y. Martin and H. K. Wickramasinghe. “Magnetic imaging by "force microscopy" with 1000 Åresolution”. In: *Applied Physics Letters* 50.20 (1987), pp. 1455–1457. DOI: http://dx.doi.org/10.1063/1.97800. URL: http://scitation.aip.org/content/aip/journal/apl/50/20/10.1063/1.97800.

[NBG08] Sebastian Neusser, Bernhard Botters, and Dirk Grundler. “Localization, confinement, and field-controlled propagation of spin waves in $Ni_{80}Fe_{20}$ antidot lattices”. In: *Phys. Rev. B* 78 (5 Aug. 2008), p. 054406. DOI: 10.1103/PhysRevB.78.054406. URL: http://link.aps.org/doi/10.1103/PhysRevB.78.054406.

[Neu11] S. Neusser. “Spin Waves in Antidot Lattices”. PhD thesis. Technische Universität München, 2011.

[Opt] *Optic course*. University of Colorado Boulder Department of Physics. 2005. URL: http://www.colorado.edu/physics/phys4510/phys4510_fa05/.

[Osb45] J. A. Osborn. “Demagnetizing Factors of the General Ellipsoid”. In: *Phys. Rev.* 67 (11-12 June 1945), pp. 351–357. DOI: 10.1103/PhysRev.67.351. URL: http://link.aps.org/doi/10.1103/PhysRev.67.351.

[Ost00] W. Ostwald. “Über die vermeintliche Isomerie des roten und gelben Quecksilberoxyds und die Oberflächenspannung fester Körper”. In: *Z. Phys. Chem* 34 (1900), pp. 495–503.

[Pat68] Carl E. Patton. “Linewidth and Relaxation Processes for the Main Resonance in the Spin-Wave Spectra of Ni-Fe Alloy Films”. In: *Journal of Applied Physics* 39.7 (1968), pp. 3060–3068. DOI: http://dx.doi.org/10.1063/1.1656733. URL: http://scitation.aip.org/content/aip/journal/jap/39/7/10.1063/1.1656733.

[Pau35] Linus Pauling. “The Structure and Entropy of Ice and of Other Crystals with Some Randomness of Atomic Arrangement”. In: *Journal of the American Chemical Society* 57.12 (1935), pp. 2680–2684. DOI: 10.1021/ja01315a102. eprint: http://dx.doi.org/10.1021/ja01315a102. URL: http://dx.doi.org/10.1021/ja01315a102.

[Pi2] *PZ82E P-5x7/P-5x8 Stage User Manual*. Physik Instrumente (PI) GmbH & Co. KG. Auf der Römerstr. 1 76228 Karlsruhe, Germany, Sept. 2013.

[PWB08] Korbinian Perzlmaier, Georg Woltersdorf, and Christian H. Back. “Observation of the propagation and interference of spin waves in ferromagnetic thin films”. In: *Phys. Rev. B* 77.5 (Feb. 2008), p. 054425. DOI: 10.1103/PhysRevB.77.054425. URL: http://link.aps.org/doi/10.1103/PhysRevB.77.054425.

[PY15] Stuart Parkin and See-Hun Yang. “Memory on the racetrack”. In: *Nat Nano* 10.3 (Mar. 2015), pp. 195–198. ISSN: 1748-3387. URL: http://dx.doi.org/10.1038/nnano.2015.41.

[QBC08] Yi Qi, T. Brintlinger, and John Cumings. “Direct observation of the ice rule in an artificial kagome spin ice”. In: *Phys. Rev. B* 77 (9 Mar. 2008), p. 094418. DOI: 10.1103/PhysRevB.77.094418. URL: http://link.aps.org/doi/10.1103/PhysRevB.77.094418.

[Ram+99] A. P. Ramirez et al. “Zero-point entropy in /‘spin ice/’”. In: *Nature* 399.6734 (May 1999), pp. 333–335. ISSN: 0028-0836. URL: http://dx.doi.org/10.1038/20619.

[Ram94] A P Ramirez. "Strongly Geometrically Frustrated Magnets". In: *Annual Review of Materials Science* 24.1 (1994), pp. 453–480. DOI: 10.1146/annurev.ms.24.080194.002321. eprint: http://dx.doi.org/10.1146/annurev.ms.24.080194.002321. URL: http://dx.doi.org/10.1146/annurev.ms.24.080194.002321.

[Ros+00] S. Rosenkranz et al. "Crystal-field interaction in the pyrochlore magnet $Ho_2Ti_2O_7$". In: *Journal of Applied Physics* 87.9 (2000), pp. 5914–5916. DOI: http://dx.doi.org/10.1063/1.372565. URL: http://scitation.aip.org/content/aip/journal/jap/87/9/10.1063/1.372565.

[Rou+15] O. Rousseau et al. "Realization of a micrometre-scale spin-wave interferometer". In: *Scientific Reports* 5 (May 2015), p. 9873. URL: http://dx.doi.org/10.1038/srep09873.

[Roy] S. C. Dutta Roy. *Circuit Theory*. Department of Electrical Engineering. URL: http://textofvideo.nptel.iitm.ac.in/video.php?courseId=108102042.

[Rud+09] Andreas Rudolph et al. "Ferromagnetic GaAs/GaMnAs Core-Shell Nanowires Grown by Molecular Beam Epitaxy". In: *Nano Letters* 9.11 (2009). PMID: 19731920, pp. 3860–3866. DOI: 10.1021/nl9020717. eprint: http://dx.doi.org/10.1021/nl9020717. URL: http://dx.doi.org/10.1021/nl9020717.

[Ruf+12] Daniel Ruffer et al. "Magnetic states of an individual Ni nanotube probed by anisotropic magnetoresistance". In: *Nanoscale* 4 (16 2012), pp. 4989–4995. DOI: 10.1039/C2NR31086D. URL: http://dx.doi.org/10.1039/C2NR31086D.

[Rug+90] D. Rugar et al. "Magnetic force microscopy: General principles and application to longitudinal recording media". In: *Journal of Applied Physics* 68.3 (1990), pp. 1169–1183. DOI: http://dx.doi.org/10.1063/1.346713. URL: http://scitation.aip.org/content/aip/journal/jap/68/3/10.1063/1.346713.

[Rüf+14] Daniel Rüffer et al. "Anisotropic magnetoresistance of individual CoFeB and Ni nanotubes with values of up to 1.4% at room temperature". In: *APL Mater.* 2.7, 076112 (2014). DOI: http://dx.doi.org/10.1063/1.4891276. URL: http://scitation.aip.org/content/aip/journal/aplmater/2/7/10.1063/1.4891276.

[Rüf14] Daniel Rüffer. "Magnetic states and spin-wave modes in single ferromagnetic nanotubes". PhD thesis. ÉCOLE POLYTECHNIQUE FÉDÉRALE DE LAUSANNE, 2014.

[SA77] T. Suntola and J. Antson. *Method for producing compound thin films*. US Patent 4,058,430. Nov. 1977. URL: http://www.google.de/patents/US4058430.

[Sch13] Thomas Schwarze. "SpinWaves in 2D and 3D Magnonic Crystals: From Nanostructured Ferromagnetic Materials to Chiral Helimagnets". PhD thesis. Technischen Universität München, 2013.

[SE43] R. I. Sarbacher and W. A. Edson. *Hyper and Ultrahigh Frequencyy Engineering*. New York: J. Wiley & Sons, Inc., 1943.

[She+12] Yichen Shen et al. "Dynamics of artificial spin ice: a continuous honeycomb network". In: *New Journal of Physics* 14.3 (2012), p. 035022. URL: http://stacks.iop.org/1367-2630/14/i=3/a=035022.

[Sil+99] T. J. Silva et al. "Inductive measurement of ultrafast magnetization dynamics in thin-film Permalloy". In: *Journal of Applied Physics* 85.11 (1999), pp. 7849–7862. DOI: http://dx.doi.org/10.1063/1.370596. URL: http://scitation.aip.org/content/aip/journal/jap/85/11/10.1063/1.370596.

[Sim01] Rainee N. Simons. *Coplanar Waveguide Circuits, Components, and Systems*. Wiley-interscience John Wiley & sons, inc, 2001.

[Sko08] R. Skomski. *Simple models of magnetism*. Oxford University Press, Oxford, 2008.

[Son+05] Sang Jun Son et al. "Magnetic Nanotubes for Magnetic-Field-Assisted Bioseparation, Biointeraction, and Drug Delivery". In: *Journal of the American Chemical Society* 127.20 (2005). PMID: 15898772, pp. 7316–7317. DOI: 10.1021/ja0517365. eprint: http://dx.doi.org/10.1021/ja0517365. URL: http://dx.doi.org/10.1021/ja0517365.

[Srs] URL: http://www.thinksrs.com/downloads/PDFs/ApplicationNotes/AboutLIAs.pdf.

[Sun92] Tuomo Suntola. "Papers presented at the International Workshop on Science and Technology of Thin Films for the 21st Century, Evanston,IL, USA, July 28-August 2, 1991 Atomic layer epitaxy". In: *Thin Solid Films* 216.1 (1992), pp. 84 – 89. ISSN: 0040-6090. DOI: http://dx.doi.org/10.1016/0040-6090(92)90874-B. URL: http://www.sciencedirect.com/science/article/pii/004060909290874B.

[SW74] N. L. Schryer and L. R. Walker. "The motion of 180° domain walls in uniform dc magnetic fields". In: *Journal of Applied Physics* 45.12 (1974), pp. 5406–5421. DOI: http://dx.doi.org/10.1063/1.1663252. URL: http://scitation.aip.org/content/aip/journal/jap/45/12/10.1063/1.1663252.

[TDC86] G Toulouse, S Dehaene, and J P Changeux. "Spin glass model of learning by selection". In: *Proceedings of the National Academy of Sciences* 83.6 (1986), pp. 1695–1698. eprint: http://www.pnas.org/content/83/6/1695.full.pdf. URL: http://www.pnas.org/content/83/6/1695.abstract.

[Tec04] Agilent Technologies. *Network Analyzer Basics*. 2004.

[Tfp] *TANDEM FABRY-PEROT INTERFEROMETER TFP-1 Operator Manual*. JRS Scientific Instruments. Im Grindel 6 8932 Mettmenstetten, Switzerland.

[Tho56] W. Thomson. "On the Electro-Dynamic Qualities of Metals:–Effects of Magnetization on the Electric Conductivity of Nickel and of Iron". In: *Proceedings of the Royal Society of London* 8 (1856), pp. 546–550. ISSN: 03701662. URL: http://www.jstor.org/stable/111415.

[TP07] Luc Thomas and Stuart Parkin. "Current Induced Domain-wall Motion in Magnetic Nanowires". In: *Handbook of Magnetism and Advanced Magnetic Materials*. John Wiley & Sons, Ltd, 2007. ISBN: 9780470022184. DOI: 10.1002/9780470022184.hmm210. URL: http://dx.doi.org/10.1002/9780470022184.hmm210.

[US04] W. Casey Uhlig and Jing Shi. "Systematic study of the magnetization reversal in patterned Co and NiFe Nanolines". In: *Applied Physics Letters* 84.5 (2004), pp. 759–761. DOI: http://dx.doi.org/10.1063/1.1645332. URL: http://scitation.aip.org/content/aip/journal/apl/84/5/10.1063/1.1645332.

[VB10] V. Vlaminck and M. Bailleul. "Spin-wave transduction at the submicrometer scale: Experiment and modeling". In: *Phys. Rev. B* 81 (1 Jan. 2010), p. 014425. DOI: 10.1103/PhysRevB.81.014425. URL: http://link.aps.org/doi/10.1103/PhysRevB.81.014425.

[Vog+12] K. Vogt et al. "Spin waves turning a corner". In: *Applied Physics Letters* 101.4, 042410 (2012). DOI: http://dx.doi.org/10.1063/1.4738887. URL: http://scitation.aip.org/content/aip/journal/apl/101/4/10.1063/1.4738887.

[Wal57] L. R. Walker. “Magnetostatic Modes in Ferromagnetic Resonance”. In: *Phys. Rev.* 105 (2 Jan. 1957), pp. 390–399. DOI: 10.1103/PhysRev.105.390. URL: http://link.aps.org/doi/10.1103/PhysRev.105.390.

[Wan+06] R. F. Wang et al. “Artificial "spin ice" in a geometrically frustrated lattice of nanoscale ferromagnetic islands”. In: *Nature* 439.7074 (Jan. 2006), pp. 303–306. ISSN: 0028-0836. URL: http://dx.doi.org/10.1038/nature04447.

[Wan07] Ruifang Wang. “GEOMETRICAL MAGNETIC FRUSTRATION AND DEMAGNETIZATION OF ARTIFICIAL SPIN ICE”. PhD thesis. Pennsylvania State University, 2007.

[WBL02] A. S. Wills, R. Ballou, and C. Lacroix. “Model of localized highly frustrated ferromagnetism: The *kagomé* spin ice”. In: *Phys. Rev. B* 66 (14 Oct. 2002), p. 144407. DOI: 10.1103/PhysRevB.66.144407. URL: http://link.aps.org/doi/10.1103/PhysRevB.66.144407.

[WE64] R. S. Wagner and W. C. Ellis. “VAPOR-LIQUID-SOLID MECHANISM OF SINGLE CRYSTAL GROWTH”. In: *Applied Physics Letters* 4.5 (1964), pp. 89–90. DOI: http://dx.doi.org/10.1063/1.1753975. URL: http://scitation.aip.org/content/aip/journal/apl/4/5/10.1063/1.1753975.

[Web+12] D. P. Weber et al. “Cantilever Magnetometry of Individual Ni Nanotubes”. In: *Nano Letters* 12.12 (2012). PMID: 23134122, pp. 6139–6144. DOI: 10.1021/nl302950u. eprint: http://dx.doi.org/10.1021/nl302950u. URL: http://dx.doi.org/10.1021/nl302950u.

[Web14] Dennis Patrick Weber. “Dynamic Cantilever Magnetometry of Individual Ferromagnetic Nanotubes”. PhD thesis. Philosophisch-Naturwissenschaftlichen Fakultät der Universität Basel, 2014.

[Wen69] C.P. Wen. “Coplanar Waveguide: A Surface Strip Transmission Line Suitable for Nonreciprocal Gyromagnetic Device Applications”. In: *Microwave Theory and Techniques, IEEE Transactions on* 17.12 (Dec. 1969), pp. 1087–1090. DOI: 10.1109/TMTT.1969.1127105.

[Yan+11] Ming Yan et al. “Fast domain wall dynamics in magnetic nanotubes: Suppression of Walker breakdown and Cherenkov-like spin wave emission”. In: *Applied Physics Letters* 99.12, 122505 (2011). DOI: http://dx.doi.org/10.1063/1.3643037. URL: http://scitation.aip.org/content/aip/journal/apl/99/12/10.1063/1.3643037.

[Yan+13] Ming Yan et al. “Spin-Cherenkov effect and magnonic Mach cones”. In: *Phys. Rev. B* 88 (22 Dec. 2013), p. 220412. DOI: 10.1103/PhysRevB.88.220412. URL: http://link.aps.org/doi/10.1103/PhysRevB.88.220412.

[Yu+13] Haiming Yu et al. “Omnidirectional spin-wave nanograting coupler”. In: *Nat Commun* 4 (Nov. 2013), pp. –. URL: http://dx.doi.org/10.1038/ncomms3702.

[Zei13] Katharina Zeissler. “MAGNETIC AND ELECTRICAL TRANSPORT PROPERTIES OF ARTIFICIAL SPIN ICE”. PhD thesis. Imperial College London, 2013.

[Zha+04] Daihua Zhang et al. “Magnetite (Fe3O4) Core-Shell Nanowires: Synthesis and Magnetoresistance”. In: *Nano Letters* 4.11 (2004), pp. 2151–2155. DOI: 10.1021/nl048758u. eprint: http://dx.doi.org/10.1021/nl048758u. URL: http://dx.doi.org/10.1021/nl048758u.

[Zhu05] Yimei Zhu, ed. *MODERN TECHNIQUES FOR CHARACTERIZING MAGNETIC MATERIALS*. Springer US, 2005. DOI: 10.1007/b101202.

Publications

- V. S. Bhat, F. Heimbach, I. Stasinopoulos, and D. Grundler: Magnetization dynamics of topological defects and the spin solid in a kagome artificial spin ice, Phys. Rev. B **93**, 140401(R) (2016)
- Haiming Yu, O. d'Allivy Kelly, V. Cros, R. Bernard, P. Bortolotti, A. Anane, F. Brandl, F. Heimbach, and D. Grundler: Approaching soft x-ray wavelengths in nanomagnet-based microwave technology, Nature Communications **7**, 11255 (2016)
- K. Baumgaertl , F. Heimbach, S. Maendl, D. Rüffer, A. Fontcuberta i Morral, D. Grundler: Magnetization reversal in individual Py and CoFeB nanotubes locally probed via anisotropic magnetoresistance and anomalous Nernst effect, Appl. Phys. Lett. **108**, 132408 (2016)
- J. Klein, J. Wierzbowski, A. Regler, J. Becker, F. Heimbach, K. Müller, M. Kaniber, and J. Finley: Stark Effect Spectroscopy of Mono- and Few-Layer MoS2, Nano Lett. **16** (3), pp 1554−1559 (2016)
- B. Gross, D. P. Weber, D. Ruffer, A. Buchter, F. Heimbach, A. Fontcuberta i Morral, D. Grundler, and M. Poggio: Dynamic cantilever magnetometry of individual CoFeB nanotubes, Phys. Rev. B **93**, 064409 (2016)
- A. Buchter, R. Wolbing, M. Wyss, O. F. Kieler, T. Weimann, J. Kohlmann, A. B. Zorin, D. Ruffer, F. Matteini, G. Tütüncüoglu, F. Heimbach, A. Kleibert, A. Fontcuberta i Morral, D. Grundler, R. Kleiner, D. Koelle and M. Poggio: Magnetization reversal of an individual exchange-biased permalloy nanotube, Phys. Rev. B **92**, 214432 (2015)
- D. Rüffer, M. Slot, R. Huber, T. Schwarze, F. Heimbach, G. Tütüncüoglu, F. Matteini, E. Russo-Averchi, A. Kovács, R. Dunin-Borkowski, R. R. Zamani, J. R. Morante, J. Arbiol, A. Fontcuberta i Morral, and D. Grundler: Anisotropic magnetoresistance of individual CoFeB and Ni nanotubes with values of up to 1.4% at room temperature, APL Mater **2**, 076112 (2014)

Acknowledgements

I would like to express gratitude to all people who contributed to this work. In particular:

- Prof. Uli Gerland for supervision of the PhD examination, Prof. Dr. Dirk Grundler for being the first examiner, Prof. Martin Brandt for being the second examiner.
- Prof. Dr. Dirk Grundler for giving me the chance to work at E10, for many fruitful discussions about all aspects of my work and for giving me all opportunities to evolve into a good scientist.
- Tobias Stückler for EDFMR tube measurements.
- Dr. Daniel Rüffer from EPFL for the fabrication of Nanotube samples.
- Dr. Rupert Huber, Dr. Florian Brandl, Dr. Thomas Schwarze, Dr. Florian Herzog and Prof. Haiming Yu for fruitful collaboration at E10.
- Stefan Mändl and Schorsch Sauther, for the support at the BLS setup.
- Dr. Andras Kovàcs from Forschungszentrum Juelich for providing graphical material.
- All members of the Nanotube project for the fruitful collaboration.
- Vinayak Bhat for proofreading parts of my thesis and his simulations.
- my brothers for proofreading my thesis.
- Thomas Rapp, Thomas Neukel, Stephan Lichtenauer, Johannes Seitz and Paul Berberich for frequent and immediate technical support.
- Claudine Voelcker for organizational support.
- All coworkers at E10 for collaboration and great atmosphere: Ioannis Stasinopoulos, Stephan Albert, Matthias Brasse, Stefanos Chalkidis, Stefan Weichselbaumer, Johannes Mendil, Korbinian BaumgÃd'rtl and Dr. Marc Wilde.
- All my friends and family who have supported me throughout this whole time.

The research leading to these results has received funding from the German Excellence Cluster Nanosystems Initiative Munich II (NIM II), the DFG in the German priority program SPP1538 spincaloricttransport viaprojectGR1640/5-2, and the Transregio TRR80 "From electronic correlations to functionality". The support is gratefully acknowledged.